

Tipping microtubule polymerization:

Insights from in vitro reconstitution

Amol Aher

ISBN: 978-90-393-6900-5

The studies described in this thesis were performed at the division of Cell Biology at the Faculty of Science of Utrecht University in Utrecht, the Netherlands.

Cover: Processively growing tips in the sky.

Cover by Amol Aher
Printed by Gildeprint

Copyright by Amol Aher, 2017

Tipping microtubule polymerization: Insights from in vitro reconstitution

**Het controleren van microtubuli polymerisatie:
inzichten van in vitro reconstituties
(met een samenvatting in het Nederlands)**

Proefschrift

ter verkrijging van de graad van doctor aan de Universiteit Utrecht op gezag van de rector magnificus, prof.dr. G.J. van der Zwaan, ingevolge het besluit van het college voor promoties in het openbaar te verdedigen op woensdag 29 november 2017 des middags te 12.45 uur

door

Amol Bapurao Aher

geboren op 19 april 1989 te Aurangabad, India

Promoter: Prof. dr. A.S. Akhmanova

“What I cannot create, I do not understand”

Richard Feynman

Table of contents

Chapter 1	9
General Introduction	
Chapter 2	27
CLASP mediates microtubule tip and lattice repair through a single TOG domain	
Chapter 3	69
Insights into microtubule rescue from in vitro reconstitution of the CLIP-170-CLASP complex	
Chapter 4	83
Regulation of microtubule growth by a complex of chTOG, SLAIN2 and EB3: in vitro reconstitution with purified proteins	
Chapter 5	99
Centriolar CPAP/SAS-4 imparts slow processive microtubule growth	
Chapter 6	139
General Discussion	
Addendum	151
Summary	
Samenvatting	
Curriculum vitae	
List of publications	
Acknowledgements	

1

General Introduction

Amol Aher

1 Microtubules are key cytoskeletal elements that are essential for several cellular processes that include intracellular transport, cell morphogenesis, migration and cell division. Microtubules are biopolymers made of α - β tubulin heterodimers that associate longitudinally in a head to tail fashion to form a protofilament, and typically 13 protofilaments associate to form a complete tube. Microtubules are self-assembling fibers that can stochastically switch between phases of growth and shrinkage, a process known as dynamic instability (Mitchison and Kirschner, 1984). The precise regulation of the dynamic switching between phases of growth and shrinkage is particularly apparent during cell division, when microtubules form the spindle apparatus, and specifically in anaphase where depolymerising microtubules drive chromosome movement towards the spindle poles. Several Microtubule Associated Proteins (MAPs) control microtubule dynamics by favouring either growth or disassembly at the plus ends of microtubules. In this chapter, we will discuss the regulation of microtubule plus end dynamics in different settings and provide an overview of the factors responsible for this regulation.

General Introduction

Microtubules are composed of tubulin dimers that can self-assemble spontaneously in vitro, while in cells, microtubule polymerization typically occurs from a template such as the γ -tubulin ring complex. The α - β tubulin heterodimers are arranged in a head to tail manner so that β -tubulins are exposed at the microtubule plus end and α -tubulins are exposed at the minus end (Figure 1). α and β -tubulin subunits have GTP bound to them at the N-site (non-exchangeable site) and E-site (exchangeable site), respectively. GTP bound to α -tubulin has been proposed to stabilise the dimer with its bound magnesium (Menendez et al., 1998), whereas GTP bound to β -tubulin gets hydrolysed to GDP after incorporation into the lattice. This occurs with a time delay resulting in the formation of a GTP cap (Mitchison and Kirschner, 1984). Microtubule stability is governed by the presence of the stabilizing GTP cap at the end of a growing microtubule: polymerizing microtubules have the GTP cap, whereas the loss of the cap results in a switch from growth to depolymerization (an event termed catastrophe). Growing microtubules have been reported to have either blunt ends or protrusions of tubulin sheets ranging from 50 to 2000 nm in length (Chretien et al., 1995; Mandelkow et al., 1991). The latter may represent ageing tip structures, which have been proposed to predispose a microtubule to a catastrophe (Coombes et al., 2013; Gardner et al., 2011) (Figure 1). When a microtubule starts depolymerizing, straight protofilaments at the end alter their conformation into outwardly curled peeling ones (Arnal et al., 2000; Mandelkow et al., 1991). Recent high resolution cryo-EM studies showed that GTP hydrolysis leads to microtubule lattice compaction along the longitudinal inter-dimer interface at the E-site leading to rearrangements in both the α and β tubulin subunits (Alushin et al., 2014). It was proposed that GTP hydrolysis leads to a conformational strain at the E-site, which is relieved upon depolymerisation, leading to the formation of peeling protofilaments.

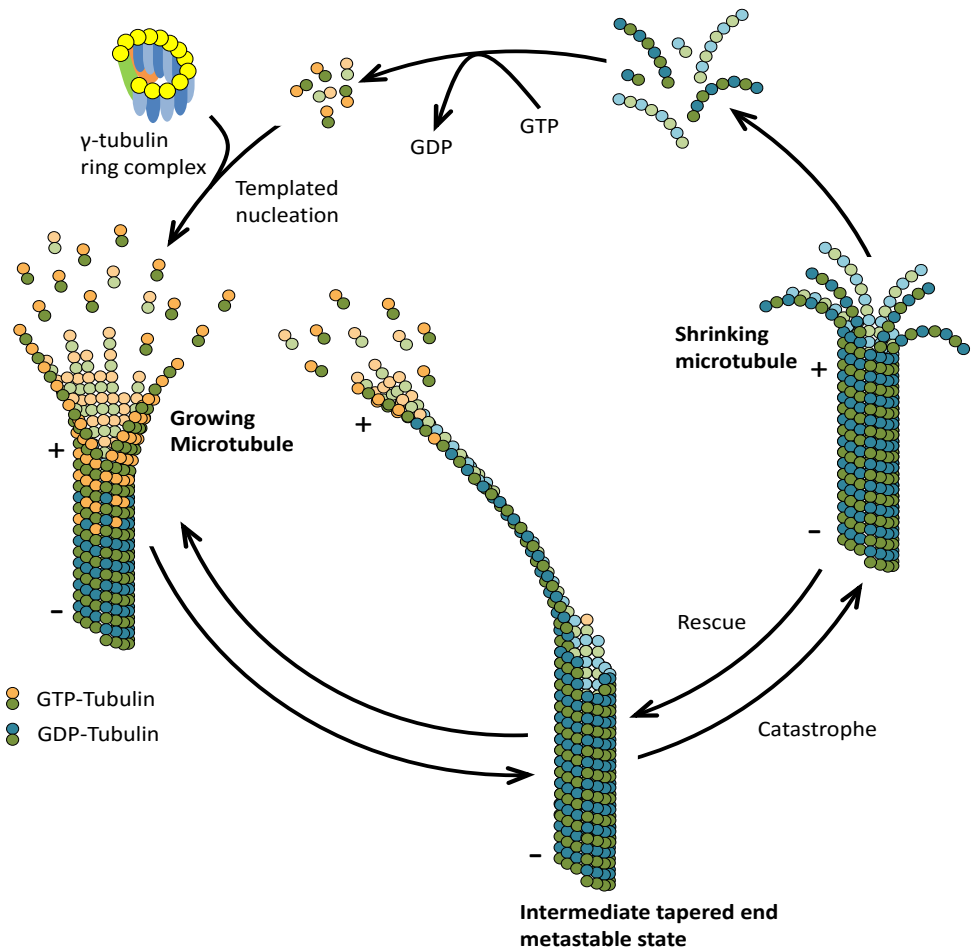


Figure 1. Microtubule dynamic instability.

Microtubules initiate polymerization mostly from a γ -tubulin ring complex template in cells. Microtubules polymerize with the addition of GTP-tubulin dimers at the growing end which get hydrolysed following a time-delay resulting in the formation of a GTP-cap at the end. Hydrolysis is accompanied by change in the conformation of the curved GTP-tubulin at the end to a straight GDP-tubulin in the lattice. Loss of the GTP-cap leads to destabilization of the microtubule and the switch to a shrinking state (a catastrophe) with inside-out coiled peeling protofilaments. Microtubules have been proposed to go through a tapered intermediate state when the stabilising GTP cap is lost beyond a certain threshold which predisposes it to a catastrophe. Depolymerising microtubules can also transit back to the polymerization phase (a rescue).

Microtubule dynamics can be tuned by enriching specific tubulin isotypes or by changes in the microtubule lattice that occur at some distance from the GTP-hydrolysis site (Pamula et al., 2016; Ti et al., 2016; Vemu et al., 2016). Recently it was shown that microtubule lifetime is also governed by the lattice stability, especially when microtubules are under mechanical strain: exchange of tubulin dimers can be observed along the lattice

(Aumeier et al., 2016; de Forges et al., 2016; Schaedel et al., 2015). The dynamic switching behaviour is regulated by MAPs (Akhmanova and Steinmetz, 2015), which may recognize specific microtubule features. For example, End Binding protein family, CLIP170 and XMAP215 recognize microtubule tips (Bieling et al., 2008; Brouhard et al., 2008; Gard and Kirschner, 1987; Komarova et al., 2009), whereas other MAPs, such as MAP2 and Tau, bind uniformly along the microtubule lattice (Hawkins et al., 2013; Kar et al., 2003).

1

Regulation of microtubule plus ends by End Binding proteins

End binding proteins (EBs) autonomously track growing microtubule plus ends through the CH (calponin homology) domain at their N terminus. The CH domain is followed by a linker region and a coiled coil domain that is required for dimerization (Akhmanova and Steinmetz, 2008). EBs recruit to growing microtubule ends a variety of plus end tracking proteins (+TIPs). This function depends on the C-terminal EB homology domain (Akhmanova and Steinmetz, 2015; Honnappa et al., 2009; Jiang et al., 2012; Kumar et al., 2017) or on the EB tails that bear a C-terminal tyrosine residue (Bieling et al., 2008). Cryo-electron tomography of *in vitro* assembled microtubules showed that EB1 binds to both the outwardly curved incomplete sheet-like structures reported to be present in growing microtubule ends by earlier cryo-EM studies (Chretien et al., 1995; Mandelkow et al., 1991) and to the complete tube structures (Guesdon et al., 2016).

Microtubules in cells or microtubules nucleated from centrosomes *in vitro* are mostly in a 13 protofilament configuration (Evans et al., 1985), with 15-protofilament microtubules reported in the touch receptor neurons in *C. elegans* (Bounoutas et al., 2009) and 11-protofilament microtubules found in other types of worm cells (Chalfie and Thomson, 1982). Microtubules assembled *in vitro* by spontaneous nucleation display a variable number of protofilaments, and transitions in protofilament number along a microtubule have been reported (Chretien et al., 1992). High resolution structural studies indicate that EBs drive tubulin assembly into a 13 protofilament microtubule configuration (des Georges et al., 2008; Vitre et al., 2008; Zhang et al., 2015). Cryo-EM analysis revealed that the CH domain of Mal3 (the EB homolog in fission yeast) binds to a pocket between two adjacent protofilaments close to the longitudinal interface between two dimers and is excluded from the seam (Maurer et al., 2012). This interaction mode enables EBs to recognise the GTP cap, since GTP bound to the β -tubulin at the E-site is in close proximity to the binding pocket. Improving the resolution of cryo-EM structures of the EB3 CH domain bound to microtubules assembled with GTP analogs like GTP- γ S and GMPCPP or with GDP confirmed that EBs bridge microtubule protofilaments, promote GTP hydrolysis and also lead to a compaction of the microtubule lattice (Zhang et al., 2015). Interestingly, recently it was shown that the yeast EB homolog Bim1 binds yeast microtubules at both the interdimer and intradimer tubulin contacts between protofilaments, whereas it only decorates the interdimer sites in mammalian microtubules (Howes et al., 2017). This suggests that subtle differences in

the conserved tubulin residues can lead to significant deviations in binding of a MAP.

Although varied effects of EBs on microtubule dynamics have been reported, there is an emerging consensus that EBs increase microtubule growth rate and catastrophe frequency and sensitize the plus ends to microtubule destabilizing drugs (Bieling et al., 2007; Doodhi et al., 2016; Komarova et al., 2009; Li et al., 2011; Mohan et al., 2013). In vitro reconstitution and image analysis revealed that EB1 binds slightly behind the very end of the microtubule, whereas the XMAP215 polymerase proteins bind to the outmost microtubule tip (Maurer et al., 2014). EB1 binding to the plus ends was also suggested to shorten the lifetime of the protective GTP cap (Maurer et al., 2014). Using classical tubulin dilution experiments to monitor the delay in catastrophe induction at growing microtubule ends indicative of the state of the protective GTP cap, it was shown that EBs decrease the momentary microtubule stability (Duellberg et al., 2016; Zhang et al., 2015). It is possible that this occurs because EBs accelerates the maturation of the lattice and induces a conformational strain by lattice compaction. In the future it would be interesting to test if the destabilizing effects of EBs at the plus end can be countered by changing the microtubule lattice conformation alone.

XMAP215/chTOG/Stu2 family of microtubule polymerases

Xenopus microtubule associated protein of 215 kDa (XMAP215) was first identified in Xenopus egg extracts and characterised as a microtubule plus end growth-promoting factor (Gard and Kirschner, 1987). Depletion experiments in frog extracts and classic reconstitution experiments using purified components showed that XMAP215 promotes microtubule growth by antagonizing the destabilizing effects of the Kinesin central motor 1 (XKCM1, a Kinesin-13 family member) (Kinoshita et al., 2001; Tournebise et al., 2000). The XMAP215 family of proteins are characterized by the presence of an array of TOG domains, each of which can bind to a tubulin dimer with high affinity. X-ray crystal structures of the TOG domain have shown that it has a paddle-like shape composed of HEAT repeats, α -helices stacked next to each other and separated by conserved loops. These loops interact with α - β tubulin heterodimer, which is in a curved conformation present in solution but becomes straight once incorporated in the microtubule lattice (Al-Bassam et al., 2007; Ayaz et al., 2014; Ayaz et al., 2012; Slep and Vale, 2007). The presence of a C-terminal microtubule lattice-binding region combined with the ability of TOG domains to bind to tubulin dimers that are curved and thus can occur only at the end but not within the microtubule lattice confer to XMAP215 the capacity to recognize microtubule tips (Brouhard et al., 2008; Widlund et al., 2011).

XMAP215 acts as a microtubule polymerase: through its multiple TOG domains, it locally increases tubulin concentration in the vicinity of the plus ends and accelerates tubulin subunit addition to these ends (Ayaz et al., 2012). In vitro reconstitution experiments using purified XMAP215 or Stu2 (Suppressor of tubulin 2, the yeast homolog of XMAP215) have shown that they increase growth rate of single microtubules by autonomously targeting to the plus ends (Brouhard et al., 2008; Podolski et al., 2014;

Widlund et al., 2011). Recently, a reconstitution with EB1, XMAP215 and tubulin showed that these three components were sufficient to reproduce in vitro microtubule growth rates that are comparable to the physiological growth rates observed in vivo (Zanic et al., 2013). EB1 and XMAP215 do not interact with each other, but they allosterically affect each other's activity by binding distinct regions at the plus end to promote microtubule polymerization (Maurer et al., 2014; Zanic et al., 2013).

1 Although XMAP215 can localize to the plus ends by itself, in cells it has been shown to be targeted to the plus ends by linker proteins like Sentin in *Drosophila* or SLAIN2 in mammalian cells. These linker proteins connect Msps, the *Drosophila* homolog of XMAP215, or chTOG, its mammalian homolog, to EB1 (Bouchet et al., 2016; Li et al., 2011; Li et al., 2012; van der Vaart et al., 2011). The fission yeast *Schizosaccharomyces pombe* has two XMAP215 orthologs - Alp14 (Altered polarity protein 14) and Dis1. Alp14 autonomously tracks growing plus ends independently of Mal3 and accelerates microtubule assembly (Al-Bassam et al., 2012). In contrast, the other XMAP215 ortholog, Dis1, binds directly to Mal3, the fission yeast counterpart of EB1, through the recently characterized LxxPTPh motif (Kumar et al., 2017), and the two proteins synergistically increase microtubule growth rates (Matsuo et al., 2016). This suggests that XMAP215 and EB1 exert their synergistic effects on microtubule polymerization either allosterically or through direct/indirect interactions at the plus ends.

CLIP and CLASP families of rescue factors

Cytoplasmic linker proteins (CLIPs) were the first identified +TIPs. They were initially discovered as linkers of microtubules to endocytic vesicles and were later shown to be associated with growing microtubule plus ends in live cells (Perez et al., 1999; Pierre et al., 1992). CLIP family of proteins, including the long isoform CLIP-170 and the short isoform CLIP-115, are characterized by the presence of two tandemly arranged CAP-Gly (Cytoskeleton Associated Protein Glycine rich) domains followed by a long coiled coil domain responsible for dimerization. CLIP-170 also contains “zinc knuckle” domains followed by a C-terminal tail that ends with a tyrosine residue (Pierre et al., 1994). The C-terminal EEY motif of CLIP-170 can bind to the CAP-Gly domain thereby serving an autoinhibitory function, which is relieved upon the binding of CAP-Gly domains to microtubules (Lansbergen et al., 2004; Weisbrich et al., 2007). When bound to microtubules, CLIP-170 can through its tail recruit other factors, such as the dynein-dynactin complex (Moughamian et al., 2013; Splinter et al., 2012). At microtubule plus ends, CLIPs recognise a composite site that is made up of the tyrosinated tail in α -tubulin and the end binding protein (Bieling et al., 2008; Lansbergen et al., 2004; Weisbrich et al., 2007). The plus end localization of the yeast homolog of CLIP-170, Tip1, has been shown to be dependent on the EB homolog, Mal3 and the motor protein Tea2 (Bieling et al., 2007; Busch et al., 2004). CLIPs act as rescue factors increasing the frequency of transitions from microtubule depolymerization to polymerization (Arnal et al., 2004; Komarova et al., 2002). Recent studies have suggested that CLIP-

170 stimulates microtubule rescue at specific microtubule lattice sites enriched in GTP tubulin (GTP islands), which coincide with the sites under mechanical stress (de Forges et al., 2016). It has also been shown that a rescue can also be initiated at sites of damage by the self-repair properties of microtubules alone (Aumeier et al., 2016; Schaedel et al., 2015).

CLASPs were identified as CLIP-associated proteins tracking the growing plus ends by binding the coiled coil region of CLIP or targeting EBs through the SxIP motifs (Akhmanova et al., 2001; Honnappa et al., 2009; Mimori-Kiyosue et al., 2005). The *Drosophila* homolog of CLASP, MAST/Orbit has been shown to be important for the mitotic flux in dividing cells and also for the proper spindle microtubule dynamics (Maiato et al., 2003; Maiato et al., 2005). CLASPs contain two or three TOG-like domains similar to the ones in XMAP215 family, and they were also hypothesized to bind to tubulin dimers (Al-Bassam et al., 2010; Leano et al., 2013). X-ray crystallography showed that the second and the third TOG domain of human CLASP have different curvatures at the tubulin binding interface and also prefer distinct tubulin dimer curvatures induced upon drug binding leading to distinct biochemical activities (Maki et al., 2015). Since the tubulin binding interface of the second TOG domain of CLASP was not compatible with binding the curved conformation of α - β tubulin dimers in solution, it was proposed that either this TOG domain or tubulin dimers undergo a conformational change upon binding (Leano et al., 2013).

Reconstitution experiments with purified *Schizosaccharomyces pombe* CLASP, Cls1p, or the *Drosophila* homolog of CLASP, MAST/Orbit, have shown that CLASP acts as a rescue factor by binding at a high density to microtubule lattice sites that serve as rescue points (Al-Bassam et al., 2010; Moriwaki and Goshima, 2016). Pause induction by *Drosophila* CLASP has also been reported (Moriwaki and Goshima, 2016). Therefore, although both the XMAP215 family and CLASP family of proteins have tubulin binding TOG domains, they exhibit distinct activities on microtubule polymerization dynamics by increasing growth rate and acting as rescue or pausing factors, respectively. Since tubulin binding domains combined with a microtubule lattice binding region can make a minimal polymerization module (Widlund et al., 2011), it would be interesting to dissect a minimal biochemical module essential for making a rescue factor.

Regulation of microtubule dynamics by motor proteins

Apart from their involvement in intracellular transport and microtubule organization, motor proteins, in particular the members of the Kinesin-4, Kinesin-8 and Kinesin-13 family are known to impact microtubule dynamics at the plus end. One of the mitotic kinesins, a member of the Kinesin-4 family, Kif4a, has been shown to interact with the anti-parallel microtubule bundler PRC1, translocate to the microtubule plus ends and inhibit their growth, and thus induce formation of stable microtubule overlaps in anaphase (Bieling et al., 2010; Subramanian et al., 2010). Another Kinesin-4 member, KIF7, has been shown to be an immobile motor that dampens microtubule growth rate and increases the catastrophe frequency and is essential to control the length of cilia

(He et al., 2014). KIF21A, a motile Kinesin-4, has been shown to target growing plus ends by moving processively along microtubules, slow down their growth and suppress catastrophes (van der Vaart et al., 2013). Recently, *in vitro* reconstitution experiments have shown that KIF21B, yet another motile Kinesin-4, is a potent microtubule pausing factor that moves to microtubule plus ends, concentrates there through its multiple microtubule-binding domains and arrests microtubule elongation (van Riel et al., 2017).

1 Kinesin-8 family motors that include the budding yeast Kip3p and human KIF18A are highly processive motors that facilitate microtubule length-dependent depolymerization (Stumpff et al., 2008; Varga et al., 2009). Kip3p, by virtue of the additional microtubule binding site present at the C-terminus of this motor protein, displays high processivity and accumulates at the plus ends increasing the off rate of tubulin and thus inducing microtubule depolymerisation (Gupta et al., 2006; Mayr et al., 2011; Stumpff et al., 2011; Varga et al., 2009). Interestingly, very recent work showed that Kip3 can sense and stabilize tubulin curvature, ultimately leading to microtubule disassembly (Arellano-Santoyo et al., 2017).

Kinesin-13 family members are different from all other kinesins because their motor is located in the middle of the molecule and they are immotile. The best characterised member of the Kinesin-13 family is the depolymerizing kinesin MCAK or KIF2C (the mammalian counterpart of the previously mentioned *Xenopus* XKCM1). This motor can target microtubule ends by its motor domain using lattice diffusion and lead to microtubule depolymerisation both from the plus and minus end (Helenius et al., 2006; Hunter et al., 2003). It has been shown that MCAK destabilizes the lateral contacts between tubulin dimers at the plus end; furthermore, the engagement of the motor domain with tubulin induces a conformational change in the tubulin dimer that is incompatible with its lattice retention, thereby inducing depolymerisation (Burns et al., 2014). The presence of the KVD motif in the MCAK motor domain and the presence of a neck linker N-terminal to the motor are essential for the depolymerisation activity and the lattice diffusion properties, respectively (Hertzer et al., 2006; Ogawa et al., 2004). Furthermore, MCAK interacts with EBs, which can counter the ability of this kinesin to prevent microtubule outgrowth but can also promote its targeting to polymerising ends and potentiate catastrophe induction (Montenegro Gouveia et al., 2010).

A huddle at the plus end: Factors influencing +TIP activities

Microtubule plus ends associate with proteins that can autonomously track the growing plus end, motor proteins that accumulate at the plus end or proteins that hitchhike through EBs. The net effect of these multiple factors on microtubule growth dynamics depends on the concentration of specific players, their affinity for the microtubule plus ends or EBs, synergistic or antagonistic effects, allosteric effects on the microtubule ends, post-translational modifications regulating protein activities, steric effects exerted by their multiple domains and alterations in the microtubule plus end structure. Most +TIPs track the growing plus ends dynamically and display a rapid turnover at the plus

ends, with residence times that were shown to be at the order of hundreds of milliseconds *in vitro* (Bieling et al., 2008; Bieling et al., 2007; Montenegro Gouveia et al., 2010).

In vitro reconstitution assays have shown that CLIP-170 dynamically tracks growing plus ends by recognizing the tyrosinated tails present in α -tubulin and EB (Bieling et al., 2008). Furthermore, in mammalian cells, SLAIN2, the adaptor protein for polymerase chTOG that tracks growing plus ends by its multiple EB1-binding SxIP sites also possesses a C-terminal tyrosine-containing tail that is recognized by CLIP-170 (van der Vaart et al., 2011), and this interaction might make the plus end tracking of both proteins more robust. CLIPs also bind to CLASPs which track the growing plus ends by virtue of their two SxIP motifs (Akhmanova et al., 2001; Mimori-Kiyosue et al., 2005). Although the plus end targeting CAP-Gly domains of CLIP-170 bind to the tail region of EBs, a recent study showed that a high concentration of an SxIP peptide that binds to the EB homology domain can compete CLIP-170 off the plus end (Duellberg et al., 2014). It was proposed that the binding of an SxIP peptide induced structuring of the EB tail and might possibly affect CAP-Gly binding. Allosteric effects induced by SxIP binding to EB can thus alter recruitment of other proteins through EB tail.

It has been demonstrated that phosphorylation of the EB-homology domain targeting SxIP motif in CLASPs by the glycogen synthase kinase 3β (GSK3 β) reduces CLASP association with the plus ends (Kumar et al., 2009). Apart from their interaction with EBs, CLASPs also bind to the basic/serine-rich region of SLAIN2 (van der Vaart et al., 2011) and possibly also recognise some plus end-specific features of the microtubule structure through their TOG domains (Maki et al., 2015). In light of these multiple interactions that target CLIPs or CLASPs to the plus end, it would be interesting to test if the residence time of these proteins at microtubule tips increases in the presence of their +TIP partners.

EBs have been shown to modulate the microtubule plus end structure by making the microtubule lattice more compact (Zhang et al., 2015), which possibly results in the synergistic effects on microtubule growth with XMAP215 (Zanic et al., 2013). In mammalian cells, the adaptor protein SLAIN2 and in *Drosophila*, Sentin possibly add another mechanism to ensure the robust plus end tracking of XMAP215 homologs chTOG/Msps, which can also load onto microtubules by their C-terminal positively charged region and by recognising tubulin curvature at the growing plus ends (Li et al., 2012; van der Vaart et al., 2011). The mammalian EB-binding protein SLAIN2, which interacts with CLIP, CLASP and chTOG, possibly acts like an adhesive factor that provides additional binding sites for different +TIPs and thus reduces the competition between them. MAPs can also exert their effect on microtubule plus end growth by modulating the end structure. For example, kinesin KIF21B induces pausing of microtubule plus end thereby resulting in a loss of EBs and likely also their partners from the plus ends (van Riel et al., 2017). Similarly, MCAK recognises the microtubule tip-specific features at both ends inducing peeling of protofilaments (Burns et al., 2014).

Regulation of centriolar microtubule growth

Centrioles are evolutionarily conserved microtubule based cellular organelles with a remarkable 9-fold radial symmetry. They are essential for the formation of centrosomes, cilia and flagella (Gonczy, 2012). Centrioles are characterized by nine triplets of microtubules arranged in an anti-clockwise manner. The 9-fold symmetric centriole structure was shown to be templated by the Spindle assembly defective-6 (SAS-6) oligomerization-driven cartwheel at the proximal end (Kitagawa et al., 2011; van Breugel et al., 2011). Each microtubule triplet has an A-microtubule with the complete 13 protofilament configuration and a B- and a C-microtubule with 10 protofilaments arranged in an inside-out fashion (Guichard et al., 2012). The A-microtubule is assembled from a γ -tubulin ring complex-like conical structure from the proximal to the distal end, whereas the B and C microtubules most likely elongate bidirectionally, as suggested by the presence of outwardly curled extensions (Guichard et al., 2010). Although centrioles are non-compartmentalized organelles, centriolar microtubules exhibit growth rates of tens of nanometers per hour, reaching a final length of around 450 nm and being extremely stable after that (Chretien et al., 1997; Paintrand et al., 1992). This is in contrast to cytoplasmic microtubules that grow with the rate of 10-20 microns per minute and exhibit dynamic instability (Akhmanova and Steinmetz, 2008).

Recent studies have characterized the molecular players involved in the centriole elongation process. Even though centrioles are present in the cytoplasmic pool of tubulin, centriolar microtubule assembly and stabilization post-assembly is very tightly regulated by a number of specific microtubule/tubulin binding proteins. Centrobin/Centrosomal protein of 120 kDa (CEP120), Centrosomal protein of 135 kDa (CEP135) and Centrosomal P4.1-associated protein (CPAP) are some of the candidates characterized for either microtubule or tubulin binding abilities, and some of them also interact with each other, adding another potential layer of regulation (Gudi et al., 2011; Hsu et al., 2008; Lin et al., 2013a; Lin et al., 2013b). CEP120 has been shown to be localized specifically to daughter centrioles and is essential for proper centriole elongation (Mahjoub et al., 2010). CEP120 mediates centriole elongation in a manner dependent on its microtubule binding domain and on its direct interaction with CPAP (Lin et al., 2013b). Through an interaction with CPAP and SPICE1, CEP120 recruits another centriolar protein, CEP135 (also known as Bld10p), which is essential for proper centriole assembly (Comartin et al., 2013). CEP135 is critical for the assembly of a complete centriole, and its depletion results in shortened centrioles or centrioles lacking microtubules altogether (Mottier-Pavie and Megraw, 2009; Roque et al., 2012). CEP135 localizes primarily to the proximal part of the centriole at the cartwheel-microtubule connection, where it has been proposed to stabilize the structure via its microtubule binding coiled coil domain (Hiraki et al., 2007; Jerka-Dziadosz et al., 2010; Kraatz et al., 2016). Centriolar coiled-coil protein of 110 kDa (CP110) localizes to the distal end of centrioles and restricts their length (Kleylein-Sohn et al., 2007; Schmidt et al., 2009). CP110 is recruited to the centriole by CEP97 and the complex of these two proteins is essential for preventing cilia formation (Spektor et

al., 2007). CP110 exhibits an antagonistic relationship with another centriole assembly factor, CPAP: CPAP overexpression or CP110 depletion both result in overly elongated centrioles (Schmidt et al., 2009). This led to the model that CPAP promotes centriole elongation, whereas CP110 capping activity at the distal end limits centriole length.

It has been shown that overexpression of CPAP/SAS-4 that localizes in the proximal part of the centriole results in overly elongated centrioles, whereas its depletion results in cells with a procentriole lacking microtubule triplets (Kohlmaier et al., 2009; Schmidt et al., 2009; Tang et al., 2009). This suggests that CPAP has a role in the initial centriolar microtubule assembly process. CPAP interacts directly with the γ -tubulin ring complex and may function in the initiation of the A-microtubule assembly (Hung et al., 2000). CPAP binds to another centriolar protein, SCL-interrupting locus protein (STIL), which is essential for pro-centriole formation in a complex with SAS-6 (Tang et al., 2011). Further evidence for the role of CPAP in microtubule assembly comes from the experiments demonstrating that CPAP has a tubulin-binding PN2-3 domain that can sequester tubulin dimers and destabilize microtubules (Cormier et al., 2009; Hsu et al., 2008; Hung et al., 2000).

Recently, a reconstitution study has shown that purified SAS-6 alone which is capable of forming dimers which then associate through their N-terminus to form a ring. These rings can autonomously organise into stacks, explaining the stacked assembly of the SAS-6 rings at the procentriole (Guichard et al., 2017). In the future it would be interesting to understand how such structures recruit the tubulin- or microtubule-binding centriole assembly factors and how their cooperative or antagonistic activities lead to the precise control of centriole length. In vitro reconstitution experiments with purified centriolar proteins will be very useful in this context. Also how the triplet microtubules are established with non-canonical contacts between protofilaments of A and B microtubule and between B and C microtubule is an open question. Identification and characterization of molecular factors that drive the bidirectional assembly of the 10-protofilament B and C microtubules will be needed to solve this enigma.

Scope of this thesis

In this chapter, we discussed the modulation of microtubule assembly and disassembly and the transitions between these two states by different microtubule associated proteins acting at the plus end. Over the years, through a combination of structural, biophysical and cellular approaches, significant progress has been achieved in understanding of the regulation of microtubule dynamics by cellular factors.

In Chapter 2, we address the role of CLASP at the plus ends of growing microtubules using an in vitro assay to reconstitute microtubule dynamics. We find that CLASP predominantly modulates microtubule dynamics by suppressing spontaneous and induced catastrophes (the switch from growth to shrinkage). We dissect the minimal biochemical modules in CLASP that lead to suppression of catastrophes and induction of rescues (switches from shrinkage to growth). We further demonstrate that CLASP-mediated stabilization at the

plus end results in the restoration of a tapered plus end with a partial subset of protofilaments into a complete structure. We also probe the ability of CLASP to repair damaged microtubule lattices and show that it leads to stabilization and thereby recovery of complete microtubules.

In Chapter 3, we investigate microtubule rescues by extending the reconstitution to the CLIP-170-CLASP complex. We find that CLIP-170, previously proposed to be a rescue factor did not alter microtubule dynamics autonomously at the concentration used in the assay. On the other hand, it increased the rescues induced by its interacting partner CLASP, most likely by increasing its association with the microtubule lattice.

In Chapter 4, we expand our reconstitution assays to investigate the regulation of microtubule growth by the mammalian adaptor-polymerase complex, SLAIN2-chTOG. We demonstrate that EB3 and chTOG can promote microtubule polymerization rates close to the ones observed in cells. The adaptor protein SLAIN2 does not stabilize microtubules but further enhances the effect of chTOG at the plus end. Furthermore, we show that chTOG-induced fast polymerization counteracts the ability of the microtubule depolymerase MCAK to block microtubule outgrowth from pre-formed templates.

In Chapter 5, we characterise tubulin binding of one of the centriolar proteins, CPAP/SAS-4 using X-ray crystallography and biochemical approaches. Using a truncated version of CPAP together with dynamic microtubules, we show that it autonomously tracks growing microtubule plus ends by binding to a specific site on the terminal tubulin dimers. CPAP dampens microtubule dynamics by slowing down microtubule elongation and reducing the frequency of catastrophes. The activities of the protein are dependent on the tubulin binding PN2-3 domain. We further test the impact of the CPAP-tubulin interaction on centriole elongation in cells and find that CPAP mutants deficient in tubulin binding lead to overly elongated centrioles. We thus uncover the capacity of CPAP to prevent overgrowth of centriolar microtubules.

In Chapter 6, we place our findings in a general context and discuss the potential directions in which this research can be developed in future.

References

- Akhmanova, A., C.C. Hoogenraad, K. Drabek, T. Stepanova, B. Dortland, T. Verkerk, W. Vermeulen, B.M. Burgering, C.I. De Zeeuw, F. Grosveld, and N. Galjart. 2001. Clasps are CLIP-115 and -170 associating proteins involved in the regional regulation of microtubule dynamics in motile fibroblasts. *Cell*. 104:923-935.
- Akhmanova, A., and M.O. Steinmetz. 2008. Tracking the ends: a dynamic protein network controls the fate of microtubule tips. *Nat Rev Mol Cell Biol*. 9:309-322.
- Akhmanova, A., and M.O. Steinmetz. 2015. Control of microtubule organization and dynamics: two ends in the limelight. *Nat Rev Mol Cell Biol*. 16:711-726.
- Al-Bassam, J., H. Kim, G. Brouhard, A. van Oijen, S.C. Harrison, and F. Chang. 2010. CLASP promotes microtubule rescue by recruiting tubulin dimers to the microtubule. *Dev Cell*. 19:245-258.
- Al-Bassam, J., H. Kim, I. Flor-Parra, N. Lal, H. Velji, and F. Chang. 2012. Fission yeast Alp14 is a dose-dependent plus end-tracking microtubule polymerase. *Mol Biol Cell*. 23:2878-2890.
- Al-Bassam, J., N.A. Larsen, A.A. Hyman, and S.C. Harrison. 2007. Crystal structure of a TOG domain: conserved features of XMAP215/Dis1-family TOG domains and implications for tubulin binding. *Structure*. 15:355-362.

- Alushin, G.M., G.C. Lander, E.H. Kellogg, R. Zhang, D. Baker, and E. Nogales. 2014. High-resolution microtubule structures reveal the structural transitions in α -tubulin upon GTP hydrolysis. *Cell*. 157:1117-1129.
- Arellano-Santoyo, H., E.A. Geyer, E. Stokasimov, G.Y. Chen, X. Su, W. Hancock, L.M. Rice, and D. Pellman. 2017. A Tubulin Binding Switch Underlies Kip3/Kinesin-8 Depolymerase Activity. *Dev Cell*. 42:37-51 e38.
- Arnal, I., C. Heichette, G.S. Diamantopoulos, and D. Chretien. 2004. CLIP-170/tubulin-curved oligomers coassemble at microtubule ends and promote rescues. *Curr Biol*. 14:2086-2095.
- Arnal, I., E. Karsenti, and A.A. Hyman. 2000. Structural transitions at microtubule ends correlate with their dynamic properties in *Xenopus* egg extracts. *J Cell Biol*. 149:767-774.
- Aumeier, C., L. Schaedel, J. Gaillard, K. John, L. Blanchoin, and M. Thery. 2016. Self-repair promotes microtubule rescue. *Nat Cell Biol*. 18:1054-1064.
- Ayaz, P., S. Munyoki, E.A. Geyer, F.A. Piedra, E.S. Vu, R. Bromberg, Z. Otwinowski, N.V. Grishin, C.A. Brautigam, and L.M. Rice. 2014. A tethered delivery mechanism explains the catalytic action of a microtubule polymerase. *Elife*. 3:e03069.
- Ayaz, P., X. Ye, P. Huddleston, C.A. Brautigam, and L.M. Rice. 2012. A TOG: α -tubulin complex structure reveals conformation-based mechanisms for a microtubule polymerase. *Science*. 337:857-860.
- Bieling, P., S. Kandels-Lewis, I.A. Telley, J. van Dijk, C. Janke, and T. Surrey. 2008. CLIP-170 tracks growing microtubule ends by dynamically recognizing composite EB1/tubulin-binding sites. *J Cell Biol*. 183:1223-1233.
- Bieling, P., L. Laan, H. Schek, E.L. Munteanu, L. Sandblad, M. Dogterom, D. Brunner, and T. Surrey. 2007. Reconstitution of a microtubule plus-end tracking system in vitro. *Nature*. 450:1100-1105.
- Bieling, P., I.A. Telley, and T. Surrey. 2010. A minimal midzone protein module controls formation and length of antiparallel microtubule overlaps. *Cell*. 142:420-432.
- Bouchet, B.P., I. Noordstra, M. van Amersfoort, E.A. Katrukha, Y.C. Ammon, N.D. Ter Hoeve, L. Hodgson, M. Dogterom, P.W. Derksen, and A. Akhmanova. 2016. Mesenchymal Cell Invasion Requires Cooperative Regulation of Persistent Microtubule Growth by SLAIN2 and CLASP1. *Dev Cell*. 39:708-723.
- Bounoutas, A., R. O'Hagan, and M. Chalfie. 2009. The multipurpose 15-prot filament microtubules in *C. elegans* have specific roles in mechanosensation. *Curr Biol*. 19:1362-1367.
- Brouhard, G.J., J.H. Stear, T.L. Noetzel, J. Al-Bassam, K. Kinoshita, S.C. Harrison, J. Howard, and A.A. Hyman. 2008. XMAP215 is a processive microtubule polymerase. *Cell*. 132:79-88.
- Burns, K.M., M. Wagenbach, L. Wordeman, and D.C. Schriemer. 2014. Nucleotide exchange in dimeric MCAK induces longitudinal and lateral stress at microtubule ends to support depolymerization. *Structure*. 22:1173-1183.
- Busch, K.E., J. Hayles, P. Nurse, and D. Brunner. 2004. Tea2p kinesin is involved in spatial microtubule organization by transporting tip1p on microtubules. *Dev Cell*. 6:831-843.
- Chalfie, M., and J.N. Thomson. 1982. Structural and functional diversity in the neuronal microtubules of *Caenorhabditis elegans*. *J Cell Biol*. 93:15-23.
- Chretien, D., B. Buendia, S.D. Fuller, and E. Karsenti. 1997. Reconstruction of the centrosome cycle from cryoelectron micrographs. *J Struct Biol*. 120:117-133.
- Chretien, D., F. Metoz, F. Verde, E. Karsenti, and R.H. Wade. 1992. Lattice defects in microtubules: protofilament numbers vary within individual microtubules. *J Cell Biol*. 117:1031-1040.
- Comartin, D., G.D. Gupta, E. Fussner, E. Coyaud, M. Hasegan, M. Archinti, S.W. Cheung, D. Pinchev, S. Lawo, B. Raught, D.P. Bazett-Jones, J. Luders, and L. Pelletier. 2013. CEP120 and SPICE1 cooperate with CPAP in centriole elongation. *Curr Biol*. 23:1360-1366.
- Coombes, C.E., A. Yamamoto, M.R. Kenzie, D.J. Odde, and M.K. Gardner. 2013. Evolving tip structures can explain age-dependent microtubule catastrophe. *Curr Biol*. 23:1342-1348.
- Cormier, A., M.J. Clement, M. Knossow, S. Lachkar, P. Savarin, F. Toma, A. Sobel, B. Gigant, and P.A. Curmi. 2009. The PN2-3 domain of centrosomal P4.1-associated protein implements a novel mechanism for tubulin sequestration. *J Biol Chem*. 284:6909-6917.
- de Forges, H., A. Pilon, I. Cantaloube, A. Pallandre, A.M. Haghiri-Gosnet, F. Perez, and C. Pous.

2016. Localized Mechanical Stress Promotes Microtubule Rescue. *Curr Biol.* 26:3399-3406.
- des Georges, A., M. Katsuki, D.R. Drummond, M. Osei, R.A. Cross, and L.A. Amos. 2008. Mal3, the *Schizosaccharomyces pombe* homolog of EB1, changes the microtubule lattice. *Nat Struct Mol Biol.* 15:1102-1108.
- Doodhi, H., A.E. Prota, R. Rodriguez-Garcia, H. Xiao, D.W. Custer, K. Bargsten, E.A. Katrukha, M. Hilbert, S. Hua, K. Jiang, I. Grigoriev, C.P. Yang, D. Cox, S.B. Horwitz, L.C. Kapitein, A. Akhmanova, and M.O. Steinmetz. 2016. Termination of Protofilament Elongation by Eribulin Induces Lattice Defects that Promote Microtubule Catastrophes. *Curr Biol.* 26:1713-1721.
- Duellberg, C., N.I. Cade, D. Holmes, and T. Surrey. 2016. The size of the EB cap determines instantaneous microtubule stability. *Elife.* 5.
- Duellberg, C., M. Trokter, R. Jha, I. Sen, M.O. Steinmetz, and T. Surrey. 2014. Reconstitution of a hierarchical +TIP interaction network controlling microtubule end tracking of dynein. *Nat Cell Biol.* 16:804-811.
- Evans, L., T. Mitchison, and M. Kirschner. 1985. Influence of the centrosome on the structure of nucleated microtubules. *J Cell Biol.* 100:1185-1191.
- Gard, D.L., and M.W. Kirschner. 1987. A microtubule-associated protein from *Xenopus* eggs that specifically promotes assembly at the plus-end. *J Cell Biol.* 105:2203-2215.
- Gardner, M.K., M. Zanic, C. Gell, V. Bormuth, and J. Howard. 2011. Depolymerizing kinesins Kip3 and MCAK shape cellular microtubule architecture by differential control of catastrophe. *Cell.* 147:1092-1103.
- Gonczy, P. 2012. Towards a molecular architecture of centriole assembly. *Nat Rev Mol Cell Biol.* 13:425-435.
- Gudi, R., C. Zou, J. Li, and Q. Gao. 2011. Centrobintubulin interaction is required for centriole elongation and stability. *J Cell Biol.* 193:711-725.
- Guesdon, A., F. Bazile, R.M. Buey, R. Mohan, S. Monier, R.R. Garcia, M. Angevin, C. Heichette, R. Wieneke, R. Tampe, L. Duchesne, A. Akhmanova, M.O. Steinmetz, and D. Chretien. 2016. EB1 interacts with outwardly curved and straight regions of the microtubule lattice. *Nat Cell Biol.* 18:1102-1108.
- Guichard, P., D. Chretien, S. Marco, and A.M. Tassin. 2010. Procentriole assembly revealed by cryo-electron tomography. *EMBO J.* 29:1565-1572.
- Guichard, P., A. Desfosses, A. Maheshwari, V. Hachet, C. Dietrich, A. Brune, T. Ishikawa, C. Sachse, and P. Gonczy. 2012. Cartwheel architecture of *Trichonympha* basal body. *Science.* 337:553.
- Guichard, P., V. Hamel, M. Le Guennec, N. Banterle, I. Iacovache, V. Nemcikova, I. Fluckiger, K.N. Goldie, H. Stahlberg, D. Levy, B. Zuber, and P. Gonczy. 2017. Cell-free reconstitution reveals centriole cartwheel assembly mechanisms. *Nat Commun.* 8:14813.
- Gupta, M.L., Jr., P. Carvalho, D.M. Roof, and D. Pellman. 2006. Plus end-specific depolymerase activity of Kip3, a kinesin-8 protein, explains its role in positioning the yeast mitotic spindle. *Nat Cell Biol.* 8:913-923.
- Hawkins, T.L., D. Sept, B. Mogessie, A. Straube, and J.L. Ross. 2013. Mechanical properties of doubly stabilized microtubule filaments. *Biophys J.* 104:1517-1528.
- He, M., R. Subramanian, F. Bangs, T. Omelchenko, K.F. Liem, Jr., T.M. Kapoor, and K.V. Anderson. 2014. The kinesin-4 protein Kif7 regulates mammalian Hedgehog signalling by organizing the cilium tip compartment. *Nat Cell Biol.* 16:663-672.
- Helenius, J., G. Brouhard, Y. Kalaidzidis, S. Diez, and J. Howard. 2006. The depolymerizing kinesin MCAK uses lattice diffusion to rapidly target microtubule ends. *Nature.* 441:115-119.
- Hertzer, K.M., S.C. Ems-McClung, S.L. Kline-Smith, T.G. Lipkin, S.P. Gilbert, and C.E. Walczak. 2006. Full-length dimeric MCAK is a more efficient microtubule depolymerase than minimal domain monomeric MCAK. *Mol Biol Cell.* 17:700-710.
- Hiraki, M., Y. Nakazawa, R. Kamiya, and M. Hirono. 2007. Bld10p constitutes the cartwheel-spoke tip and stabilizes the 9-fold symmetry of the centriole. *Curr Biol.* 17:1778-1783.
- Honnappa, S., S.M. Gouveia, A. Weisbrich, F.F. Damberger, N.S. Bhavesh, H. Jawhari, I. Grigoriev, F.J. van Rijssel, R.M. Buey, A. Lawera, I. Jelesarov, F.K. Winkler, K. Wuthrich, A. Akhmanova, and M.O. Steinmetz. 2009. An EB1-binding motif acts as a microtubule tip localization signal. *Cell.*

- 138:366-376.
- Howes, S.C., E.A. Geyer, B. LaFrance, R. Zhang, E.H. Kellogg, S. Westermann, L.M. Rice, and E. Nogales. 2017. Structural differences between yeast and mammalian microtubules revealed by cryo-EM. *J Cell Biol.*
- Hsu, W.B., L.Y. Hung, C.J. Tang, C.L. Su, Y. Chang, and T.K. Tang. 2008. Functional characterization of the microtubule-binding and -destabilizing domains of CPAP and d-SAS-4. *Exp Cell Res.* 314:2591-2602.
- Hung, L.Y., C.J. Tang, and T.K. Tang. 2000. Protein 4.1 R-135 interacts with a novel centrosomal protein (CPAP) which is associated with the gamma-tubulin complex. *Mol Cell Biol.* 20:7813-7825.
- Hunter, A.W., M. Caplow, D.L. Coy, W.O. Hancock, S. Diez, L. Wordeman, and J. Howard. 2003. The kinesin-related protein MCAK is a microtubule depolymerase that forms an ATP-hydrolyzing complex at microtubule ends. *Mol Cell.* 11:445-457.
- Jerka-Dziadosz, M., D. Gogendeau, C. Klotz, J. Cohen, J. Beisson, and F. Koll. 2010. Basal body duplication in *Paramecium*: the key role of Bld10 in assembly and stability of the cartwheel. *Cytoskeleton (Hoboken).* 67:161-171.
- Jiang, K., G. Toedt, S. Montenegro Gouveia, N.E. Davey, S. Hua, B. van der Vaart, I. Grigoriev, J. Larsen, L.B. Pedersen, K. Bezstarosti, M. Lince-Faria, J. Demmers, M.O. Steinmetz, T.J. Gibson, and A. Akhmanova. 2012. A Proteome-wide screen for mammalian SxIP motif-containing microtubule plus-end tracking proteins. *Curr Biol.* 22:1800-1807.
- Kar, S., J. Fan, M.J. Smith, M. Goedert, and L.A. Amos. 2003. Repeat motifs of tau bind to the insides of microtubules in the absence of taxol. *EMBO J.* 22:70-77.
- Kinoshita, K., I. Arnal, A. Desai, D.N. Drechsel, and A.A. Hyman. 2001. Reconstitution of physiological microtubule dynamics using purified components. *Science.* 294:1340-1343.
- Kitagawa, D., I. Vakonakis, N. Olieric, M. Hilbert, D. Keller, V. Olieric, M. Bortfeld, M.C. Erat, I. Fluckiger, P. Gonczy, and M.O. Steinmetz. 2011. Structural basis of the 9-fold symmetry of centrioles. *Cell.* 144:364-375.
- Kleylein-Sohn, J., J. Westendorf, M. Le Clech, R. Habadanck, Y.D. Stierhof, and E.A. Nigg. 2007. Plk4-induced centriole biogenesis in human cells. *Dev Cell.* 13:190-202.
- Kohlmaier, G., J. Loncarek, X. Meng, B.F. McEwen, M.M. Mogensen, A. Spektor, B.D. Dynlacht, A. Khodjakov, and P. Gonczy. 2009. Overly long centrioles and defective cell division upon excess of the SAS-4-related protein CPAP. *Curr Biol.* 19:1012-1018.
- Komarova, Y., C.O. De Groot, I. Grigoriev, S.M. Gouveia, E.L. Munteanu, J.M. Schober, S. Honnappa, R.M. Buey, C.C. Hoogenraad, M. Dogterom, G.G. Borisy, M.O. Steinmetz, and A. Akhmanova. 2009. Mammalian end binding proteins control persistent microtubule growth. *J Cell Biol.* 184:691-706.
- Komarova, Y.A., A.S. Akhmanova, S. Kojima, N. Galjart, and G.G. Borisy. 2002. Cytoplasmic linker proteins promote microtubule rescue in vivo. *J Cell Biol.* 159:589-599.
- Kraatz, S., P. Guichard, J.M. Obbineni, N. Olieric, G.N. Hatzopoulos, M. Hilbert, I. Sen, J. Missimer, P. Gonczy, and M.O. Steinmetz. 2016. The Human Centriolar Protein CEP135 Contains a Two-Stranded Coiled-Coil Domain Critical for Microtubule Binding. *Structure.*
- Kumar, A., C. Manatschal, A. Rai, I. Grigoriev, M.S. Degen, R. Jaussi, I. Kretschmar, A.E. Prota, R. Volkmer, R.A. Kammerer, A. Akhmanova, and M.O. Steinmetz. 2017. Short Linear Sequence Motif LxxPTPh Targets Diverse Proteins to Growing Microtubule Ends. *Structure.* 25:924-932 e924.
- Kumar, P., K.S. Lyle, S. Gierke, A. Matov, G. Danuser, and T. Wittmann. 2009. GSK3beta phosphorylation modulates CLASP-microtubule association and lamella microtubule attachment. *J Cell Biol.* 184:895-908.
- Lansbergen, G., Y. Komarova, M. Modesti, C. Wyman, C.C. Hoogenraad, H.V. Goodson, R.P. Lemaitre, D.N. Drechsel, E. van Munster, T.W. Gadella, Jr., F. Grosveld, N. Galjart, G.G. Borisy, and A. Akhmanova. 2004. Conformational changes in CLIP-170 regulate its binding to microtubules and dynactin localization. *J Cell Biol.* 166:1003-1014.
- Leano, J.B., S.L. Rogers, and K.C. Slep. 2013. A cryptic TOG domain with a distinct architecture underlies CLASP-dependent bipolar spindle formation. *Structure.* 21:939-950.
- Li, W., T. Miki, T. Watanabe, M. Kakeno, I.

- Sugiyama, K. Kaibuchi, and G. Goshima. 2011. EB1 promotes microtubule dynamics by recruiting Sentin in *Drosophila* cells. *J Cell Biol.* 193:973-983.
- Li, W., T. Moriwaki, T. Tani, T. Watanabe, K. Kaibuchi, and G. Goshima. 2012. Reconstitution of dynamic microtubules with *Drosophila* XMAP215, EB1, and Sentin. *J Cell Biol.* 199:849-862.
- Lin, Y.C., C.W. Chang, W.B. Hsu, C.J. Tang, Y.N. Lin, E.J. Chou, C.T. Wu, and T.K. Tang. 2013a. Human microcephaly protein CEP135 binds to hSAS-6 and CPAP, and is required for centriole assembly. *EMBO J.* 32:1141-1154.
- Lin, Y.N., C.T. Wu, Y.C. Lin, W.B. Hsu, C.J. Tang, C.W. Chang, and T.K. Tang. 2013b. CEP120 interacts with CPAP and positively regulates centriole elongation. *J Cell Biol.* 202:211-219.
- Mahjoub, M.R., Z. Xie, and T. Stearns. 2010. Cep120 is asymmetrically localized to the daughter centriole and is essential for centriole assembly. *J Cell Biol.* 191:331-346.
- Maiato, H., E.A. Fairley, C.L. Rieder, J.R. Swedlow, C.E. Sunkel, and W.C. Earnshaw. 2003. Human CLASP1 is an outer kinetochore component that regulates spindle microtubule dynamics. *Cell.* 113:891-904.
- Maiato, H., A. Khodjakov, and C.L. Rieder. 2005. *Drosophila* CLASP is required for the incorporation of microtubule subunits into fluxing kinetochore fibres. *Nat Cell Biol.* 7:42-47.
- Maki, T., A.D. Grimaldi, S. Fuchigami, I. Kaverina, and I. Hayashi. 2015. CLASP2 Has Two Distinct TOG Domains That Contribute Differently to Microtubule Dynamics. *J Mol Biol.* 427:2379-2395.
- Mandelkow, E.M., E. Mandelkow, and R.A. Milligan. 1991. Microtubule dynamics and microtubule caps: a time-resolved cryo-electron microscopy study. *J Cell Biol.* 114:977-991.
- Matsuo, Y., S.P. Maurer, M. Yukawa, S. Zakian, M.R. Singleton, T. Surrey, and T. Toda. 2016. An unconventional interaction between Dis1/TOG and Mal3/EB1 in fission yeast promotes the fidelity of chromosome segregation. *J Cell Sci.* 129:4592-4606.
- Maurer, S.P., N.I. Cade, G. Bohner, N. Gustafsson, E. Boutant, and T. Surrey. 2014. EB1 accelerates two conformational transitions important for microtubule maturation and dynamics. *Curr Biol.* 24:372-384.
- Maurer, S.P., F.J. Fourniol, G. Bohner, C.A. Moores, and T. Surrey. 2012. EBs recognize a nucleotide-dependent structural cap at growing microtubule ends. *Cell.* 149:371-382.
- Mayr, M.I., M. Storch, J. Howard, and T.U. Mayer. 2011. A non-motor microtubule binding site is essential for the high processivity and mitotic function of kinesin-8 Kif18A. *PLoS One.* 6:e27471.
- Menendez, M., G. Rivas, J.F. Diaz, and J.M. Andreu. 1998. Control of the structural stability of the tubulin dimer by one high affinity bound magnesium ion at nucleotide N-site. *J Biol Chem.* 273:167-176.
- Mimori-Kiyosue, Y., I. Grigoriev, G. Lansbergen, H. Sasaki, C. Matsui, F. Severin, N. Galjart, F. Grosveld, I. Vorobjev, S. Tsukita, and A. Akhmanova. 2005. CLASP1 and CLASP2 bind to EB1 and regulate microtubule plus-end dynamics at the cell cortex. *J Cell Biol.* 168:141-153.
- Mitchison, T., and M. Kirschner. 1984. Dynamic instability of microtubule growth. *Nature.* 312:237-242.
- Mohan, R., E.A. Katrukha, H. Doodhi, I. Smal, E. Meijering, L.C. Kapitein, M.O. Steinmetz, and A. Akhmanova. 2013. End-binding proteins sensitize microtubules to the action of microtubule-targeting agents. *Proc Natl Acad Sci U S A.* 110:8900-8905.
- Montenegro Gouveia, S., K. Leslie, L.C. Kapitein, R.M. Buey, I. Grigoriev, M. Wagenbach, I. Smal, E. Meijering, C.C. Hoogenraad, L. Wordeman, M.O. Steinmetz, and A. Akhmanova. 2010. In vitro reconstitution of the functional interplay between MCAK and EB3 at microtubule plus ends. *Curr Biol.* 20:1717-1722.
- Moriwaki, T., and G. Goshima. 2016. Five factors can reconstitute all three phases of microtubule polymerization dynamics. *J Cell Biol.* 215:357-368.
- Mottier-Pavie, V., and T.L. Megraw. 2009. *Drosophila* bld10 is a centriolar protein that regulates centriole, basal body, and motile cilium assembly. *Mol Biol Cell.* 20:2605-2614.
- Moughamian, A.J., G.E. Osborn, J.E. Lazarus, S. Maday, and E.L. Holzbaur. 2013. Ordered recruitment of dynactin to the microtubule plus-end is required for efficient initiation of retrograde axonal transport. *J Neurosci.* 33:13190-13203.

- Ogawa, T., R. Nitta, Y. Okada, and N. Hirokawa. 2004. A common mechanism for microtubule destabilizers-M type kinesins stabilize curling of the protofilament using the class-specific neck and loops. *Cell*. 116:591-602.
- Paintrand, M., M. Moudjou, H. Delacroix, and M. Bornens. 1992. Centrosome organization and centriole architecture: their sensitivity to divalent cations. *J Struct Biol*. 108:107-128.
- Pamula, M.C., S.C. Ti, and T.M. Kapoor. 2016. The structured core of human beta tubulin confers isotype-specific polymerization properties. *J Cell Biol*. 213:425-433.
- Perez, F., G.S. Diamantopoulos, R. Stalder, and T.E. Kreis. 1999. CLIP-170 highlights growing microtubule ends in vivo. *Cell*. 96:517-527.
- Pierre, P., R. Pepperkok, and T.E. Kreis. 1994. Molecular characterization of two functional domains of CLIP-170 in vivo. *J Cell Sci*. 107 (Pt 7):1909-1920.
- Pierre, P., J. Scheel, J.E. Rickard, and T.E. Kreis. 1992. CLIP-170 links endocytic vesicles to microtubules. *Cell*. 70:887-900.
- Podolski, M., M. Mahamdeh, and J. Howard. 2014. Stu2, the budding yeast XMAP215/Dis1 homolog, promotes assembly of yeast microtubules by increasing growth rate and decreasing catastrophe frequency. *J Biol Chem*. 289:28087-28093.
- Roque, H., A. Wainman, J. Richens, K. Kozyrska, A. Franz, and J.W. Raff. 2012. *Drosophila* Cep135/Bld10 maintains proper centriole structure but is dispensable for cartwheel formation. *J Cell Sci*. 125:5881-5886.
- Schaedel, L., K. John, J. Gaillard, M.V. Nachury, L. Blanchoin, and M. Thery. 2015. Microtubules self-repair in response to mechanical stress. *Nat Mater*. 14:1156-1163.
- Schmidt, T.I., J. Kleylein-Sohn, J. Westendorf, M. Le Clech, S.B. Lavoie, Y.D. Stierhof, and E.A. Nigg. 2009. Control of centriole length by CPAP and CP110. *Curr Biol*. 19:1005-1011.
- Slep, K.C., and R.D. Vale. 2007. Structural basis of microtubule plus end tracking by XMAP215, CLIP-170, and EB1. *Mol Cell*. 27:976-991.
- Spektor, A., W.Y. Tsang, D. Khoo, and B.D. Dynlacht. 2007. Cep97 and CP110 suppress a cilia assembly program. *Cell*. 130:678-690.
- Splinter, D., D.S. Razafsky, M.A. Schlager, A. Serra-Marques, I. Grigoriev, J. Demmers, N. Keijzer, K. Jiang, I. Poser, A.A. Hyman, C.C. Hoogenraad, S.J. King, and A. Akhmanova. 2012. BICD2, dynactin, and LIS1 cooperate in regulating dynein recruitment to cellular structures. *Mol Biol Cell*. 23:4226-4241.
- Stumpff, J., Y. Du, C.A. English, Z. Maliga, M. Wagenbach, C.L. Asbury, L. Wordeman, and R. Ohi. 2011. A tethering mechanism controls the processivity and kinetochore-microtubule plus-end enrichment of the kinesin-8 Kif18A. *Mol Cell*. 43:764-775.
- Stumpff, J., G. von Dassow, M. Wagenbach, C. Asbury, and L. Wordeman. 2008. The kinesin-8 motor Kif18A suppresses kinetochore movements to control mitotic chromosome alignment. *Dev Cell*. 14:252-262.
- Subramanian, R., E.M. Wilson-Kubalek, C.P. Arthur, M.J. Bick, E.A. Campbell, S.A. Darst, R.A. Milligan, and T.M. Kapoor. 2010. Insights into antiparallel microtubule crosslinking by PRC1, a conserved nonmotor microtubule binding protein. *Cell*. 142:433-443.
- Tang, C.J., R.H. Fu, K.S. Wu, W.B. Hsu, and T.K. Tang. 2009. CPAP is a cell-cycle regulated protein that controls centriole length. *Nat Cell Biol*. 11:825-831.
- Tang, C.J., S.Y. Lin, W.B. Hsu, Y.N. Lin, C.T. Wu, Y.C. Lin, C.W. Chang, K.S. Wu, and T.K. Tang. 2011. The human microcephaly protein STIL interacts with CPAP and is required for procentriole formation. *EMBO J*. 30:4790-4804.
- Ti, S.C., M.C. Pamula, S.C. Howes, C. Duellberg, N.I. Cade, R.E. Kleiner, S. Forth, T. Surrey, E. Nogales, and T.M. Kapoor. 2016. Mutations in Human Tubulin Proximal to the Kinesin-Binding Site Alter Dynamic Instability at Microtubule Plus- and Minus-Ends. *Dev Cell*. 37:72-84.
- Tournebize, R., A. Popov, K. Kinoshita, A.J. Ashford, S. Rybina, A. Pozniakovskiy, T.U. Mayer, C.E. Walczak, E. Karsenti, and A.A. Hyman. 2000. Control of microtubule dynamics by the antagonistic activities of XMAP215 and XKCM1 in *Xenopus* egg extracts. *Nat Cell Biol*. 2:13-19.
- van Breugel, M., M. Hirono, A. Andreeva, H.A. Yanagisawa, S. Yamaguchi, Y. Nakazawa, N. Morgner, M. Petrovich, I.O. Ebong, C.V. Robinson, C.M. Johnson, D. Veprintsev, and B. Zuber. 2011. Structures of SAS-6 suggest its organization in centrioles. *Science*. 331:1196-1199.

- 1
- van der Vaart, B., C. Manatschal, I. Grigoriev, V. Olieric, S.M. Gouveia, S. Bjelic, J. Demmers, I. Vorobjev, C.C. Hoogenraad, M.O. Steinmetz, and A. Akhmanova. 2011. SLAIN2 links microtubule plus end-tracking proteins and controls microtubule growth in interphase. *J Cell Biol.* 193:1083-1099.
- van der Vaart, B., W.E. van Riel, H. Doodhi, J.T. Kevenaar, E.A. Katrukha, L. Gumy, B.P. Bouchet, I. Grigoriev, S.A. Spangler, K.L. Yu, P.S. Wulf, J. Wu, G. Lansbergen, E.Y. van Battum, R.J. Pasterkamp, Y. Mimori-Kiyosue, J. Demmers, N. Olieric, I.V. Maly, C.C. Hoogenraad, and A. Akhmanova. 2013. CFEOM1-associated kinesin KIF21A is a cortical microtubule growth inhibitor. *Dev Cell.* 27:145-160.
- van Riel, W.E., A. Rai, S. Bianchi, E.A. Katrukha, Q. Liu, A.J. Heck, C.C. Hoogenraad, M.O. Steinmetz, L.C. Kapitein, and A. Akhmanova. 2017. Kinesin-4 KIF21B is a potent microtubule pausing factor. *Elife.* 6.
- Varga, V., C. Leduc, V. Bormuth, S. Diez, and J. Howard. 2009. Kinesin-8 motors act cooperatively to mediate length-dependent microtubule depolymerization. *Cell.* 138:1174-1183.
- Vemu, A., J. Atherton, J.O. Spector, A. Szyk, C.A. Moores, and A. Roll-Mecak. 2016. Structure and Dynamics of Single-isoform Recombinant Neuronal Human Tubulin. *J Biol Chem.* 291:12907-12915.
- Vitre, B., F.M. Coquelle, C. Heichette, C. Garnier, D. Chretien, and I. Arnal. 2008. EB1 regulates microtubule dynamics and tubulin sheet closure in vitro. *Nat Cell Biol.* 10:415-421.
- Weisbrich, A., S. Honnappa, R. Jaussi, O. Okhrimenko, D. Frey, I. Jelesarov, A. Akhmanova, and M.O. Steinmetz. 2007. Structure-function relationship of CAP-Gly domains. *Nat Struct Mol Biol.* 14:959-967.
- Widlund, P.O., J.H. Stear, A. Pozniakovsky, M. Zanic, S. Reber, G.J. Brouhard, A.A. Hyman, and J. Howard. 2011. XMAP215 polymerase activity is built by combining multiple tubulin-binding TOG domains and a basic lattice-binding region. *Proc Natl Acad Sci U S A.* 108:2741-2746.
- Zanic, M., P.O. Widlund, A.A. Hyman, and J. Howard. 2013. Synergy between XMAP215 and EB1 increases microtubule growth rates to physiological levels. *Nat Cell Biol.* 15:688-693.
- Zhang, R., G.M. Alushin, A. Brown, and E. Nogales. 2015. Mechanistic Origin of Microtubule Dynamic Instability and Its Modulation by EB Proteins. *Cell.* 162:849-859.

2

CLASP mediates microtubule tip and lattice repair through a single TOG domain

Amol Aher¹, Maurits Kok², Ashwani Sharma³, Ankit Rai¹, Natacha Olieric³, Ruddi Rodriguez-Garcia¹, Eugene A. Katrukha¹, Tobias Weinert³, Vincent Olieric⁴, Lukas C. Kapitein¹, Michel O. Steinmetz³, Marileen Dogterom² and Anna Akhmanova ^{1#}

1 Cell Biology, Department of Biology, Faculty of Science, Utrecht University, Padualaan 8, 3584 CH Utrecht, the Netherlands.

2 Department of Bionanoscience, Kavli Institute of Nanoscience, Delft University of Technology, van der Maasweg 9, 2629 HZ, Delft, the Netherlands

3 Laboratory of Biomolecular Research, Division of Biology and Chemistry, Paul Scherrer Institut, CH-5232 Villigen PSI, Switzerland.

4 Swiss Light Source, Paul Scherrer Institut, CH-5232 Villigen PSI, Switzerland.

Abstract

Microtubules are dynamic cytoskeletal filaments composed of tubulin dimers, which polymerize into linear protofilaments that associate laterally to form tubes. Microtubule tips and lattices can be destabilized by different factors, but how stable microtubules are reformed after destabilization is poorly understood. Here, we show that CLASPs act as catastrophe suppressors by inhibiting depolymerization of incomplete microtubule tips and allowing their recovery into complete tubes. CLASPs counteract microtubule destabilization induced by drugs or physical barriers, and promote repair of damaged microtubule lattices. These activities depend on a single TOG-like domain of CLASP, TOG2, which does not bind to free tubulin. Another TOG-like CLASP domain, TOG3, induces rescues but cannot suppress catastrophes, demonstrating that these activities are mechanistically distinct. These functions are modulated by the N- and C-terminal domains of CLASPs that flank TOG2 and TOG3. We propose that CLASPs act as protofilament-stabilizing proteins, with the unique TOG2 domain being the primary determinant of CLASP activity.

Microtubules (MTs) are essential for most cellular processes such as cell division, differentiation and migration. MTs are dynamic polymers composed of tubulin dimers, which attach to each other in a head-to-tail fashion to form protofilaments that interact laterally to form a hollow tube¹. MTs can alternate between phases of growth, shortening and pause, and numerous cellular factors participate in organizing MT networks by controlling different aspects of MT dynamics^{2, 3}. In particular, switching to MT depolymerization, termed a catastrophe, can be induced by intrinsic MT properties, such as GTP hydrolysis and the associated changes in the structure of MT tips, but also by extrinsic factors, such as encounters with obstacles⁴ or MT-targeting agents^{2, 5}. It is currently poorly understood how MT tips that are destabilized by intrinsic or extrinsic processes can be repaired to ensure continuous MT polymerization and the integrity of the MT shaft. Interestingly, blocking just one MT protofilament can disrupt MT growth and induce a catastrophe⁶, but it is unclear how severe the accompanying aberrations in MT structure can be, and whether and how they can be restored. Furthermore, recent work has shown that the damage and repair of MT shafts can affect the mechanical and dynamic properties of MTs, for example, by changing MT flexibility and inducing rescues (switches from shortening to growth)⁷⁻⁹. MT damage and destabilization can have a profound effect on processes ranging from intracellular transport to cell division, but little is known about the molecular mechanisms controlling MT repair.

Cytoplasmic linker associated proteins (CLASPs) are excellent candidates to mediate MT repair because they are well known to increase MT stability and abundance in mitosis and interphase. CLASP depletion leads to severe spindle defects such as monopolar or multipolar spindles, and aneuploidy^{10, 11}. CLASPs bind to the plus ends of spindle MTs and are essential for proper spindle MT dynamics and MT polymerization near kinetochores, supporting the poleward flux of kinetochore fibers^{10, 12}. CLASP homologues stabilize overlapping MTs in the mitotic spindle of fission yeast¹³ and induce MT pausing in *Drosophila* S2 cells¹⁴.

In worms, CLASPs are required for the assembly of the central spindle in embryos¹⁵ and suppress catastrophes in muscle cells¹⁶. In plants, CLASPs are important for catastrophe inhibition when MTs grow around sharp cell edges¹⁷. In migrating mammalian cells, CLASPs stimulate MT rescues at leading cell edges in 2D¹⁸ and inhibit catastrophes at the tips of mesenchymal cells forming protrusions in a 3D matrix¹⁹. Moreover, CLASPs also participate in spindle pole organization¹¹ and can promote γ -tubulin-dependent MT nucleation at the Golgi²⁰; such templated MT nucleation is likely to be mechanistically related to MT polymerase or anti-catastrophe activities²¹.

The ability of CLASPs to induce MT rescues, inhibit catastrophes and induce pausing has been reconstituted *in vitro*²²⁻²⁴. However, it is currently unclear whether rescue induction and catastrophe suppression are biochemically distinct processes or represent the same activity targeted to MT shafts and tips, respectively. Different CLASP homologues contain two or three TOG-like domains, protein modules known to bind to tubulin, and it has been proposed that CLASPs act like MT polymerases by promoting the recruitment of tubulin dimers^{22, 24}. However, unlike the TOG-domain containing MT polymerases of the XMAP215/ch-TOG family, CLASPs do not accelerate but rather slow down MT growth^{23, 24}, and the known structures of CLASP TOG-like domains are incompatible with binding to free tubulin due to their highly convex architecture^{25, 26}. It is thus possible that CLASPs affect MT end structures by binding to highly curved protofilaments at MT ends²⁶.

Here, we used *in vitro* MT dynamics assays to show that CLASPs potently suppress MT catastrophes that occur spontaneously or are induced by MT-depolymerizing agents and physical barriers, and that CLASPs prevent depolymerization and promote repair of damaged MT lattices. We demonstrate that a single TOG-like domain of CLASP, TOG2, which does not bind free tubulin, is sufficient to induce rescues and, when targeted to MT plus ends, suppresses catastrophes. Another TOG-like CLASP domain, TOG3, promotes rescues but does not inhibit catastrophes, demonstrating that these activities are mechanistically distinct. The additional folded domains present in CLASPs do not bind to tubulin but rather have autoregulatory and MT tip targeting functions. Furthermore, we show that CLASP stabilizes incomplete MT structures and enables their recovery. Together, our data suggest that CLASPs, through their unique TOG2 domain, stimulate MT growth and repair by acting as protofilament-stabilizing factors.

RESULTS

A complex of CLASP2 α and EB3 suppresses catastrophes and promotes templated MT nucleation

To investigate the impact of CLASP2 α on MT dynamics, we purified it from HEK293T cells (Supplementary Fig. 1a) and analyzed its activity using an *in vitro* reconstitution assay^{6, 27}, in which MT growth from GMPCPP-stabilized seeds is observed by Total Internal Reflection Fluorescence microscopy (TIRFM). In the presence of tubulin alone, full length GFP-tagged CLASP2 α showed some binding to MT lattices and a very weak enrichment at

Figure 1

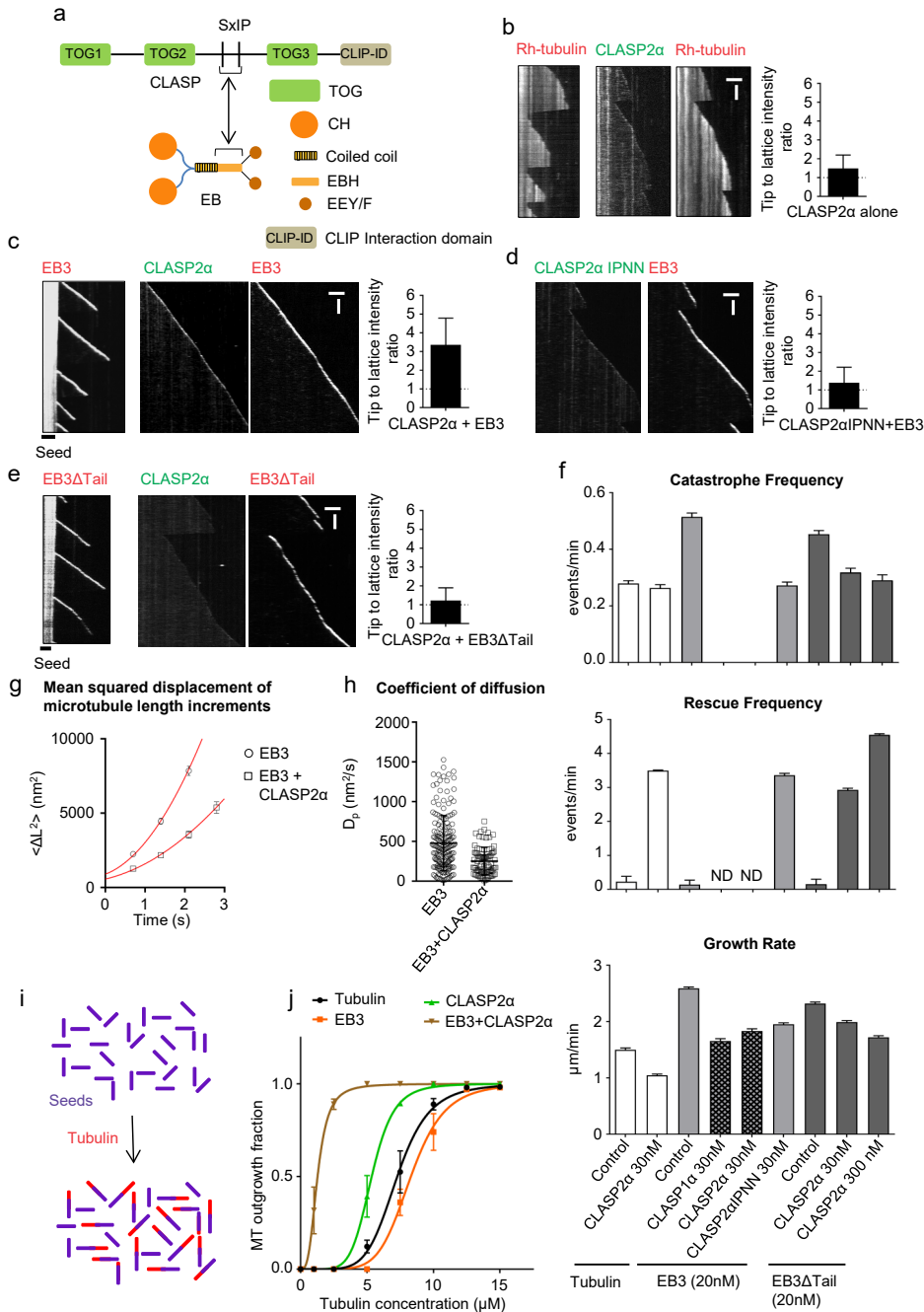


Figure 1. CLASP2α promotes processive MT polymerization and MT outgrowth from a template

(a) A scheme of CLASP and EB domain organization and CLASP-EB interaction.

(b-e) Kymographs of MT plus end growth with rhodamine-tubulin alone or together with 30 nM GFP-CLASP2α (b), 20 nM mCherry-EB3 alone or together with 30 nM GFP-CLASP2α (c), 20 nM mCherry-EB3 and 30 nM GFP-CLASP2αIPNN (d) and 20 nM mCherry-EB3ΔTail alone or together with 30 nM GFP-

CLASP2 α (e). Plots of fluorescence intensity ratio of CLASP2 α at the growing MT plus end and MT lattice are shown on the right, $n=27$ (b), 26 (c), 25 (d) and 30 (e). Scale bars: 2 μm (horizontal) and 60 s (vertical). (f) Parameters of MT plus end dynamics in the presence of rhodamine-tubulin alone or together with 20 nM mCherry-EB3 or together with 20 nM mCherry-EB3 Δ Tail in combination with the indicated CLASP constructs at 30 nM or 300 nM as indicated. Number of growth events analyzed: for tubulin alone, $n=135$, tubulin with GFP-CLASP2 α , $n=134$, mCherry-EB3 alone, $n=207$, mCherry-EB3 with GFP-CLASP1 α , $n=75$, mCherry-EB3 with GFP-CLASP2 α , $n=52$, mCherry-EB3 with GFP-CLASP2 α IPNN, $n=182$, mCherry-EB3 Δ Tail, $n=182$, mCherry-EB3 Δ Tail and GFP-CLASP2 α , $n=174$, mCherry-EB3 Δ Tail and 300 nM GFP-CLASP2 α , $n=128$. Error bars represent SEM.

(g,h) Average of the mean squared displacement (MSD) of MT length increments, plotted over time (g) and the values of the diffusion constant D_p , obtained from fits of the MSD curves (h). Data are shown for MTs grown either in the presence of EB3 alone or together with 30 nM of CLASP2 α . The average diffusion constant of $506 \pm 41 \text{ nm}^2/\text{s}$ for control and $316 \pm 25 \text{ nm}^2/\text{s}$ in presence of CLASP2 α were estimated from fits to the data (red line). Each dot in (h) represents the diffusion constant estimated for an individual MT growth event; control ($n=183$), CLASP2 α ($n=88$).

(i,j) Schematic of the MT outgrowth assay and plot of the fraction of the total GMPCPP seeds that show MT outgrowth in 15 minutes at increasing tubulin concentrations with tubulin alone (black) or together with GFP-EB3 (200 nM) (orange) or together with GFP-CLASP2 α (100 nM) (green) or together with GFP-EB3 (200 nM) and GFP-CLASP2 α (100 nM) (brown). For increasing tubulin concentrations in case of tubulin alone, $n=92, 96, 105, 82, 97, 87, 161, \text{ and } 127$ GMPCPP seeds respectively, for 200 nM GFP-EB3, $n=69, 73, 68, 77, 80, 83, 106$ and 96 GMPCPP seeds respectively, for 100 nM GFP-CLASP2 α , $n=119, 122, 118, 119, 145, 110, 119$ and 115 GMPCPP seeds respectively and for 200 nM GFP-EB3 together with 100 nM GFP-CLASP2 α , $n=107, 54, 85, 88, 70, 87, 85$ and 70 GMPCPP seeds respectively. Data are from 2 experiments. Error bars represent SD. Solid lines indicate the sigmoidal equation fit to the data. Tubulin concentration for half-maximal MT outgrowth for tubulin alone = 7.28 ± 0.08 , for 200 nM GFP-EB3 = 8.30 ± 0.11 , for 100 nM GFP-CLASP2 α = 5.35 ± 0.04 , for 100 nM GFP-CLASP2 α and 200 nM GFP-EB3 = 1.28 ± 0.01 . Hill slopes for the fits with tubulin alone = 5.99 ± 0.34 , for EB3 = 6.53 ± 0.49 , for CLASP2 α = 6.46 ± 0.31 and for CLASP2 α and EB3 = 3.16 ± 0.07 .

MT tips (Fig. 1a,b, Supplementary Fig. 1a). However, when mCherry-EB3 was included in the assay, CLASP2 α strongly accumulated at MT plus ends (Fig. 1a,c). MT tip recruitment of CLASP2 α was abrogated by mutating the Ile and Pro residues of the two tandemly arranged SxIP motifs in the middle of the protein to asparagines (IPNN mutant) (Fig. 1d). Similarly, removal of the acidic tail of EB3 (EB3 Δ Tail) abolished the tip recruitment as these polypeptide sequences are essential for the binding between CLASP2 and EBs²⁸ (Fig. 1e).

Analysis of MT dynamics showed that 30 nM CLASP2 α had a mild inhibitory effect on the MT growth rate both with and without EB3 (Fig. 1f). Strikingly, when recruited to MT tips by EB3, CLASP2 α completely suppressed catastrophes (Fig. 1c,f). Also CLASP1 α , the CLASP2 α paralogue that shares a very similar domain organization, accumulated at MT plus ends in the presence of EB3 and suppressed MT catastrophes (Fig. 1f, Supplementary Fig. 1a,b). Catastrophe suppression was not observed when EB3 was absent or when the binding between CLASP2 α and EB3 was abolished (Fig. 1b-f). We next attempted to compensate for the lack of interaction between CLASP2 α and EB3 by increasing the concentration of CLASP2 α from 30 to 300 nM in the presence of EB3 Δ Tail, but found that it was insufficient to achieve the same MT tip accumulation of CLASP2 α as observed with 30 nM CLASP2 α in the presence of full length EB3 (Supplementary Figure 1c,d). Consistently, we observed no catastrophe suppression in these

conditions (Fig. 1f). Nonetheless, we observed a strong CLASP2 α -dependent increase in MT rescues, which did not require CLASP2 α accumulation at MT tips (Fig. 1b-f). We note that for conditions where no catastrophes were observed, the rescue frequency could not be measured. We conclude that CLASPs potently suppress catastrophes when concentrated on MT tips by EB3, and promote rescues in an EB-independent manner.

To get a better insight into how CLASPs suppress catastrophes, we examined the dynamics of growing MT tips in more detail. By fitting MT fluorescence intensity profiles to the error function to determine the MT tip position at sub-pixel resolution, we found that the length variability for MTs grown in the presence of EB3 and CLASP2 α was significantly lower than with EB3 alone (Fig. 1g,h, Supplementary Figure 1e,f). These data indicate that CLASP2 α promotes smooth MT extension by preventing transient episodes of MT tip shortening, suggesting that in the presence of CLASP2 α MT plus ends are more stable.

It has been shown that factors that destabilize MT tips, like MT depolymerizing kinesin-13 MCAK, suppress MT outgrowth from templates, such as stable MT seeds or centrosomes, whereas catastrophe-suppressing factors such as TPX2 promote MT outgrowth, an effect that becomes particularly obvious at low tubulin concentrations²¹. We performed similar assays in which we looked at MT outgrowth from GMPCPP seeds and found that EB3 mildly inhibited MT outgrowth, while CLASP2 α alone mildly increased the MT outgrowth frequency (Fig. 1i,j, Supplementary Fig. 1g). When combined, CLASP2 α and EB3 dramatically increased MT outgrowth from GMPCPP seeds, strongly lowering its kinetic threshold: half maximal MT outgrowth was observed at a tubulin concentration that was almost 6 fold lower than in the presence of tubulin alone (Fig. 1j, Supplementary Fig. 1g). These results support the notion that CLASP2 α in complex with EB3 potently promotes the formation of stably growing MT plus ends.

A single MT-tip targeted TOG-like domain of CLASP2 is sufficient to suppress catastrophes

CLASP1 α and 2 α consist of three TOG-like domains (termed TOG1, 2 and 3) and a C-terminal domain responsible for interactions with CLIP-170 and other partners, CLIP-Interacting Domain (CLIP-ID)^{29, 30} (Fig. 1a). By targeting single CLASP2 domains or their different combinations to MT tips and lattices using a positively charged SxIP containing peptide of CLASP2 (termed “S” in different abbreviations, Fig. 2a), we found that TOG2 was necessary and sufficient to suppress catastrophes, while TOG1, TOG3, CLIP-ID and the SxIP peptide alone had no effect (Fig. 2a-c, Supplementary Fig. 2a). Catastrophe suppression was not dependent on the linker region preceding TOG2 but was abrogated when the conserved residues in TOG2, W339, R462 and R504, corresponding to the residues which contribute to MT binding in CLASP1 and to tubulin binding in the XMAP215/ch-TOG family proteins²⁵, were individually mutated to glutamates (Fig. 2a-c, Supplementary Fig. 2a, b). The catastrophe-suppressing properties of CLASP2 TOG2 are unique, because TOG1, TOG3 and CLIP-ID domains of CLASP2 or either of the first

Figure 2

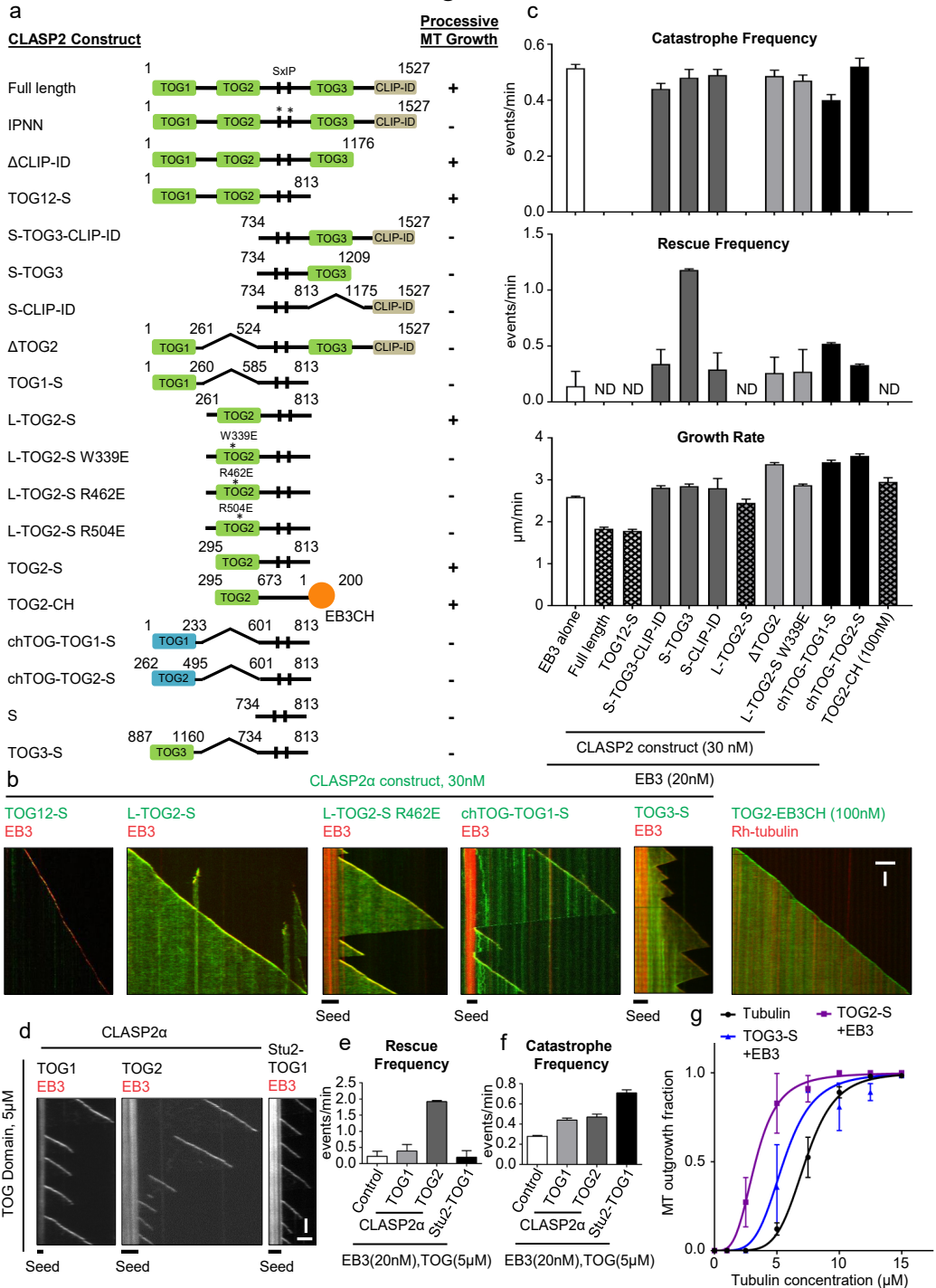


Figure 2. The second TOG-like domain of CLASP2 is necessary and sufficient for catastrophe suppression. (a) A scheme of different CLASP2 constructs used. Processive MT growth is the condition in which no catastrophes were observed within 10 min in the assay with 20 nM mCherry-EB3.

(b) Representative kymographs showing MT plus end growth in the presence of 20 nM mCherry-EB3 and GFP-fusions of the indicated fusion proteins. EB3-CH domain fusion was used at 100 nM, all the other proteins at 30 nM. Scale bars: 2 μm (horizontal) and 60 s (vertical).

(c) Parameters of MT plus end dynamics in the presence of 20 nM mCherry-EB3 alone or together with the indicated GFP-fusion proteins. Protein concentrations were as in (b). Number of growth events analyzed: for mCherry-EB3 alone, $n=207$, together with GFP-CLASP2 α , $n=75$, with TOG12-S, $n=96$, with S-TOG3-CLIP-ID, $n=110$, with S-TOG3, $n=70$, with S-CLIP-ID, $n=136$, with TOG2-S, $n=62$, with TOG2-S W339E, $n=118$, with chTOG-TOG1-S, $n=47$, with chTOG-TOG2-S, $n=78$ and for TOG2-EB3CH alone, $n=45$. Error bars represent SEM.

(d) Representative kymographs showing MT plus end dynamics in the presence of 20 nM mCherry-EB3 and 5 μM of the indicated TOG domains from CLASP2 α or Stu2. Scale bars: 2 μm (horizontal) and 60 s (vertical).

(e, f) MT plus end rescue and catastrophe frequencies in the presence of 20 nM mCherry-EB3 alone ($n=207$) or together with 5 μM of CLASP2 α TOG1 ($n=61$) or TOG2 ($n=100$) or with Stu2-TOG1 ($n=146$). Error bars represent SEM.

(g) Plot of the fraction of the total GMPCPP seeds that show MT outgrowth at increasing tubulin concentrations with tubulin alone (black curve) or GFP-EB3 (200nM) together with either GFP-TOG3-S (100nM) (blue) or TOG2-S (100nM) (purple). For increasing tubulin concentrations in case of tubulin alone, $n=92, 96, 105, 82, 97, 87, 161, \text{ and } 127$ GMPCPP seeds respectively, for GFP-TOG3-S, $n=61, 52, 53, 56, 71, 59, 61$ and 88 GMPCPP seeds respectively and for GFP-TOG2-S, $n=70, 64, 50, 50, 55, 66, 63$ and 63 GMPCPP seeds respectively. Data are from 2 experiments. Error bars represent SD. Solid lines indicate the sigmoidal equation fit to the data. Tubulin concentration for half-maximal MT outgrowth for tubulin alone = 7.28 ± 0.08 , for GFP-TOG2-S with GFP-EB3 = 3.29 ± 0.07 and for GFP-TOG3-S with GFP-EB3 = 5.54 ± 0.32 . Hill slope for the fits with tubulin alone = 5.99 ± 0.34 , for GFP-TOG2-S with GFP-EB3 = 3.56 ± 0.21 and for GFP-TOG3-S with GFP-EB3 = 4.59 ± 1.11 .

two TOG domains of ch-TOG had no effect on MT growth processivity when targeted to MT tips by an SxIP peptide (Fig. 2a-c, Supplementary Fig. 2a,b). Complete catastrophe inhibition could also be achieved by a direct fusion of the CLASP2 TOG2 to the MT tip-binding calponin homology (CH) domain of EB3 (Fig. 2a-c, Supplementary Fig. 2a). Importantly, unlike the other GFP-tagged fusion proteins used in this study, which were purified from HEK293T cells, the GFP-TOG2-EB3-CH protein was purified from bacteria, excluding possible contamination with MT regulators as a source of catastrophe-suppressing activity (Fig. 2a-c, Supplementary Fig. 2a). The TOG2-EB3-CH fusion thus represents a minimal MT plus end-binding protein capable of suppressing catastrophes.

MT tip-targeted TOG2 had a little impact on the MT growth rate (Fig. 2c), while a TOG1-TOG2-S fusion reduced the MT growth rate similarly to the full length CLASP2 α , suggesting that this effect might be caused by TOG1 or the TOG1-TOG2 combination (Fig. 2c). The TOG3-S fusion promoted rescues, although this effect was suppressed when the C-terminal CLIP-ID domain was also included (Fig. 2a-c, and see below). The rescue activity of MT tip-targeted TOG2 could not be assessed due to complete absence of catastrophes. We therefore investigated the activity of TOG2 without the EB3- and MT lattice-binding SxIP peptide and found that while it had little effect at nanomolar concentrations, it did cause a significant increase in rescue frequency at a concentration of 5 μM . In contrast, the TOG1 domain of CLASP2 or the tubulin-binding TOG domain of the yeast ch-TOG homologue, Stu2, did not show such an effect, although all tested TOG domains mildly promoted catastrophes at 5 μM concentration (Fig. 2d-f, Supplementary

Fig. 2a). The Stu2-TOG1 but not the TOG-like domains of CLASP2 somewhat reduced the MT growth rate, likely by sequestering tubulin dimers (Fig. 2d-f, Supplementary Fig. 2c). Furthermore, both the rescue-promoting TOG3-S and catastrophe-suppressing TOG2-S in combination with EB3 individually lowered the kinetic threshold for MT outgrowth from GMPCPP seeds (Fig. 2g), but the effect was milder than with the full length protein (Fig. 1j).

Previous analyses of the TOG2 and TOG3 domains of CLASP2 showed that they interact with tubulin ring-like oligomers but have only a low affinity for MT lattices²⁶. We confirmed that the binding of TOG2 and TOG3 to stabilized MTs was weak, while TOG1 and CLIP-ID did not bind to MTs at all, and none of these domains interacted with tubulin (Supplementary Fig. 2d-h). Together, these results show that TOG2 can potently regulate MT plus end dynamics when targeted to MT plus ends and has an intrinsic rescue activity, although it does not bind to tubulin, which is in contrast to the TOG domains of XMAP215/ch-TOG family of MT polymerases.

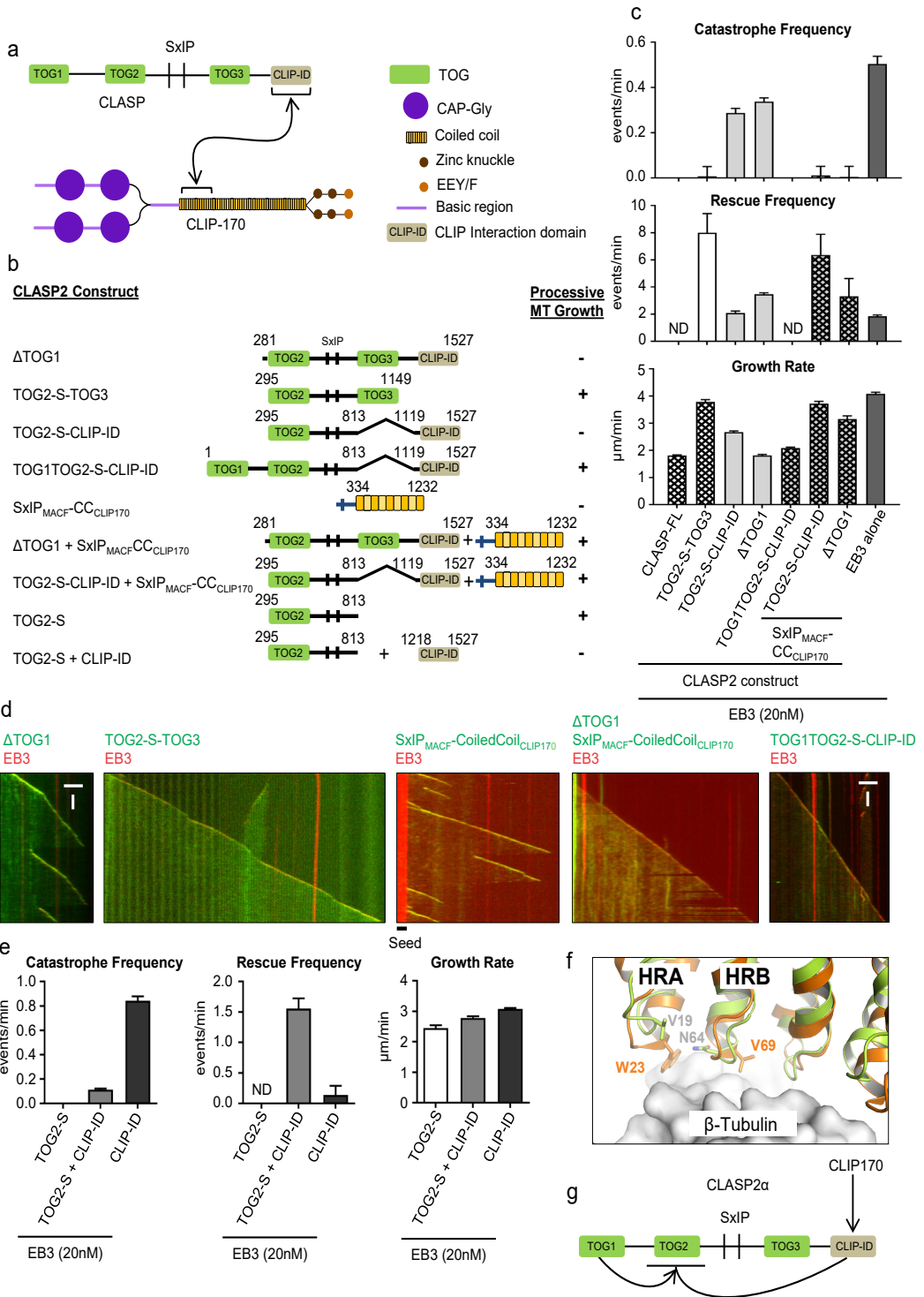
Autoregulatory interactions between CLASP2 α TOG domains

As mentioned above, TOG1 of CLASP2 α had no MT- or tubulin-binding activities. Strikingly, the deletion of this domain (which converted CLASP2 α to the equivalent of the naturally occurring splice isoform CLASP2 γ), abrogated catastrophe suppression characteristic for the full length CLASP2 α , in agreement with a previous publication²⁴ (Fig. 3a-d). This was surprising, as the TOG2 domain sufficient for catastrophe suppression was fully retained in this deletion mutant. Further deletion mapping showed that the presence of CLIP-ID prevented catastrophe inhibition by TOG2, just as it suppressed MT rescue by CLASP2-TOG3 (Fig. 2a-c, Fig. 3a-d, Supplementary Fig. 2a,b, 3a,b). An excess (500 nM) of purified CLIP-ID could reduce the catastrophe-suppressing activity of MT tip-bound TOG2, while by itself this protein had little effect on catastrophe inhibition (Fig. 3e, Supplementary Fig. 3c).

To explain these results, we hypothesized that CLIP-ID has an autoinhibitory activity that can be relieved by TOG1. If this were the case, then the binding to partners might release the CLIP-ID-induced inhibition of constructs lacking TOG1. To test this idea, we targeted the CLASP binding coiled-coil domain of CLIP-170 (Fig. 3a) to MT tips by fusing it to the EB-binding SxIP motif of MACF2²⁸ (Fig. 3b). While by itself this fusion had little effect on MT catastrophes, its addition potently increased the anti-catastrophe activity of all TOG2-containing CLASP2 constructs that lacked TOG1 (Fig. 3a-d, Supplementary Fig. 3b). These results suggest that CLIP-ID, when it is not bound to partners such as CLIP-170, has an inhibitory effect on TOG2, and likely also on TOG3, and that TOG1 can relieve this inhibition.

The crystal structure of TOG1 showed a conserved TOG-domain fold, but also demonstrated that the conserved residues required for tubulin interaction are lacking (Fig. 3f, Supplementary Fig. 3e), thus explaining why this domain does not bind to either

Figure 3



2

Figure 3. The C-terminal CLIP-interacting domain shows auto-inhibitory activity which is relieved by the first TOG-like domain or by CLIP170.

(a) A scheme of the CLASP-CLIP-170 interaction.

(b) A scheme of the different CLASP and CLIP170 constructs used. Conditions showing processive MT growth in the presence of 20 nM mCherry-EB3 are indicated based on (c).

(c) Parameters of MT plus end dynamics in the presence of 20 nM mCherry-EB3 and the indicated constructs. Number of growth events: for mCherry-EB3 together with GFP-CLASP2 α , n=75, with TOG2-S-TOG3, n=62, with TOG2-S-CLIP-ID, n=101, with Δ TOG1, n=141, with TOG1TOG2-S-CLIP-ID, n=64, for mCherry-EB3 and SxIPMACF-CCCLIP170 alone n=217, and together with TOG2-S-CLIP-ID, n=72, with Δ TOG1, n=50. Error bars represent SEM. (d) Representative kymographs showing MT plus end dynamics in the presence of 20 nM mCherry-EB3 together with the indicated fusion proteins. Scale bars: 2 μ m (horizontal) and 60 s (vertical).

(e) Parameters of MT plus end dynamics in the presence of 20 nM mCherry-EB3 with 30 nM TOG2-S alone (n=62) or together with 500 nM CLIP-ID (n=96) or with CLIP-ID alone (n=115). n= number of growth events. Error bars represent SEM.

(f) Superposition of the structure of hsCLASP2-TOG1 and scStu2-TOG1 at the β -tubulin binding interface.

(g) Model for regulation of CLASP activity. CLIP-interacting domain inhibits the catastrophe suppressing activity of TOG2. In the context of the full-length CLASP2 α , this auto-inhibition is relieved by the presence of TOG1, whereas in CLASP2 isoforms like CLASP2 β , which lack TOG1, the auto-inhibition is relieved by engaging CLIP-ID with the CLIP-170 coiled coil domain.

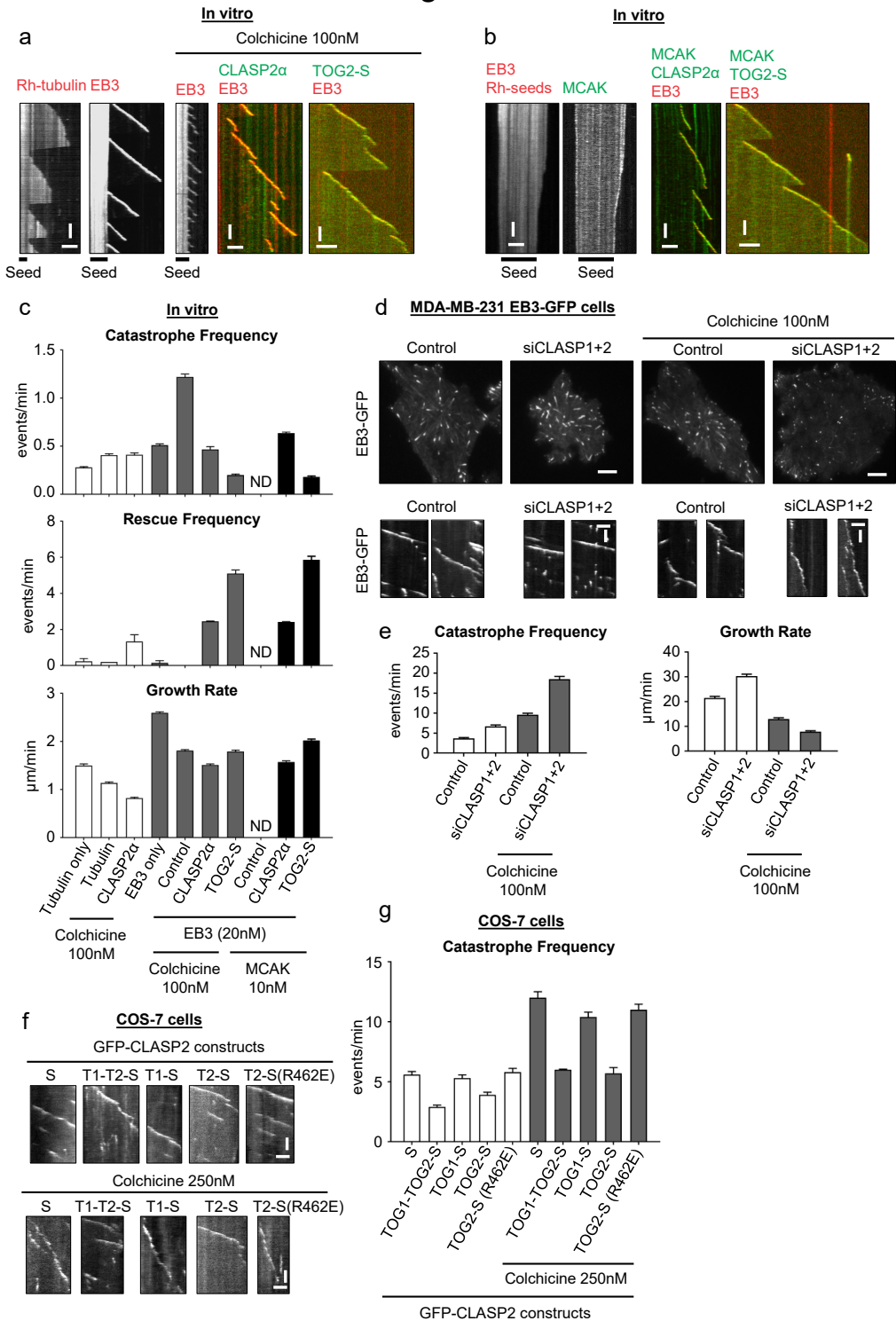
tubulin or MTs (Supplementary Fig. 2d,e). We also checked whether TOG1 could bind to alternative tubulin structures, such as tubulin rings induced by dolastatin or vinblastine, but found this not to be the case (Supplementary Fig. 3d). Thus, in contrast to a previous publication suggesting that the ability of TOG1 to bind tubulin is required for CLASP activity²⁴, we establish that TOG1 has an autoregulatory function (Fig. 3g). Based on this conclusion, we speculate that the TOG1-containing CLASP1/2 α isoforms are constitutively active whereas the CLASP2 β / γ isoforms, which lack TOG1²⁹, are autoinhibited.

CLASP2 suppresses catastrophes induced by MT-depolymerizing agents

The data described above revealed that CLASPs suppress spontaneous catastrophes. However, in cells catastrophes are often induced by specific factors that destabilize MT plus ends, such as MT depolymerases⁵. To test if CLASPs can counteract the action of such factors, we first tested the effect of MT depolymerizing drugs such as colchicine and vinblastine, which potentially promote catastrophes in the presence of EBs³¹. We found that CLASP2 α indeed promoted long MT polymerization events at drug concentrations that strongly perturbed MT growth (Fig. 4a,c, Supplementary Fig. 4a). Similarly, CLASP2 α counteracted the activity of the MT depolymerase MCAK, even when the latter was added at a concentration that, in the absence of CLASP2 α , was sufficient to completely block MT outgrowth and cause depolymerization of MT seeds (Fig. 4b,c, Supplementary Fig. 4b). The minimal catastrophe-suppressing module TOG2-S could also counteract the catastrophe-inducing action of colchicine and promoted MT growth in the presence of MCAK, and was even more effective than full length CLASP2 α (Fig. 4a-c).

We next tested whether CLASPs can protect MTs from drug-induced catastrophes in cells. Simultaneous depletion of CLASP1 and CLASP2 in MDA-MB-231 cells stably expressing EB3-GFP led to a mild increase in the MT catastrophe frequency in internal

Figure 4



2

Figure 4. CLASP2 α suppresses catastrophes induced by MT destabilizing agents in vitro and in cells.

(a) Kymographs showing MT plus end dynamics in the presence of rhodamine-tubulin alone or with 20 nM mCherry-EB3 or in the presence of 100 nM colchicine with 20 nM mCherry-EB3 alone or together with 30 nM GFP-CLASP2 α . Scale bars: 2 μ m (horizontal) and 60 s (vertical).

(b) Kymographs showing MT plus end depolymerization in the presence of 20 nM mCherry-EB3 and 10 nM GFP-MCAK, or plus end growth dynamics when 30 nM GFP-CLASP2 α or GFP-TOG2-S are added. Scale bars: 2 μ m (horizontal) and 60 s (vertical).

(c) Parameters of MT plus end dynamics in the presence of the indicated of proteins, with or without 100 nM Colchicine. Number of growth events analyzed: for rhodamine-tubulin alone, $n=135$, with colchicine, $n=110$, with colchicine and GFP-CLASP2 α , $n=68$, for mCherry-EB3 alone, $n=207$, for mCherry-EB3 with colchicine, $n=228$, for mCherry-EB3 with Colchicine and GFP-CLASP2 α , $n=136$ and for mCherry-EB3 with colchicine and GFP-TOG2-S, $n=241$. For mCherry-EB3 with GFP-MCAK and GFP-CLASP2, $n=144$ and for mCherry-EB3 together with GFP-MCAK and GFP-TOG2-S, $n=227$. Error bars represent SEM.

(d) Still images of MDA-MB-231 cells stably expressing EB3-GFP and kymographs showing MT plus end growth in control or CLASP1 and CLASP2 depleted cells alone or together with 100 nM colchicine. Scale bar: 5 μ m (cell images), 2 μ m (horizontal) and 60 s (vertical) (for kymographs).

(e) MT plus end catastrophe frequency and growth rates in MDA-MB-231 cells stably expressing EB3-GFP after transfection either with control or CLASP1 and CLASP2 siRNAs, untreated or treated with 100 nM colchicine. Number of growth events from left to right, $n=53$, 106, 53 and 123. Error bars represent SEM.

(f) Kymographs showing MT plus end dynamics in COS-7 cells expressing the indicated GFP-fusions; cells were untreated or treated with 250 nM Colchicine. Scale bars: 2 μ m (horizontal) and 15 s (vertical).

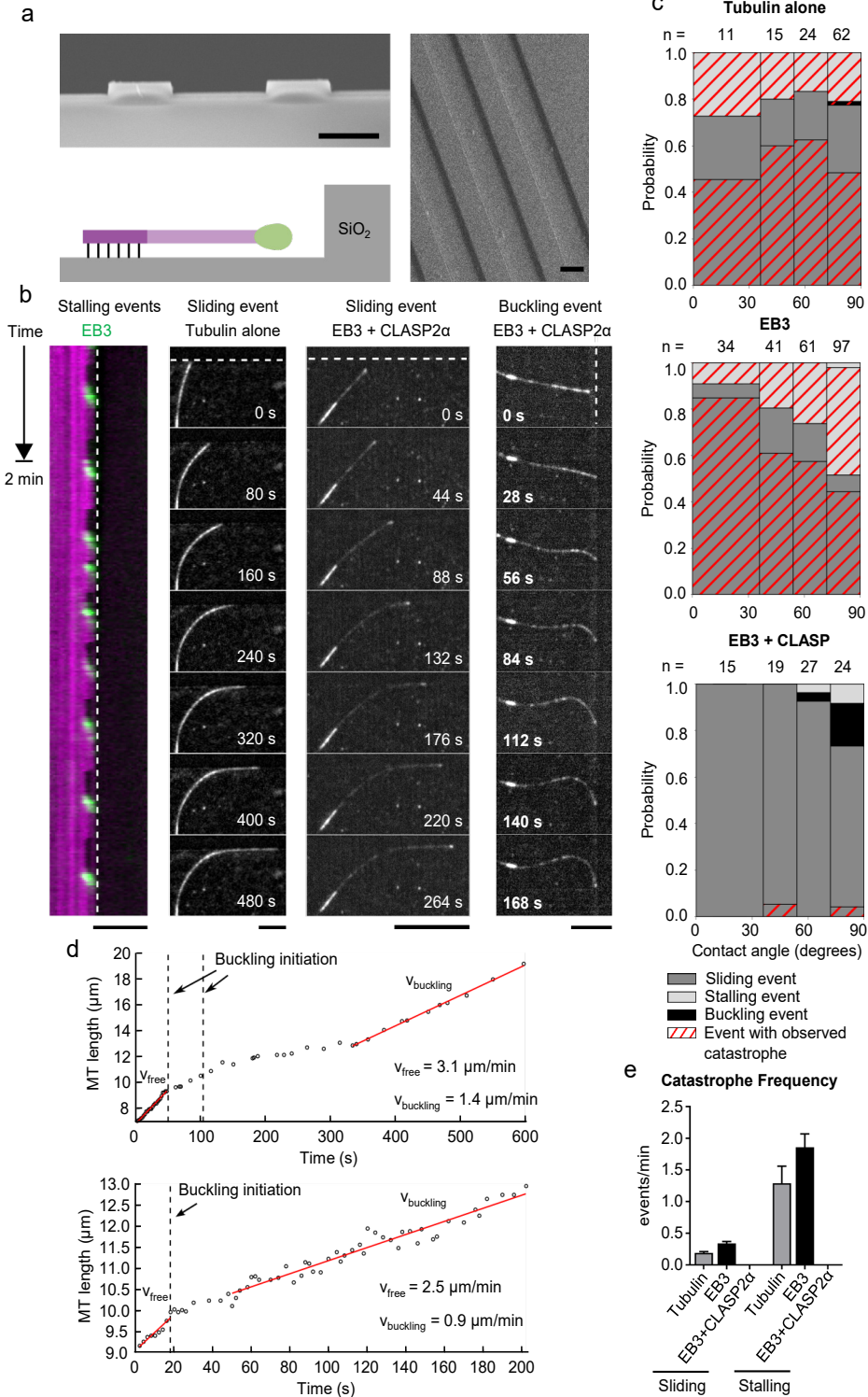
(g) MT plus end catastrophe frequency in COS-7 cells shown in (f). Numbers of growth events from left to right $n=61$, 61, 65, 64 and 65 (without colchicine) and with 250 nM colchicine, $n=61$, 65, 92, 47 and 70 (with 250 nM colchicine). Error bars represent SEM.

cell regions and resulted in a strong catastrophe increase in cells treated with colchicine (Fig. 4d,e). Importantly, the expression of MT tip-targeted CLASP2 TOG1-TOG2-S and TOG2-S fusions, but not of TOG1-S or the mutated version of TOG2-S, caused a mild catastrophe inhibition in control cells and strongly suppressed catastrophes in colchicine-treated cells (Fig. 4f,g, Supplementary Fig. 4c,d). These data show that CLASPs potentially counteract catastrophes induced by agents that perturb the MT end structure.

CLASP suppresses force-induced catastrophes

Next, we investigated whether CLASP is capable of suppressing catastrophes induced by compressive forces. It was previously shown that when a growing MT polymerizes against a solid barrier, the ensuing compressive force can advance the onset of a catastrophe⁴. We used micro-fabricated barriers composed of SiO₂ etched on a glass coverslip³². This fabrication process resulted in 1.7 μ m high barriers enclosing 15 μ m wide channels (Fig. 5a). MTs were allowed to grow from GMPCPP-stabilized seeds inside the channels and polymerize towards the barriers from varying angles and distances. The interaction of the MT plus end with the barrier gave rise to three different possible outcomes: sliding (bending and growing along the barrier), stalling, and buckling (Fig. 5b, Supplementary Videos 1-5). Stalling indicates that a MT is unable to overcome the compressive force build-up during barrier contact and therefore cannot continue polymerizing, but instead remains in a static contact with the barrier until the onset of a catastrophe. Buckling occurs when a MT contacting the barrier keeps growing while its end remains at the same position at the barrier (indicative of a moderate compressive force).

Figure 5



2

Figure 5. CLASP2 α inhibits force-induced catastrophes in the presence of EB3.

(a) Scanning Electron Microscope images with cross-sectional and top-down view of the SiO₂ barriers. The cartoon illustrates the MT-barrier interaction of a seed-nucleated MT in the presence of MT tip-binding proteins. Scale bars: 10 μ m.

(b) Representative kymograph and three-frame averaged montages of the three types of events during MT-barrier contact: stalling, sliding, and buckling. The location of the barrier is denoted by dashed white lines. All experiments were performed at 30°C, with the following concentrations when present: tubulin (15 μ M), EB3 (20 nM), CLASP (30 nM). Scale bars: 10 μ m. See also Supplementary Videos 1-5.

(c) Probability of the event type during MT-barrier contact as a function of the contact angle, with 90° being perpendicular to the barrier. The red hatched events ended with a catastrophe.

(d) MT growth during two buckling events. Vertical dotted lines indicate the start of a buckling event. The first graph contains two buckling initiation events, as the MT tip slipped during the first event. MT growth velocities are significantly lower during buckling compared to free growth.

(e) MT plus end catastrophe frequency during barrier contact for MTs sliding or stalling in the presence of tubulin alone or together with 20 nM mCherry-EB3 alone or with 20 nM mCherry-EB3 and 30 nM GFP-CLASP2 α . For sliding events, n=88, 156 and 77 and for stalling events, n=23,77 and 3 for MTs grown in the presence of tubulin alone, together with mCherry-EB3 and with both mCherry-EB3 and GFP-CLASP2 α . Error bars represent SEM.

In the absence of EB3 and CLASP, sliding behavior predominated for all contact angles due to the smooth surface of the barriers, while the addition of EB3 led to an increase in stalling events, particularly when the seeds were perpendicular to the barriers (Fig. 5b,c, Supplementary Video 1,2). The catastrophe frequency during contact in both cases was higher for stalling than for sliding, and was particularly high for MTs stalled at barriers in the presence of EB3, clearly showing that the MT plus end is less stable at high compressive forces in these conditions (Fig. 5e). Strikingly, the addition of EB3 and CLASP2 α resulted in persistent MT growth almost devoid of observable catastrophes for all event types (Fig. 5d, Supplementary Video 3,4,5). A few buckling events were observed in the presence of EB3 and CLASP2 α at almost perpendicular contact angles (Fig. 5d, Supplementary Video 4,5). During buckling, the MT growth speed decreased compared to the growth speed prior to barrier contact, but remained constant after an initial pausing phase (Fig. 5d). These data show that CLASP can prevent destabilization of a growing MT tip during barrier contact even at high compressive forces during buckling.

A few CLASP monomers stabilize incomplete MT structures

To get insight into the mechanism underlying CLASP activity, we first investigated its residence at MT tips and lattices. As published before³³, we found that mammalian CLASPs are monomeric (Fig. 6a). The interactions of CLASP2 α and TOG2-S with MT tips and lattices in the presence of EB3 were very transient (Fig. 6b-d), with an average residence time at tips of ~0.2-0.3s, similar to what was previously described for other MT tip-tracking proteins^{27, 34, 35}. Next, by using single GFP-CLASP2 α molecules immobilized in a separate chamber on the coverslip used for the MT dynamics assay, we estimated the number of CLASP molecules necessary for catastrophe suppression and rescue induction. Due to the exponential decay of the TIRF field, the brightness of a molecule attached to a MT compared to a molecule attached to the glass surface would be lower, but our previous

Figure 6

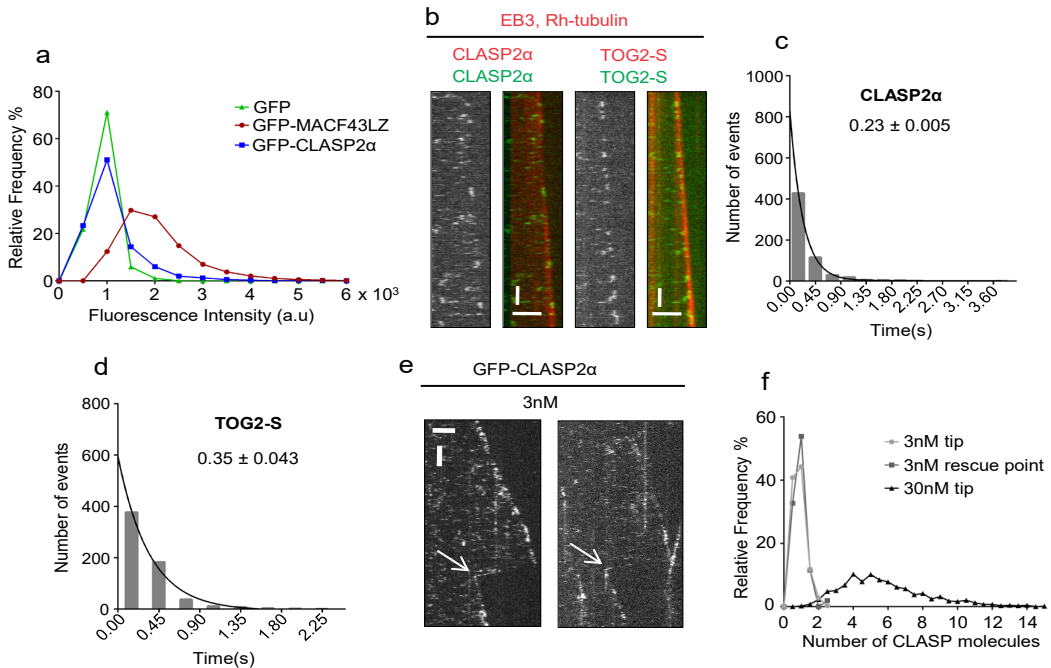


Figure 6. A small number of CLASP molecules can suppress catastrophe and induce rescue.

(a) Distributions of fluorescence intensity values for single molecules of GFP (green, mean intensity value = $0.92 \times 10^3 \pm 0.25 \times 10^3$) ($n=846$ molecules analyzed), GFP-CLASP2 α (blue, mean = $1.2 \times 10^3 \pm 1.3 \times 10^3$) ($n=2341$) and GFP-MACF43-LZ (red, mean = $2.12 \times 10^3 \pm 1.5 \times 10^3$) ($n=7516$).

(b) Kymographs showing MT plus end and lattice turnover for GFP-CLASP2 α and TOG2-S for MTs grown in the presence of 20 nM mCherry-EB3, rhodamine-tubulin together with both 30 nM mCherry-CLASP2 α and 0.5 nM GFP-CLASP2 α or 30 nM mCherry-TOG2-S and 0.5 nM GFP-TOG2-S. Scale bars: 2 μ m (horizontal) and 2 s (vertical).

(c, d) Exponential fits of the distributions of dwell times at the MT tip for CLASP2 α (mean time = 0.23 ± 0.005 s), $n=608$ tip events (c) and TOG2-S (mean time = 0.35 ± 0.043 s), $n=622$ tip events (d).

(e) Kymographs showing MT plus end dynamics in the presence of 3 nM GFP-CLASP2 α and 20 nM mCherry EB3 (only green channel shown). Scale bars: 2 μ m (horizontal) and 30 s (vertical).

(f) Distributions of the number of GFP-CLASP2 α molecules in the presence of 20 nM mCherry EB3 at growing MT plus ends ($n=1078$ tip events) and at rescue points ($n=17$ rescue events) in the presence of 3 nM GFP-CLASP2 α , and at growing MT plus end with 30 nM GFP-CLASP2 α ($n=1393$ tip events).

analysis showed that the underestimate is in the range of 10%³⁶. We found that one or two transiently binding molecules were sufficient to induce rescues at 3 nM CLASP2 α (Fig. 6e,f). Rescues often occurred after a short event of CLASP2 α tracking the depolymerizing MT end (Fig. 6e). In contrast to the previous work on yeast and *Drosophila* CLASPs^{22, 23}, rescues thus did not require the accumulation of immobile CLASP clusters on the MT lattice. At the MT tip, 4-7 CLASP molecules were typically present in conditions when catastrophes were fully suppressed (Fig. 6f). Together, these data indicate that a relatively small number of CLASP molecules (less than 10) are sufficient to suppress catastrophes, and even fewer CLASP molecules can promote rescues.

Interestingly, the examination of kymographs of MT growth in the presence of CLASPs

Figure 7

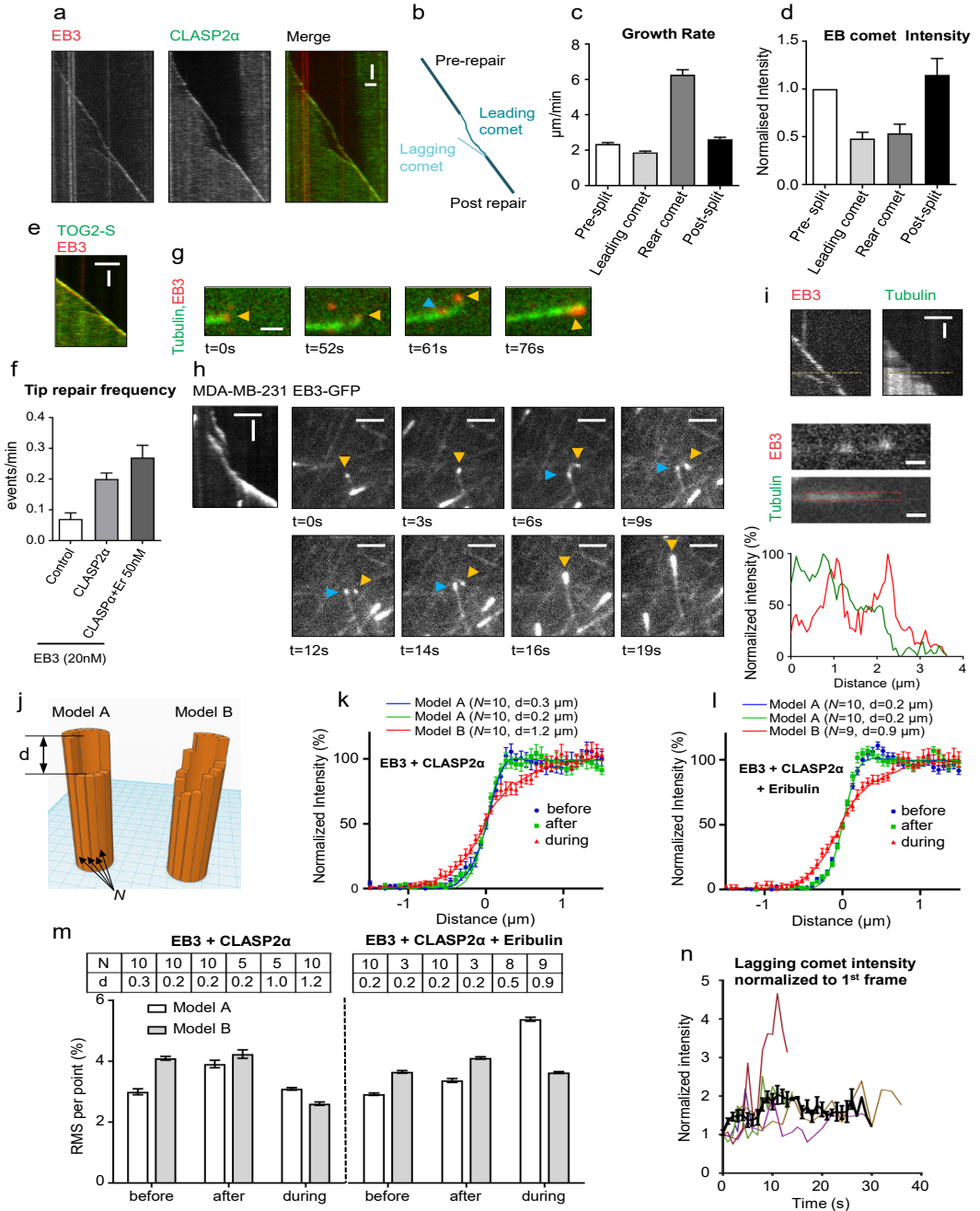


Figure 7. CLASP2 α stabilizes incomplete MT tip structures.

(a, b) Kymographs showing a MT tip repair (split comet) event with 20 nM mCherry-EB3 and 30nM GFP-CLASP2 α (a), a schematic of the same event is shown in (b). Scale bars: 2 μm (horizontal) and 60 s (vertical). (c, d) Growth rates (c) ($n=65$ events) and the EB-comet intensities (d) ($n=17$ events) before, during and after comet splitting. EB-comet intensities are normalized to the comet intensity before splitting. (e) Kymograph showing a tip repair event in the presence of 20 nM mCherry-EB3 and 30 nM TOG2-S. Scale

bars: 2 μm (horizontal) and 45 s (vertical).

(f) Frequency of tip repair for MTs grown in the presence of 20 nM mCherry-EB3 alone ($n=49$) or together with 30 nM TagBFP-CLASP2 α ($n=103$) or in the presence of 20 nM mCherry-EB3, 30 nM TagBFP-CLASP2 α and 50 nM Eribulin-A488 ($n=56$). The frequency was calculated by dividing the number of observed tip repair events by the total growth time, n =number of MTs analyzed in each condition. Error bars represent SEM.

(g) Still images of a MT grown in the presence of Alexa488-tubulin, 20 nM mCherry-EB3 and 30 nM TagBFP-CLASP2 α showing curling in the region between the leading and the lagging comet. Arrowheads point to the EB comets, yellow points to the leading and blue to the rear comet. Scale bar: 1 μm . See also Supplementary Video 6.

(h) Kymograph and corresponding still images showing a MT tip repair event in MDA-MB-231 cells stably expressing EB3-GFP. The yellow arrowhead points to the leading comet and the blue one to the rear comet. Scale bars: 2 μm (horizontal) and 5 s (vertical) (kymograph) and 2 μm (cell image). See also Supplementary Video 7.

(i) Kymograph showing a MT tip repair event in the presence of HiLyte-488 tubulin, 20 nM mCherry-EB3 and 30 nM TagBFP-CLASP2 α , still images and line-scans along the red (EB3) and green (tubulin) channel during tip repair. Scale bars: 2 μm (horizontal) and 30 s (vertical) (kymograph) and 0.5 μm (still images).

(j) Illustration of two different MT end tapering models representing sharp (Model A, left) and gradual (Model B, right) loss of protofilaments.

(k, l) Averaged tip intensity profiles of tubulin channel (green) for MTs grown in the presence of 20 nM mCherry-EB3 and 30 nM TagBFP-CLASP2 α (k), $n=16$, 17 and 17 for before, after and during tip repair, respectively, and for MTs grown in the presence of 20 nM mCherry-EB3, 30 nM TagBFP-CLASP2 α and 50 nM Eribulin, $n=40$, 44 and 27 for before, after and during tip repair, respectively. Error bars represent SEM. Lines correspond to the best fits of simulations with the optimal model type and parameter values indicated at the top of each plot.

(m) The distribution of minimal residuals between simulated and experimental profiles depending on the model. Top table shows optimal parameter values for each case (d is in μm). For each case $n=3$. Error bars represent SD.

(n) Changes of the mCherry-EB3 comet intensity over time for the lagging comet before the tip repair. Individual traces represent a single tip repair event. The black line is the average of several time traces ($n=22$). Intensity values were normalized to the value at the first time point.

often revealed the appearance of “split” EB3 comets – events whereby a MT tip growth slowed down and was subsequently restored by a “catching up” EB3 comet that appeared behind the growing tip and was moving more rapidly than the “leading” comet (Fig. 7a-d). It has been previously shown that such events could be occasionally observed with MTs grown in the presence of EB3 and that their frequency can be strongly increased by the protofilament-blocking agent eribulin, indicating that they represent elongation of an incomplete MT⁶. In the presence of CLASPs, or just its MT tip-targeted TOG2 domain, such MT tip repair events could be observed frequently and became very long, with the duration often exceeding 60 s and the length of up to 3-4 μm (Fig. 7e, f, Supplementary Fig. 5a-b). The idea that some protofilaments are missing in the MT end corresponding to the “leading” comet was supported by the observation that such ends were often bent or curled (Fig. 7g, Supplementary Video 6). Split comet events, which could also exhibit curling, were also observed in cells (Fig. 7h, Supplementary Video 7), indicating that they are not an artifact of in vitro reconstitution.

To test if comet splitting is indeed caused by stalling of a part of the protofilaments, we collected data in the presence of TagBFP-CLASP2 α , mCherry-EB3 and HiLyte488-labeled tubulin and analyzed MT intensity profiles in the tubulin channel at different time points

during comet splitting (Fig. 7i). As expected, the MT intensity in the region between the leading and lagging comets was lower than the region behind the lagging comet (Fig. 7i, bottom panel). We considered two simple models of MT tip “erosion”: a subset of N protofilaments could be shortened by a uniform value d from the growing tip, creating a sharp drop in intensity (Model A, Fig. 7j), or the erosion could be gradual, and we assumed that the lengths of the missing parts of N protofilaments were distributed exponentially with characteristic value d (Model B, Fig. 7j). Using these models, we performed Monte-Carlo simulations of the MT intensity, assuming that a MT has 13 protofilaments and that tubulin dimers are labeled with a probability equal to the fraction of labeled tubulin in the reaction (Supplementary Fig. 5 c-g, see Methods for details).

We analyzed two types of experimental data, the “control” situation with CLASP2 α and EB3, or the situation where the reaction was supplemented with 50 nM eribulin, which increases the frequency of split comets (Fig. 7f). For each condition, experimental intensity profiles of tubulin were recorded at three time points: before, during and after the catching-up event (Fig. 7k, l, blue, green and red, respectively). The time point during catching-up was selected at the moment when the distance between comets was approximately equal to 1 μm . For each model, the parameters N and d were varied in search of values minimizing the residual between the experimental and theoretical profiles (Fig. 7m). Results for both “before” and “after” conditions were very similar and favored Model A (sharp drop) with $N=10$ missing protofilaments (or 3 protruding protofilaments) with a characteristic length d of 0.2-0.3 μm (Fig. 7k,l, m). For the “catching-up” phases, the experimental profiles were better approximated by Model B (gradual) with 9-10 missing protofilaments and a much longer erosion length d of 0.9-1.2 μm (Fig. 7k,l, m). If the assumption of gradual tip erosion from Model B is correct, this means that the rear EB comet intensity should gradually increase during the catching-up event, as more protofilaments are joining it. Indeed, the averaging of multiple time traces for EB catch-up rear comets shows an increase in intensity during growth (Fig. 7n), supporting the results of modeling.

Taken together, our results show that a few monomeric CLASP molecules, transiently associated with MT tips, prevent the onset of a catastrophe at MT ends missing a critical number of protofilaments and promote their repair to restore the MT tip structure (Supplementary Fig. 5h).

CLASP can stall depolymerization of damaged MTs and induce their repair

To further explore the capacity of CLASP to repair MTs, we performed laser-mediated MT severing experiments. In the presence of tubulin alone or together with EB3, we found that severed MT lattices always depolymerize from their plus ends, as described previously³⁷. In the presence of CLASP2 α , with or without EB3, MT plus-end depolymerization was strongly inhibited or even completely stalled (Fig. 8a,b). Next, we induced partial MT damage by performing laser irradiation next to a MT, which often caused the MT to bend progressively at the laser damage site and eventual breaking off the lattice. This was

Figure 8

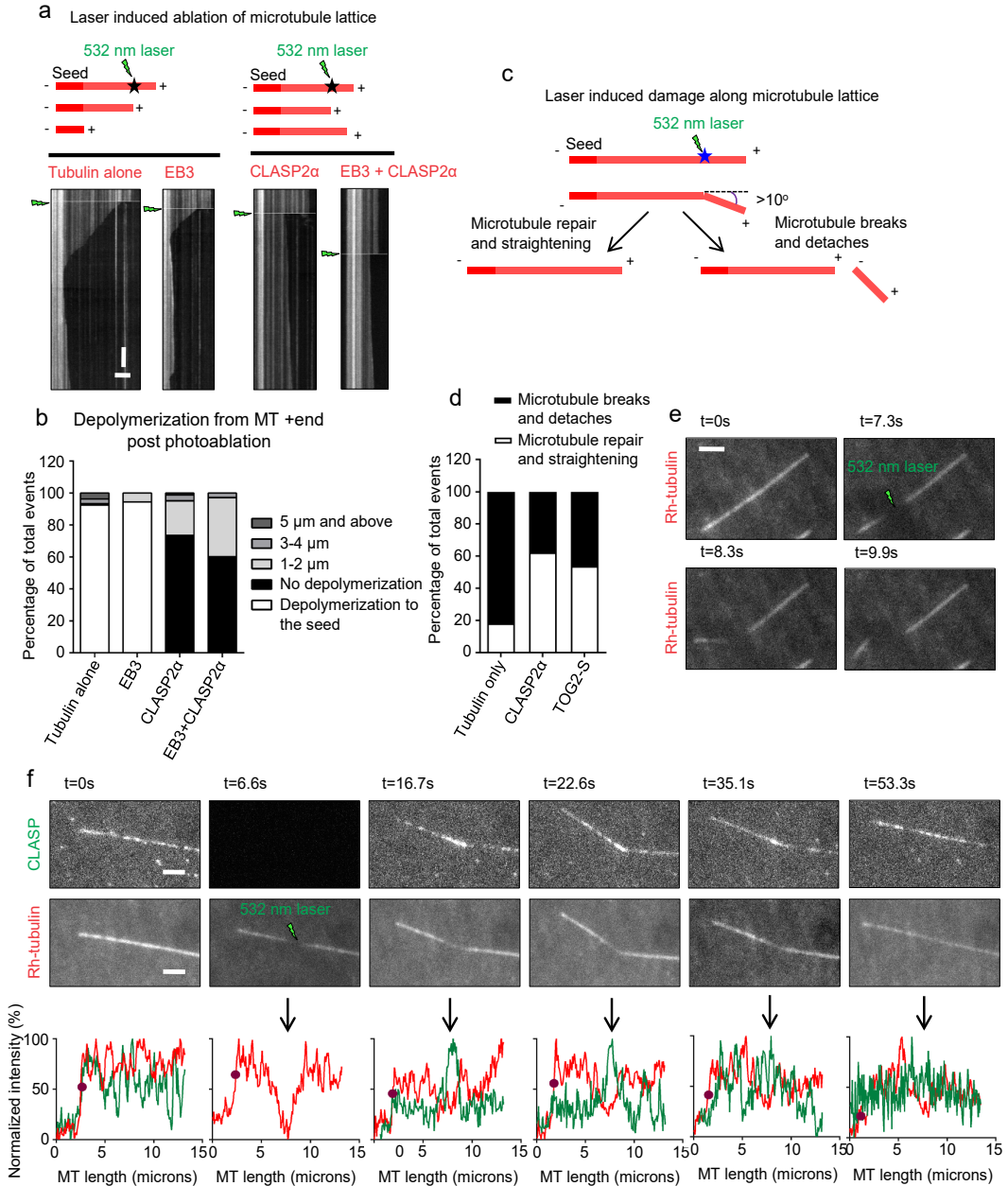


Figure 8. CLASP2α or its second TOG-like domain can mediate MT lattice repair.

(a) A scheme of a photoablation experiment using a 532 nm pulsed laser and kymographs showing the outcome of laser severing of a MT in the presence of rhodamine-tubulin alone or together with 20 nM mCherry-EB3, or 30 nM mCherry-CLASP2α, or both. Scale bars: 3 μm (horizontal) and 6 s (vertical).

(b) Plot showing the percentage of different outcomes after photoablation for the newly generated MT plus end in the presence of rhodamine-tubulin alone (n=132), together with 20 nM mCherry-EB3 (n=54), 30 nM mCherry-CLASP2α (n=83) or both 20 nM mCherry-EB3 and 30 nM mCherry-CLASP2α (n=68). n=number of MTs analyzed.

- (c) A scheme of different outcomes after photodamage of a MT. Events when a MT bends to an angle $>10^\circ$ at the point of photodamage result either in MT repair and straightening or MT breaking.
- (d) Plot showing the percentage of total events resulting in either MT breaking or repair at the point of photodamage in the presence of tubulin alone ($n=23$) or together with either 30 nM GFP CLASP2 α ($n=53$) or 30 nM TOG2-S ($n=54$).
- (e, f) Time lapse images of a dynamic MT grown in the presence of rhodamine-tubulin alone (e) or together with 30 nM GFP-CLASP2 α (f) damaged at a point along the lattice. In (f), intensity profiles along the MT for the CLASP and tubulin channel are shown below with the arrow pointing to the site of photodamage. The purple circle on the plot indicates the end of the MT. Scale bar: 2 μm .

most likely due to the dissociation of tubulin dimers from the damaged MT lattice and subsequent loss of mechanical integrity (Fig. 8c). In the presence of tubulin alone, MTs bent by more than 10° after photo-damage typically broke (Fig. 8d,e), although in 18% of the events MTs straightened again (Fig. 8d), suggesting that they were repaired (Fig. 8d,e). These data are in agreement with previous work showing that damaged MT lattices can be repaired by tubulin incorporation⁷⁻⁹. When these experiments were performed in the presence of CLASP2 α , the protein rapidly accumulated at the site of the damage (Fig. 8f, Supplementary Video 8) and the frequency of successful repair of MTs bent at a damaged site by an angle of more than 10° increased threefold to 62% (Fig. 8d). The TOG2-S fusion could also autonomously enrich at the damaged site and promote repair (Fig. 8d, Supplementary Fig. 6, Supplementary Video 9). Taken together, these data show that CLASPs can autonomously recognize damaged MT sites and stabilize incomplete MT structures to promote repair of MT tips and lattices.

DISCUSSION

CLASPs are among the most conserved regulators of MT dynamics, which are present in animals, plants and fungi^{13, 38, 39}. In this paper, by performing a detailed analysis of the activities of individual CLASP domains combined with diverse perturbations of MT structure and dynamics, we showed that CLASPs enhance the repair of incomplete or damaged MTs and thus promote MT stability.

Previous work demonstrated that CLASPs can promote rescues in different systems^{30,39}. CLASPs can also suppress catastrophes, but it was not clear whether this is a biochemically distinct activity or whether it reflects increased rescue frequency in the vicinity of the MT tip²². By analogy with other TOG domain-containing members of the XMAP215/ch-TOG family, which bind to free tubulin and promote their association with growing MT ends, it was proposed that CLASPs promote rescues by recruiting tubulin dimers to MTs^{22, 24}. However, several lines of data do not fit well with such a model. First, the TOG-like domains of CLASPs, when tested individually, do not bind tubulin, most likely because they display a much more convex shape than the tubulin-binding TOG domains of XMAP215/ch-TOG family members^{25, 26}. Second, CLASPs do not accelerate but rather inhibit the MT growth rate, an observation that is difficult to reconcile with a polymerase activity. Third, bona fide MT polymerases such as XMAP215 do not block catastrophes or induce rescues in vitro⁴⁰, and our experiments showed that targeting of

individual tubulin-binding TOG domains of the mammalian XMAP215 homologue ch-TOG to growing MT tips had little effect on catastrophes and rescues. In contrast, we found that artificial targeting of a single TOG-like domain of CLASP2, TOG2, to growing MT plus ends was sufficient to completely suppress catastrophes and thus recapitulate one major activity of the full length protein. Importantly, although TOG2 does not bind to tubulin, several of its residues expected to be engaged in interactions with a MT based on the analysis of other TOG domains, are required for catastrophe suppression. Furthermore, it has been shown that TOG2, although only weakly binding to stabilized MTs, displays a higher affinity to drug-stabilized tubulin ring-like oligomers²⁶. These data suggest that CLASPs might stabilize incomplete MT structures such as curved, protruding protofilaments to prevent MT disassembly (Supplementary Fig. 5h). We provided direct support for this idea by showing that in the presence of CLASPs, MTs could tolerate the loss of a significant number of protofilaments without undergoing a catastrophe. In the presence of CLASPs, protruding protofilaments kept elongating until the lagging protofilaments would catch up, leading to MT repair.

It is likely that the unique convex architecture of TOG2 with an additional N-terminal helix that stabilizes the domain's paddle-like HEAT repeat structure^{25, 26} is important for recognition and stabilization of partial, curved MT structures. The ability of CLASP2 to mildly enrich at MT tips and accumulate at the sites of MT damage supports this idea. Furthermore, a single TOG2 domain could also promote rescues, even when it completely lacked any MT lattice targeting domains such as positively charged linker regions. Since TOG2 has no affinity for tubulin and only a weak affinity for stabilized MTs, these data can best be explained by the interaction of this domain with depolymerizing MT ends. In the presence of CLASPs, subsets of protofilaments at plus ends can undergo shrinkage and regrowth on the scale of several microns, with CLASPs promoting stabilization and repair of these partial MT tip structures.

Another TOG-like domain of CLASP2, TOG3, did not suppress catastrophes but promoted rescues. This domain is structurally different from TOG2, binds better to vinblastine-stabilized tubulin spiral-like oligomers and stabilized MTs, but interacts less well with the more curved tubulin rings induced with soblidotin²⁶. It is possible that TOG2 and TOG3 bind to peeling protofilaments with different curvature or have different ability to stabilize lateral contacts between protofilaments. Irrespective of the exact mechanism, the distinct activities of TOG2 and TOG3 demonstrate that the catastrophe suppression and rescue induction activities of CLASPs are mechanistically different (Supplementary Fig. 7). This view is supported by our observation that more CLASP molecules were needed to suppress catastrophes than to induce rescues, and therefore, for catastrophe inhibition CLASPs had to be concentrated near MT plus ends by binding to EBs.

Strikingly, stalling of depolymerization of artificially damaged MTs could be achieved by CLASP alone. We found that CLASP2 α efficiently blocks depolymerization of a severed MT or repairs a damaged MT lattice, although it did not by itself suppress catastrophes

and depolymerization of dynamic MTs. In growing MTs, catastrophes might be initiated by rapid depolymerization of a few strongly protruding protofilaments. This would be in line with the model hypothesizing that increased tapering of MT plus ends leads to catastrophe^{41, 42}. It is possible that preventing progressive peeling of a few protruding protofilaments is more demanding than stalling the initiation of outward protofilament curling of a freshly severed blunt MT.

Many cytoskeletal proteins are known to be controlled by autoinhibitory interactions, which are released by the binding of their partners. Here, we showed that CLASPs also belong to this category of cytoskeletal proteins, because their C-terminal domains (CLIP-ID), responsible for the interactions with the majority of known CLASP partners such as CLIP-170, LL5 β , GCC185, CENP-E and Xkid^{20, 29, 43-45}, can inhibit the MT-directed activities of TOG2 and TOG3. Interestingly, we found that the N-terminal TOG domain of CLASP, TOG1, which does not bind to either MTs or tubulin because it lacks the conserved residues necessary for contacting tubulin, can release the autoinhibition. TOG1 is present in CLASP1/2 α isoforms but absent in CLASP2 β and CLASP2 γ isoforms²⁹. CLASP2 can thus be expressed both as a constitutively active isoform and as isoforms that require partner binding for their activation, which might be important for increasing the activity of CLASPs at specific cellular sites such as mitotic kinetochores or the cell cortex.

Interestingly, our findings provide insight into how CLASPs work in different cellular settings. For example, the ability to suppress catastrophes fits well with the fact that CLASPs promote processive MT growth at kinetochores, a process that is required for spindle flux¹². The ability of MTs in the presence of the CLASP-EB complex to make a sharp turn and to continue growing at a glass barrier explains how CLASPs can help MTs to navigate around sharp edges in plant cells¹⁷. The observation that CLASPs inhibit catastrophes during encounters with physical barriers also helps explaining how CLASP1 participates in driving persistent MT growth at the tips of cancer cells during invasion into a 3D matrix¹⁹. Such persistent MT growth in the vicinity of the cell cortex prevents the retraction of cell protrusions in 3D and supports their elongation. In this context, modeling suggested that this property can be due to the increased ability of growing MTs to withstand compression¹⁹.

CLASPs also have a very well documented rescue activity^{30, 39}. Previous work with yeast and fly CLASP proteins showed a significant correlation between rescue sites and the presence of immobilized CLASP clusters^{22, 23}. In contrast, in our reconstitutions rescues were induced by a few mammalian CLASP molecules exchanging rapidly on the MT lattice. Furthermore, the strong MT repair-promoting properties of CLASPs suggest that they can stimulate rescues induced by MT damage^{7, 9}. A more efficient and fast repair of MT lattices by CLASPs might explain the fact that when CLASPs are depleted, the GTP content and thus the EB accumulation along MT shafts increases, a phenotype that could be rescued by the TOG2 domain of CLASP2 alone⁴⁶.

Finally, the finding that the CLASP-EB complex strongly lowered the kinetic threshold

for template-based MT outgrowth explains why CLASPs can stimulate γ -tubulin-dependent MT nucleation from the Golgi²⁰. The observation that the overall MT polymer mass is reduced in CLASP-depleted cells¹⁸ suggests that CLASPs might also play a role in promoting MT nucleation from the centrosome. Both TOG2 and TOG3 are likely to cooperate in this process, as they both display partial activity compared to the full length CLASP2 α protein. Taken together, our data reveal how a combination of distinct domains with anti-catastrophe, rescue, partner binding and autoregulatory activities make CLASPs potent MT growth promoting factors; their ability to bind partial MT structures further characterizes them as autonomous MT repair factors.

2 Methods

DNA constructs, cell lines and cell culture

CLASP truncations expressed in mammalian cells were made from the full length constructs described previously^{18, 29} in modified pEGFP-C1 or pmCherry-C1 vectors with a StrepII tag. Ch-TOG construct was a gift of S. Royle (University of Warwick, UK). MDA-MB-231 cells stably expressing EB3-GFP19 were cultured in DMEM supplemented with 10% FCS. COS-7 and HEK 293T cells were cultured in DMEM/F10 (1:1 ratio, Lonza, Basel, Switzerland) supplemented with 10% FCS. For siRNA transfection, MDA-MB-231 cells stably expressing EB3-GFP were simultaneously treated with siRNAs specific for CLASP1 and CLASP218 or with control (luciferase) siRNA19 for 72 hours. EB3-GFP comets were imaged in live cells on a TIRF microscope and kymographs were analyzed to determine the effects of CLASP1/2 depletion on MT plus end dynamic). For overexpression of CLASP2 constructs, COS-7 cells were transiently transfected with different StrepII-GFP-CLASP2 constructs (as indicated in the figures) for 12 hours, and the GFP signals of these constructs were used to quantify MT dynamics. Live imaging of COS-7 cells overexpressing different constructs of CLASP2 in the presence of colchicine (250 nM) was performed within 40 min of colchicine treatment. HEK293T, MDA-MB-231 and COS-7 cell lines used here were not found in the database of commonly misidentified cell lines maintained by ICLAC and NCBI BioSample, were not authenticated and were negative for mycoplasma contamination.

Protein purification from HEK293T cells for in vitro reconstitution assays

GFP-CLASP1 α , mCherry-CLASP2 α , Tag-BFP-CLASP2 α , GFP-CLASP2 α , its TOG-domain truncations, point mutants, fusion proteins with the TOG domains of chTOG and coiled coil of CLIP-170, and GFP-MCAK used in the in vitro reconstitutions assays were purified from HEK293T cells using the Strep(II)-streptactin affinity purification. Cells were harvested 2 days after transfection. Cells from a 15 cm dish were lysed in 500 μ l of lysis buffer (50 mM HEPES, 300 mM NaCl and 0.5% Triton X-100, pH 7.4) supplemented with protease inhibitors (Roche) on ice for 15 minutes. The supernatant obtained from the cell lysate after centrifugation at 21,000 x g for 20 minutes was incubated with 40 μ l of

StrepTactin Sepharose beads (GE) for 45 minutes. The beads were washed 3 times in the lysis buffer without the protease inhibitors. The protein was eluted with 40 μ l of elution buffer (50 mM HEPES, 150 mM NaCl, 1 mM MgCl₂, 1 mM EGTA, 1 mM dithiothreitol (DTT), 2.5 mM d-Desthiobiotin and 0.05% Triton X-100, pH 7.4). Purified proteins were snap-frozen and stored at -80 °C.

Cloning, protein expression and purification from E. coli

Each human CLASP2 TOG construct (see Figure 2a) was cloned into a pET-based bacterial expression vector using the restriction free positive selection method⁴⁷. All recombinant proteins contained either an N-terminal thioredoxin-6xHis or 6xHis cleavable tag for affinity purification. For standard expression, the proteins were transformed into the E. coli expression strain BL21(DE3). Transformed cells were incubated at 37 °C until an OD₆₀₀ of 0.4 to 0.6 was reached. The cultures were subsequently cooled down to 20 °C prior to induction with 0.4 mM isopropyl 1-thio- β -galactopyranoside (IPTG, Sigma). Expression was carried out overnight at 20° C. Cells were harvested by centrifugation at 4°C for 15-20 min and lysed by sonication (50 mM HEPES, pH 8.0, 500 mM NaCl, 10 mM Imidazole, 10% Glycerol, 2 mM β -mercaptoethanol, proteases inhibitors (Roche)). The crude extracts were cleared by centrifugation at 20,000 x g for 20 min and the supernatants were filtered through a 0.45 micron filter before purification.

TOG domain proteins were purified by immobilized metal-affinity chromatography (IMAC) on HisTrap HP Ni²⁺ Sepharose columns (GE Healthcare) at 4°C according to the manufacturer's instructions. The thioredoxin-6xHis or 6xHis tags were cleaved by 3C protease during dialysis against lysis buffer (without proteases inhibitors). Cleaved samples were reapplied onto an IMAC column to separate the cleaved products from the respective tags and potentially uncleaved protein. Processed proteins were concentrated and gel filtrated on a HiLoad Superdex 75 16/60 size exclusion chromatography column (GE Healthcare) equilibrated in 20 mM Tris HCl, pH 7.5, 150 mM NaCl, 2 mM DTT. Protein fractions were analyzed by Coomassie stained SDS-PAGE. Fractions containing the target protein were pooled and concentrated by ultrafiltration. Protein concentrations were estimated by UV at 280 nm and the pure proteins were aliquoted, flash frozen in liquid nitrogen and stored at -80°C.

MT pelleting assay

MT pelleting assays were performed as previously described⁴⁸. Briefly, taxol-stabilized MTs were assembled in BRB80 buffer (80 mM PIPES-KOH, pH 6.8, 1 mM MgCl₂, 1 mM EGTA) from pure bovine brain tubulin at 1 mg/mL. 50 μ l of polymerized MTs were incubated 20 min with 20 μ l of the protein of interest at 2 mg/mL (diluted to the desired protein concentration with 2 x BRB80 buffer) and 50 μ l of BRB80. The mixture was centrifuged at 25°C for 20 min at 180,000 x g. Mix, supernatant and pellet fractions were analyzed by Coomassie stained 12% SDS-PAGE. As controls, MTs alone and individual TOG domains

were processed the same way.

Isothermal Titration Calorimetry (ITC)

All the proteins were buffer exchanged to BRB80 buffer supplemented with 50mM NaCl by overnight dialysis at 4°C. ITC experiments were performed at 25°C using an ITC200 system (Microcal) by step wise addition of different TOG domain proteins (syringe concentration was 150 μ M for CLASP2 TOG1, TOG2 and TOG3, 200 μ M for CLIP-ID, and 250 μ M for Stu2 TOG1) in the ITC cell containing 15 μ M bovine brain tubulin. The resulting heats were integrated and fitted in Origin (OriginLab) using the standard 'one set of sites' model implemented in the software package. Only for Stu2 TOG1 the dissociation constant of binding to tubulin could be determined ($K_d=18.8 \pm 3.21$ nM).

Crystallization, data collection and structure solution

CLASP2-TOG1 (HsCLASP2 residues 2-228) crystals were obtained by the hanging-drop vapor diffusion method at 20°C in the Morpheus crystallization condition B12 (Molecular Dimensions) by mixing 2 μ L of the protein at 7 mg/mL with 2 μ L of the reservoir solution. Crystals appeared over-night and were frozen directly in liquid nitrogen. A single-wavelength anomalous diffraction experiment from intrinsic sulfur atoms (S-SAD) was performed at the macromolecular crystallography super-bending magnet beamline X06DA (PXIII) at the Swiss Light Source, Villigen, Switzerland. 360° native data sets were collected at 1.0 Å wavelength on a single crystal at 100 K. Multi-orientation 360° data were collected on the same crystal at 100 K at a wavelength of 2.066 Å with 0.2° oscillation and 0.1 sec exposure at 8 different orientations of the PRIGo multi-axis goniometer⁴⁹, as previously described⁵⁰. The sample-to-detector distance was set to 120 mm. The data were processed using XDS (Kabsch, W. (2010a). XDS. Acta Cryst. D66, 125-132.) and scaled and merged with XSCALE51. The high-resolution data cut-off was based on the statistical indicators CC1/2 and CC^{*}⁵². Substructure determination and phasing were performed with SHELXC/D/E53 using the HKL2MAP interface⁵⁴. The successful SHELXD substructure solution that was found in a search for 20 sites had a CCall and a CCweak of 41.27 and 23.45, respectively. 154 cycles of density modification resulted in a clear separation of hands. Model building was performed using Buccaneer^{55, 56}. The resulting model was improved through iterative model rebuilding in Coot⁵⁷ and refined in the PHENIX software package⁵⁸. The quality of the structure was assessed with MolProbity⁵⁹. See Supplementary Table S1 for crystallography data collection and refinement statistics. The structure was deposited in the PDB with the accession code 5NR4.

In vitro MT dynamics assays

Reconstitution of MT growth dynamics in vitro was performed as described previously³⁵. GMPCPP-stabilized MT seeds (70% unlabeled tubulin, 18% biotin tubulin and 12% of rhodamine-tubulin or HiLyte 488 tubulin) were prepared as described before⁶⁰. Flow

chambers, assembled from plasma-cleaned glass coverslips and microscopic slides were functionalized by sequential incubation with 0.2 mg/ml PLL-PEG-biotin (Susos AG, Switzerland) and 1 mg/ml NeutrAvidin (Invitrogen) in MRB80 buffer (80 mM piperazine-N,N[prime]-bis(2-ethanesulfonic acid), pH 6.8, supplemented with 4 mM MgCl₂, and 1 mM EGTA. MT seeds were attached to the coverslip through biotin-NeutrAvidin interactions. Flow chambers were further blocked with 1 mg/ml κ -casein. The reaction mixture with or without CLASP proteins (MRB80 buffer supplemented with 15 μ M porcine brain tubulin, 0.5 μ M rhodamine-tubulin, 50 mM KCl, 1 mM guanosine triphosphate, 0.2 mg/ml κ -casein, 0.1% methylcellulose, and oxygen scavenger mix [50 mM glucose, 400 μ g/ml glucose oxidase, 200 μ g/ml catalase, and 4 mM DTT]) was added to the flow chamber after centrifugation in an Airfuge for 5 minutes at 119,000 \times g. For experiments in the presence of EB3, concentration of mCherry-EB3 or GFP-EB3 was as indicated in the figures and rhodamine-tubulin was excluded from the assay. The flow chamber was sealed with vacuum grease, and dynamic MTs were imaged immediately at 30 °C using TIRF microscopy. All tubulin products were from Cytoskeleton Inc.

TIRF microscopy

In vitro reconstitution assays were imaged on a TIRF microscope setup as described previously³¹ or on an Ilas² TIRF setup. In brief, we used an inverted research microscope Nikon Eclipse Ti-E (Nikon) with the perfect focus system (Nikon), equipped with Nikon CFI Apo TIRF 100x 1.49 N.A. oil objective (Nikon) and controlled with MetaMorph 7.7.5 software (Molecular Devices). The microscope was equipped with TIRF-E motorized TIRF illuminator modified by Roper Scientific France/PICT-IBiSA, Institut Curie. To keep the in vitro samples at 30 °C, a stage top incubator model INUBG2E-ZILCS (Tokai Hit) was used. For excitation, 491 nm 100 mW Calypso (Cobolt) and 561 nm 100 mW Jive (Cobolt) lasers were used. We used ET-GFP 49002 filter set (Chroma) for imaging of proteins tagged with GFP or ET-mCherry 49008 filter set (Chroma) for imaging of proteins tagged with mCherry. Fluorescence was detected using an EMCCD Evolve 512 camera (Roper Scientific) with the intermediate lens 2.5X (Nikon C mount adapter 2.5X) or using the CoolSNAP HQ2 CCD camera (Roper Scientific) without an additional lens. In both cases the final magnification was 0.063 μ m/pixel.

Ilas² system (Roper Scientific, Evry, FRANCE) is a dual laser illuminator for azimuthal spinning TIRF (or Hilo) illumination and with a custom modification for targeted photomanipulation. This system was installed on Nikon Ti microscope (with the perfect focus system, Nikon), equipped with 150 mW 488 nm laser and 100 mW 561 nm laser, 49002 and 49008 Chroma filter sets, EMCCD Evolve mono FW DELTA 512x512 camera (Roper Scientific) with the intermediate lens 2.5X (Nikon C mount adapter 2.5X), CCD camera CoolSNAP MYO M-USB-14-AC (Roper Scientific) and controlled with MetaMorph 7.8.8 software (Molecular Device). To keep the in vitro samples at 30°C, a stage top incubator model INUBG2E-ZILCS (Tokai Hit) was used. The final resolution using EMCCD camera

was 0.065 $\mu\text{m}/\text{pixel}$, using CCD camera it was 0.045 $\mu\text{m}/\text{pixel}$.

Both microscopes were equipped with an ILas system (Roper Scientific France/ PICT-IBiSA) for FRAP and photoablation. The 532 nm Q-switched pulsed laser (Teem Photonics) was used for photoablation on the TIRF microscope.

Analysis of MT plus end dynamics in vitro

Kymographs were generated using the ImageJ plugin KymoResliceWide (<http://fiji.sc/KymoResliceWide>). MT dynamics parameters were determined from kymographs using an optimized version of the custom made JAVA plug in for ImageJ as described previously^{35, 61, 62}. ~ 100 -200 MT growth events were analyzed per condition.

The relative standard error for catastrophe frequency was calculated as described previously⁶². The relative standard error of mean rescue frequency was calculated in the same way as the standard error of the mean catastrophe frequency, i.e. $SE_r = \bar{f}_r \frac{SE_{r_{sh}}}{\bar{t}_{sh}}$, where \bar{f}_r, \bar{t}_{sh} are average values and $SE_{f_r}, SE_{t_{sh}}$ are standard errors of rescue frequency and shortening time respectively. The number of observed rescue events for control was relatively small as compared to the catastrophes, so we assumed that they follow a Poisson distribution. The standard deviation of the rescue frequency was calculated as the square root of its mean value and the standard error was calculated according to

$$SE_{f_r} = \frac{\sqrt{\bar{f}_r}}{\sqrt{N_r}}$$

where \bar{f}_r and SE_{f_r} are the average and the standard error of the rescue frequency and N_r is the number of rescues⁶³.

In vitro template-based MT outgrowth assay

GMPCPP MT seeds labeled with HiLyte 488 tubulin were attached to the coverslips through biotin-neutravidin interaction as described above. After washing out unbound seeds, the flow chambers were blocked with 1 mg/ml κ -casein followed by the polymerization reaction mixture as above with different concentrations of Rhodamine-labeled tubulin. The nucleation probability was estimated as the fraction of the total GMPCPP seeds that showed MT outgrowth within 15 min imaging window. The nucleation probabilities over different tubulin concentration were fitted to the sigmoidal equation using GraphPad Prism 7.

Microfabrication of SiO₂ barriers

Fabrication of the SiO₂ barriers was achieved by subsequent deposition, lithography, and plasma etching steps, as previously described in³². Our method differs from this protocol, by using PE-CVD (Oxford Instruments PlasmaPro 80) to deposit a 1.7 μm layer of SiO₂, and by plasma-etching with a mixture of CHF₃/O₂ to ensure an anisotropic etch. The barriers were 10 μm wide and 1.7 μm high, enclosing channels with a width of 15 μm .

MT growth against SiO₂ barriers and analysis of barrier contact events

The micro-fabricated samples were passivated with PLL-PEG-biotin and κ -casein. Biotinylated GMPCPP-stabilized seeds were attached to the surface via streptavidin. The direction of flow of the seed mix was perpendicular to the barriers in order to favour perpendicular MT-barrier contact events. The height and straightness of the barriers in combination with methyl-cellulose in solution prevents MTs from growing over the barriers. The experiments without CLASP in solution were imaged on an Olympus TIRF microscope with a 60x, 1.45 NA oil immersion objective, using an additional magnification of 1.6 to obtain 96x image magnification. Images were collected on two Andor iXon Ultra 897 EMCCD cameras for simultaneous dual-colour acquisition. The experiments with CLASP2 α were imaged on a ilas² TIRF setup described in the TIRF microscopy section. All MT-barrier contact events were separated into three different event types, i.e. sliding, stalling, and buckling. The contact angle of a MT with a barrier and the barrier contact times were determined and analyzed with a custom written MATLAB script, adapted from⁶⁴. The catastrophe frequency was determined by counting the number of observed catastrophes and dividing this by the time a MT spends in contact with the barrier. The statistical error was obtained by dividing this number by the square root of the number of measured contact events. The growth of buckling MTs was determined by manually tracking the MT (Fig. 5d).

Quantification of the intensities of EB comets

To obtain the intensity values of EB comets in Fig. 7d, we collected the intensity profiles of mCherry-EB3 comets along several time points for each individual growth event by averaging across 6-pixel wide lines. The intensity profile for each time point was fitted to a Gaussian function with the background intensity (I_{BG}) to obtain the amplitude of the comet's peak I_A according to:

$$I_p(x, t) = I_{BG}(t) + I_A(t)e^{-\frac{(x-x_c)^2}{2\sigma^2}}$$

The final values were obtained by averaging the $I_A(t)$ for each individual growth event.

Tip-averaging of MT intensity profiles

To build average HyLite 488 tubulin intensity distribution at the growing tip (Fig. 7k,l) we generated intensity profiles of 6 pixel thick line (400nm) of 2-3 μ m length with its middle point positioned approximately at the MT tip using Fiji⁶⁵ (similar to⁶⁶). Resulting profiles $I(x)$ were fitted with the error function shifted in x using custom written MATLAB script:

$$I(x) = I_{BG} + \frac{1}{2} I_{AMP} \left(1 + \operatorname{erf} \left(\frac{x - x_c}{\sqrt{2}\sigma} \right) \right)$$

where fitting parameter I_{BG} corresponds to the intensity of background, I_{AMP} to the

amplitude of the fluorescent signal, x_c to the position of the MT tip and σ to the degree of tip tapering convolved with microscope's point spread function (PSF) (see Supplementary Fig. 5e,g). Each profile was shifted by its x_c value, background subtracted with I_{BG} and normalized by I_{AMP} (Supplementary Fig. 5e,g).

End tapering simulations

Monte-Carlo simulations of MTs tips were performed using 13 element- (protofilament-) wide regular array with 8 nm longitudinal distance between dimers as a MT lattice representation (Supplementary Fig. 5c). Absent length of N protofilaments was constant and defined by parameter d for Model A. For Model B it was randomly sampled from an exponential distribution with parameter d. Present tubulin dimers were labeled with a probability equal to the fraction of labeled tubulin in the corresponding experiment (0.09). Only labeled dimers were assumed to generate intensity profile in molecule number (Supplementary Fig. 5c) and its version convoluted with PSF of used microscope (Supplementary Fig. 5d). The PSF was approximated with a Gaussian function with the standard deviation of 122 nm. Convoluted intensity values were binned together according to the image pixel size (65 nm) and the Gaussian noise was added leading to the signal-to-noise ratio of 7 observed in experiment (Supplementary Fig. 5f). Noise containing profiles were fitted and normalized using the same procedure as described in the previous section. For a single iteration of simulation, we used the same number of MTs as in the corresponding experimental condition with lengths determined from the fitting. A total of 50 iterations were run and averaged for each parameters combination of N and d. Residual between simulated and experimental profiles was calculated as a sum of squared differences using only those pixels in x which contain all individual profiles. The final fitting result was obtained by varying N and d independently in a search for a minimal residual value (Fig. 7m).

Analysis of MT growth variability

Time lapse images of growing MTs labeled with HiLyte 488 tubulin were recorded at intervals of 0.7 s for 5 min and 350-400 ms of exposure time. To estimate the position of the MT plus end, we fitted MT intensity profiles as described above. Subsequently, the change in MT length over time was calculated as $\Delta L(t)=L(t)-L(\text{first frame})$. Next, as described previously⁶⁷, we calculated the average mean squared displacement (MSD) of the MT length increments $\langle \Delta L^2 \rangle(\tau)$ for increasing values of time delay τ . We then fitted $\langle \Delta L^2 \rangle(\tau)$ to an MSD equation containing diffusion with drift:

$$\langle \Delta L^2 \rangle(\tau) = v_g^2 \tau^2 + 2D_p \tau + \sigma_{err}^2 \quad \text{where } \tau \text{ corresponds to delay, } v_g \text{ is the average speed of growth, } D_p \text{ is the effective diffusion coefficient for the MT polymerization and } \sigma_{err} \text{ is the experimental error.}$$

Single-molecule fluorescence intensity analysis of CLASP2 α

Diluted protein samples of GFP, GFP-MACF43-LZ²⁸ and GFP-CLASP2 α were immobilized in adjacent flow chambers of the same plasma cleaned glass coverslip as described previously⁶¹. The flow chambers were washed with MRB80 buffer and sealed with vacuum grease and immediately imaged with a TIRF microscope. 10-20 images of previously unexposed coverslip areas were acquired with 100 ms exposure time and low laser power. GFP, GFP-MACF43LZ and GFP-CLASP2 α were located in different chambers of the same coverslip, so the same imaging conditions could be preserved. Single molecule fluorescence spots were detected and fitted with 2D Gaussian function using custom written ImageJ plugin DoM_Utrecht (https://github.com/ekatruxha/DoM_Utrecht). The fitted peak intensity values were used to build fluorescence intensity histograms.

CLASP molecule counting at MT tips and rescue points

To determine the number of molecules of CLASP2 α at a MT tip, we immobilized single molecules of CLASP2 α onto the coverslip of one of the flow chambers and performed the in vitro reconstitution assay in the adjacent chamber of the same coverslip as described previously⁶¹. Images of unbleached CLASP2 α single molecules were acquired first and using the same imaging/illumination conditions, time lapse imaging was performed with the in vitro assay with CLASP2 α at 3 nM or 30 nM, using 100 ms exposure and 2 s intervals for 5 minutes. The plus end localized CLASP2 α molecules or the molecules present at the rescue site were manually located in each frame and fitted with 2D Gaussian, the amplitude of which was used for the intensity analysis. For CLASP2 α at the rescue site, 2-3 frames after rescue initiation were used to get the intensity values. To build the distributions of CLASP2 α molecule numbers at the MT tip, each CLASP2 α intensity value at the MT plus end or a rescue site was normalized by the average CLASP2 α single molecule intensity from the adjacent chamber.

Author Contributions

A.Ah, M.K, A.S., L.C.K, M.O.S., M.D. and A.Ak. designed experiments, analyzed data and wrote the paper. A.Ah., M.K, A.S, A.R. N.O., R.R.-G performed experiments and data analysis, T.W. and V.O. contributed to solving TOG1 structure, and E.A. K. carried out data analysis and modeling. A.Ak. coordinated the project.

Acknowledgements

We thank S.Royle for the gift of ch-TOG construct, and the beamline scientists at beamlines X06DA of the Swiss Light Source (Paul Scherrer Institut, Villigen, Switzerland) for technical assistance with the X-ray data collection. This work was supported by the European Research Council Synergy grant 609822 to M.D. and A.Ak., and grants from the Swiss National Science Foundation (31003A_166608 to M.O.S.), and EMBO Long Term Fellowship to A.S. The structural data reported in this paper are available in PDB (PDB

code 5NR4).

Competing financial interests

The authors declare no competing financial interests.

References

- 1.Desai, A. & Mitchison, T.J. Microtubule polymerization dynamics. *Annu Rev Cell Dev Biol* 13, 83-117 (1997).
- 2.Akhmanova, A. & Steinmetz, M.O. Control of microtubule organization and dynamics: two ends in the limelight. *Nat Rev Mol Cell Biol* 16, 711-726 (2015).
- 3.Mimori-Kiyosue, Y. Shaping microtubules into diverse patterns: molecular connections for setting up both ends. *Cytoskeleton (Hoboken)* 68, 603-618 (2011).
- 4.Janson, M.E., de Dood, M.E. & Dogterom, M. Dynamic instability of microtubules is regulated by force. *J Cell Biol* 161, 1029-1034 (2003).
- 5.Gardner, M.K., Zanic, M. & Howard, J. Microtubule catastrophe and rescue. *Curr Opin Cell Biol* 25, 14-22 (2013).
- 6.Doodhi, H. et al. Termination of Protofilament Elongation by Eribulin Induces Lattice Defects that Promote Microtubule Catastrophes. *Curr Biol* 26, 1713-1721 (2016).
7. de Forges, H. et al. Localized Mechanical Stress Promotes Microtubule Rescue. *Curr Biol* 26, 3399-3406 (2016).
8. Schaedel, L. et al. Microtubules self-repair in response to mechanical stress. *Nat Mater* 14, 1156-1163 (2015).
9. Aumeier, C. et al. Self-repair promotes microtubule rescue. *Nat Cell Biol* 18, 1054-1064 (2016).
- 10.Maiato, H. et al. Human CLASP1 is an outer kinetochore component that regulates spindle microtubule dynamics. *Cell* 113, 891-904. (2003).
- 11.Logarinho, E. et al. CLASPs prevent irreversible multipolarity by ensuring spindle-pole resistance to traction forces during chromosome alignment. *Nat Cell Biol* 14, 295-303 (2012).
- 12.Maiato, H., Khodjakov, A. & Rieder, C.L. Drosophila CLASP is required for the incorporation of microtubule subunits into fluxing kinetochore fibres. *Nat Cell Biol* 7, 42-47 (2005).
- 13.Bratman, S.V. & Chang, F. Stabilization of overlapping microtubules by fission yeast CLASP. *Dev Cell* 13, 812-827 (2007).
- 14.Sousa, A., Reis, R., Sampaio, P. & Sunkel, C.E. The Drosophila CLASP homologue, Mast/Orbit regulates the dynamic behaviour of interphase microtubules by promoting the pause state. *Cell Motil Cytoskeleton* (2007).
- 15.Maton, G. et al. Kinetochore components are required for central spindle assembly. *Nat Cell Biol* 17, 953 (2015).
- 16.Lacroix, B. et al. In situ imaging in *C. elegans* reveals developmental regulation of microtubule dynamics. *Dev Cell* 29, 203-216 (2014).
- 17.Ambrose, C., Allard, J.F., Cytrynbaum, E.N. & Wasteney, G.O. A CLASP-modulated cell edge barrier mechanism drives cell-wide cortical microtubule organization in *Arabidopsis*. *Nat Commun* 2, 430 (2011).
- 18.Mimori-Kiyosue, Y. et al. CLASP1 and CLASP2 bind to EB1 and regulate microtubule plus-end dynamics at the cell cortex. *J Cell Biol* 168, 141-153 (2005).
- 19.Bouchet, B.P. et al. Mesenchymal Cell Invasion Requires Cooperative Regulation of Persistent Microtubule Growth by SLAIN2 and CLASP1. *Dev Cell* 39, 708-723 (2016).
- 20.Efimov, A. et al. Asymmetric CLASP-dependent nucleation of noncentrosomal microtubules at the trans-Golgi network. *Dev Cell* 12, 917-930 (2007).
- 21.Wieczorek, M., Bechstedt, S., Chaaban, S. & Brouhard, G.J. Microtubule-associated proteins control the kinetics of microtubule nucleation. *Nat Cell Biol* 17, 907-916 (2015).
- 22.Al-Bassam, J. et al. CLASP promotes microtubule rescue by recruiting tubulin dimers to the microtubule. *Dev Cell* 19, 245-258 (2010).
- 23.Moriwaki, T. & Goshima, G. Five factors can reconstitute all three phases of microtubule polymerization dynamics. *J Cell Biol* 215, 357-368 (2016).
- 24.Yu, N. et al. Isolation of Functional Tubulin

- dimers and of Tubulin-Associated Proteins from Mammalian Cells. *Curr Biol* 26, 1728-1736 (2016).
25. Leano, J.B., Rogers, S.L. & Slep, K.C. A cryptic TOG domain with a distinct architecture underlies CLASP-dependent bipolar spindle formation. *Structure* 21, 939-950 (2013).
 26. Maki, T., Grimaldi, A.D., Fuchigami, S., Kaverina, I. & Hayashi, I. CLASP2 Has Two Distinct TOG Domains That Contribute Differently to Microtubule Dynamics. *J Mol Biol* 427, 2379-2395 (2015).
 27. Bieling, P. et al. Reconstitution of a microtubule plus-end tracking system in vitro. *Nature* 450, 1100-1105 (2007).
 28. Honnappa, S. et al. An EB1-binding motif acts as a microtubule tip localization signal. *Cell* 138, 366-376 (2009).
 29. Akhmanova, A. et al. Clasps are CLIP-115 and -170 associating proteins involved in the regional regulation of microtubule dynamics in motile fibroblasts. *Cell* 104, 923-935. (2001).
 30. Al-Bassam, J. & Chang, F. Regulation of microtubule dynamics by TOG-domain proteins XMAP215/Dis1 and CLASP. *Trends Cell Biol* 21, 604-614 (2011).
 31. Mohan, R. et al. End-binding proteins sensitize microtubules to the action of microtubule-targeting agents. *Proc Natl Acad Sci U S A* 110, 8900-8905 (2013).
 32. Kalisch, S.M., Laan, L. & Dogterom, M. Force generation by dynamic microtubules in vitro. *Methods Mol Biol* 777, 147-165 (2011).
 33. Drabek, K. et al. Role of CLASP2 in microtubule stabilization and the regulation of persistent motility. *Curr Biol* 16, 2259-2264 (2006).
 34. Bieling, P. et al. CLIP-170 tracks growing microtubule ends by dynamically recognizing composite EB1/tubulin-binding sites. *J Cell Biol* 183, 1223-1233 (2008).
 35. Montenegro Gouveia, S. et al. In Vitro Reconstitution of the Functional Interplay between MCAK and EB3 at Microtubule Plus Ends. *Curr Biol* 20, 1717-1722 (2010).
 36. van Riel, W.E. et al. Kinesin-4 KIF21B is a potent microtubule pausing factor. *Elife* 6 (2017).
 37. Walker, R.A., Inoue, S. & Salmon, E.D. Asymmetric behavior of severed microtubule ends after ultraviolet-microbeam irradiation of individual microtubules in vitro. *J Cell Biol* 108, 931-937 (1989).
 38. Ruan, Y. & Wasteneys, G.O. CLASP: a microtubule-based integrator of the hormone-mediated transitions from cell division to elongation. *Curr Opin Plant Biol* 22, 149-158 (2014).
 39. Galjart, N. CLIPs and CLASPs and cellular dynamics. *Nat Rev Mol Cell Biol* 6, 487-498 (2005).
 40. Zanic, M., Widlund, P.O., Hyman, A.A. & Howard, J. Synergy between XMAP215 and EB1 increases microtubule growth rates to physiological levels. *Nat Cell Biol* 15, 688-693 (2013).
 41. Coombes, C.E., Yamamoto, A., Kenzie, M.R., Odde, D.J. & Gardner, M.K. Evolving tip structures can explain age-dependent microtubule catastrophe. *Curr Biol* 23, 1342-1348 (2013).
 42. Duellberg, C., Cade, N.I. & Surrey, T. Microtubule aging probed by microfluidics-assisted tubulin washout. *Mol Biol Cell* 27, 3563-3573 (2016).
 43. Lansbergen, G. et al. CLASPs attach microtubule plus ends to the cell cortex through a complex with LL5beta. *Dev Cell* 11, 21-32 (2006).
 44. Hannak, E. & Heald, R. Xorbit/CLASP links dynamic microtubules to chromosomes in the *Xenopus* meiotic spindle. *J Cell Biol* 172, 19-25 (2006).
 45. Patel, K., Nogales, E. & Heald, R. Multiple domains of human CLASP contribute to microtubule dynamics and organization in vitro and in *Xenopus* egg extracts. *Cytoskeleton (Hoboken)* 69, 155-165 (2012).
 46. Grimaldi, A.D. et al. CLASPs are required for proper microtubule localization of end-binding proteins. *Dev Cell* 30, 343-352 (2014).
 47. Olieric, N. et al. Automated seamless DNA co-transformation cloning with direct expression vectors applying positive or negative insert selection. *BMC Biotechnol* 10, 56 (2010).
 48. Campbell, J.N. & Slep, K.C. alpha-Tubulin and microtubule-binding assays. *Methods Mol Biol* 777, 87-97 (2011).
 49. Waltersperger, S. et al. PRIGO: a new multi-axis goniometer for macromolecular crystallography. *J Synchrotron Radiat* 22, 895-900 (2015).
 50. Weinert, T. et al. Fast native-SAD phasing for routine macromolecular structure determination

- Nat Methods 12, 131-133 (2015).
51. Kabsch, W. Integration, scaling, space-group assignment and post-refinement. *Acta Crystallogr D Biol Crystallogr* 66, 133-144 (2010).
52. Karplus, P.A. & Diederichs, K. Linking crystallographic model and data quality. *Science* 336, 1030-1033 (2012).
53. Sheldrick, G.M. Experimental phasing with SHELXC/D/E: combining chain tracing with density modification. *Acta Crystallogr D Biol Crystallogr* 66, 479-485 (2010).
54. Pape, T. & Schneider, T.R. HKL2MAP: a graphical user interface for macromolecular phasing with SHELX programs. *J Appl Crystallogr* 37, 843-844 (2004).
55. Cowtan, K. The Buccaneer software for automated model building. 1. Tracing protein chains. *Acta Crystallogr D Biol Crystallogr* 62, 1002-1011 (2006).
56. Cowtan, K. Fitting molecular fragments into electron density. *Acta Crystallogr D Biol Crystallogr* 64, 83-89 (2008).
57. Emsley, P. & Cowtan, K. Coot: model-building tools for molecular graphics. *Acta Crystallogr D Biol Crystallogr* 60, 2126-2132 (2004).
58. Adams, P.D. et al. PHENIX: a comprehensive Python-based system for macromolecular structure solution. *Acta Crystallogr D Biol Crystallogr* 66, 213-221 (2010).
59. Chen, V.B. et al. MolProbity: all-atom structure validation for macromolecular crystallography. *Acta Crystallogr D Biol Crystallogr* 66, 12-21 (2010).
60. Gell, C. et al. Microtubule dynamics reconstituted in vitro and imaged by single-molecule fluorescence microscopy. *Methods Cell Biol* 95, 221-245 (2010).
61. Sharma, A. et al. Centriolar CPAP/SAS-4 Imparts Slow Processive Microtubule Growth. *Dev Cell* 37, 362-376 (2016).
62. Taylor, J.R. *An Introduction to Error Analysis*. University Science Books, Sausalito; 1997.
63. Smal, I., Grigoriev, I., Akhmanova, A., Niessen, W.J. & Meijering, E. Accurate estimation of microtubule dynamics using kymographs and variable-rate particle filters. *Conf Proc IEEE Eng Med Biol Soc* 1, 1012-1015 (2009).
64. Ruhnnow, F., Zwicker, D. & Diez, S. Tracking single particles and elongated filaments with nanometer precision. *Biophys J* 100, 2820-2828 (2011).
65. Schindelin, J. et al. Fiji: an open-source platform for biological-image analysis. *Nat Methods* 9, 676-682 (2012).
66. Maurer, S.P. et al. EB1 accelerates two conformational transitions important for microtubule maturation and dynamics. *Curr Biol* 24, 372-384 (2014).
67. Gardner, M.K. et al. Rapid microtubule self-assembly kinetics. *Cell* 146, 582-592 (2011).
68. Davis, I.W., Murray, L.W., Richardson, J.S. & Richardson, D.C. MOLPROBITY: structure validation and all-atom contact analysis for nucleic acids and their complexes. *Nucleic Acids Res* 32, W615-619 (2004).

Supplementary Information

Supplementary Figure 1. CLASPs suppress catastrophes and promote MT outgrowth from GMPCPP-stabilized seeds.

(a) Coomassie blue stained gels with GFP, mCherry and TagBFP-fusions of CLASP2 α , GFP-fusions of the SxIP mutant CLASP2 α , EB3 and mCherry-fusions of EB3 and EB3 Δ Tail. All CLASP proteins were purified from HEK293T cells whereas the EB3 proteins were purified from *E. coli*.

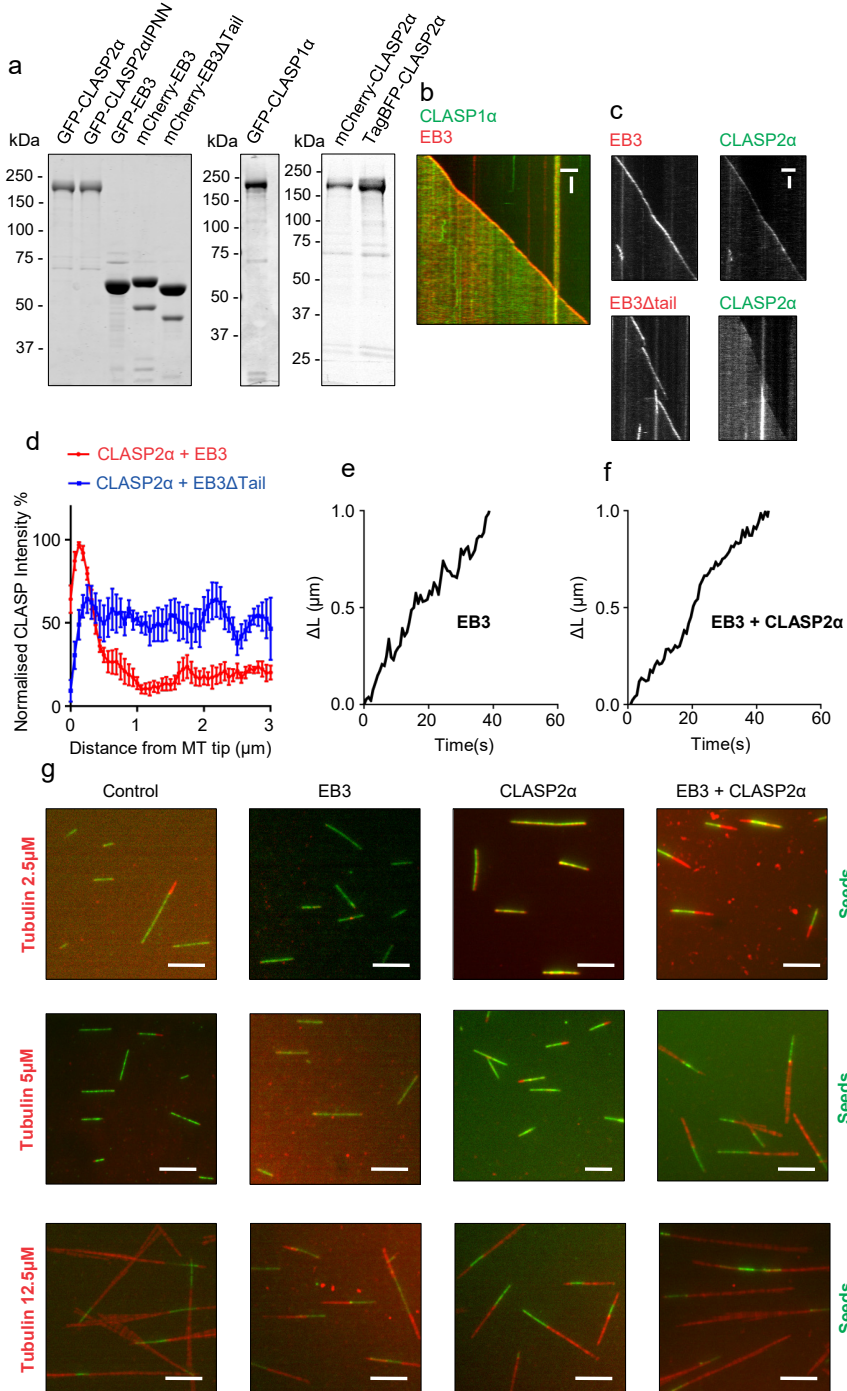
(b) Kymograph showing MT plus end dynamics in the presence of 20 nM mCherry-EB3 and 30 nM GFP-CLASP1 α . Scale bars: 2 μ m (horizontal) and 60 s (vertical).

(c, d) Kymographs illustrating MT plus end growth for MTs grown in the presence of 30 nM GFP-CLASP2 α and 20 nM mCherry-EB3 or 300 nM GFP-CLASP2 α and 20 nM mCherry-EB3 Δ tail (c) and normalized mean fluorescence intensity profiles along a growing MT plus end in the CLASP channel in the same conditions (d). Scale bars: 2 μ m (horizontal) and 30 s (vertical). 8 MT profiles were used for averaging.

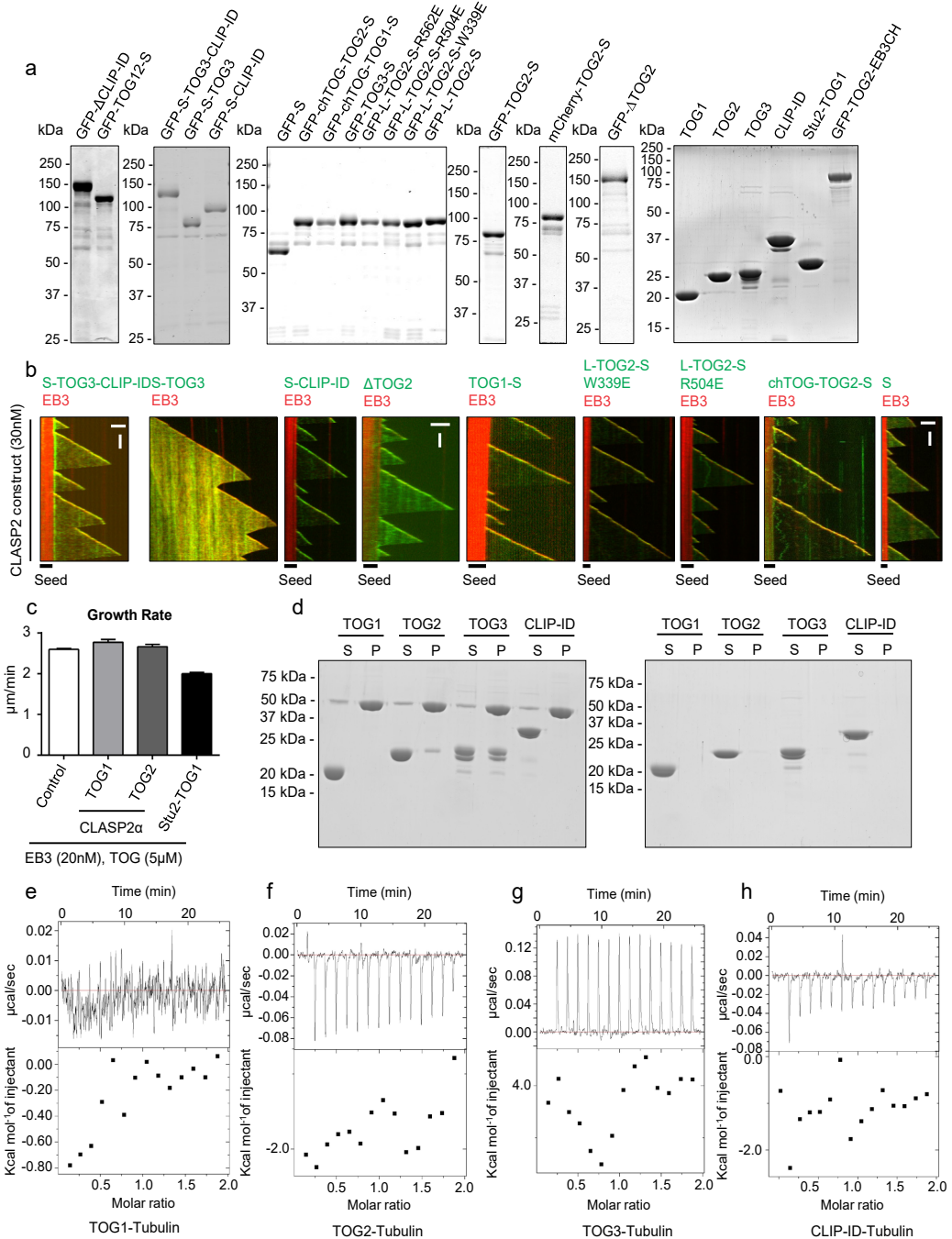
(e, f) Individual time traces of MT tip position in the presence of 20 nM mCherry-EB3 alone (e) or together with 30 nM GFP-CLASP2 α (f).

(g) Maximum intensity projections of MT outgrowth (red) from HiLyte488-labeled GMPCPP seeds (green) in the presence of 2.5 μ M, 5 μ M and 12.5 μ M rhodamine-labeled tubulin alone or together with 200 nM GFP-EB3 or 100 nM GFP-CLASP2 α or both. Scale bar: 5 μ m.

Supplementary Figure 1



Supplementary Figure 2



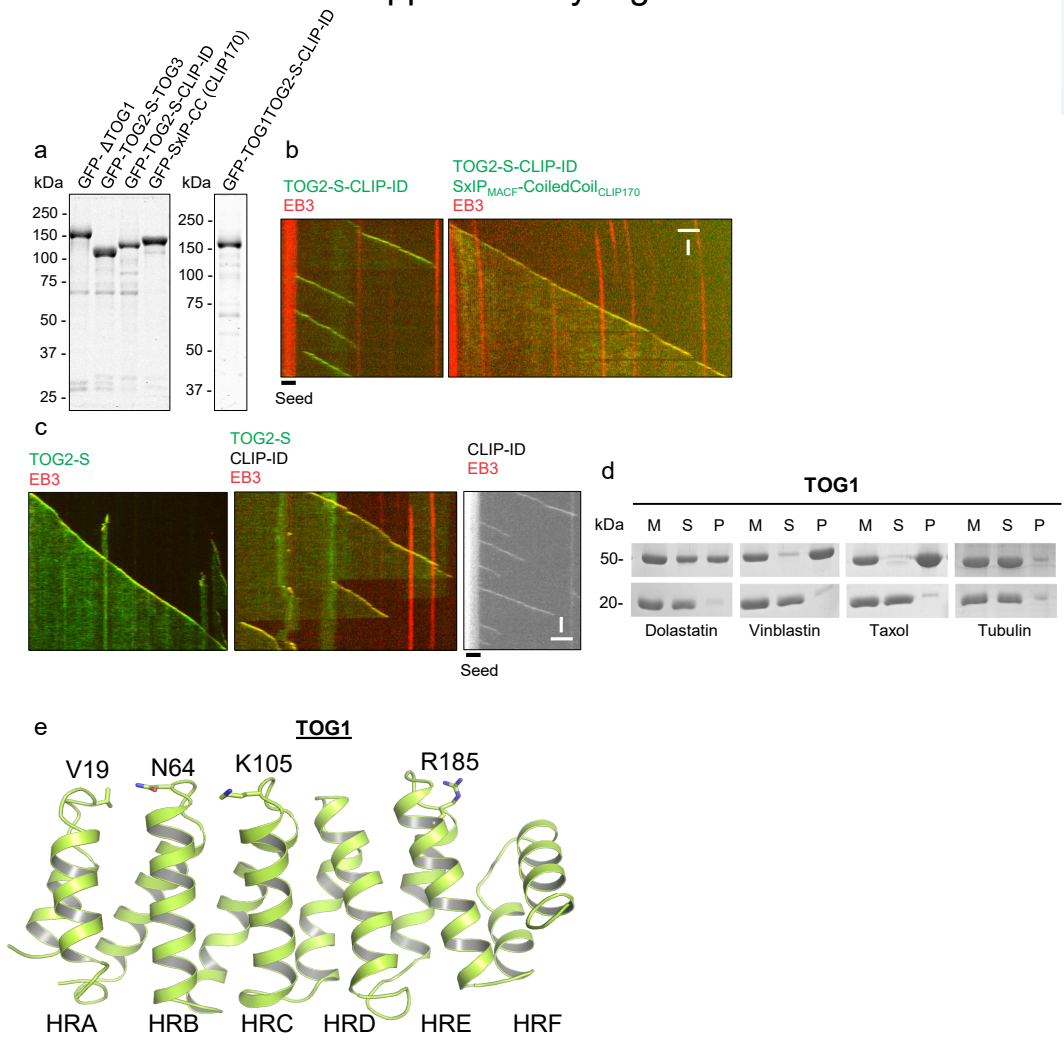
Supplementary Figure 2. TOG2 domain of CLASP2 is necessary and sufficient for catastrophe suppression.

(a) Coomassie blue stained gels with GFP-fusions of full-length CLASP2 α , TOG domain deletions, SxIP-fusions of different individual TOG domains, point mutants or chimeras with SxIP of CLASP2 α fused to chTOG-TOG domains and mCherry-fusion of TOG2-S purified from HEK293T cells and the individual

TOG domains of CLASP2 α , STU2-TOG1 and the GFP-fusion of CLASP2 α -TOG2 domain fused to EB3-CH domain purified from *E. coli*.
 (b) Kymographs showing MT plus end dynamics in the presence of 20 nM mCherry-EB3 and 30 nM GFP-fusions of the indicated CLASP2 α -TOG domain combinations, point mutants or SxIP motif of CLASP2 α fused to chTOG-TOG domain or alone. Scale bars: 2 μ m (horizontal) and 60 s (vertical).
 (c) MT plus end growth rates in the presence of 20 nM mCherry-EB3 alone or together with 5 μ M of CLASP2 α -TOG1 or TOG2 domains or with Stu2-TOG1 domain.
 (d) MT pelleting assays with CLASP2 α -TOG1, TOG2, TOG3 and the CLIP-interacting domains with taxol-stabilized MTs.
 (e-h) ITC analysis of the interaction between tubulin and the CLASP2 α -TOG1, TOG2, TOG3 or the CLIP-interacting domain.

Supplementary Figure 3

2



Supplementary Figure 3. TOG1 domain of CLASP2 has an autoregulatory function and does not interact with MTs or tubulin oligomers.

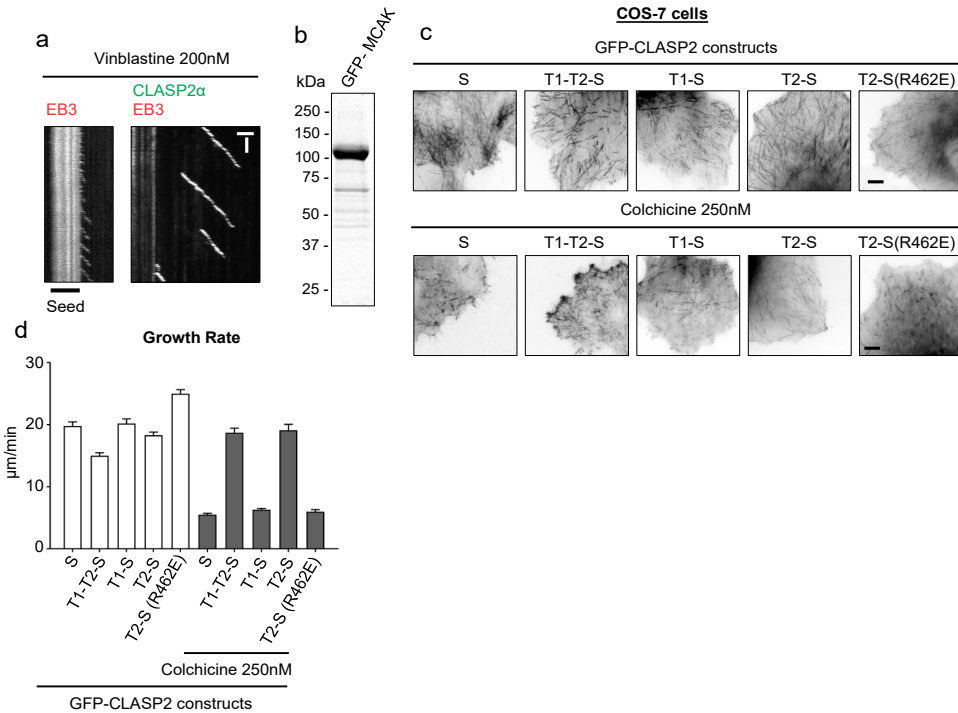
(a) Coomassie blue stained gels with the indicated GFP-fusions, purified from HEK293T cells.
 (b,c) Kymographs showing MT plus end dynamics in the presence of 20 nM mCherry-EB3 and together with the indicated proteins. 30 nM GFP-CLASP fusions, 30 nM of the MACF-CLIP-170 coiled coil fusion and

500 nM CLIP-ID were used. Scale bars: 2 μm (horizontal) and 60 s (vertical).

(d) MT pelleting of CLASP2 α -TOG1 domain with tubulin-dolastatin rings, tubulin-vinblastine spirals, taxol-stabilized MTs or tubulin alone, as indicated.

(e) Crystal structure of the CLASP2 α -TOG1 domain with the indicated HEAT repeats and the residues at the intra-HEAT loop regions.

Supplementary Figure 4



Supplementary Figure 4. CLASP suppresses catastrophes induced by MT-depolymerizing agents.

(a) Kymographs showing MT plus end dynamics in the presence of 20 nM mCherry-EB3 together with either 200 nM vinblastine alone or 30 nM GFP-CLASP2 α . Scale bars: 2 μm (horizontal) and 60 s (vertical).

(b) Coomassie blue stained gel with GFP-MCAK.

(c) Maximum intensity projections illustrating time lapse imaging of COS-7 cells expressing GFP fusions of different TOG domain combinations of CLASP2 α or a TOG2 point mutant fused to the SxIP motif of CLASP2 α ; cells were untreated or treated with 250 nM colchicine. Scale bar: 5 μm .

(d) MT plus end growth rates in COS-7 cells shown in (c).

Supplementary Figure 5. Characterization of MT tip repair events.

(a, b) Distributions of the duration (a) and length (b) of tip repair events, mean time = 54 ± 4 s; mean length = 1.6 ± 0.1 microns from $n=65$ events. Error bars represent SEM.

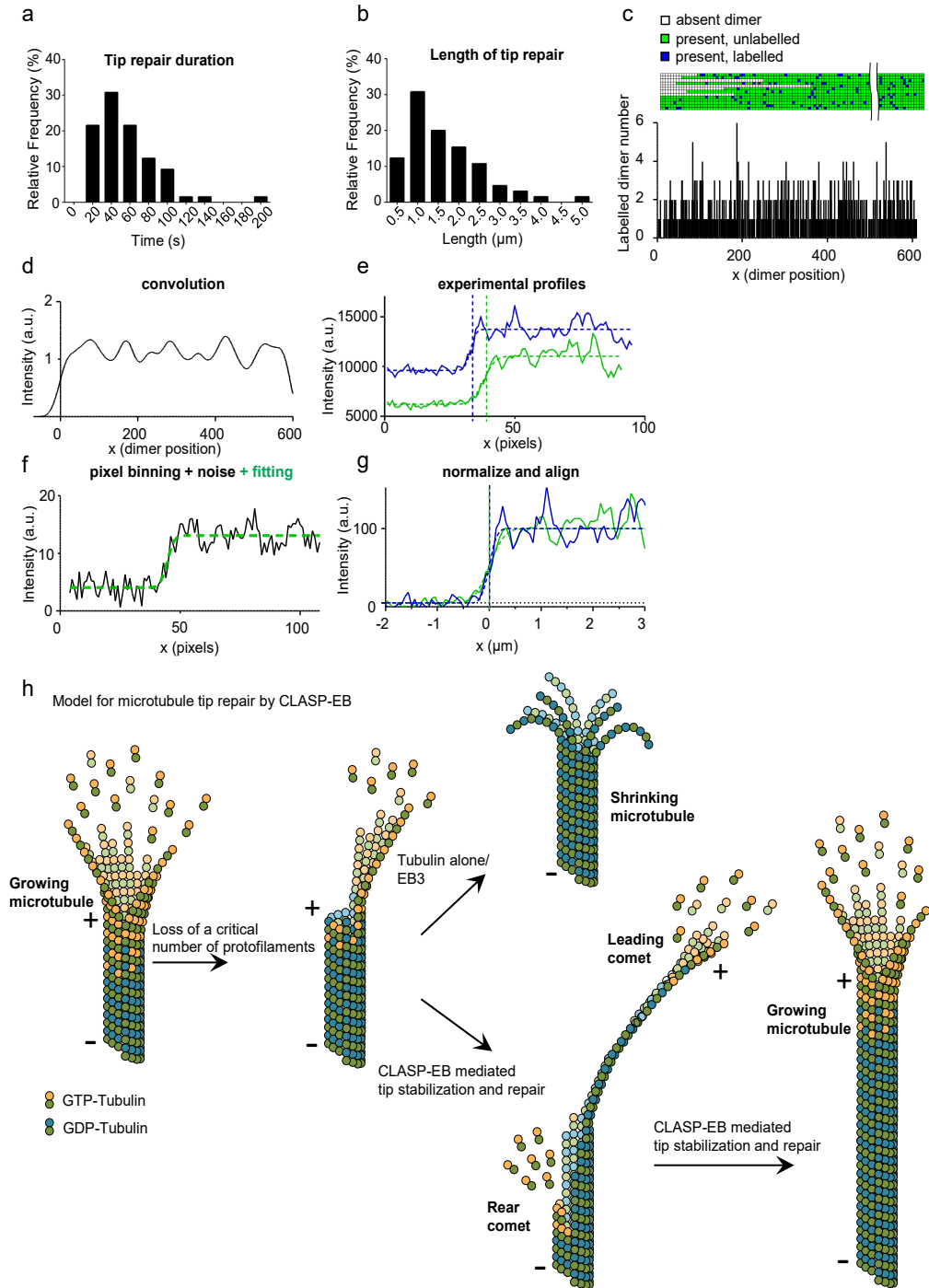
(c) Schematic view of MT structure used for Monte-Carlo simulations and an example of labeled dimer number distribution along MT length for a single random realization of simulation.

(d) Intensity profile after convolution of dimer number density from (c) with the point spread function of a microscope.

(e) Intensity profile from (d) after binning in x with the experimental image pixel size and noise addition (black solid line) and corresponding error function fitting (green dashed line).

(f) Examples of experimentally measured MT tip intensity profiles (solid lines) and corresponding error function fittings (dashed lines), vertical lines mark a position of tip derived from the fitting.

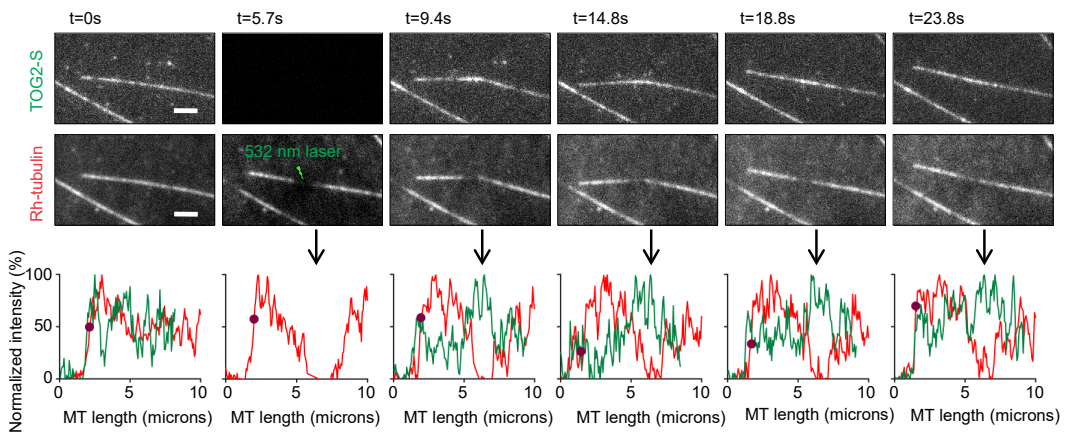
Supplementary Figure 5



2

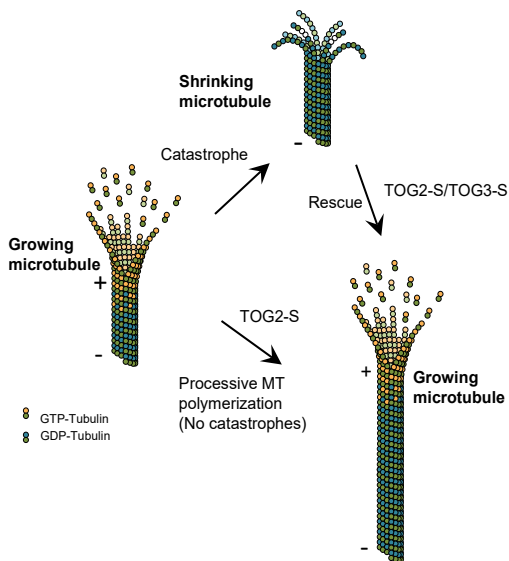
(g) Experimental intensity profiles from (f) (solid lines) and corresponding fitted curves (dashed lines) after background subtraction, alignment and normalization.
 (h) Model for MT tip repair mediated by CLASP and EB.

Supplementary Figure 6

**Supplementary Figure 6. MT lattice repair by TOG2 domain of CLASP2.**

Time lapse sequence images of a dynamic MT grown in the presence of rhodamine-tubulin and 30 nM GFP-TOG2-S damaged at a point along the lattice as indicated. The corresponding intensity profiles along the MT for the TOG2-S and tubulin channel are shown below with the arrow pointing to the site of photodamage. The purple circle on the plot indicates the end of the MT. Scale bar: 2 μm .

Supplementary Figure 7

**Supplementary Figure 7. A scheme illustrating catastrophe suppressing and rescue activities of the distinct TOG domains of CLASP.**

Both TOG2 and TOG3 can promote rescues, but only TOG2 can suppress catastrophes.

Supplementary Table 1. X ray crystallography data collection and refinement statistics.

Data Collection ^a	Native	S-SAD
Wavelength (Å)	1	2.066
Resolution range (Å) ^b	38.49 - 1.19 (1.24 - 1.19)	47.12 - 2.14 (2.2 - 2.14)
Space group	P 1 21 1	P 1 21 1
Unit cell a, b, c (Å) α, β, γ (°)	66.08, 47.12, 74.15, 90, 115.83, 90	66.05, 47.12, 74.02, 90, 115.797, 90
Total reflections	797853 (62543)	831552 (6204)
Unique reflections	128081 (11920)	21534 (1379)
Multiplicity	6.2 (5.1)	38.62 (4.50)
Completeness (%)	99 (95)	93.49 (60.91)
Mean I/sigma(I)	13.42 (0.84)	64.0 (10.2)
Wilson B-factor	12.78	-
R-merge	0.07116 (1.571)	0.056 (0.119)
R-meas	0.07762 (1.748)	0.056 (0.132)
CC1/2 ^c	1 (0.3)	0.999 (0.984)
CC*	1 (0.679)	Chi
Refinement		orientations/oscillations :
R-work	0.2003 (0.2917)	Chi0/360°
R-free	0.2137 (0.3135)	Chi5/360°
Macromolecules	3368	Chi10/360°
Water	770	Chi15/360°
RMS(bonds) (Å)	0.008	Chi20/360°
RMS(angles) (°)	1.27	Chi25/360°
Ramachandran favored (%) ^d	99	Chi30/360°
Ramachandran outliers (%) ^d	0	Chi35/360°

B-factors	
Average B-factor	21.22
Macromolecules	19.03
Solvent	30.80

^a Highest resolution shell statistics are in parentheses.
^b Resolution cutoffs were chosen based on CC1/2 and Mean I/sigma(I)⁵²
^c As defined by Karplus and Diederichs⁵²
^d As defined by MolProbity⁶⁸

3

Insights into microtubule rescue from in vitro reconstitution of the CLIP-170-CLASP complex.

Amol Aher¹, Wouter Mul¹, Qingyang Liu¹, A. F. Maarten Altelaar² and Anna Akhmanova¹

1 Cell Biology, Department of Biology, Faculty of Science, Utrecht University, Padualaan 8, 3584 CH Utrecht, the Netherlands.

2 Biomolecular Mass Spectrometry and Proteomics, Bijvoet Center for Biomolecular Research, and Utrecht Institute for Pharmaceutical Sciences and The Netherlands Proteomics Centre, Utrecht University, Padualaan 8, 3584 CH Utrecht, the Netherlands

Abstract

The dynamic growth of microtubules is an essential property underlying diverse cellular processes such as cell-division, migration and morphogenesis. Microtubule associated proteins modulate this behavior either autonomously or through their binding partners. In this report, we reconstituted microtubule growth in the presence of CLIP-170, a protein previously reported to be a rescue factor. We found that CLIP-170 tracked growing microtubule plus ends together with EB3. Contrary to the observations in cells, we found that purified full length CLIP-170 lacked rescue activity of its own. Furthermore, it did not alter the microtubule growth rate or catastrophe frequency, indicating that it is not an autonomous regulator of microtubule dynamics. However, a binding partner of CLIP-170, CLASP2 α , is a potent microtubule rescue factor, and we found that CLIP-170 enhanced the rescue activity of CLASP2 α , whereas EB3 suppressed the rescue activity of both CLASP2 α alone and CLASP2 α combined with CLIP-170. Analysis of CLASP localization dynamics revealed that CLASP2 α -mediated rescue events predominantly occurred at sites where CLASP2 α molecules were already present at microtubule lattice. CLIP-170 further increased the frequency of CLASP-induced rescues initiated by microtubule lattice bound CLASP. Our work suggests that in cells, CLIP-170 might induce rescues by enhancing CLASP association with microtubules.

Microtubules grown from purified tubulin switch stochastically between growth and shrinkage. However, in cells, this behaviour is regulated by several motile and immotile microtubule associated proteins (Akhmanova and Steinmetz, 2015). One of the less well understood aspects of microtubule dynamics is the switching from depolymerization to polymerization, a process termed rescue. CLIP and CLASP families of proteins have been implicated as rescue factors based on cellular and in vitro experiments (Al-Bassam et al., 2010; Arnal et al., 2004; Komarova et al., 2002; Mimori-Kiyosue et al., 2005). In this report, we revisit the function of CLIP-170 and reconstitute the activity of the CLIP170-CLASP complex on dynamic microtubules to gain insight into microtubule rescues.

CLIP-170 was initially isolated as a factor linking microtubules to endocytic vesicles and was subsequently identified as the first microtubule plus end tracking protein (Perez et al., 1999; Pierre et al., 1994; Pierre et al., 1992). In vertebrates, CLIP-170 tracks growing microtubule plus ends by recognizing the tyrosinated tails in α -tubulin and the end binding proteins (EBs) through its N-terminal CAP-Gly domains (Bieling et al., 2008; Mishima et al., 2007). The plus end localization of the yeast CLIP-170 homolog, Tip1, has been shown to be dependent on the EB homolog Mal3 and the kinesin motor Tea2 (Bieling et al., 2007; Busch et al., 2004). The C-terminal part of CLIP-170 contains two “zinc knuckles” and an EEY/F motif, which together can cause autoinhibition of the protein by binding to the CAP-Gly domains within the same molecule (Lansbergen et al., 2004). Binding of the CAP-Gly domains of CLIP-170 to microtubule plus end relieves this autoinhibition (Lansbergen et al., 2004). Plus end-associated CLIP-170 can then act as a hub promoting recruitment of other factors like p150Glued, LIS1, CLASP and SLAIN2 (Akhmanova et

al., 2001; Lansbergen et al., 2004; van der Vaart et al., 2011; Weisbrich et al., 2007). CLIP-170 modulates microtubule dynamics by increasing the frequency of rescues (Arnal et al., 2004; Komarova et al., 2002). Recently, it was also shown that CLIP-170 could trigger fast actin polymerization by microtubule plus ends through its interaction with formins (Henty-Ridilla et al., 2016; Lewkowicz et al., 2008).

CLASPs were identified as CLIP-associated proteins and were shown to act as rescue factors in cells and in vitro (Akhmanova et al., 2001; Al-Bassam et al., 2010; Mimori-Kiyosue et al., 2005; Yu et al., 2016). The current model suggests that a rescue is initiated along the microtubule lattice by tubulin exchange with the aid of a protein containing multiple tubulin binding domains, such as CLASP (Al-Bassam et al., 2010). CLIP-170-mediated rescues have been proposed to be due to recognition of the so-called 'GTP-islands' (microtubule lattice sites containing GTP tubulin) (de Forges et al., 2016; Dimitrov et al., 2008). GTP islands might arise as remnants of the GTP cap or as sites where microtubule lattice was damaged and repaired by tubulin incorporation; such lattice self-repair sites can serve as microtubule rescue points also independently of CLIP-170 (Aumeier et al., 2016; Schaedel et al., 2015).

In this report, we revisited the effect of CLIP-170 on microtubule dynamics and confirmed that it co-localizes with EB at the growing plus end. Interestingly, we found that CLIP-170 did not induce rescues on its own but stimulated CLASP-induced rescues. CLASP could induce rescues autonomously when present in trace amounts and exhibited higher rescue activity in combination with CLIP-170. Reconstitution experiments with EB3, CLIP-170 and CLASP showed that EB3 suppresses CLASP-induced rescues. We quantified different types of rescue events based on CLASP localization dynamics and found that rescues were predominantly initiated at sites where CLASP molecules were already present at the microtubule lattice. CLIP-170 increased the frequency of such events, suggesting that it might act by increasing the affinity of CLASP for microtubules.

RESULTS

CLASP mediates CLIP-170 induced rescues

We investigated the effect of CLIP-170 on dynamic microtubules in an in vitro reconstitution assay in which microtubules are grown from GMPCPP seeds and imaged using Total Internal Reflection Fluorescence (TIRF) microscopy (Bieling et al., 2007; Sharma et al., 2016). To test the purity of CLIP-170, we performed mass spectrometry analysis, which revealed that endogenous CLASP2, a known CLIP-170 interactor, was present in the sample (Akhmanova et al., 2001)(Figure 1A, G). We then increased the ionic strength of the washing buffer during purification from 300 mM to 1000 mM and found that CLASP2 no longer co-purified with CLIP-170 (Figure 1H). We termed these purified CLIP-170 samples CLIP-170_{lowsalt} and CLIP-170_{highsalt}. We found that when combined with EB3, CLIP-170_{lowsalt} tracked the growing plus ends co-localizing with EB3 (Figure 1B, D). Analysis of parameters of microtubule dynamics revealed that CLIP170_{lowsalt} increased the frequency

Figure 1

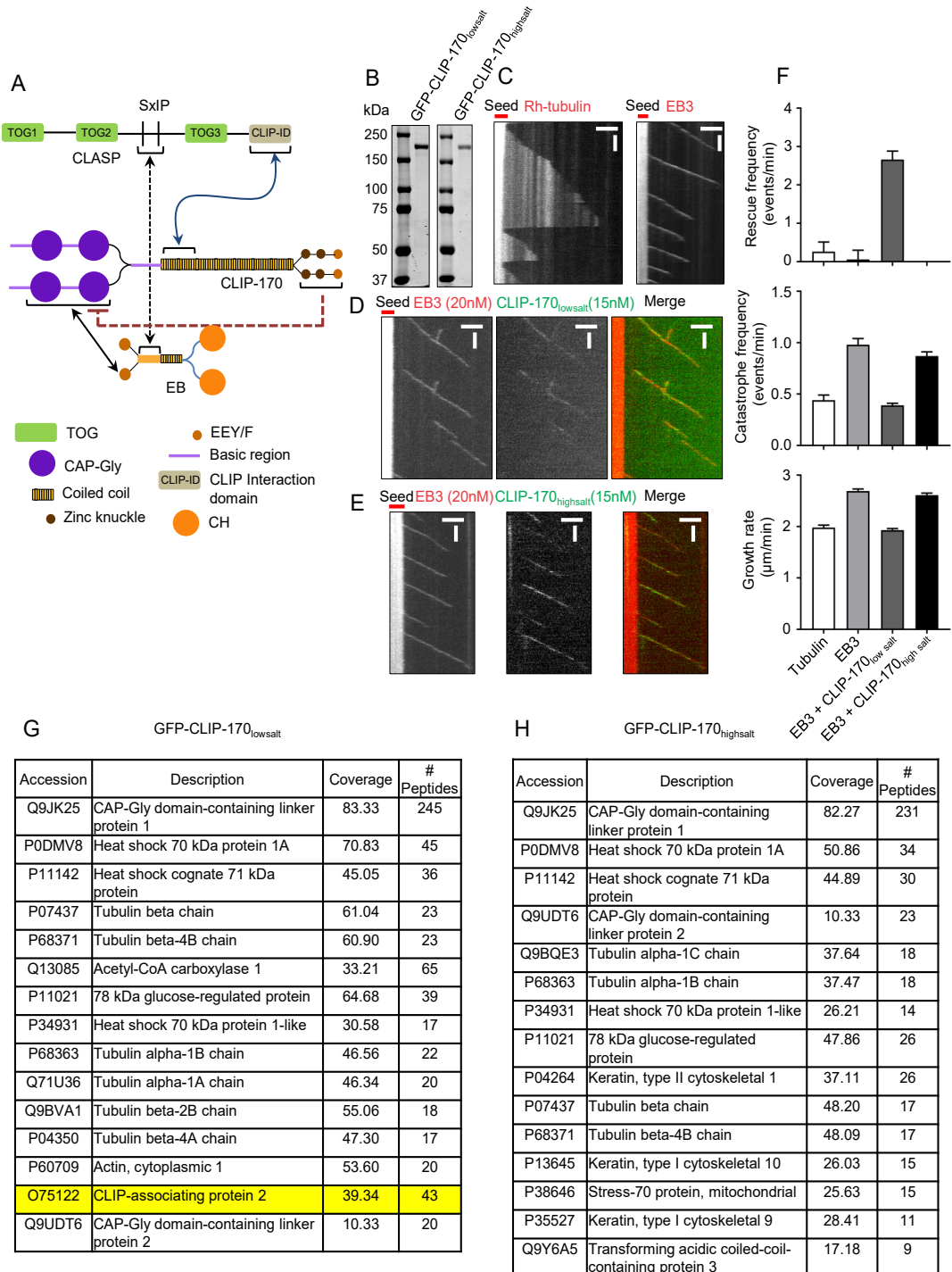


Figure 1. CLIP-170 does not induce rescues on its own but promotes CLASP induced rescues. (A) A scheme of interactions between CLASP, CLIP-170 and EB.

(B) Coomassie blue stained gel showing GFP-CLIP-170 purified from HEK293T cells with 300 mM NaCl containing wash buffer during purification (CLIP-170_{lowsalt}) or with 1000 mM NaCl containing wash buffer (CLIP-170_{highsalt}) during purification.

(C-E) Kymographs of microtubule plus end growth with rhodamine-tubulin alone or together with 20 nM mCherry-EB3 (C), 20 nM mCherry-EB3 together with 15 nM GFP-CLIP-170_{lowsalt} (D) or 20 nM mCherry-EB3 together with 15 nM GFP-CLIP-170_{highsalt} (E). Scale bars: 3 μ m (horizontal) and 60 s (vertical).

(F) Microtubule rescue frequency, catastrophe frequency and growth rate for microtubules grown in the presence of rhodamine-tubulin alone or together with 20 nM mCherry-EB3, 20 nM mCherry-EB3 together with 15 nM CLIP-170_{lowsalt} or 20 nM mCherry-EB3 together with 15 nM CLIP-170_{highsalt}. Number of growth events analyzed: for tubulin alone, $n=100$; 20 nM mCherry-EB3, $n=164$; for assays with 20 nM mCherry-EB3 and 15 nM GFP-CLIP-170_{lowsalt}, $n=111$ and for assays with 20 nM mCherry-EB3 together with 15 nM GFP-CLIP-170_{highsalt}, $n=113$. Data are from 2 independent experiments. Error bars represent SEM.

of rescue events compared to tubulin alone or tubulin together with EB3 (Figure 1D, F). Next, we tested the impact of CLIP-170_{highsalt} on microtubule dynamics. We found that CLIP-170_{highsalt} also tracked growing plus ends with EB3 but did not affect rescue frequency (Figure 1 E, F). We also found that CLIP170_{lowsalt} containing co-purified CLASP2 mildly suppressed catastrophes and reduced microtubule growth rates, which is consistent with the effects of CLASP2 on microtubule dynamics (Chapter 2) (Figure 1F). This suggests that CLIP-170 does not induce rescues on its own but possibly participates in CLASP2-induced rescues.

CLIP-170 enhances CLASP-induced rescues whereas EB suppresses rescues

To test the idea that CLIP promotes CLASP2-induced rescues, we investigated the effect of CLIP-170 without co-purified CLASP2 (CLIP-170_{highsalt}, referred to as CLIP-170 hereafter) together with trace amounts of purified CLASP2 α (Figure 2A). We found that 0.7 nM CLASP2 α increased the frequency of rescue events compared to microtubules grown in the presence of tubulin alone or with tubulin and EB3 (Figure 2B, C). We note that the CLASP2 α preparation used in this chapter was different from the one used in Chapter 2, and appeared much more potent in rescue induction, as here we observed 2.67 ± 0.14 rescues/min with 0.7 nM CLASP2 α , while in Chapter 2 we reported 3.50 ± 0.02 rescues/min with 30 nM CLASP2 α (compare Figure 2C of the current chapter to Figure 1f in Chapter 2). The possible reasons underlying these observations will be discussed below.

Combining 0.7 nM CLASP2 α with 15 nM CLIP-170 further increased the rescue frequency (Figure 2B, C). Consistent with the previous experiments, we found that 0.7 nM CLASP2 α slightly reduced the catastrophe frequency (Figure 2C). When 20 nM EB3 was included in the assay, rescues were strongly suppressed, and a significant number of rescues was only observed when both CLIP-170 and CLASP were present (Figure 2C). This suggests that rescue initiation is not dependent on the plus end tracking of CLASP, which relies on EB proteins, but may require CLIP-170-dependent association of CLASP with microtubule lattice.

Figure 2

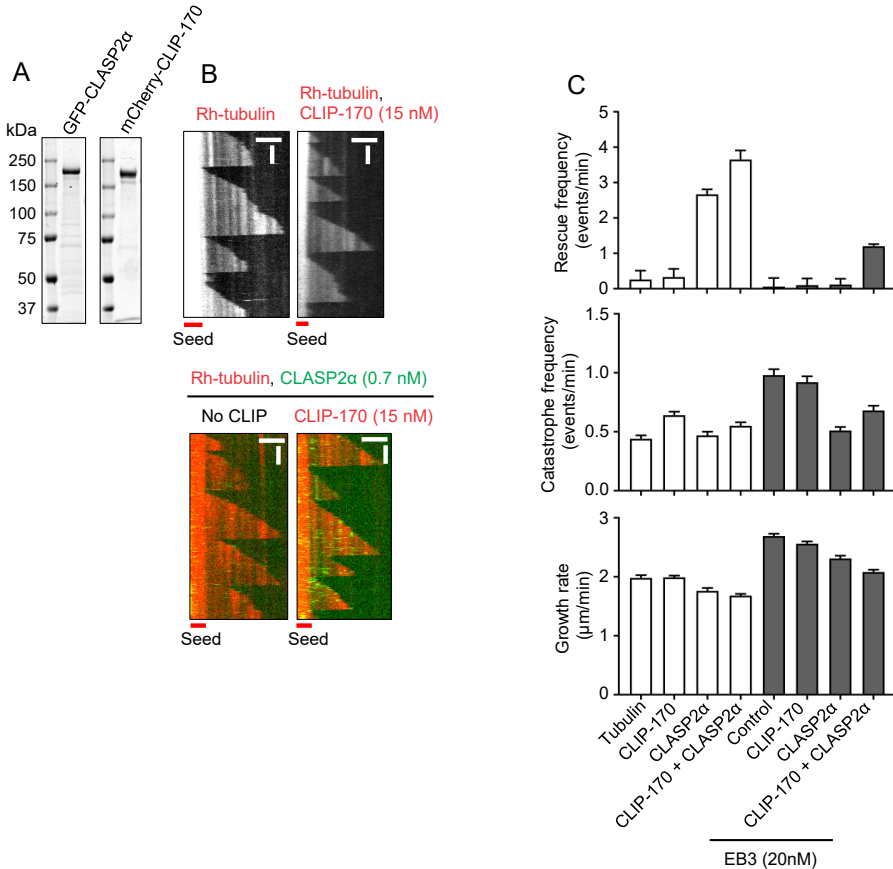


Figure 2. CLIP-170 enhances CLASP induced rescues whereas EB3 suppresses rescues.

(A) Coomassie blue stained gel showing GFP-CLASP2 α and GFP-CLIP-170 purified from HEK293T cells with 1000 mM NaCl containing wash buffer (CLIP-170_{highsalt}) during purification.

(B) Kymographs of microtubule plus end growth with rhodamine-tubulin alone, together with 15 nM mCherry-CLIP-170_{highsalt} or with 0.7 nM GFP-CLASP2 α or 15 nM mCherry-CLIP-170_{highsalt} and 0.7 nM GFP-CLASP2 α . Scale bars: 3 μm (horizontal) and 60 s (vertical).

(F) Microtubule rescue frequency, catastrophe frequency and growth rate for microtubules grown in the presence of rhodamine-tubulin alone, together with 15 nM mCherry-CLIP-170_{highsalt}, with 0.7 nM GFP-CLASP2 α , or with 15 nM mCherry-CLIP-170_{highsalt} and 0.7 nM GFP-CLASP2 α in the absence and presence of 20 nM mCherry-EB3. Number of growth events analyzed: for tubulin alone, $n=100$; for 0.7 nM GFP-CLASP2 α , $n=117$; for 15 nM mCherry-CLIP-170_{highsalt}, $n=169$; for 0.7

14nM GFP-CLASP2 α and 15 nM mCherry-CLIP-170_{highsalt}, $n=139$; for assays with 20 nM mCherry-EB3, $n=164$ for EB3 alone, for 0.7 nM GFP-CLASP2 α , $n=101$; for 15 nM mCherry-CLIP-170_{highsalt}, $n=129$; for 0.7 nM GFP-CLASP2 α and 15 nM mCherry-CLIP-170_{highsalt}, $n=206$. Data are from 2 independent experiments. Error bars represent SEM.

CLIP-170 promotes rescues induced by microtubule lattice-bound CLASP

To further investigate the nature of CLASP-induced rescue events, we classified them based on CLASP2 α dynamics. The analysis was performed in the absence of EB3, as rescues were much more frequent in these conditions. We note that in these experiments with 0.7 nM CLASP2 α , the density of CLASP binding to microtubule lattices was higher and many

Figure 3

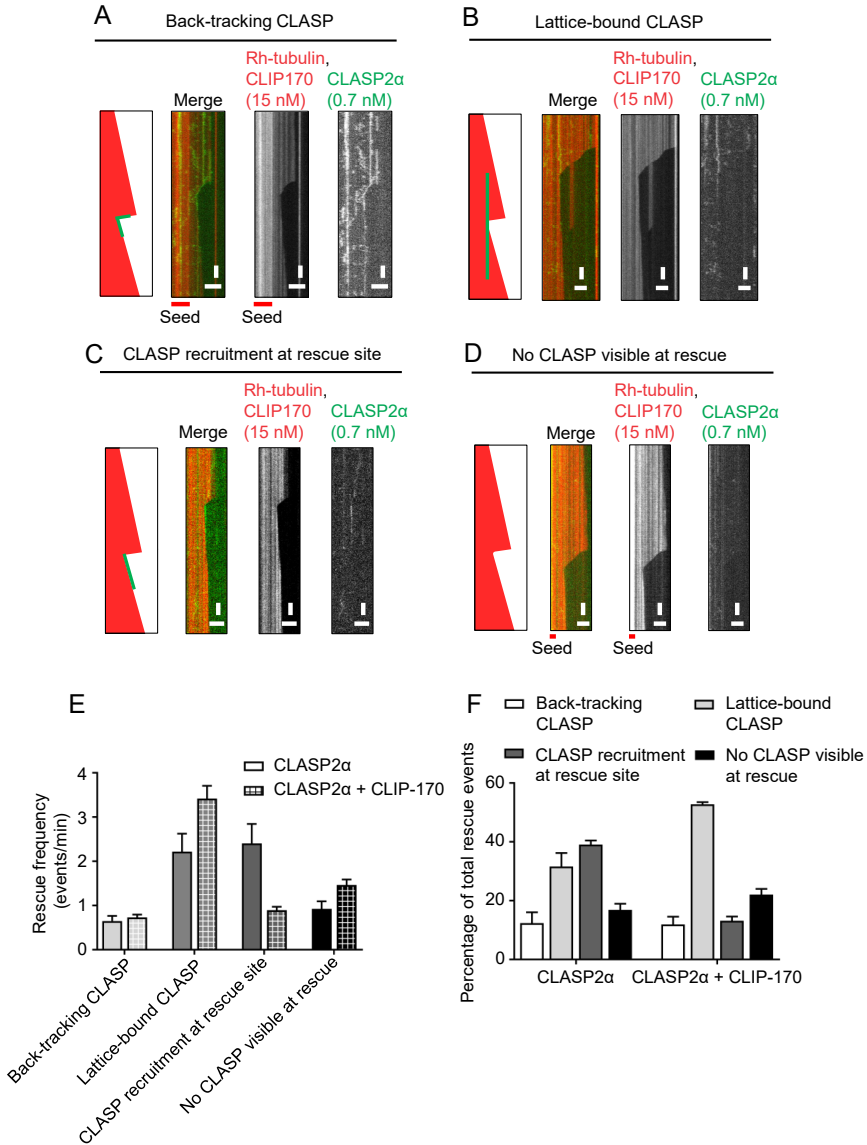


Figure 3. CLIP-170 promotes rescues induced by microtubule lattice-bound CLASP.

(A-D) Illustrative schemes and single and dual color kymographs showing rescues observed in the presence of 0.7 nM GFP-CLASP2 α and 15 nM mCherry-CLIP-170^{highsalt} categorized based on CLASP localization dynamics at the rescue event.

(E) Plot showing the frequencies of the four types of rescue events for microtubules grown in the presence of rhodamine tubulin together with 0.7 nM GFP-CLASP2 α or 0.7 nM GFP-CLASP2 α and 15 nM mCherry-CLIP-170^{highsalt}. Number of growth events analysed for CLASP2 α alone, n=215 and for CLASP2 α with CLIP-170, n=155. Data are from 3 independent experiments. Error bars represent SEM.

(F) Quantification of the four types of rescue events as percentage of the total rescue events. Data are from 3 independent experiments. Error bars represent SEM.

3 more events with a long residence time were observed compared to the data we reported in Chapter 2 with 3 nM CLASP2 α (compare Figure 3A-C of the current chapter to Figure 6b,e of Chapter 2). We again attribute these differences to the variability in CLASP preparations, as discussed below; however, the fact that EB3 was included in the experiments shown in Chapter 2 but not here could also play a role. Regardless of these differences, we could distinguish three types of events with CLASP present at the rescue site: rescue initiation preceded by CLASP2 α tracking the depolymerising microtubule end, rescue at the site where a depolymerising microtubule encountered a pre-bound CLASP2 α molecule, and rescue that coincided with CLASP2 α recruitment (Figure 3 A-C). We also observed events where no CLASP2 α signal could be detected at the rescue site possibly due to photo-bleaching of CLASP2 α molecules (Figure 3D). Quantification of frequencies of different types of events showed that rescues induced by CLASP2 α already present at the microtubule lattice or recruited at the site of rescue initiation were predominant (Figure 3E). In the presence CLIP-170, the rescues induced by lattice-bound CLASP2 α became the most frequent ones (Figure 3E). Next, we looked at the distribution of the different types of rescue events. Consistent with the rescue frequency analysis, we found that CLIP-170 increased the percentage of rescue events initiated at sites where lattice-bound CLASP2 α was already present: such events constituted 53% of total rescues compared to 32% in the presence of CLASP2 α alone (Figure 3F).

Discussion

CLIP-170 was initially proposed to be a rescue factor in cells based on experiments with a dominant negative CLIP-170 construct that lacked the CAP-Gly domains: when overexpressed, this construct strongly reduced rescue frequency (Komarova et al., 2002). This was most likely due to the binding of the C-terminal domain of CLIP-170 to the CAP-Gly domains of the endogenous CLIP-170 and the ensuing inhibition of its microtubule association. In the current study, we investigated the impact of purified CLIP-170 on microtubule dynamics, thereby ruling out indirect effects caused by the presence of other microtubule regulators. We found that CLIP-170 does not exhibit rescue activity but promotes rescues stimulated by CLASP2, which is a potent rescue factor. It is possible that the suppression of CLIP-170 interaction with microtubules by the dominant negative mutant reduced the amount of CLASP2 α on microtubules, resulting in a diminished rescue frequency.

Our *in vitro* reconstitution experiments are consistent with the fact that no rescue induction was observed in the presence of the yeast CLIP-170 homologue, Tip1, when it was combined with Mal3 and Tea2 in a microtubule plus end tracking assay (Bieling et al., 2007). However, our data seemingly contradict the previous work that showed that a purified fragment of mammalian CLIP-170, which contains the N-terminal CAP-Gly domains and a part of the dimeric coiled coil region is sufficient to induce rescues (Arnal et al., 2004). Importantly, in this paper the authors used a much higher concentration of

CLIP-170 fragment (1 μM), and in the few assays performed at lower concentration of CLIP-170 fragment (160 nm), the concentration of tubulin was extremely high (50 μM , compared to 15 μM used by us). These CLIP-170 concentrations exceed the physiological range: in cells, the concentration of CLIP-170 was estimated to be ~ 40 nM (Dragestein et al., 2008). Another in vitro study in which the effects of purified EB1 and the CAP-Gly domains were tested (Lopus et al., 2012) also reported a moderate increase in rescues, but also at high (250 nM-2 μM) concentrations. Moreover, in these assays the proper behaviour of the purified EB1 and CLIP-170 fragment (e.g. their ability to track growing microtubule ends) was not demonstrated. Taken together, the data suggest that although CLIP-170 can have autonomous effects on microtubule dynamics when its concentration is high, at nanomolar concentrations characteristic for cells, this protein might primarily act by potentiating the activity of its binding partner CLASP.

Examining the dynamics of CLASP during rescue revealed that in most cases, the transition of a depolymerizing microtubule to a polymerizing one was driven by microtubule lattice-bound CLASP molecules. We note that the rescue activity of CLASP2 α used in Chapter 2 appeared to be lower than that used in the current Chapter, and this correlated with more dense and prolonged events of CLASP2 α binding to microtubule lattice. Protein association with microtubule lattice is well known to strongly depend on electrostatic interactions. We envisage two scenarios explaining the observed differences. First, it is possible that the lattice binding of CLASP is suppressed by the association with negatively charged C-terminal domains of the EBs. The inclusion of EB3 in the assay can explain the differences between the single molecule behaviour of CLASP2 α observed in Figure 3 of the current Chapter compared to Figure 6 of Chapter 2. However, it is still puzzling that using 0.7 nM CLASP2 α in the presence of tubulin alone, we observed here a rescue frequency similar to that seen in Chapter 2 in the same conditions with 30 nM CLASP2 α . A possible explanation of this discrepancy is that although both protein preparations were produced in a similar way using HEK293T cells, the two samples have a slightly different degree of CLASP phosphorylation, because phosphates are easily lost during protein purification. CLASP association with microtubules is notorious for being exquisitely sensitive to multisite phosphorylation (Akhmanova et al., 2001; Wittmann and Waterman-Storer, 2005). It is possible that the CLASP2 α preparation used in this Chapter is somewhat less phosphorylated and, therefore, has a higher affinity for microtubule lattice.

CLIP-170 increased the proportion of rescues induced by microtubule lattice-bound CLASP2 α , suggesting that the CLASP-CLIP-170 complex has a higher propensity for lattice binding. Interestingly, we found that EB3 suppressed CLASP2 α induced rescues. This could be due to several reasons. First, it is possible that EBs reduce the amount of CLASP bound along the microtubule lattice and available for inducing rescues either by concentrating CLASP at the plus ends of microtubules (Mimori-Kiyosue et al., 2005), or by directly interfering with CLASP binding to GDP-microtubule lattice, to which EBs

themselves have only a low affinity (Maurer et al., 2011). Second, EB1 was shown to inhibit templated microtubule nucleation in vitro (Wieczorek et al., 2015). This could account for rescue suppression, considering that a rescue represents a microtubule outgrowth event from the microtubule lattice initially lacking a GTP cap and is thus mechanistically similar to template-based microtubule nucleation. In the future, it would be interesting to try to distinguish between these possibilities by performing reconstitution assays in which the CLASP-EB interaction is perturbed. This would be easy to do using CLASP with mutated SxIP motifs together with EB3 or using an EB3 mutant without the C-terminal EB Homology (EBH) domain together with intact CLASP.

To further test the idea that CLIP increases CLASP induced rescues, it will be interesting in future to investigate if the CLASP interacting domain alone could restore the activity of the full length protein in CLIP-170 knockout cells.

3

Experimental Procedures

DNA constructs, cell lines and cell culture

CLIP-170 and CLASP2 α proteins expressed in mammalian cells were made in modified pEGFP-C1 or pmCherry-C1 vectors respectively with a StrepII tag. HEK 293T cells were cultured in DMEM/F10 (1:1 ratio, Lonza, Basel, Switzerland) supplemented with 10% FCS.

Protein purification from HEK293T cells for in vitro reconstitution assays

GFP-CLIP-170, mCherry-CLIP-170 and GFP-CLASP2 α used in the in vitro reconstitutions assays were purified from HEK293T cells using the Strep(II)-streptactin affinity purification. Cells were harvested 2 days after transfection. Cells from a 15 cm dish were lysed in 500 μ l of lysis buffer (50 mM HEPES, 300 mM NaCl and 0.5% Triton X-100, pH 7.4) supplemented with protease inhibitors (Roche) on ice for 15 minutes. The supernatant obtained from the cell lysate after centrifugation at 21,000 x g for 20 minutes was incubated with 40 μ l of StrepTactin Sepharose beads (GE) for 45 minutes. The beads were washed 3 times in the lysis buffer without the protease inhibitors either with 300 mM NaCl or 1000 mM NaCl for GFP-CLIP-170_{lowsalt} and GFP-CLIP-170_{highsalt} respectively. The protein was eluted with 40 μ l of elution buffer (50 mM HEPES, 150 mM NaCl, 1 mM MgCl₂, 1 mM EGTA, 1 mM dithiothreitol (DTT), 2.5 mM d-Desthiobiotin and 0.05% Triton X-100, pH 7.4). Purified proteins were snap-frozen and stored at -80 °C.

In vitro microtubule dynamics assays

Reconstitution of microtubule growth dynamics in vitro was performed as described previously (Sharma et al., 2016). GMPCPP-stabilized microtubule seeds (70% unlabeled tubulin, 18% biotin tubulin and 12% of rhodamine-tubulin) were prepared as described before. Flow chambers, assembled from plasma-cleaned glass coverslips and microscopic slides were functionalized by sequential incubation with 0.2 mg/ml PLL-PEG-biotin

(Susos AG, Switzerland) and 1 mg/ml NeutrAvidin (Invitrogen) in MRB80 buffer (80 mM piperazine-N,N[prime]-bis(2-ethanesulfonic acid), pH 6.8, supplemented with 4 mM MgCl₂, and 1 mM EGTA. Microtubule seeds were attached to the coverslip through biotin-NeutrAvidin interactions. Flow chambers were further blocked with 1 mg/ml κ -casein. The reaction mixture with or without proteins (MRB80 buffer supplemented with 15 μ M porcine brain tubulin, 0.5 μ M rhodamine-tubulin, 50 mM KCl, 1 mM guanosine triphosphate, 0.2 mg/ml κ -casein, 0.1% methylcellulose, and oxygen scavenger mix [50 mM glucose, 400 μ g/ml glucose oxidase, 200 μ g/ml catalase, and 4 mM DTT]) was added to the flow chamber after centrifugation in an Airfuge for 5 minutes at 119,000 \times g. For experiments in the presence of EB3, concentration of mCherry-EB3 or GFP-EB3 was as indicated in the figures and rhodamine-tubulin was excluded from the assay. The flow chamber was sealed with vacuum grease, and dynamic microtubules were imaged immediately at 30 °C using TIRF microscopy. All tubulin products were from Cytoskeleton Inc.

TIRF microscopy

In vitro reconstitution assays were imaged on a TIRF microscope setup as described previously or on an Ilas2 TIRF setup. In brief, we used an inverted research microscope Nikon Eclipse Ti-E (Nikon) with the perfect focus system (Nikon), equipped with Nikon CFI Apo TIRF 100x 1.49 N.A. oil objective (Nikon) and controlled with MetaMorph 7.7.5 software (Molecular Devices). The microscope was equipped with TIRF-E motorized TIRF illuminator modified by Roper Scientific France/PICT-IBiSA, Institut Curie. To keep the in vitro samples at 30 °C, a stage top incubator model INUBG2E-ZILCS (Tokai Hit) was used. For excitation, 491 nm 100 mW Calypso (Cobolt) and 561 nm 100 mW Jive (Cobolt) lasers were used. We used ET-GFP 49002 filter set (Chroma) for imaging of proteins tagged with GFP or ET-mCherry 49008 filter set (Chroma) for imaging of proteins tagged with mCherry. Fluorescence was detected using an EMCCD Evolve 512 camera (Roper Scientific) with the intermediate lens 2.5X (Nikon C mount adapter 2.5X) or using the CoolSNAP HQ2 CCD camera (Roper Scientific) without an additional lens. In both cases the final magnification was 0.063 μ m/pixel.

Ilas2 system (Roper Scientific, Evry, FRANCE) is a dual laser illuminator for azimuthal spinning TIRF (or Hilo) illumination and with a custom modification for targeted photomanipulation. This system was installed on Nikon Ti microscope (with the perfect focus system, Nikon), equipped with 150 mW 488 nm laser and 100 mW 561 nm laser, 49002 and 49008 Chroma filter sets, EMCCD Evolve mono FW DELTA 512x512 camera (Roper Scientific) with the intermediate lens 2.5X (Nikon C mount adapter 2.5X), CCD camera CoolSNAP MYO M-USB-14-AC (Roper Scientific) and controlled with MetaMorph 7.8.8 software (Molecular Device). To keep the in vitro samples at 30°C, a stage top incubator model INUBG2E-ZILCS (Tokai Hit) was used. The final resolution using EMCCD camera was 0.065 μ m/pixel, using CCD camera it was 0.045 μ m/pixel.

Both microscopes were equipped with an ILas system (Roper Scientific France/PICT-IBiSA) for FRAP and photoablation. The 532 nm Q-switched pulsed laser (Teem Photonics) was used for photoablation on the TIRF microscope.

Analysis of microtubule plus end dynamics in vitro

Kymographs were generated using the ImageJ plugin KymoResliceWide (<http://fiji.sc/KymoResliceWide>). Microtubule dynamics parameters were determined from kymographs using an optimized version of the custom made JAVA plug in for ImageJ as described previously.

The relative standard error for catastrophe frequency was calculated as described previously. The relative standard error of mean rescue frequency was calculated in the same way as the standard error of the mean catastrophe frequency, i.e. ,

$$SE_r = \bar{f}_r \frac{SE_{t_{sh}}}{\bar{t}_{sh}}$$

where are \bar{f}_r, \bar{t}_{sh} average values and $SE_{f_r}, SE_{t_{sh}}$ are standard errors of rescue frequency and shortening time respectively. The number of observed rescue events for control was relatively small as compared to the catastrophes, so we assumed that they follow a Poisson distribution. The standard deviation of the rescue frequency was calculated as the square root of its mean value and the standard error was calculated according to:

$$SE_{f_r} = \frac{\sqrt{\bar{f}_r}}{\sqrt{N_r}}$$

, where \bar{f}_r and SE_{f_r} are the average and the standard error of the rescue frequency and N_r is the number of rescues.

Acknowledgements

This work was supported by the European Research Council Synergy grant 609822 to A.Ak., the Netherlands Organization for Scientific Research (NWO) through a VIDI grant (723.012.102) and as part of the National Roadmap Large-scale Research Facilities of the Netherlands (project number 184.032.201) to A.F.M.A. and NWO-CW ECHO grant (711.011.005) to A.Ak.

References

- Akhmanova, A., C.C. Hoogenraad, K. Drabek, T. Stepanova, B. Dortland, T. Verkerk, W. Vermeulen, B.M. Burgering, C.I. De Zeeuw, F. Grosveld, and N. Galjart. 2001. Clasps are CLIP-115 and -170 associating proteins involved in the regional regulation of microtubule dynamics in motile fibroblasts. *Cell*. 104:923-935.
- Akhmanova, A., and M.O. Steinmetz. 2015. Control of microtubule organization and dynamics: two ends in the limelight. *Nat Rev Mol Cell Biol*. 16:711-726.
- Al-Bassam, J., H. Kim, G. Brouhard, A. van Oijen, S.C. Harrison, and F. Chang. 2010. CLASP promotes microtubule rescue by recruiting tubulin dimers to the microtubule. *Dev Cell*. 19:245-258.
- Arnal, I., C. Heichette, G.S. Diamantopoulos, and D. Chretien. 2004. CLIP-170/tubulin-curved oligomers coassemble at microtubule ends and promote rescues. *Curr Biol*. 14:2086-2095.
- Aumeier, C., L. Schaedel, J. Gaillard, K. John, L. Blanchoin, and M. Thery. 2016. Self-repair promotes microtubule rescue. *Nat Cell Biol*. 18:1054-1064.
- Bieling, P., S. Kandels-Lewis, I.A. Telley, J. van Dijk, C. Janke, and T. Surrey. 2008. CLIP-170 tracks growing microtubule ends by dynamically recognizing composite EB1/tubulin-binding sites. *J Cell Biol*. 183:1223-1233.
- Bieling, P., L. Laan, H. Schek, E.L. Munteanu, L. Sandblad, M. Dogterom, D. Brunner, and T. Surrey. 2007. Reconstitution of a microtubule plus-end tracking system in vitro. *Nature*. 450:1100-1105.
- Busch, K.E., J. Hayles, P. Nurse, and D. Brunner. 2004. Tea2p kinesin is involved in spatial microtubule organization by transporting tip1p on microtubules. *Dev Cell*. 6:831-843.
- de Forges, H., A. Pilon, I. Cantaloube, A. Pallandre, A.M. Haghiri-Gosnet, F. Perez, and C. Pous. 2016. Localized Mechanical Stress Promotes Microtubule Rescue. *Curr Biol*. 26:3399-3406.
- Dimitrov, A., M. Quesnoit, S. Moutel, I. Cantaloube, C. Pous, and F. Perez. 2008. Detection of GTP-tubulin conformation in vivo reveals a role for GTP remnants in microtubule rescues. *Science*. 322:1353-1356.
- Dragestein, K.A., W.A. van Cappellen, J. van Haren, G.D. Tsididis, A. Akhmanova, T.A. Knoch, F. Grosveld, and N. Galjart. 2008. Dynamic behavior of GFP-CLIP-170 reveals fast protein turnover on microtubule plus ends. *J Cell Biol*. 180:729-737.
- Henty-Ridilla, J.L., A. Rankova, J.A. Eskin, K. Kenny, and B.L. Goode. 2016. Accelerated actin filament polymerization from microtubule plus ends. *Science*. 352:1004-1009.
- Komarova, Y.A., A.S. Akhmanova, S. Kojima, N. Galjart, and G.G. Borisy. 2002. Cytoplasmic linker proteins promote microtubule rescue in vivo. *J Cell Biol*. 159:589-599.
- Lansbergen, G., Y. Komarova, M. Modesti, C. Wyman, C.C. Hoogenraad, H.V. Goodson, R.P. Lemaitre, D.N. Drechsel, E. van Munster, T.W. Gadella, Jr., F. Grosveld, N. Galjart, G.G. Borisy, and A. Akhmanova. 2004. Conformational changes in CLIP-170 regulate its binding to microtubules and dynactin localization. *J Cell Biol*. 166:1003-1014.
- Lewkowicz, E., F. Herit, C. Le Clainche, P. Bourdoncle, F. Perez, and F. Niedergang. 2008. The microtubule-binding protein CLIP-170 coordinates mDia1 and actin reorganization during CR3-mediated phagocytosis. *J Cell Biol*. 183:1287-1298.
- Lopus, M., C. Manatschal, R.M. Buey, S. Bjelic, H.P. Miller, M.O. Steinmetz, and L. Wilson. 2012. Cooperative stabilization of microtubule dynamics by EB1 and CLIP-170 involves displacement of stably bound P(i) at microtubule ends. *Biochemistry*. 51:3021-3030.
- Maurer, S.P., P. Bieling, J. Cope, A. Hoenger, and T. Surrey. 2011. GTPgammaS microtubules mimic the growing microtubule end structure recognized by end-binding proteins (EBs). *Proc Natl Acad Sci U S A*. 108:3988-3993.
- Mimori-Kiyosue, Y., I. Grigoriev, G. Lansbergen, H. Sasaki, C. Matsui, F. Severin, N. Galjart, F. Grosveld, I. Vorobjev, S. Tsukita, and A. Akhmanova. 2005. CLASP1 and CLASP2 bind to EB1 and regulate microtubule plus-end dynamics at the cell cortex. *J Cell Biol*. 168:141-153.
- Mishima, M., R. Maesaki, M. Kasa, T. Watanabe, M. Fukata, K. Kaibuchi, and T. Hakoshima. 2007. Structural basis for tubulin recognition by cytoplasmic linker protein 170 and its autoinhibition. *Proc Natl Acad Sci U S A*. 104:10346-10351.
- Perez, F., G.S. Diamantopoulos, R. Stalder, and T.E. Kreis. 1999. CLIP-170 highlights growing

- microtubule ends in vivo. *Cell*. 96:517-527.
- Pierre, P., R. Pepperkok, and T.E. Kreis. 1994. Molecular characterization of two functional domains of CLIP-170 in vivo. *J Cell Sci*. 107 (Pt 7):1909-1920.
- Pierre, P., J. Scheel, J.E. Rickard, and T.E. Kreis. 1992. CLIP-170 links endocytic vesicles to microtubules. *Cell*. 70:887-900.
- Schaedel, L., K. John, J. Gaillard, M.V. Nachury, L. Blanchoin, and M. Thery. 2015. Microtubules self-repair in response to mechanical stress. *Nat Mater*. 14:1156-1163.
- Sharma, A., A. Aher, N.J. Dynes, D. Frey, E.A. Katrukha, R. Jaussi, I. Grigoriev, M. Croisier, R.A. Kammerer, A. Akhmanova, P. Gonczy, and M.O. Steinmetz. 2016. Centriolar CPAP/SAS-4 Imparts Slow Processive Microtubule Growth. *Developmental cell*. 37:362-376.
- van der Vaart, B., C. Manatschal, I. Grigoriev, V. Olieric, S.M. Gouveia, S. Bjelic, J. Demmers, I. Vorobjev, C.C. Hoogenraad, M.O. Steinmetz, and A. Akhmanova. 2011. SLAIN2 links microtubule plus end-tracking proteins and controls microtubule growth in interphase. *J Cell Biol*. 193:1083-1099.
- Weisbrich, A., S. Honnappa, R. Jaussi, O. Okhrimenko, D. Frey, I. Jelesarov, A. Akhmanova, and M.O. Steinmetz. 2007. Structure-function relationship of CAP-Gly domains. *Nat Struct Mol Biol*. 14:959-967.
- Wieczorek, M., S. Bechstedt, S. Chaaban, and G.J. Brouhard. 2015. Microtubule-associated proteins control the kinetics of microtubule nucleation. *Nat Cell Biol*. 17:907-916.
- Wittmann, T., and C.M. Waterman-Storer. 2005. Spatial regulation of CLASP affinity for microtubules by Rac1 and GSK3beta in migrating epithelial cells. *J Cell Biol*. 169:929-939.
- Yu, N., L. Signorile, S. Basu, S. Ottema, J.H. Lebbink, K. Leslie, I. Smal, D. Dekkers, J. Demmers, and N. Galjart. 2016. Isolation of Functional Tubulin Dimers and of Tubulin-Associated Proteins from Mammalian Cells. *Curr Biol*. 26:1728-1736.

4

Regulation of microtubule growth by a complex of chTOG, SLAIN2 and EB3: in vitro reconstitution with purified proteins.

Amol Aher¹, and Anna Akhmanova¹

¹ Cell Biology, Department of Biology, Faculty of Science, Utrecht University, Padualaan 8, 3584 CH Utrecht, the Netherlands.

Abstract

Microtubules are dynamic biopolymers that switch between phases of growth and shrinkage. This behavior is modulated by a network of plus end binding proteins. Here, we reconstituted microtubule growth in the presence of the mammalian microtubule polymerase chTOG. Together with EB3, chTOG accelerated microtubule growth to rates comparable to those observed *in vivo*. SLAIN2, an adaptor protein connecting chTOG to EBs, further increased microtubule growth rates when combined with EB3 and chTOG. This suggests that SLAIN2 can augment chTOG function, in agreement with observations in cells. chTOG alone or combined with SLAIN2 in the presence of EB3 could antagonize the ability of the kinesin-13 MCAK to block microtubule outgrowth. However, chTOG, either alone or in complex with SLAIN2, promoted rather than suppressed microtubule catastrophes, and these proteins could not counteract the catastrophe-inducing activity of MCAK. This is in contrast to published data showing that in cells, SLAIN2 and chTOG suppress catastrophes. This discrepancy is most likely explained by the interplay between chTOG, SLAIN2 and additional cellular factors, which together control the processivity of microtubule polymerization.

4 Introduction

Microtubules are cytoskeletal filaments important for diverse cellular processes including cell division, migration and intracellular transport. Microtubules exhibit dynamic switching between phases of growth and shrinkage, a process termed dynamic instability. This dynamic behavior has been proposed to be driven by the hydrolysis of GTP bound to the β -tubulin (Mitchison and Kirschner, 1984). Multiple microtubule associated proteins that regulate this switching behavior either autonomously or through their binding partners have been characterized (Akhmanova and Steinmetz, 2015).

Microtubule polymerases of the XMAP215/chTOG/Stu2 family are autonomous microtubule plus end tracking proteins that promote microtubule growth both in interphase and in mitosis by binding tubulin through their TOG domains (Bonfils et al., 2007; Cullen et al., 1999; van der Vaart et al., 2011; Wang and Huffaker, 1997). The mammalian family member, chTOG (colonic and hepatic tumor overexpressed gene), is also essential for stabilization of kinetochore fibers in the mitotic spindle, where it crossbridges microtubules by acting in a complex with TACC3 and clathrin (Booth et al., 2011; Royle, 2013). TOG domains of the XMAP215/chTOG/Stu2 proteins can bind to $\alpha\beta$ tubulin dimers in a curved conformation. Such curved tubulins are present only at microtubule tips, because the dimers undergo straightening upon incorporation into microtubule lattice. Preference for curved tubulin subunits combined with the C-terminal microtubule lattice binding region and the ordering of TOG domains confers to XMAP215 and its homologs their plus end specificity (Ayaz et al., 2014; Ayaz et al., 2012). Reconstitution experiments using purified XMAP215/chTOG/Stu2 proteins have demonstrated that they increase microtubule growth rates 2 to 20 fold depending on the species and protein concentrations used in

the experiments (Brouhard et al., 2008; Li et al., 2012; Roostalu et al., 2015; Widlund et al., 2011). It was also shown that XMAP215 and its yeast, fly, and human homologs autonomously track both growing and depolymerizing plus ends (Al-Bassam et al., 2012; Brouhard et al., 2008; Li et al., 2012; Roostalu et al., 2015).

End binding proteins (EBs, which in vertebrates include EB1, EB2 and EB3) also track the growing plus ends autonomously through their N-terminal CH domain, which senses the nucleotide state of tubulin (Komarova et al., 2009; Maurer et al., 2012; Zhang et al., 2015). Through their C-terminus, EBs recruit to microtubule plus ends numerous binding partners (Akhmanova and Steinmetz, 2008). In vitro, EBs increase microtubule growth rates and catastrophe frequency (Doodhi et al., 2016; Mohan et al., 2013), although in cells loss of EBs has no major impact on microtubule growth rate but reduces processivity of microtubule growth (Komarova et al 2009). EBs lead to the maturation of the microtubule plus end and also promote compaction of microtubule lattice (Maurer et al., 2014; Zhang et al., 2015). Recently, it was shown that purified XMAP215 and EB1 constitute the minimal plus end-binding module that can accelerate microtubule growth rate up to 20 μm per minute, a value that is in the higher range of the microtubule growth rates observed in vivo (Zanic et al., 2013). It has been shown that EB and XMAP215 bind to distinct regions at the plus end of a microtubule and do not interact with each other either (Maurer et al., 2014). The current model proposes that EB binding allosterically affects XMAP215 activity, an effect that could potentially be due to EB-induced changes in microtubule tip structure or the microtubule lattice compaction.

Although XMAP215 family proteins can autonomously track growing plus ends, in *Drosophila* and mammalian cells, they have been shown to be targeted to the growing plus end by EB-binding adaptor proteins Sentin and SLAIN1/2, respectively (Li et al., 2011; van der Vaart et al., 2011). Furthermore, fission yeast harbors two chTOG homologs, Dis1, which binds directly to the EB homolog Mal3, and Alp14 that functions in an EB-independent manner (Al-Bassam et al., 2012; Matsuo et al., 2016). This suggests that additional mechanisms might ensure robust microtubule tip localization of chTOG in the crowded plus end environment. Mammalian SLAIN2 tracks the growing plus ends in an EB dependent manner through its multiple SxIP like motifs. It recruits chTOG through the N-terminus and also binds other plus end binding proteins, such as CLIP-170 and CLASP, through its C-terminus (van der Vaart et al., 2011). Interestingly, depletion of SLAINs perturbs microtubule growth: catastrophes become more frequent and microtubule growth episodes become irregular, interrupted by depolymerization events, leading to the reduction of the average microtubule growth rate (Bouchet et al., 2016; van der Vaart et al., 2012; van der Vaart et al., 2011). Depletion of chTOG has a similar effect (Bouchet et al., 2016; van der Vaart et al., 2012; van der Vaart et al., 2011), which, however, contradicts the work with purified proteins, because chTOG together with EB increase catastrophe frequency in vitro (Zanic et al., 2013). One possibility is that SLAIN2, when present in a complex with chTOG and EB, would modify their properties explaining the discrepancy

between the data obtained in vitro and in cells.

To investigate the effects of SLAIN2 and SLAIN2-chTOG complex on microtubule dynamics, we performed in vitro reconstitution assays using purified proteins. In this report, we characterize the effects of the mammalian microtubule polymerase chTOG on microtubule growth rate and catastrophe frequency. We also analyze the impact of SLAIN2 alone or together with chTOG on microtubule dynamics. Finally, we look at the ability of SLAIN2 and the SLAIN2-chTOG complex to antagonize microtubule growth-blocking activity of MCAK. Our data indicate that these proteins, when present in different combinations, can potently regulate microtubule growth. However, our in vitro assays do not fully recapitulate the in vivo observations, suggesting that cellular activities of chTOG and SLAIN2 require additional factors.

RESULTS

chTOG increases microtubule polymerization rate

To characterize the effects of mammalian microtubule polymerase chTOG on microtubule growth, we used an in vitro reconstitution assay in which dynamic microtubules are nucleated from GMPCPP seeds and monitored with TIRF microscopy (Bieling et al., 2007; Sharma et al., 2016). We purified GFP tagged chTOG from HEK293T cells and investigated its effects on dynamic microtubules (Figure 1A). Kymographs of microtubules grown in the presence of rhodamine-labeled tubulin and 100 nM chTOG-GFP showed association of chTOG with polymerizing as well as depolymerizing plus end (Figure 1B, lower panel, left), in agreement with previous work (Roostalu et al., 2015). chTOG accumulation at the ends of GMPCPP seeds was also seen in the absence of microtubule growth (Figure 1B, lower panel). Microtubules grown in the presence of 100 nM mCherry-EB3 and 100 nM chTOG-GFP exhibited the same chTOG accumulation pattern as without EB3 (Figure 1B, lower panel, right), although the duration of growth episodes was strongly reduced when both proteins were present (Figure 1B).

Next, we examined the impact of chTOG on the parameters of microtubule dynamics. We tested different concentrations of chTOG ranging from 25 nM to 200 nM either in the presence of rhodamine-labeled tubulin alone or together with 100 nM mCherry-EB3 at a constant tubulin concentration of 15 μM . In the absence of EB3, chTOG increased the microtubule growth rate approximately threefold, from $3.40 \pm 0.08 \mu\text{m min}^{-1}$ for tubulin alone to $10.52 \pm 0.20 \mu\text{m min}^{-1}$ for tubulin with 100 nM of chTOG-GFP (Figure 1C, upper panel). Similarly, the catastrophe frequency increased 2.5 fold, from $0.28 \pm 0.02 \text{ min}^{-1}$ for tubulin alone to $0.69 \pm 0.03 \text{ min}^{-1}$ for tubulin with 100 nM chTOG-GFP (Figure 1C, lower panel). The effects on both the growth rate and catastrophe frequency seemed to reach saturation beyond 100 nM chTOG. Microtubule growth rate increased from $5.16 \pm 0.04 \mu\text{m min}^{-1}$ in the case of EB3 alone to $15.87 \pm 0.16 \mu\text{m min}^{-1}$ in the presence of 100 nM chTOG GFP (Figure 1C, upper panel). Similar to the assays without EB3, a two fold increase in the catastrophe frequency was observed (Figure 1C, lower panel). Thus both

Figure 1

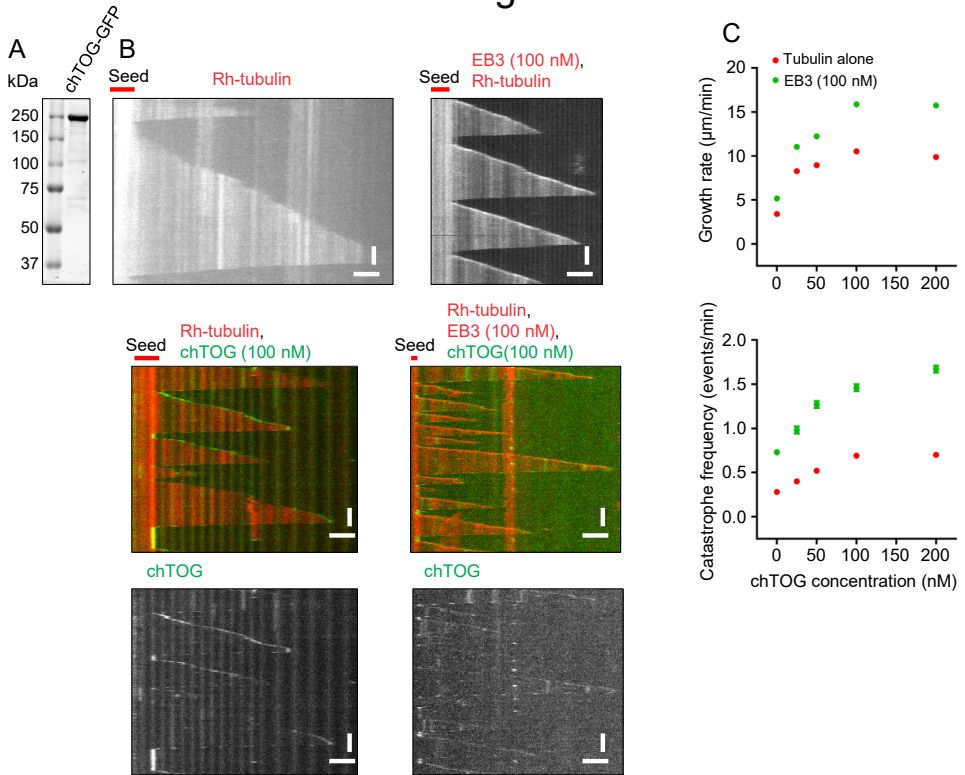


Figure 1. The mammalian microtubule polymerase chTOG increases microtubule polymerization rate to physiological levels in the presence of EB3.

(A) Coomassie blue stained gel showing chTOG-GFP purified from HEK293T cells.

(B) Kymographs of microtubule plus end growth with rhodamine-tubulin alone or together with 100 nM mCherry-EB3 and together with 100 nM chTOG-GFP. chTOG channels are shown below the dual color kymographs for chTOG alone or together with EB3. Scale bars: 3 μm (horizontal) and 60 s (vertical).

(C) Microtubule growth rate and catastrophe frequencies for microtubules grown in the presence of rhodamine-tubulin alone (red) or together with 100 nM mCherry-EB3 (green) at the indicated chTOG-GFP concentrations. Number of growth events analyzed: for tubulin alone, $n=98$; tubulin with chTOG-GFP, $n=66, 105, 190$ and 218 for 25 nM, 50 nM, 100 nM and 200 nM chTOG-GFP respectively; for assays with 100 nM mCherry-EB3, $n=211$; 100 nM mCherry-EB3 with chTOG-GFP, $n=282, 347, 466, 586$ for 25 nM, 50 nM, 100 nM and 200 nM chTOG respectively. Data are from 2-3 experiments. Error bars represent SEM.

EB3 and chTOG promote microtubule growth rates and increase catastrophe frequency and when combined, lead to microtubule growth rates close to the ones observed in vivo, in line with previous observations with the frog polymerase XMAP215 and EB1 (Zanic et al., 2013).

SLAIN2 increases microtubule polymerization rate and catastrophe frequency in the presence of chTOG

SLAIN2 was shown to connect chTOG to EBs (van der Vaart et al., 2011) (a scheme of the interactions between these proteins is shown in Figure 2A). To investigate the effect

Figure 2

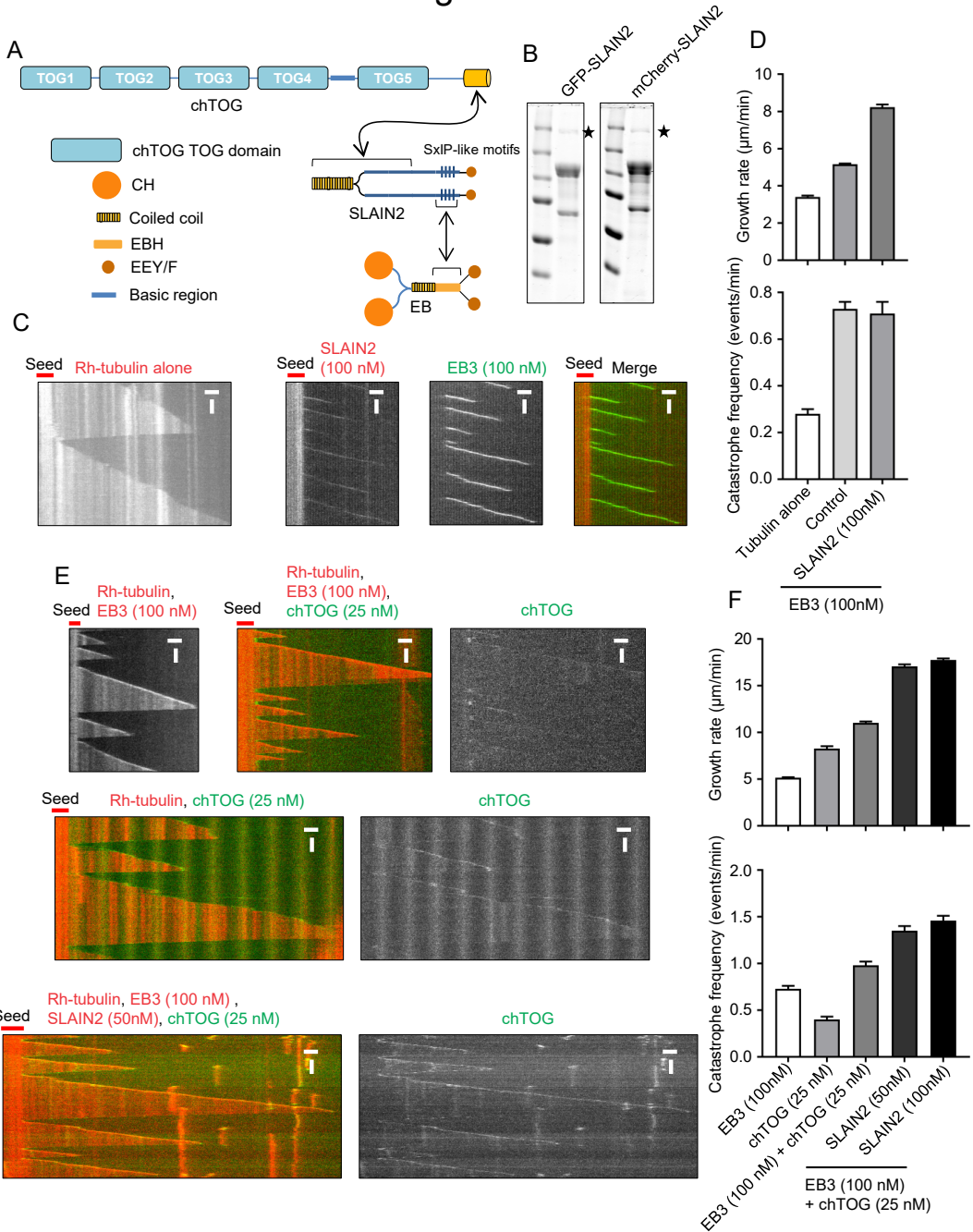


Figure 2. SLAIN2 increases microtubule polymerization rate and catastrophe frequency in the presence of chTOG.

(A) A scheme of interaction between chTOG, SLAIN2 and EB.

(B) Coomassie blue stained gel showing GFP and mCherry tagged SLAIN2 purified from HEK293T cells.

(C) Representative kymographs showing microtubule plus end dynamics in the presence of rhodamine tubulin alone or with 100 nM mCherry-SLAIN2 and 100 nM GFP-EB3. Scale bars: 3 μm (horizontal) and

60 s (vertical).

(D) Microtubule growth rate and catastrophe frequency for microtubules grown in the presence of rhodamine-tubulin alone, together with 100 nM mCherry-EB3 or with 100 nM mCherry-SLAIN2 and 100 nM GFP-EB3. Number of growth events analyzed: tubulin alone, $n=98$, 100 nM mCherry-EB3, $n=211$ and $n=63$ for 100 nM GFP-EB3 together with 100 nM mCherry-SLAIN2. Error bars represent SEM.

(E) Kymographs illustrating microtubule plus end growth in the presence of rhodamine tubulin together with 100 nM mCherry-EB3 or 25 nM chTOG-GFP alone (upper panel), and in the presence of rhodamine tubulin, 100 nM mCherry-EB3 and 25 nM chTOG-GFP, with or without 50 nM mCherry-SLAIN2. chTOG channels are shown next to the dual color kymographs for chTOG alone or chTOG and EB3 or chTOG, SLAIN2 and EB3. Scale bars: 3 μm (horizontal) and 60 s (vertical).

(F) Microtubule growth rate and catastrophe frequencies for microtubules grown in the presence of rhodamine-tubulin together with 100 nM mCherry-EB3, 25 nM chTOG-GFP, 25 nM chTOG-GFP and 100 nM mCherry-EB3, or with 100 nM mCherry-EB3, 25 nM chTOG-GFP and 50 nM mCherry-SLAIN2. Scale bars: 3 μm (horizontal) and 60 s (vertical). Number of growth events analyzed: $n=211$ for 100 nM mCherry-EB3, $n=66$ for 25 nM chTOG-GFP, $n=282$ for 100 nM mCherry-EB3 and 25 nM chTOG-GFP, $n=282$ for 100 nM mCherry-EB3, 25 nM chTOG-GFP and 50 nM mCherry-SLAIN2 and $n=409$ for 100 nM mCherry-EB3, 25 nM chTOG-GFP and 100 nM mCherry-SLAIN2. Data are from 2 experiments. Error bars represent SEM.

of SLAIN2 on microtubule dynamics, we performed assays in the presence of EB3 either with SLAIN2 alone, or in combination with chTOG. We found that in the presence of EB3, SLAIN2 tracked growing microtubule plus ends and co-localized with EB3 (Figure 2B, C). Analysis of the microtubule dynamics parameters revealed that SLAIN2 leads to an increase in growth velocity, although this could be due to the presence of co-purified endogenous chTOG (indicated by asterisk, Figure 2B, D). When tested together with 25 nM chTOG-GFP and 100 nM mCherry-EB3, the conditions when the effect of chTOG on growth rate and catastrophes is not saturated, 50 nM mCherry-SLAIN2 further increased microtubule growth rate by a factor of 1.6 (Figure 2F). At 100 nM mCherry-SLAIN2, microtubule growth rate of $17.75 \pm 0.18 \mu\text{m min}^{-1}$ was observed, again a 1.6 fold increase compared to $11.03 \pm 0.14 \mu\text{m min}^{-1}$ in the presence of 100 nM mCherry-EB3 and 25 nM chTOG. Similar to the effect of increasing chTOG concentration, the addition of SLAIN2 in the presence of chTOG resulted in an increase in catastrophe frequency, although by itself SLAIN2 had no impact on catastrophes (Figure 2C-F). We note that the recruitment of chTOG to the growing plus ends appeared to be more robust when both SLAIN2 and EB3 were present compared to EB3 alone (Figure 2E). It is thus possible that in the presence of chTOG, SLAIN2 primarily acts by recruiting it to the plus end and thus increasing both the growth rate and catastrophe frequency. However, an autonomous effect of SLAIN2 on microtubule polymerization remains a distinct possibility, which would need to be further tested, ideally by obtaining SLAIN2 preparations completely devoid of chTOG. Importantly, our data suggest that in vitro, SLAIN2 by itself does not have stabilizing effects on the microtubule plus end, and when combined with chTOG, promotes rather than suppresses catastrophes, opposite to the observations in cells (Bouchet et al., 2016; van der Vaart et al., 2012; van der Vaart et al., 2011).

Fast microtubule polymerization antagonizes MCAK activity

We next investigated the microtubule growth-promoting activity of the SLAIN2-chTOG

Figure 3

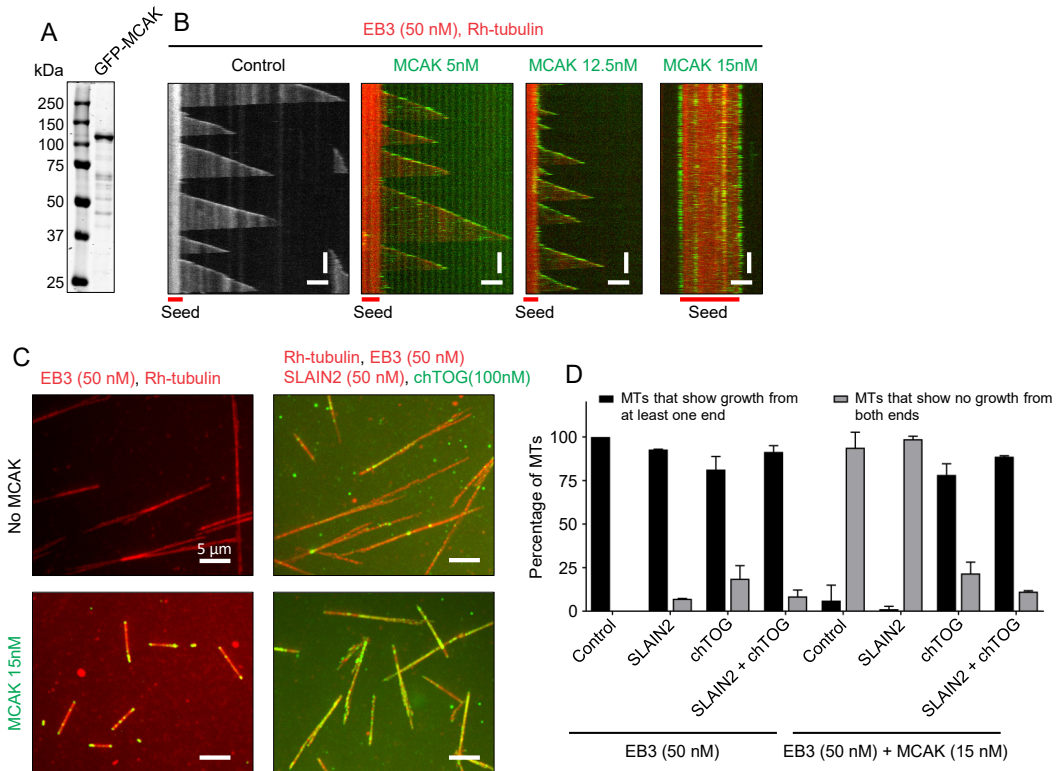


Figure 3. chTOG antagonizes microtubule growth-blocking activity of MCAK.

(A) Coomassie blue stained gel showing GFP-MCAK purified from HEK293T cells.

(B) Representative kymographs showing microtubule plus end dynamics in the presence of rhodamine tubulin with 50 nM mCherry-EB3 alone or together with 5 nM, 12.5 nM and 15 nM GFP-MCAK. Scale bars: 3 μ m (horizontal) and 60 s (vertical).

(C) Micrographs showing maximum intensity projections of microtubules grown from rhodamine labeled seeds (bright red) in the presence of rhodamine tubulin alone or with 50 nM mCherry-EB3, 50 nM mCherry-SLAIN2 and 100 nM chTOG-GFP together with (lower panel) or without (upper panel) 15 nM GFP-MCAK. Scale bar: 5 μ m (horizontal)

(D) Plot showing the percentage of GMPCPP seeds showing no microtubule outgrowth or outgrowth from at least one end in the presence of rhodamine tubulin with 50 nM mCherry-EB3, 50 nM mCherry-SLAIN2 and 50 nM GFP-EB3, 50 nM mCherry-EB3 and 100 nM chTOG-GFP, or 50 nM mCherry-EB3, 50 nM mCherry-SLAIN2 and 100 nM chTOG-GFP with or without 15 nM GFP-MCAK. Number of microtubules (n) analysed from 2 experiments without MCAK, $n=153, 98, 95$ and 104 , and for experiments with MCAK $n=163, 87, 102$ and 89 for microtubules grown in the presence of EB3 alone or combined with SLAIN2 or chTOG or both SLAIN2 and chTOG, respectively, at the above mentioned concentrations.

module in the presence of the microtubule depolymerase MCAK. We tested increasing concentrations of GFP-MCAK (Figure 3A) in the presence of 50 nM mCherry-EB3 and found that at 15 nM it accumulates at the ends of GMPCPP seeds and blocks their growth [Figure 3B, C (left, top and bottom panels)]. We next tested the ability of SLAIN2, chTOG or both to promote microtubule growth under these conditions. We found that in the presence of 50 nM mCherry-EB3 and 15 nM MCAK, 94% of the microtubules did not

show growth from any end and 6% showed growth from at least one end (Figure 3D). In the presence of SLAIN2, only 1% of the microtubules showed growth from at least one end whereas in the presence of chTOG, this percentage was increased to 78% (Figure 3D, Figure 4A). The combination of SLAIN2 and chTOG in the assay restored microtubule growth further, as 86% of the microtubules showed growth (Figure 3D). The observation

Figure 4

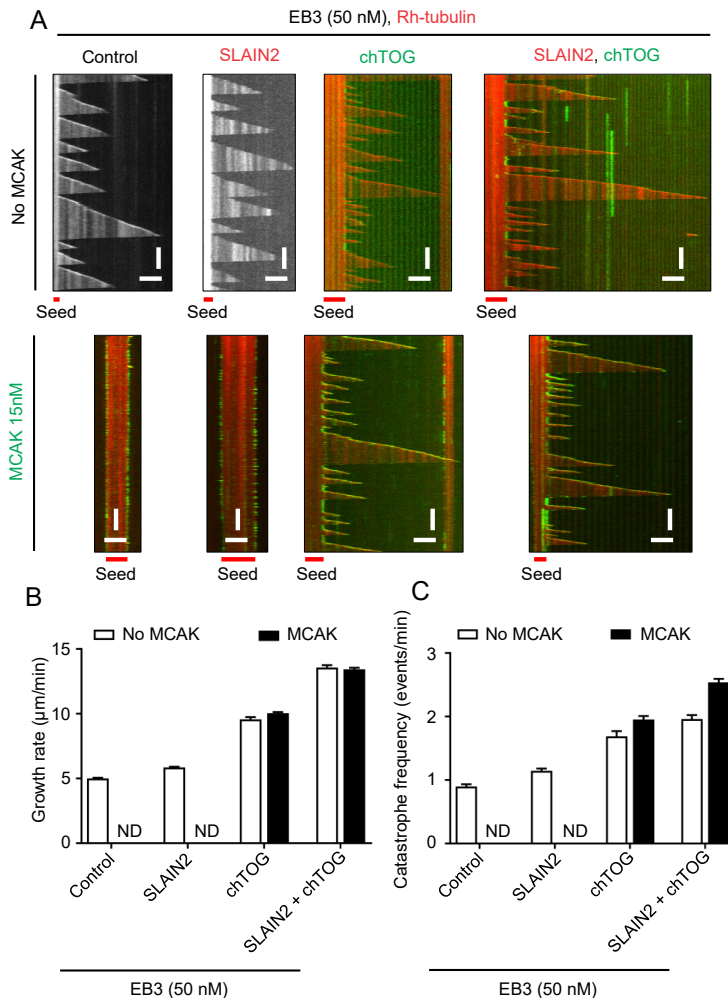


Figure 4. SLAIN2-chTOG do not suppress MCAK induced catastrophes in vitro.

(A) Representative kymographs showing microtubule plus end dynamics in the presence of rhodamine tubulin with 50 nM mCherry-EB3, 50 nM mCherry-SLAIN2 and 50 nM GFP-EB3, 50 nM mCherry-EB3 and 100 nM chTOG-GFP, or 50 nM mCherry-EB3, 50 nM mCherry-SLAIN2 and 100 nM chTOG-GFP with or without 15 nM GFP-MCAK. Scale bars: 3 μm (horizontal) and 90 s (vertical).

(B, C) Microtubule growth rate and catastrophe frequency for microtubules grown in the presence of rhodamine-tubulin together with 50 nM mCherry-EB3, 50 nM mCherry-SLAIN2 and 50 nM GFP-EB3, 50 nM mCherry-EB3 and 100 nM chTOG-GFP, or 50 nM mCherry-EB3, 50 nM mCherry-SLAIN2 and 100 nM chTOG-GFP combined with or without 15 nM GFP-MCAK. Number of growth events analyzed:

n=329 for 50 nM mCherry-EB3, n=361 for 50 nM GFP-EB3 and 50 nM mCherry-SLAIN2, n=172 for 50 nM mCherry-EB3 and 100 nM chTOG-GFP and n=367 for 50 nM mCherry-EB3, 100 nM chTOG-GFP and 50 nM mCherry-SLAIN2. For experiments with 15 nM GFP-MCAK, n=493 for EB3 and chTOG and n=724 for EB3, SLAIN2 and chTOG. Data are from 2 experiments. Error bars represent SEM. ND, not determined because no microtubule growth was observed.

that chTOG alone or combined with SLAIN2 can restore growth whereas SLAIN2 alone cannot, further suggests that SLAIN2 enhances the effect of chTOG at the plus end.

We next measured the parameters of microtubule dynamics in conditions when we did observe microtubule growth. We note that microtubule growth rate observed in these experiments was lower than that shown in Figure 1C even though 100 nM chTOG was present, because we used a lower concentration of EB3 (50 nM instead of 100 nM, Figure 4B). In these conditions, the addition of SLAIN2 together with chTOG increased microtubule growth rate and catastrophe frequency compared to chTOG alone (Figure 4B). When MCAK was also included in the assay, it had no effect on microtubule growth rate in the presence of chTOG alone or together with SLAIN2 (Figure 4B). The catastrophe frequency in the presence of MCAK increased both with chTOG alone and when SLAIN2 and chTOG were added together, suggesting that chTOG and SLAIN2 cannot suppress MCAK-induced catastrophes (Figure 4C).

4

Discussion

In the past few decades, multiple microtubule associated proteins have been identified and characterized for their effects on microtubule dynamics both in vivo and in vitro. There has been a significant progress made in terms of understanding of the mechanisms underlying the activity of individual components. But there is still a gap in correlating protein activities seen in vitro with the effects observed in cells. This could be partly due to the fact that proteins often act through their binding partners or function in a different way in the context of the crowded cellular environment. In depletion experiments in cells, removal of a protein from the complex not only takes away its activity but also perturbs the network and dynamics of its binding partners. An important next step will be to develop a systems level understanding of the interplay, allosteric effects and competition between different regulatory factors at the microtubule plus end. Gaining such an understanding will require complex multicomponent reconstitutions, as illustrated by a recent study, which has provided an example of the plus end interacting protein network that ensures robust recruitment of the minus-end directed motor dynein (Duellberg et al., 2014).

In the majority of in vitro reconstitution studies of microtubule dynamics, microtubule growth rates are an order of magnitude lower than the ones observed in cells. This has been attributed to the absence of a microtubule polymerase in the assay. In this report, we explored the effects of the mammalian microtubule polymerase chTOG on microtubule growth. We showed that chTOG together with EB3 can lead to microtubule polymerization rates comparable to the ones observed in vivo, supporting previous observations with the frog XMAP215 (Zanic et al., 2013). Catastrophe frequency was also increased, in line with

published data on XMAP215 (Zanic et al., 2013), and the effects on both microtubule growth parameters saturated at 100 nM chTOG and 100 nM EB3.

We next tested the effect of the adaptor protein SLAIN2 and found that on its own it did not alter the catastrophe frequency and mildly increased the growth rate, possibly due to the presence of co-purified endogenous chTOG or through an autonomous effect, similar to fly sentin (Li et al., 2012). When combined with EB3 and an intermediate chTOG concentration, SLAIN2 increased microtubule growth rate and also the catastrophe frequency. SLAIN2-induced increase in the growth rate in the presence of chTOG could be attributed to increased recruitment of chTOG to the plus end (Figure 2E), increased residence time of chTOG at the tip, or a combination of both. It would be interesting to test in future if the addition of SLAIN2 further increases microtubule growth rate at EB and chTOG concentrations where the effect of chTOG gets saturated (Figure 1C). It would also be interesting to test if SLAIN2 ensures plus end tracking of its binding partners chTOG, CLIP-170 and CLASP in the presence of an excess of other plus end-associated proteins, and in particular, EB ligands, such as an SxIP peptide.

Next, we revisited the classic reconstitution experiments, which showed that XMAP215 can restore microtubule growth from centrosomes countering the activity of XKCM1, the *Xenopus* MCAK homolog (Kinoshita et al., 2001; Tournebize et al., 2000). Using single microtubules grown from GMPCPP seeds, we found that fast polymerization promoted by chTOG alone or together with SLAIN2 antagonized the microtubule outgrowth-blocking activity of MCAK. However, chTOG either alone or together with SLAIN2 did not prevent MCAK from inducing catastrophes. Previous work showed that the probability that a microtubule undergoes a catastrophe depends on microtubule “age”, the time spent after initiation of microtubule growth (Gardner et al., 2011). MCAK was shown to abolish the aging process, making catastrophe occurrence random (Gardner et al., 2011). It would be interesting to know how age-induced microtubule catastrophes are affected by the presence of chTOG and SLAIN2, with and without MCAK.

Our experiments conclusively showed that in a system with purified components, SLAIN2 on its own or together with chTOG did not suppress spontaneous or MCAK-induced catastrophes, even in conditions when microtubule growth rate became as fast as that observed cells. This is in contrast to experiments in cells, where SLAIN2 or chTOG depletion leads to strongly perturbed microtubule growth with increased catastrophe frequency and reduced growth rate, although this reduction is not dramatic, and instantaneous polymerization rate during short growth events is quite normal (van der Vaart et al., 2011). The reduction of microtubule growth velocity in SLAIN2 and chTOG-depleted cells can be explained by the loss of chTOG from microtubule tips. The effect on catastrophe frequency in cells is more difficult to understand, given that SLAIN2 and chTOG promote catastrophes *in vitro*. Most likely, the absence of robust plus end localization of chTOG upon SLAIN2 depletion results in an altered microtubule tip structure and possibly a smaller GTP-cap, which would be more susceptible to the physical

barrier- or depolymerase-induced catastrophes in cells. In connection with this, it will be interesting to compare the lengths of EB-positive comets in cells and in vitro at the same microtubule growth rate. In cells, the robustness of microtubule growth appears to depend on long GTP caps (reflected by extended, 1-2 μm long EB-positive comets) (Seetapun et al., 2012). Such a comparison will help to determine whether our reconstitutions are missing specific cellular factors which confer robustness to the microtubule polymerization process in cooperation with SLAIN2 and chTOG. Relevant in this respect, SLAIN2 can recruit to microtubule tips other proteins, such as CLASP and CLIP-170, which are known to have stabilizing effects on the plus end (Al-Bassam et al., 2010; Arnal et al., 2004; Komarova et al., 2002; van der Vaart et al., 2011). Taken together, we think that resolving the controversies between the effects that the different regulators have on microtubule growth in cells and in vitro will be a productive way of gaining deeper understanding of the mechanisms governing microtubule dynamics.

Experimental Procedures

DNA constructs, cell lines and cell culture

4 chTOG and SLAIN2 proteins expressed in mammalian cells were made in modified pEGFP-N1 or pEGFP-C1/ pmCherry-C1 vectors respectively with a StrepII tag. chTOG construct was a gift of S. Royle (University of Warwick, UK). HEK 293T cells were cultured in DMEM/F10 (1:1 ratio, Lonza, Basel, Switzerland) supplemented with 10% FCS.

Protein purification from HEK293T cells for in vitro reconstitution assays

chTOG-GFP, GFP-SLAIN2, mCherry-SLAIN2 and GFP-MCAK used in the in vitro reconstitutions assays were purified from HEK293T cells using the Strep(II)-streptactin affinity purification. Cells were harvested 2 days after transfection. Cells from a 15 cm dish were lysed in 500 μl of lysis buffer (50 mM HEPES, 300 mM NaCl and 0.5% Triton X-100, pH 7.4) supplemented with protease inhibitors (Roche) on ice for 15 minutes. The supernatant obtained from the cell lysate after centrifugation at 21,000 x g for 20 minutes was incubated with 40 μl of StrepTactin Sepharose beads (GE) for 45 minutes. The beads were washed 3 times in the lysis buffer without the protease inhibitors. The protein was eluted with 40 μl of elution buffer (50 mM HEPES, 150 mM NaCl, 1 mM MgCl_2 , 1 mM EGTA, 1 mM dithiothreitol (DTT), 2.5 mM d-Desthiobiotin and 0.05% Triton X-100, pH 7.4). Purified proteins were snap-frozen and stored at -80°C .

In vitro microtubule dynamics assays

Reconstitution of microtubule growth dynamics in vitro was performed as described previously. GMPCPP-stabilized microtubule seeds (70% unlabeled tubulin, 18% biotin tubulin and 12% of rhodamine-tubulin) were prepared as described before. Flow chambers, assembled from plasma-cleaned glass coverslips and microscopic slides were functionalized by sequential incubation with 0.2 mg/ml PLL-PEG-biotin (Susos AG,

Switzerland) and 1 mg/ml NeutrAvidin (Invitrogen) in MRB80 buffer (80 mM piperazine-N,N[prime]-bis(2-ethanesulfonic acid), pH 6.8, supplemented with 4 mM MgCl₂, and 1 mM EGTA. Microtubule seeds were attached to the coverslip through biotin-NeutrAvidin interactions. Flow chambers were further blocked with 1 mg/ml κ -casein. The reaction mixture with or without proteins (MRB80 buffer supplemented with 15 μ M porcine brain tubulin, 0.5 μ M rhodamine-tubulin, 50 mM KCl, 1 mM guanosine triphosphate, 0.2 mg/ml κ -casein, 0.1% methylcellulose, and oxygen scavenger mix [50 mM glucose, 400 μ g/ml glucose oxidase, 200 μ g/ml catalase, and 4 mM DTT]) was added to the flow chamber after centrifugation in an Airfuge for 5 minutes at $119,000 \times g$. The assays with MCAK were supplemented with 1 mM ATP. For experiments in the presence of EB3, concentration of mCherry-EB3 or GFP-EB3 was as indicated in the figures and rhodamine-tubulin was excluded from the assay. The flow chamber was sealed with vacuum grease, and dynamic microtubules were imaged immediately at 30 °C using TIRF microscopy. All tubulin products were from Cytoskeleton Inc.

TIRF microscopy

In vitro reconstitution assays were imaged on a TIRF microscope setup as described previously or on an Ilas2 TIRF setup. In brief, we used an inverted research microscope Nikon Eclipse Ti-E (Nikon) with the perfect focus system (Nikon), equipped with Nikon CFI Apo TIRF 100x 1.49 N.A. oil objective (Nikon) and controlled with MetaMorph 7.7.5 software (Molecular Devices). The microscope was equipped with TIRF-E motorized TIRF illuminator modified by Roper Scientific France/PICT-IBiSA, Institut Curie. To keep the in vitro samples at 30 °C, a stage top incubator model INUBG2E-ZILCS (Tokai Hit) was used. For excitation, 491 nm 100 mW Calypso (Cobolt) and 561 nm 100 mW Jive (Cobolt) lasers were used. We used ET-GFP 49002 filter set (Chroma) for imaging of proteins tagged with GFP or ET-mCherry 49008 filter set (Chroma) for imaging of proteins tagged with mCherry. Fluorescence was detected using an EMCCD Evolve 512 camera (Roper Scientific) with the intermediate lens 2.5X (Nikon C mount adapter 2.5X) or using the CoolSNAP HQ2 CCD camera (Roper Scientific) without an additional lens. In both cases the final magnification was 0.063 μ m/pixel.

Ilas2 system (Roper Scientific, Evry, FRANCE) is a dual laser illuminator for azimuthal spinning TIRF (or Hilo) illumination and with a custom modification for targeted photomanipulation. This system was installed on Nikon Ti microscope (with the perfect focus system, Nikon), equipped with 150 mW 488 nm laser and 100 mW 561 nm laser, 49002 and 49008 Chroma filter sets, EMCCD Evolve mono FW DELTA 512x512 camera (Roper Scientific) with the intermediate lens 2.5X (Nikon C mount adapter 2.5X), CCD camera CoolSNAP MYO M-USB-14-AC (Roper Scientific) and controlled with MetaMorph 7.8.8 software (Molecular Device). To keep the in vitro samples at 30°C, a stage top incubator model INUBG2E-ZILCS (Tokai Hit) was used. The final resolution using EMCCD camera was 0.065 μ m/pixel, using CCD camera it was 0.045 μ m/pixel.

Both microscopes were equipped with an ILas system (Roper Scientific France/ PICT-IBiSA) for FRAP and photoablation. The 532 nm Q-switched pulsed laser (Teem Photonics) was used for photoablation on the TIRF microscope.

Analysis of microtubule plus end dynamics in vitro

Kymographs were generated using the ImageJ plugin KymoResliceWide (<http://fiji.sc/KymoResliceWide>). Microtubule dynamics parameters were determined from kymographs using an optimized version of the custom made JAVA plug in for ImageJ as described previously. The relative standard error for catastrophe frequency was calculated as described previously (Mohan et al., 2013).

Acknowledgements

We thank S. Royle for the gift of ch-TOG construct. This work was supported by the European Research Council Synergy grant 609822 to A.Ak.

References

- Akhmanova, A., and M.O. Steinmetz. 2008. Tracking the ends: a dynamic protein network controls the fate of microtubule tips. *Nat Rev Mol Cell Biol.* 9:309-322.
- Akhmanova, A., and M.O. Steinmetz. 2015. Control of microtubule organization and dynamics: two ends in the limelight. *Nat Rev Mol Cell Biol.* 16:711-726.
- Al-Bassam, J., H. Kim, G. Brouhard, A. van Oijen, S.C. Harrison, and F. Chang. 2010. CLASP promotes microtubule rescue by recruiting tubulin dimers to the microtubule. *Dev Cell.* 19:245-258.
- Al-Bassam, J., H. Kim, I. Flor-Parra, N. Lal, H. Velji, and F. Chang. 2012. Fission yeast Alp14 is a dose-dependent plus end-tracking microtubule polymerase. *Mol Biol Cell.* 23:2878-2890.
- Arnal, I., C. Heichette, G.S. Diamantopoulos, and D. Chretien. 2004. CLIP-170/tubulin-curved oligomers coassemble at microtubule ends and promote rescues. *Curr Biol.* 14:2086-2095.
- Ayaz, P., S. Munyoki, E.A. Geyer, F.A. Piedra, E.S. Vu, R. Bromberg, Z. Otwinowski, N.V. Grishin, C.A. Brautigam, and L.M. Rice. 2014. A tethered delivery mechanism explains the catalytic action of a microtubule polymerase. *Elife.* 3:e03069.
- Ayaz, P., X. Ye, P. Huddleston, C.A. Brautigam, and L.M. Rice. 2012. A TOG:alpha-tubulin complex structure reveals conformation-based mechanisms for a microtubule polymerase. *Science.* 337:857-860.
- Bieling, P., L. Laan, H. Schek, E.L. Munteanu, L. Sandblad, M. Dogterom, D. Brunner, and T. Surrey. 2007. Reconstitution of a microtubule plus-end tracking system in vitro. *Nature.* 450:1100-1105.
- Bonfils, C., N. Bec, B. Lacroix, M.C. Harricane, and C. Larroque. 2007. Kinetic analysis of tubulin assembly in the presence of the microtubule-associated protein TOGp. *J Biol Chem.* 282:5570-5581.
- Booth, D.G., F.E. Hood, I.A. Prior, and S.J. Royle. 2011. A TACC3/ch-TOG/clathrin complex stabilises kinetochore fibres by inter-microtubule bridging. *EMBO J.* 30:906-919.
- Bouchet, B.P., I. Noordstra, M. van Amersfoort, E.A. Katrukha, Y.C. Ammon, N.D. Ter Hoeve, L. Hodgson, M. Dogterom, P.W. Derksen, and A. Akhmanova. 2016. Mesenchymal Cell Invasion Requires Cooperative Regulation of Persistent Microtubule Growth by SLAIN2 and CLASP1. *Dev Cell.* 39:708-723.
- Brouhard, G.J., J.H. Stear, T.L. Noetzel, J. Al-Bassam, K. Kinoshita, S.C. Harrison, J. Howard, and A.A. Hyman. 2008. XMAP215 is a processive microtubule polymerase. *Cell.* 132:79-88.
- Cullen, C.F., P. Deak, D.M. Glover, and H. Ohkura. 1999. mini spindles: A gene encoding a conserved microtubule-associated protein required for the integrity of the mitotic spindle in *Drosophila*. *J Cell Biol.* 146:1005-1018.
- Doodhi, H., A.E. Prota, R. Rodriguez-Garcia, H. Xiao, D.W. Custar, K. Bargsten, E.A. Katrukha, M. Hilbert, S. Hua, K. Jiang, I. Grigoriev, C.P. Yang, D. Cox, S.B. Horwitz, L.C. Kapitein,

- A. Akhmanova, and M.O. Steinmetz. 2016. Termination of Protofilament Elongation by Eribulin Induces Lattice Defects that Promote Microtubule Catastrophes. *Curr Biol.* 26:1713-1721.
- Duellberg, C., M. Trokter, R. Jha, I. Sen, M.O. Steinmetz, and T. Surrey. 2014. Reconstitution of a hierarchical +TIP interaction network controlling microtubule end tracking of dynein. *Nat Cell Biol.* 16:804-811.
- Gardner, M.K., M. Zanic, C. Gell, V. Bormuth, and J. Howard. 2011. Depolymerizing kinesins Kip3 and MCAK shape cellular microtubule architecture by differential control of catastrophe. *Cell.* 147:1092-1103.
- Kinoshita, K., I. Arnal, A. Desai, D.N. Drechsel, and A.A. Hyman. 2001. Reconstitution of physiological microtubule dynamics using purified components. *Science.* 294:1340-1343.
- Komarova, Y., C.O. De Groot, I. Grigoriev, S.M. Gouveia, E.L. Munteanu, J.M. Schober, S. Honnappa, R.M. Buey, C.C. Hoogenraad, M. Dogterom, G.G. Borisy, M.O. Steinmetz, and A. Akhmanova. 2009. Mammalian end binding proteins control persistent microtubule growth. *J Cell Biol.* 184:691-706.
- Komarova, Y.A., A.S. Akhmanova, S. Kojima, N. Galjart, and G.G. Borisy. 2002. Cytoplasmic linker proteins promote microtubule rescue in vivo. *J Cell Biol.* 159:589-599.
- Li, W., T. Miki, T. Watanabe, M. Kakeno, I. Sugiyama, K. Kaibuchi, and G. Goshima. 2011. EB1 promotes microtubule dynamics by recruiting Sentin in *Drosophila* cells. *J Cell Biol.* 193:973-983.
- Li, W., T. Moriwaki, T. Tani, T. Watanabe, K. Kaibuchi, and G. Goshima. 2012. Reconstitution of dynamic microtubules with *Drosophila* XMAP215, EB1, and Sentin. *J Cell Biol.* 199:849-862.
- Matsuo, Y., S.P. Maurer, M. Yukawa, S. Zakian, M.R. Singleton, T. Surrey, and T. Toda. 2016. An unconventional interaction between Dis1/TOG and Mal3/EB1 in fission yeast promotes the fidelity of chromosome segregation. *J Cell Sci.* 129:4592-4606.
- Maurer, S.P., N.I. Cade, G. Bohner, N. Gustafsson, E. Boutant, and T. Surrey. 2014. EB1 accelerates two conformational transitions important for microtubule maturation and dynamics. *Curr Biol.* 24:372-384.
- Maurer, S.P., F.J. Fourniol, G. Bohner, C.A. Moores, and T. Surrey. 2012. EBs recognize a nucleotide-dependent structural cap at growing microtubule ends. *Cell.* 149:371-382.
- Mitchison, T., and M. Kirschner. 1984. Dynamic instability of microtubule growth. *Nature.* 312:237-242.
- Mohan, R., E.A. Katrukha, H. Doodhi, I. Smal, E. Meijering, L.C. Kapitein, M.O. Steinmetz, and A. Akhmanova. 2013. End-binding proteins sensitize microtubules to the action of microtubule-targeting agents. *Proc Natl Acad Sci U S A.* 110:8900-8905.
- Roostalu, J., N.I. Cade, and T. Surrey. 2015. Complementary activities of TPX2 and chTOG constitute an efficient importin-regulated microtubule nucleation module. *Nat Cell Biol.* 17:1422-1434.
- Royle, S.J. 2013. Protein adaptation: mitotic functions for membrane trafficking proteins. *Nat Rev Mol Cell Biol.* 14:592-599.
- Seetapun, D., B.T. Castle, A.J. McIntyre, P.T. Tran, and D.J. Odde. 2012. Estimating the microtubule GTP cap size in vivo. *Curr Biol.* 22:1681-1687.
- Sharma, A., A. Aher, N.J. Dynein, D. Frey, E.A. Katrukha, R. Jaussi, I. Grigoriev, M. Croisier, R.A. Kammerer, A. Akhmanova, P. Gonczy, and M.O. Steinmetz. 2016. Centriolar CPAP/SAS-4 Imparts Slow Processive Microtubule Growth. *Developmental cell.* 37:362-376.
- Tournebize, R., A. Popov, K. Kinoshita, A.J. Ashford, S. Rybina, A. Pozniakovsky, T.U. Mayer, C.E. Walczak, E. Karsenti, and A.A. Hyman. 2000. Control of microtubule dynamics by the antagonistic activities of XMAP215 and XKCM1 in *Xenopus* egg extracts. *Nat Cell Biol.* 2:13-19.
- van der Vaart, B., M.A. Franker, M. Kuijpers, S. Hua, B.P. Bouchet, K. Jiang, I. Grigoriev, C.C. Hoogenraad, and A. Akhmanova. 2012. Microtubule plus-end tracking proteins SLAIN1/2 and ch-TOG promote axonal development. *J Neurosci.* 32:14722-14728.
- van der Vaart, B., C. Manatschal, I. Grigoriev, V. Olieric, S.M. Gouveia, S. Bjelic, J. Demmers, I. Vorobjev, C.C. Hoogenraad, M.O. Steinmetz, and A. Akhmanova. 2011. SLAIN2 links microtubule plus end-tracking proteins and controls microtubule growth in interphase. *J Cell Biol.* 193:1083-1099.

- Wang, P.J., and T.C. Huffaker. 1997. Stu2p: A microtubule-binding protein that is an essential component of the yeast spindle pole body. *J Cell Biol.* 139:1271-1280.
- Widlund, P.O., J.H. Stear, A. Pozniakovsky, M. Zanic, S. Reber, G.J. Brouhard, A.A. Hyman, and J. Howard. 2011. XMAP215 polymerase activity is built by combining multiple tubulin-binding TOG domains and a basic lattice-binding region. *Proc Natl Acad Sci U S A.* 108:2741-2746.
- Zanic, M., P.O. Widlund, A.A. Hyman, and J. Howard. 2013. Synergy between XMAP215 and EB1 increases microtubule growth rates to physiological levels. *Nat Cell Biol.* 15:688-693.
- Zhang, R., G.M. Alushin, A. Brown, and E. Nogales. 2015. Mechanistic Origin of Microtubule Dynamic Instability and Its Modulation by EB Proteins. *Cell.* 162:849-859.

5

Centriolar CPAP/SAS-4 imparts slow processive microtubule growth

Ashwani Sharma^{1#}, Amol Aher^{2#}, Nicola J. Dynes^{3#}, Daniel Frey¹, Eugene A. Katrukha², Rolf Jaussi¹, Ilya Grigoriev², Marie Croisier⁴, Richard A. Kammerer¹, Anna Akhmanova^{2*}, Pierre Gönczy^{3*}, and Michel O. Steinmetz^{1*}

¹Laboratory of Biomolecular Research, Department of Biology and Chemistry, Paul Scherrer Institut, Villigen PSI, Switzerland

²Cell Biology, Faculty of Science, Utrecht University, Utrecht, the Netherlands

³Swiss Institute for Experimental Cancer Research (ISREC), School of Life Sciences, Swiss Federal Institute of Technology (EPFL), Lausanne, Switzerland

⁴Bio-EM Facility, School of Life Sciences, Swiss Federal Institute of Technology (EPFL), Lausanne, Switzerland

#These authors contributed equally to the work

*Corresponding authors: a.akhmanova@uu.nl, pierre.gonczy@epfl.ch, michel.steinmetz@psi.ch

Abstract

Centrioles are fundamental and evolutionarily conserved microtubule-based organelles whose assembly is characterized by microtubule growth rates that are orders of magnitude slower than those of cytoplasmic microtubules. Several centriolar proteins can interact with tubulin or microtubules, but how they ensure the exceptionally slow growth of centriolar microtubules has remained mysterious. Here, we bring together crystallographic, biophysical and reconstitution assays to demonstrate that the human centriolar protein CPAP (SAS-4 in worms and flies) binds and “caps” microtubule plus-ends by associating with a site of β -tubulin engaged in longitudinal tubulin-tubulin interactions. Strikingly, we uncover that CPAP activity dampens microtubule growth and stabilizes microtubules by inhibiting catastrophes and promoting rescues. We further establish that the capping function of CPAP is important to limit growth of centriolar microtubules in cells. Our results suggest that CPAP acts as a molecular lid that ensures slow assembly of centriolar microtubules and, thereby, contributes to organelle length control.

Introduction

Centrioles are evolutionarily conserved organelles that are pivotal for the formation of cilia, flagella and centrosomes, and are thus critical for fundamental cellular processes such as signaling, polarity, motility and division (reviewed in (Azimzadeh and Marshall, 2010; Bornens, 2012; Jana et al., 2014; Gönczy, 2012)). Owing to their central role in such diverse cellular processes, centriole aberrations contribute to a range of severe human diseases, including ciliopathies, primary microcephaly and cancer (reviewed in (Nigg and Raff, 2009; Gönczy, 2015)). Microtubules are the major constituent of centrioles and are arranged in a radial nine-fold symmetrical array that forms a barrel-shaped centriolar wall (reviewed in (Azimzadeh and Marshall, 2010; Bornens, 2012; Jana et al., 2014; Gönczy, 2012)). Centriolar microtubules are unique in exhibiting exceptionally slow growth rates of a few tens of nanometers per hour and being very stable after their formation (Kuriyama and Borisy, 1981; Chretien et al., 1997). Such properties likely contribute to setting centriole length, which is extremely conserved across evolution. The behavior of centriolar microtubules is in stark contrast to that of their cytoplasmic counterparts, which assemble up to four orders of magnitude faster and are highly dynamic (Kinoshita et al., 2001). The molecular mechanisms that impart the exceptional slow growth rate and stability of centriolar microtubules are not known.

Several centriolar proteins that can directly interact with tubulin and/or microtubules have been identified, including CEP120, CEP135, Centrobin and CPAP (Gudi et al., 2011; Lin et al., 2013a; Lin et al., 2013b; Hsu et al., 2008). CPAP (SAS-4 in worms and flies) is of particular interest, since it is the only component amongst the ones listed above that is present and essential for centriole formation from worm to man (Kohlmaier et al., 2009; Schmidt et al., 2009; Tang et al., 2009; Kirkham et al., 2003; Leidel and Gönczy, 2003). The importance of CPAP is further substantiated by the fact that homozygous mutations in

the corresponding gene lead to autosomal recessive primary microcephaly, a devastating human disease with drastically reduced neuron numbers and thus brain size (Bond et al., 2005). Interestingly, CPAP overexpression induces overly long centrioles in human cells (Kohlmaier et al., 2009; Schmidt et al., 2009; Tang et al., 2009), which interferes with cell division (Kohlmaier et al., 2009; Schmidt et al., 2009; Tang et al., 2009). Together, these observations suggest that CPAP somehow regulates centriolar microtubule growth to produce fully functional centrioles. How this role is exerted at a mechanistic level remains elusive.

CPAP comprises a tubulin-binding domain (PN2-3), a positively charged microtubule-binding domain (MBD), a coiled-coil dimerization domain and a C-terminal G-box (Figure 1A). The PN2-3 domain is of prime interest as this region is highly conserved across evolution and found exclusively in CPAP/SAS-4 proteins. PN2-3 sequesters tubulin dimers and has been shown to destabilize microtubules both in vitro and in cells (Hsu et al., 2008; Cormier et al., 2009; Hung et al., 2004). How this observation can be reconciled with the presence of overly long centrioles upon CPAP overexpression, which is suggestive of the protein enhancing centriolar microtubule elongation, has remained puzzling. Here, to elucidate the fundamental mechanism of action of CPAP/SAS-4 proteins, we set out to decipher how CPAP impacts microtubules using structural, biophysical and cell biological approaches. We first report a high resolution structure of $\alpha\beta$ -tubulin in a complex with the PN2-3 domain of CPAP. This structural information guided the design of experiments aimed at understanding the key role of CPAP in regulating centriolar microtubule behavior. Using reconstitution experiments, we demonstrate that CPAP autonomously recognizes and tracks growing microtubule plus ends. There, CPAP suppresses microtubule polymerization and increases microtubule stability by inhibiting catastrophes and promoting rescues. We further establish that the PN2-3 domain of CPAP is critical in the cellular context to restrict the extent of centriolar microtubule elongation by acting as a molecular ‘cap’.

RESULTS

Crystal structure of the SAC domain of CPAP in a complex with tubulin

To gain insight into the molecular mechanism of tubulin binding by CPAP/SAS-4 proteins, we sought to crystallize the PN2-3 domain of human CPAP in complex with tubulin (see Table S1 for all constructs generated in the course of this study). Extensive crystallization trials with complexes of tubulin and PN2-3 variants were not met with success. However, adding the β -tubulin-binding darpin (D1; (Pecqueur et al., 2012)) allowed us to solve the ternary complex formed between PN2-3, $\alpha\beta$ - tubulin and D1 (denoted the D1-tubulin-PN2-3 complex) to 2.2 Å resolution by X-ray crystallography (Figure 1A-C and Table S2). As reported previously for other structures, the D1 molecule was bound at the tip of β -tubulin in the D1-tubulin-PN2-3 complex structure, a location involved in longitudinal tubulin-tubulin contacts within microtubules (Pecqueur et al.,

by hydrophobic and polar residues of helices α H11', β H3', β H5 and β H12, and loops β H8-S7 and β H11'-H12 (Figure 1C).

The SAC-tubulin interaction is characterized by an extensive water and non-water-mediated hydrogen bonding network, as well as by hydrophobic contacts established between both main chain and side chain atoms of SAC and tubulin residues. Prominent SAC side chain contacts involve Phe375 (β Asp414, β Met416, β Glu417, β Glu420), Leu376 (β His192, β Qln193, β Glu196), Lys377 (β Glu420), Arg378 (β Glu420, β Asn426), and Phe385 (β H406, β Trp407, β Pro263). Pull down experiments had implicated Lys377 and Arg378 in tubulin binding (Hsu et al., 2008), and our findings reveal the structural basis for their importance in this interaction.

Figure 2

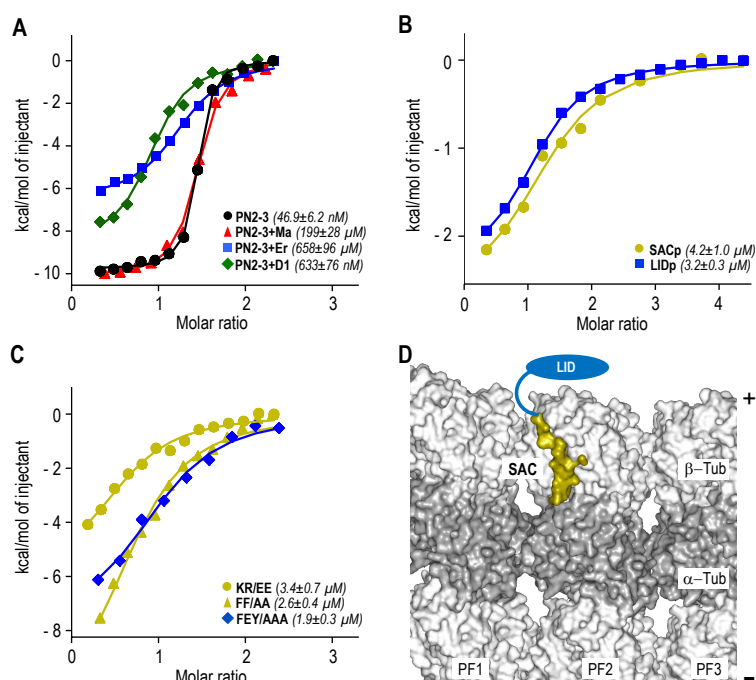


Figure 2. Interactions of PN2-3 with tubulin and microtubules.

(A-C) ITC analysis of interactions between indicated PN2-3 variants and tubulin. D1, DARPin; Er, Eribulin; Ma, Maytansine. Note that Eribulin and Maytansine bind to the vinca- and Maytansine-site on β -tubulin, respectively (Gigant et al., 2005; Prota et al., 2014; Smith et al., 2010).

(D) Binding of SAC (olive surface representation) and LID (schematically represented by a blue oval) in the context of a microtubule plus end, with three protofilaments (PF1-PF3) being represented. Light gray surface representation, β -tubulin; dark gray surface representation, α -tubulin. The plus- (+) and minus (-) ends of the microtubule are indicated on the right.

See also Figure S1 and Table S1.

Atomic model of the interaction of tubulin and PN2-3

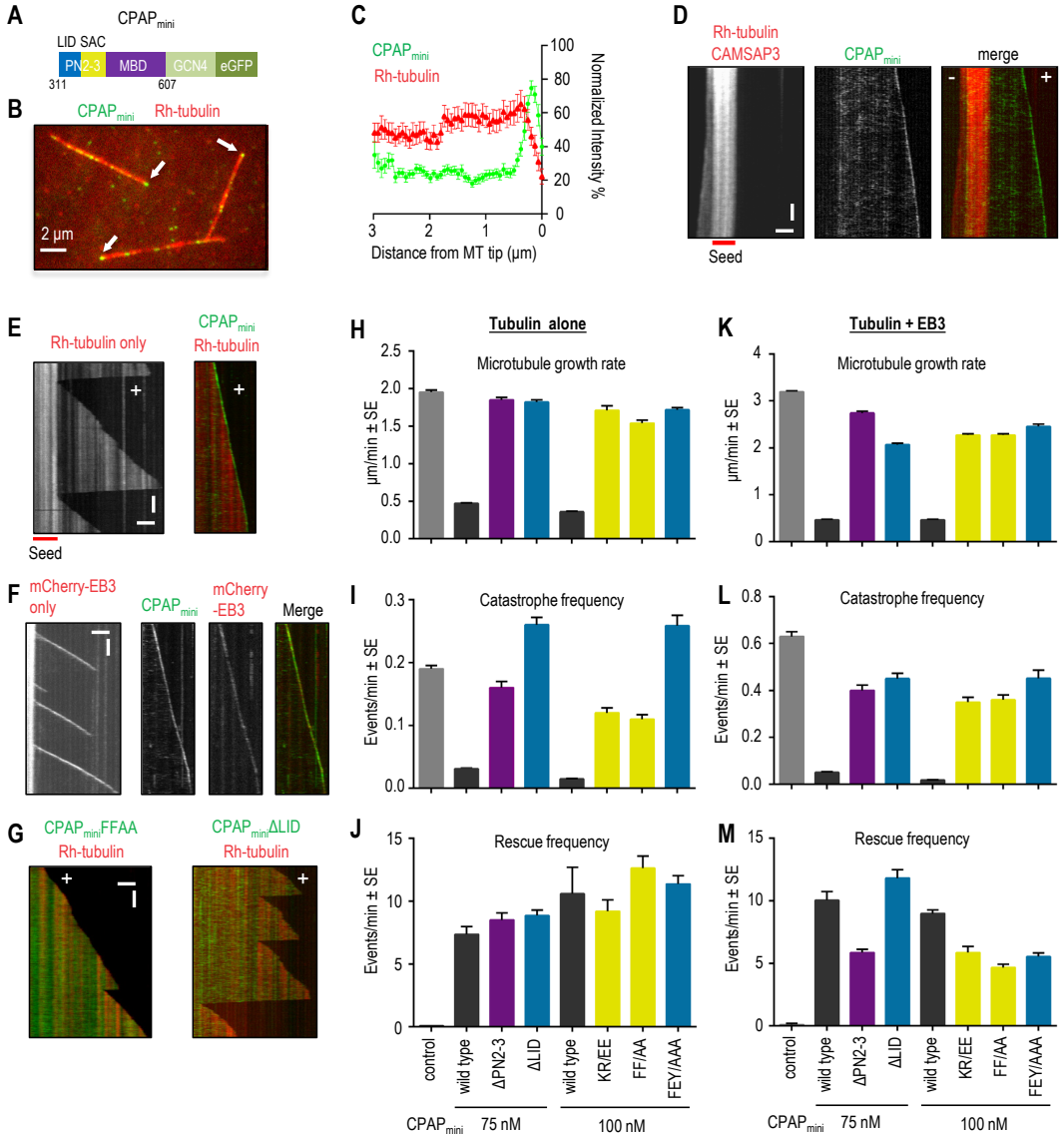
Previous studies suggested that PN2-3 inhibits exchange of the nucleotide on β -tubulin and that residues situated N-terminal to SAC also interact with tubulin (Cormier et al., 2009; Hsu et al., 2008; Hung et al., 2004). The PN2-3-tubulin-D1 structure revealed that

the N-terminus of SAC is located close to the D1-binding site at the tip of β -tubulin (Figure 1D). We therefore reasoned that the presence of D1 might hinder access of this region of CPAP to its binding site. Accordingly, isothermal titration calorimetry (ITC) experiments demonstrated that whereas PN2-3 bound tubulin with an equilibrium dissociation constant, K_d , of 47 ± 6 nM, the affinity of PN2-3 for tubulin-D1 dropped one order of magnitude (Figure 2A). Likewise, Eribulin and Maytansine, two drugs that bind near the D1- and nucleotide-binding site, and which also inhibit longitudinal tubulin-tubulin contacts in microtubules (Pecqueur et al., 2012; Prota et al., 2014; Alday and Correia, 2009), significantly impaired the affinity of PN2-3 for tubulin (Figure 2A). We conclude that the N-terminal part of PN2-3 binds to a site on the tip of β -tubulin engaged in longitudinal tubulin-tubulin interactions (Cormier et al., 2009), and therefore named this putative domain “LID”. To test whether the hydrolysis state of the exchangeable nucleotide bound to β -tubulin is important for tubulin-PN2-3 complex formation, as previously suggested for PN2-3 of *Drosophila* DmSAS-4 (Gopalakrishnan et al., 2012), we performed additional ITC experiments. As shown in Figure S1, we found similar K_d values for the interaction between human CPAP PN2-3 and GDP-, GTP-, or GMPCPP-tubulin (maximal difference of 1.3-fold). We conclude that the hydrolysis state of the nucleotide bound to β -tubulin has at most a minor effect on tubulin-PN2-3 complex formation.

To assess whether SAC and LID can bind tubulin independently, we generated two corresponding peptides, SACp and LIDp, and analyzed their tubulin-binding properties by ITC. K_d values in the low micromolar range were obtained for the interactions between tubulin and either SACp or LIDp (Figure 2B). To investigate the importance of selected SAC and LID residues for tubulin binding, we conducted further ITC experiments with mutant variants of the PN2-3 domain. Mutation of the tubulin-interacting SAC residues Lys377 and Arg378 to glutamic acid (KR/EE), or of Phe375 and Phe385 to alanine (FF/AA), reduced the affinity of PN2-3 for tubulin by two orders of magnitude (Figure 2C; compare with wild-type PN2-3 in Figure 2A). We also tested a PN2-3 mutant in which three residues in a conserved region of LID (Phe338, Glu339, Tyr341; Figure 1A) were simultaneously mutated to alanine (FEY/AAA), and also in this case obtained a K_d in the low micromolar range (Figure 2C).

These results suggest that both SAC and LID can bind independently to tubulin with low micromolar affinities, and that they cooperate to give rise to a ~ 100 -fold tighter interaction with tubulin when present together. To test whether SAC and LID could bind in the context of microtubules, we analyzed their interactions using an atomic model of a microtubule based on a cryo-electron microscopy reconstruction at 3.5 Å resolution (Zhang et al., 2015). Interestingly, this analysis showed that both SAC and LID binding interfaces are located on the outer surface, at the distal tip of the microtubule that exposes β -tubulin subunits (Figure 2D). This result indicates that CPAP could specifically target microtubule plus ends via its PN2-3 domain.

Figure 3



5

Figure 3. Effects of CPAP_{mini} on dynamic microtubules.

 (A) Schematic of CPAP_{mini} construct.

 (B) Single frame of a time-lapse movie of rhodamine (Rh)-labeled microtubules growing from rhodamine-GMPCPP-seeds in the presence of CPAP_{mini}. Arrows point to CPAP_{mini} microtubule tip accumulation.

 (C) Normalized mean intensity profiles for CPAP_{mini} and rhodamine-tubulin from 30 microtubules.

 (D) Kymographs of microtubule growth at the plus (+) and minus (-) end from a rhodamine-GMPCPP-seed with 50 nM mCherry-CAMSAP3 and 100 nM CPAP_{mini}. Scale bars, here and in other kymographs of this figure: 2 μm (horizontal) and 60 s (vertical).

 (E) Kymographs of microtubule plus-end (+) dynamics with rhodamine-tubulin alone or together with 100 nM CPAP_{mini}.

 (F) Kymographs of microtubule plus-end (+) dynamics with 20 nM mCherry-EB3 alone or together with 100 nM CPAP_{mini}.

(G) Kymographs of microtubule plus-end (+) dynamics with rhodamine-tubulin and 100 nM of the two indicated CPAP_{mini} variants.

(H-M) Microtubule plus-end growth rates, catastrophe and rescue frequencies in the presence of rhodamine-tubulin alone or together with 20 nM mCherry-EB3 and 100 nM of the indicated CPAP_{mini} variants. ~100-200 microtubule growth events from 2-4 independent experiments were analyzed per condition.

See also Figure S2 and Table S1.

CPAP tracks growing microtubule plus ends in vitro

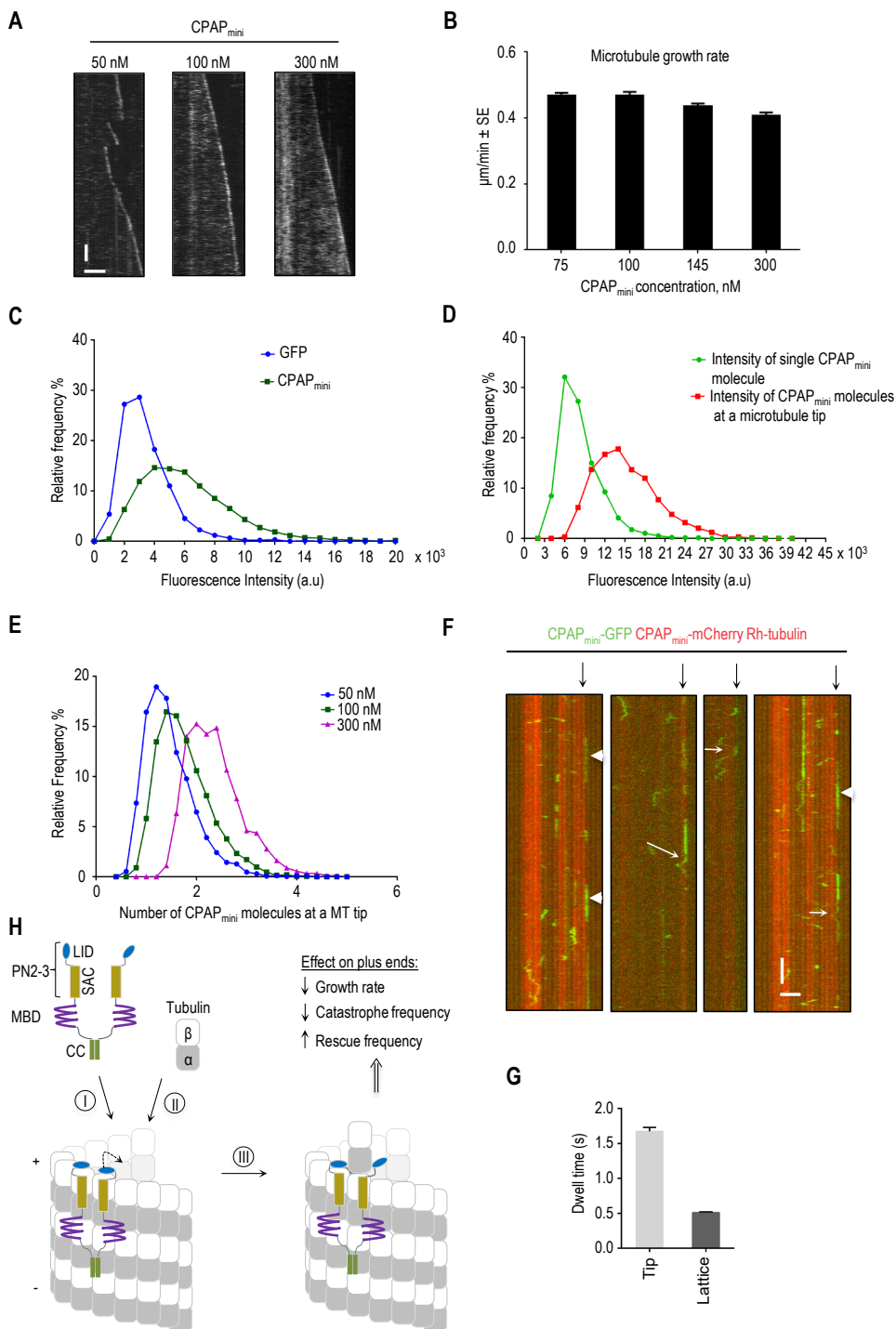
To test the idea that CPAP targets microtubule plus ends, we performed in vitro reconstitution experiments in which dynamic microtubules were grown from GMPCPP-stabilized seeds and imaged using a Total Internal Reflection Fluorescence microscopy-based assay (Bieling et al., 2007; Montenegro Gouveia et al., 2010). Since purified full length CPAP was insoluble in our hands, we engineered a soluble chimeric protein in which the PN2-3-MBD moiety was fused to the leucine zipper domain of the yeast transcriptional activator GCN4 (O'Shea et al., 1991), to mimic the dimerization imparted by the endogenous coiled-coil domain of CPAP (Zhao et al., 2010), which is required for CPAP function in centriole duplication (Kitagawa et al., 2011), as well as to GFP (the resulting protein has been dubbed CPAP_{mini}; Figures 3A and S2A).

We found that CPAP_{mini} bound weakly to the microtubule lattice; importantly, in addition, we found that CPAP_{mini} localized to, and tracked, one end of dynamic microtubules specifically (Figure 3B-E). We determined that CPAP_{mini} bound the plus end of microtubules, distinguished as such because it is negative for the minus-end targeting protein CAMSAP3 (Figure 3D) (Jiang et al., 2014). CPAP_{mini} colocalized at growing microtubule tips with the plus-end tracking protein EB3 (Figure 3F). However, in contrast to EB3, the plus-end accumulation of which critically depends on microtubule growth (Bieling et al., 2007; Montenegro Gouveia et al., 2010), CPAP_{mini} was enriched at one end of GMPCPP-stabilized microtubules even when soluble tubulin was present at a concentration insufficient for microtubule elongation (5 instead of 15 μ M tubulin; Figure S2B). These data reveal that microtubule growth is not required for plus-end recognition by CPAP_{mini}. In the absence of soluble tubulin, CPAP_{mini} localized along the entire length of GMPCPP-stabilized microtubules (data not shown), indicating that the interaction of CPAP_{mini} with soluble tubulin suppresses its binding to the microtubule lattice. Overall, we conclude that CPAP_{mini} is an autonomous microtubule plus-end tracking protein.

CPAP promotes slow and processive microtubule growth

We set out to determine the impact of CPAP_{mini} on microtubule dynamics. Strikingly, we found that CPAP_{mini} strongly reduced the rate of microtubule growth (Figure 3EH). This effect could not be explained by tubulin sequestration, because the concentration of CPAP_{mini} (75-100 nM) was much lower than that of tubulin (15 μ M). Furthermore, CPAP_{mini} dramatically reduced the frequency of catastrophes and promoted rescues, leading to highly processive microtubule polymerization (Figure 3EIJ). This effect was also observed in the presence of EB3, despite the fact that EB3 by itself causes a ~1.5 fold

Figure 4


 Figure 4. Counting of CPAP_{mini} molecules at microtubule plus ends.

(A) Kymographs illustrating growth dynamics of microtubule plus ends in the presence of 20 nM mCherry-

EB3 and indicated concentrations of CPAP_{mini}. Only the CPAP_{mini} channel is shown. Scale bars, 2 μm (horizontal) and 60 s (vertical).

(B) Microtubule growth rates at indicated concentrations of CPAP_{mini} in the presence of 20 nM mCherry-EB3.

(C) Distribution of fluorescence intensities for single molecules of GFP (blue, mean intensity value $3.4 \times 10^3 \pm 1.6 \times 10^3$) and CPAP_{mini} (green, mean intensity value $6.2 \times 10^3 \pm 3.1 \times 10^3$).

(D) Distribution of fluorescence intensity values at microtubule tips for single CPAP_{mini} molecules (green, mean intensity value $=8.3 \times 10^3 \pm 3.2 \times 10^3$) compared to 100 nM CPAP_{mini} (red, mean intensity value $15.2 \times 10^3 \pm 4.7 \times 10^3$).

(E) Distributions of the numbers of CPAP_{mini} molecules on microtubule plus ends at indicated protein concentrations of CPAP_{mini}. At 100 nM, a concentration sufficient to strongly suppress microtubule growth, ~ 2 CPAP_{mini} dimers were bound to microtubule tips (green curve).

(F) Kymographs of dynamic microtubules grown in the presence of 100 nM CPAP_{mini}-mCherry, 5 nM CPAP_{mini}-GFP and rhodamine tubulin, demonstrating CPAP_{mini} single molecule behaviour at the tip and lattice. Plus ends are indicated by black arrows. White arrows point to examples showing both lattice diffusion and tip tracking, while molecules displaying stationary behaviour at the microtubule tips are indicated by arrowheads. Scale bars, 2 μm (horizontal) and 2 s (vertical).

(G) Mean dwell times for CPAP_{mini} on the microtubule lattice (mean time $=0.51 \pm 0.01$, $n=258$) and tip (mean time $=1.67 \pm 0.06$, $n=755$) obtained from the dwell time distributions; reported means were corrected for photobleaching. Error bars represent the error of fit (Supplementary Experimental Procedures).

(H) Working model of how CPAP_{mini} ensures slow processive microtubule growth. CPAP recognizes the microtubule plus-end via tandemly arranged LID, SAC and MBD domains (I). This stabilizes the interaction of the terminal tubulin dimers, 'caps' the corresponding protofilaments and stabilizes the microtubule lattice. 'Opening' of LID (dashed curved arrow), either spontaneously and/or induced by an incoming tubulin dimer (II), enables processive microtubule tip elongation (III).

See also Figure S3 and Table S3.

5 increase in microtubule growth rate and a ~ 3 fold increase in catastrophe frequency (Figure 3F and Figure 3K-M). To test whether the artificial dimerization domain of GCN4 in CPAP_{mini} has an influence on microtubule dynamics we purified a CPAP construct that contains the endogenous coiled coil (CPAP_{long}). Although CPAP_{long} had a higher propensity for degradation and aggregation, it also bound to microtubule plus ends, very similar to CPAP_{mini}, and had a similar effect on microtubule dynamics, as it reduced both growth rate and catastrophe frequency (Figure S2D-S2G). These data demonstrate that GCN4 links CPAP_{mini} chains in a fashion similar to that of the endogenous coiled-coil domain of CPAP.

Next, we tested the effect of mutations that disrupt either the tubulin-SAC (KR/EE, FF/AA) or the tubulin-LID interaction (Δ LID, FEY/AAA) on the ability of CPAP_{mini} to regulate microtubule plus-end dynamics (Figures 1A and S2A). We found that all four mutants abrogated tip enrichment, as well as the effects on microtubule growth and catastrophes (Figures 3G-L and S2H). In contrast, all mutants as well as the dimeric version of MBD alone (Δ PN2-3), were still able to bind to the microtubule lattice and induce rescues to a similar extent as wild type CPAP_{mini} (Figure 3G-M). This result suggests that the MBD has microtubule-stabilizing properties. To further assess the mechanism underlying the activity of CPAP_{mini}, we investigated how its concentration affects microtubule dynamics. As mentioned above, at 75 nM of CPAP_{mini}, though not at lower concentrations, both the microtubule growth rate and the catastrophe frequency were strongly reduced (Figures 3H-L and 4AB). A four-fold increase in concentration of CPAP_{mini} had little additional

effect on the microtubule growth rate and catastrophe frequency, indicating that the effect of CPAP_{mini} on microtubule elongation in vitro saturates at ~75 nM (Figure 4B).

We next set out to determine the number of CPAP_{mini} molecules at microtubule plus ends. Single-molecule fluorescence intensity analysis of CPAP_{mini} in comparison to GFP confirmed that CPAP_{mini} is a dimer (Figure 4C). To determine the number of CPAP_{mini} molecules at one microtubule tip, we immobilized single CPAP_{mini} molecules on the surface of one flow chamber and performed the in vitro reconstitution assay in the adjacent chamber on the same coverslip. Images of unbleached CPAP_{mini} single molecules were acquired first, and then time lapse imaging of the in vitro assay with CPAP_{mini} was performed using the same illumination and imaging conditions. We found that approximately two dimers of CPAP_{mini} were present at microtubule tips in the presence of 100 or 300 nM protein, respectively (Figure 4DE). Our tubulin-PN2-3 structural model suggests that CPAP_{mini}, which contains two PN2-3 moieties, interacts with microtubule plus ends by binding to terminal β -tubulin subunits (Figure 2D). Our reconstitution data thus indicate that CPAP_{mini} can reach its full activity with respect to microtubule growth inhibition and catastrophe suppression by binding to approximately four to six protofilaments.

To acquire mechanistic insights into CPAP_{mini} association with the microtubule tip and lattice, we mixed 5 nM of CPAP_{mini}-GFP (Figure 4F) with 100 nM CPAP_{mini}-mCherry. This approach allowed us to observe the behavior of single CPAP_{mini}-GFP molecules in conditions where the protein inhibits microtubule growth. Rapid imaging of such samples showed that in most cases CPAP_{mini} directly associated with the microtubule plus end where it remained stationary and then detached. Occasionally, we observed CPAP_{mini} molecules diffusing towards or away from the microtubule tip (Figure 4F). The analysis of binding events of CPAP_{mini} at growing microtubule plus ends yielded an exponential dwell time distribution with a mean value of ~1.7 s (corrected for photobleaching (Helenius et al., 2006)) (Figures 4G, S3AB). The dwell time for CPAP_{mini} was longer than those observed previously for EB1, EB3 and CLIP-170 in similar conditions (values ranged between ~0.05-0.3 s (Bieling et al., 2008; Montenegro Gouveia et al., 2010)). We also observed binding and unbinding of CPAP_{mini} to the microtubule lattice, with an average dwell time of ~0.5 s (Figures 4G and S3AB). On the lattice, both stationary and mobile CPAP_{mini} molecules were detected. We noted that a single CPAP_{mini} molecule could switch between the two types of behavior (Figure 4F). Automated single particle tracking combined with mean squared displacement (MSD) analysis indicated that the mobile CPAP_{mini} molecule population undergoes one-dimensional diffusion, as the increase of the MSD value over time was linear (Figure S3C-E) (Qian et al., 1991). The diffusion coefficient of CPAP_{mini} bound to microtubule lattices was $0.03 \pm 0.0004 \mu\text{m}^2 \text{s}^{-1}$ (Table S3). This value is three times lower than that for EB3 and similar to the one for the kinesin-13 MCAK, obtained under similar conditions (Montenegro Gouveia et al., 2010).

Taken together, these results demonstrate that CPAP_{mini} localizes to microtubule plus ends mostly through direct binding and remains largely immobile at the microtubule tip

until detachment. This behavior, as well as the longer dwell times at the microtubule plus end compared to the lattice, can be explained by the presence of the LID domain, which can attach CPAP_{mini} to the tip of a protofilament. Our data further show that CPAP_{mini} can either diffuse along the lattice or bind to it in a stationary manner. We think that these two types of CPAP_{mini} behavior might be due to the presence of the MBD and SAC domains, which can independently interact with microtubule lattices. Finally, our results demonstrate that CPAP_{mini} suppresses microtubule growth and stabilizes microtubules by inhibiting catastrophes and promoting rescues. In combination with the structural and biophysical data, our reconstitution data suggest that CPAP_{mini} ensures slow processive microtubule growth by capping and stabilizing the plus ends of protofilaments (Figure 4H).

Both the SAC and MBD domains of CPAP are essential for centriole assembly

Our *in vitro* observations raised the possibility that CPAP could contribute to centriole formation in two ways: the MBD could promote centriolar microtubule assembly by stabilizing microtubules, while LID, together with SAC, might limit centriolar microtubule elongation by slowing growth of their plus ends. To test these predictions in the cellular context, we generated cell lines conditionally expressing YFP-tagged CPAP transgenes resistant to RNAi targeting endogenous CPAP (Kitagawa et al., 2011). We analyzed mitotic cells using the centriolar marker Centrin 2 as a readout of successful centriole assembly. Whereas >90% of control cells contained ≥ 4 centrioles, this was the case for less than 10% of cells depleted of endogenous CPAP (Figure 5A, 5B, 5I and S4A) (Kohlmaier et al., 2009; Schmidt et al., 2009; Tang et al., 2009). YFP-CPAP rescued this phenotype to a large extent, with >80% of cells having successfully duplicated their centrioles (Figures 5C, 5I and S4A) (Kohlmaier et al., 2009; Schmidt et al., 2009; Tang et al., 2009). Strikingly, we found that the removal of MBD (Δ MBD) completely abolished centriole assembly, to levels that are even lower than depletion of CPAP alone, likely due to dominant negative effects following dimerization of YFP-CPAP- Δ MBD with any residual endogenous CPAP (Figures 5D, 5I and S4A). We conclude that the microtubule-stabilizing effect of MBD observed *in vitro* is essential for centriole biogenesis.

We found also that CPAP constructs lacking the LID domain or with key residues mutated, YFP-CPAP- Δ LID and FEY/AAA, respectively, were able to sustain centriole assembly in ~65% of cells (Figure 5G- 5I), indicating that LID contributes to, but is not essential for, this process. In contrast, CPAP function was severely compromised upon mutation of SAC (KR/EE or FF/AA; Figure 5E, 5F and 5I), in line with previous findings (Hsu et al., 2008; Kitagawa et al., 2011; Tang et al., 2009). Impaired function of all CPAP mutants likely reflects an impact on protein activity, because localization and turnover at the centrosome were unaffected (Figures 5C-H and S4B). Overall, these results establish that MBD and SAC are critical for centriole assembly, whereas LID appears to play an accessory role in this process.

Figure 5

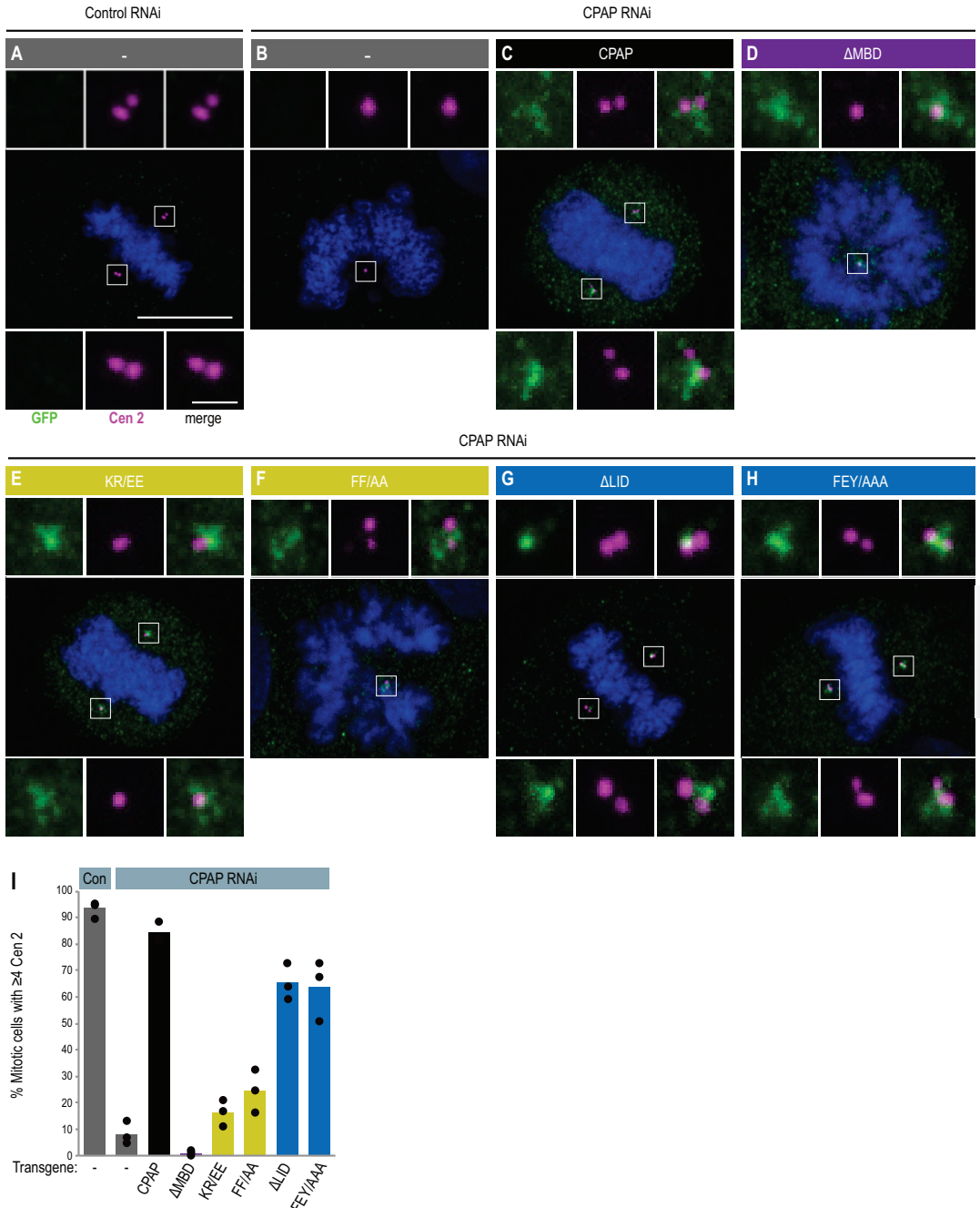


Figure 5. Effect of PN2-3 mutations on CPAP cellular function.

(A-H) Mitotic U2OS FlpIn TREX cell lines without transgene (A, B) or expressing the indicated YFP-CPAP variants (C-H), treated with control siRNA (A) or siRNA targeting endogenous CPAP (B-H), stained with antibodies against Centrin 2 (magenta) and GFP (green); DNA in blue. Scale bars, 10 μ m and 1 μ m in insets.

(I) Percentage of cells showing successful centriole duplication (≥ 4 Centrin foci). Bars show the mean of three experimental repeats, circles indicate the individual values for each experiment; $n > 100$ cells analyzed for each condition and per experiment. Full data set shown in Figure S4A. See also Figure S4 and Table S1.

CPAP regulates the length of centriolar microtubules in cells

We further investigated the function of SAC and LID by analyzing cells depleted of endogenous CPAP and overexpressing YFP-CPAP variants, which provided us with an assay system to address the contribution of distinct domains of CPAP to centriole biogenesis. In these conditions, wild type YFP-CPAP leads to the formation of overly long centrioles that contain not only CPAP, but also other centriolar markers such as Centrin 2 along their entire length (Figure 6AD), as reported for cells overexpressing wild-type CPAP in addition to having the endogenous protein (Kohlmaier et al., 2009; Schmidt et al., 2009; Tang et al., 2009). In contrast, we found no overly long centrioles upon YFP-CPAP- Δ MBD overexpression (Figure S4C-D), as anticipated from the fact that MBD is essential for centriole assembly. Mutation of SAC (KR/EE or FF/AA) led to a reduction in the proportion of cells with overly long centrioles, while deletion of LID had no such effect, again reflecting the respective impact of these variants on the ability of CPAP to sustain regular centriole assembly (Figures 6AD and S4C-D).

Intriguingly, close examination of cells depleted of endogenous CPAP and overexpressing either YFP-CPAP-FF/AA or YFP-CPAP- Δ LID revealed the presence of extended YFP-positive fibers that stemmed from centrosomes, but which did not contain centriolar markers along their length (Figure 6AC). In order to determine whether such centrosomal fibers originated from centrioles or from the pericentriolar matrix, we conducted immunofluorescence experiments with a marker surrounding the proximal end of parental centrioles (CEP63) and one marking the distal end of all centrioles (Centrin 2). This analysis revealed that $\sim 80\%$ of centrosomal fibers appeared to be continuations of the distal end of regular centrioles or of overly long centrioles, and thus termed centriole fibers (Figure 6E-F). These fibers, lacking Centrin, were often considerably longer than overly long centrioles bearing Centrin (Figure 6H) and were positive for α -tubulin (Figure 6I-J), raising the possibility that they correspond to abnormal extensions of centriolar microtubules.

To test this hypothesis, we carried out correlative light and electron microscopy (CLEM; Figures 7 and S5). In line with previous observations (Kohlmaier et al., 2009; Schmidt et al., 2009; Tang et al., 2009), we found that cells overexpressing YFP-CPAP and depleted of endogenous CPAP harbored overly long centrioles, in which microtubules extended from the distal end of the centriole (Figures 7B and 7F; compare with 7A and 7E). Strikingly, cells expressing YFP-CPAP- Δ LID also exhibited microtubule extensions from the distal end of the centriole, which attained several microns in some cases (Figure 7C and 7G). To ensure that such figures represented centriole fibers (i.e. devoid of Centrin) and not overly long centrioles (i.e. bearing Centrin), further CLEM experiments were carried out using tagRFP-Centrin 1 as an additional marker. In agreement with our immunofluorescence

Figure 6

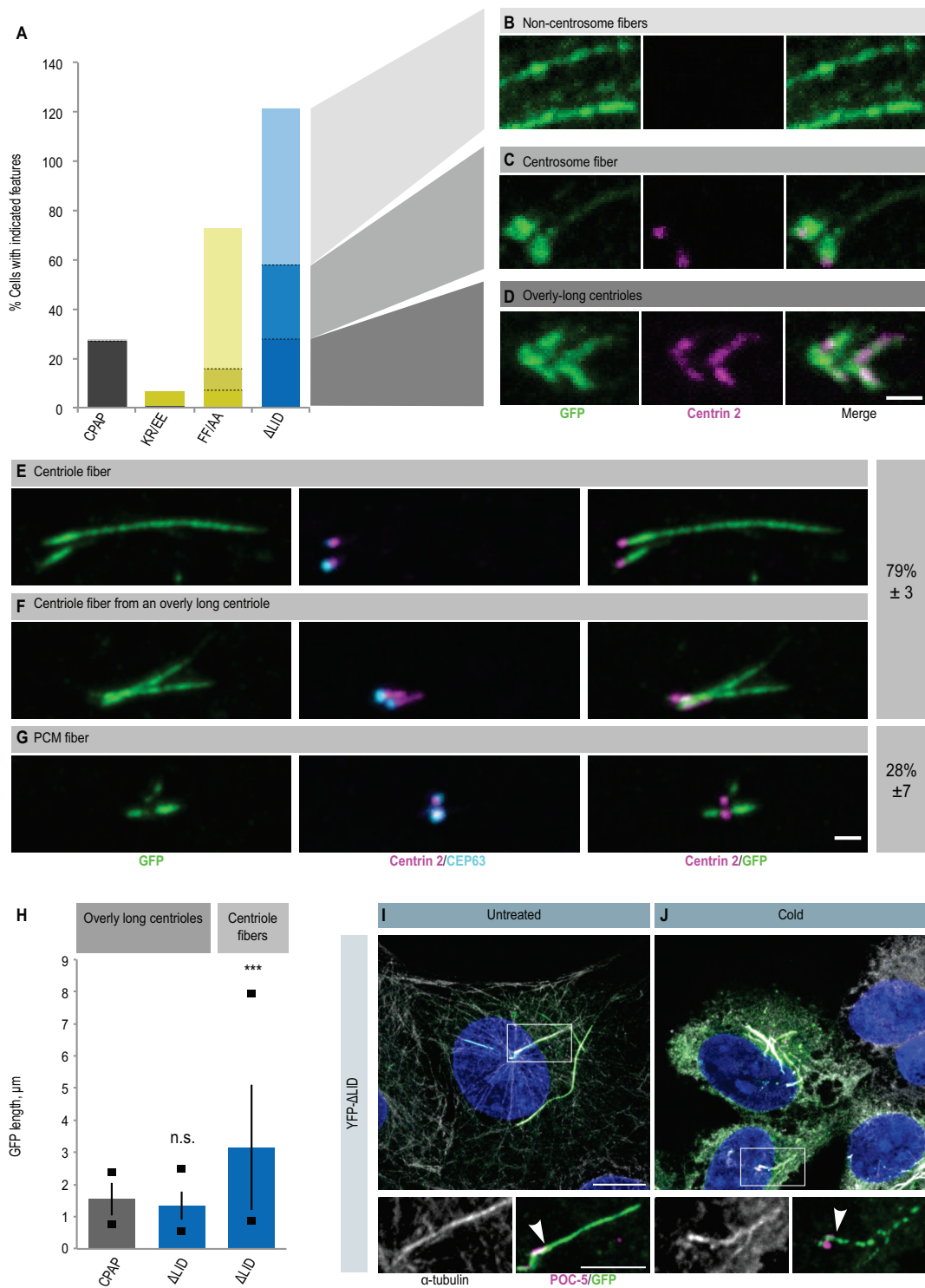


Figure 6. Fibers extend from centrioles upon expression of CPAP lacking the LID domain

(A-D) U2OS cells expressing indicated YFP-CPAP variants and depleted of endogenous CPAP by RNAi, stained with antibodies against Centrin 2 (magenta) and GFP (green). (A) Quantification of the YFP structures illustrated in (B-D) ($n > 100$ per sample). Scale bar, 1 μm . Note that the total exceeds 100% here and in (E-G) because some cells contain multiple types of structure.

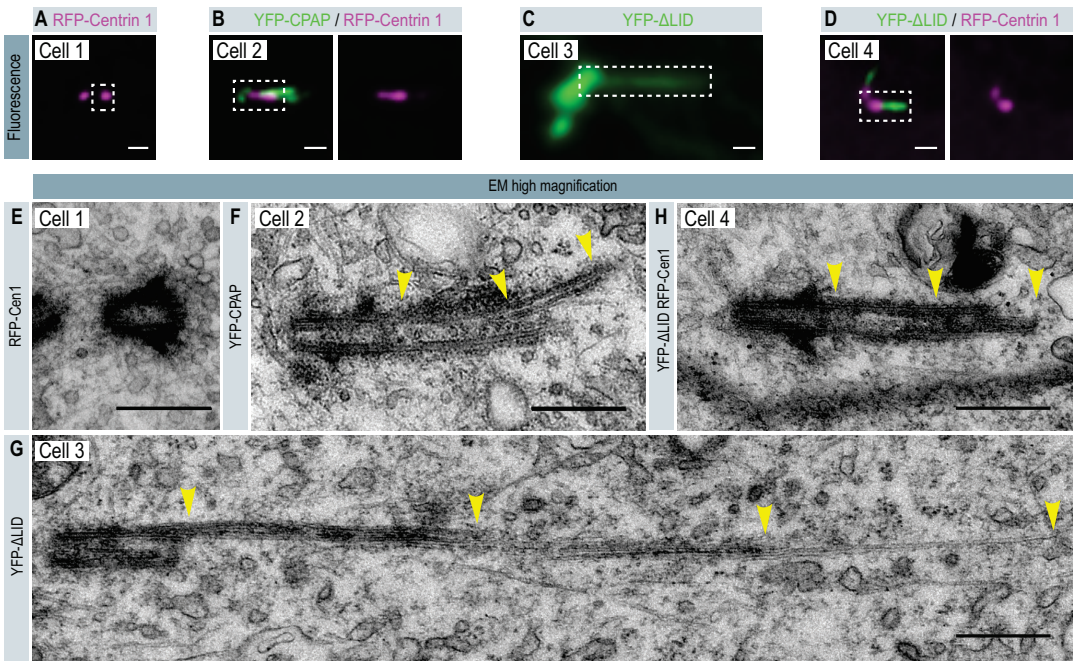
(E-G) Proportion of YFP-CPAP- Δ LID expressing cells with centriole fibers (E, F), or PCM fibers (G). Scale bar, 1 μm . Percentages are the mean of three experiments, standard deviation is indicated; $N = 9, 17,$ and 26 cells, respectively.

(H) Length of overly long centrioles and of centriole fibers in the indicated conditions determined using GFP immunofluorescence. $N = 42, 22,$ and 37 cells, respectively. Bars indicate the mean, squares indicate the minimum and maximum values, and error bars indicate the standard deviation. Students' two-sample two-tailed unequal variance t -test comparing Δ LID overly long centrioles and centriole fibers with CPAP-induced overly long centrioles: *** $p < 0.001$, n.s. not significant.

(I, J) YFP-CPAP- Δ LID cells without (I) or with (J) 1 hour incubation on ice stained with antibodies against α -tubulin (gray), GFP (green) and the distal centriole protein POC5 (magenta). Scale bars, 10 μm ; inset, 5 μm . Arrowheads indicate end of the centriole from which emanates fibers, as determined by the POC5 signal. Note that the signal of YFP-CPAP- Δ LID along the centriole fiber becomes sparser following ice-induced microtubule depolymerization.

analysis, we found that YFP-CPAP- Δ LID centriole fibers were indeed microtubules extending from the distal end of centrioles (Figure 7DH). We conclude that the activities of LID and SAC can prevent aberrant overextension of centriolar microtubules.

Figure 7

**Figure 7. Centriole fibers are centriolar microtubule extensions.**

(A-H) CLEM of cells expressing tagRFP-Centrin 1 (Cell 1; A, E), YFP-CPAP and tagRFP-Centrin 1 (Cell 2; B, F), YFP- Δ LID (Cell 3; C, G) or YFP- Δ LID plus tagRFP-Centrin-1 (Cell 4; D, H), and simultaneously depleted of endogenous CPAP using RNAi (Cells 2 to 4). (A-D) Fluorescence microscopy images of the region of interest in each cell. Scale bar 1 μm . (E-H) Corresponding high-magnification electron micrographs of one

section of the boxed region in (A-D). Yellow arrowheads indicate microtubule extensions from the distal ends of centrioles. Scale bars, 500 nm. 10 cells expressing YFP- Δ LID were analyzed, which contained a total of 28 centrioles. Of these, 3 were centrioles with an apparent normal length and structure, 2 were overly long centrioles without further microtubule extensions, 4 exhibited PCM fibers, whereas 19 harbored microtubule extensions from their distal ends (as illustrated in (G) and (H)). Of these 19 centrioles, 6 came from the experiment where cells were also expressing tagRFP-Centrin 1 and could therefore be unambiguously classified as centriole fibers (i.e., without Centrin 1 signal), rather than overly long centrioles. See also Figures S5 and S6.

DISCUSSION

Our study provides fundamental insights into the mechanisms by which the evolutionarily conserved family of CPAP/SAS-4 proteins regulate the growth of centriolar microtubules, thus contributing to setting organelle size. Whereas the crystal structure of the G-box of CPAP, either alone or in complex with a peptide derived from the centriolar protein STIL, has been solved (Zheng et al., 2014; Cottee et al., 2013; Hatzopoulos et al., 2013), high resolution structural information on the evolutionarily conserved domains interacting with tubulin and microtubules was lacking, precluding full understanding of how CPAP regulates centriole biogenesis. The structural and biophysical data presented here reveal a novel dual binding mode between tubulin and the LID plus SAC domains of PN2-3, explaining its tubulin sequestering and microtubule destabilizing activity (Hsu et al., 2008; Cormier et al., 2009; Hung et al., 2004). The finding that LID binds at the tip of β -tubulin, in combination with the structural model suggesting that PN2-3 can bind the terminal β -tubulin subunits on the outside of a microtubule, strongly suggested that PN2-3 represents an autonomous microtubule plus-end targeting domain in CPAP.

To test whether this is the case, we performed dynamic microtubule reconstitution experiments and indeed found that the sequential arrangement of LID, SAC and MBD in a dimeric configuration localizes CPAP_{mini} to growing microtubule plus ends. The plus-end localization of CPAP_{mini} is unlikely to depend on co-polymerization with tubulin, because tip localization is observed at CPAP_{mini} concentrations that are several orders of magnitude lower than that of tubulin. Analysis of the behavior of single CPAP_{mini} molecules in our in vitro reconstitution system showed that the majority of CPAP_{mini} molecules bound to microtubule plus ends directly. CPAP_{mini} also displayed one-dimensional diffusion along the microtubule lattice, as described previously for other microtubule end-interacting proteins (Brouhard et al., 2008; Bieling et al., 2008; Helenius et al., 2006; Montenegro Gouveia et al., 2010); however, diffusion did not seem to be a major contributing factor responsible for the recruitment of CPAP_{mini} to microtubule plus ends. Notably, in the context of a centriole CPAP is expected to be organized in a precise manner along the inside of the centriole wall where it binds STIL and is thus very likely not diffusive (Hatzopoulos et al., 2013).

Our reconstitution data revealed that depending on the conditions, microtubule tip-localized CPAP_{mini} slows down microtubule growth 5- to 8-fold and that only a few CPAP_{mini} molecules suffice to induce this effect. Based on the structural and biophysical results, we propose that the LID and SAC domains of CPAP_{mini} bind terminal β -tubulin

subunits exposed at the microtubule plus ends and thereby occlude the binding sites for the incoming tubulin dimers. The ability of PN2-3 to block longitudinal tubulin-tubulin interactions is reminiscent of the tubulin-sequestering protein stathmin and the microtubule plus-end capping ligands DARPin D1, Eribulin and Maytansine (Gigant et al., 2000; Pecqueur et al., 2012; Smith et al., 2010; Prota et al., 2014). However, in striking contrast to these microtubule-destabilizing and polymerization-blocking agents, CPAP_{mini} stabilizes microtubules by potently suppressing catastrophes and promoting rescues. The latter property can be attributed to the MBD, which binds strongly to the microtubule lattice and can autonomously induce rescues. The MBD is positively charged, and its binding to negatively charged microtubules likely involves an electrostatic mechanism, similar to microtubule lattice-binding regions of cytoplasmic microtubule regulators such as XMAP215/ch-TOG (Brouhard et al., 2008; Widlund et al., 2011). In order to stabilize microtubules, we assume that the MBD of CPAP_{mini} binds along, as well as between, protofilaments.

Based on these considerations, we conclude that this particular mode of binding to microtubule plus ends, due to the combination of LID, SAC, and MBD, can "cap" and stabilize terminal tubulin dimers (Figure 4H). We postulate that in this state, a capped protofilament can only be elongated by an incoming tubulin dimer if the LID domain is released and frees the interaction site needed for establishing longitudinal tubulin-tubulin contacts. The release of LID in turn weakens the CPAP_{mini}-microtubule plus-end interaction and either promotes CPAP_{mini} detachment or enables the liberated PN2-3 domain to cap the newly elongated protofilament or a neighboring one. Notably, slowing microtubule growth normally promotes catastrophes by reducing the size of the GTP cap (Walker et al., 1988; Janson et al., 2003). Accordingly, microtubule polymerization suppressors typically act as microtubule depolymerases. However, exceptions to this rule are known, including the kinesin-4 family members Xklp1/KIF4 and KIF21A, which, similarly to CPAP_{mini}, can suppress both microtubule growth and catastrophes (Bringmann et al., 2004; Bieling et al., 2010; Van der Vaart et al., 2013). The molecular basis of kinesin-4-mediated microtubule growth inhibition is not understood, but it is very likely distinct from that of CPAP_{mini}, because both Xklp1/KIF4 and KIF21A are molecular motors that can move along microtubules and accumulate at microtubule plus ends due to their processive motility (Bieling et al., 2010; Van der Vaart et al., 2013). In contrast, CPAP presents a unique arrangement of tubulin- and microtubule lattice-binding domains, which together have the potential to recognize, cap and stabilize microtubule plus ends, a mechanism that has not been previously described to our knowledge for any microtubule regulator.

In cells, centriolar microtubules grow very slowly and processively as judged from the analysis of specimens prepared from different stages of the cell cycle (Kuriyama and Borisy, 1981; Chretien et al., 1997). However, the mechanisms underlying such slow and regulated elongation have remained elusive. Our study reveals that CPAP plays a critical dual role in ensuring that this is the case. First, our data indicates that a pivotal function of

CPAP is to stabilize centriolar microtubules via its MBD, which explains why this domain is essential for centriole assembly. Second, although the capacity of LID to cap microtubule plus ends is not essential for this stabilization function, and thus for centriole formation, it exerts a negative role by limiting microtubule extension from the distal end of centrioles. The SAC domain, which interacts with the lateral side of tubulin dimers, can contribute to both microtubule stabilization and capping functions, potentially explaining why mutations in SAC affect centriole formation more strongly than those in LID. These considerations can at least partially explain why centrioles overelongate when CPAP dosage is increased (Kohlmaier et al., 2009; Schmidt et al., 2009; Tang et al., 2009); however, additional mechanisms likely control the activity of CPAP domains in cells. Our *in vitro* data revealed that ~ 2 CPAP_{mini} dimers are sufficient to limit the growth rate of a single microtubule, suggesting that the activity of CPAP has been optimized to work at sub-stoichiometric levels. In the context of the centriolar microtubule wall, we expect ~ 2 CPAP dimers to be able to access the microtubule tips of each triplet from the luminal side of the centriole (Figure S6) (Hatzopoulos et al., 2013; Sonnen et al., 2012; Tang et al., 2011).

Overall, our results reveal that CPAP is a highly specialized microtubule plus-end regulator that acts as a molecular cap to ensure slow and processive growth of centriolar microtubules. Given that endogenous CPAP is present primarily in the proximal region of mature centrioles (Kohlmaier et al., 2009; Schmidt et al., 2009; Tang et al., 2009), we propose that CPAP activity is most critical during the early stages of centriole elongation. Upon overexpression of the wild-type protein, excess CPAP molecules localize along the entire length of centrioles and could cause over-elongation of centriolar microtubules due to the microtubule stabilization activity of ectopic CPAP. Furthermore, we speculate that upon overexpression of a mutant protein lacking LID domain function, over-elongation of centriolar microtubules is exacerbated due to the lack of capping function (Figure S6).

We note that microtubule growth rates obtained *in vitro* upon CPAP_{mini} addition are still some three orders of magnitude faster than those estimated for centriolar microtubules in cells (Kuriyama and Borisy, 1981; Chretien et al., 1997). Regions of CPAP outside of the tubulin- and microtubule-binding domains, including the G-box that may organize CPAP molecules along the entire length of the microtubule wall in a precise manner (Hatzopoulos et al., 2013), as well as post-translational modifications, could be important to further bolster CPAP activity; these features are not recapitulated by the CPAP_{mini} and CPAP_{long} constructs used in our study. In addition, other centriolar proteins have been implicated in controlling centriole length, including the CPAP interacting proteins CEP120, CEP135 and Centrobin (Gudi et al., 2011; Lin et al., 2013a; Lin et al., 2013b). It will be of prime interest to assess on a mechanistic level how these proteins cooperate to impact on CPAP function or otherwise contribute to regulate organelle size.

EXPERIMENTAL PROCEDURES

Protein/peptide preparation and isothermal titration calorimetry (ITC)

Standard protein production in bacteria and peptide synthesis is described in the Supplemental Information. ITC experiments were performed at 25 °C using an ITC200 system (Microcal). Proteins were buffer-exchanged to BRB80 (80 mM PIPES-KOH, pH 6.8, supplemented with 1 mM MgCl₂, 1 mM EGTA) supplemented with 0.5 mM TCEP. 0.1–0.4 mM PN2-3 variants in the syringe were injected step-wise into 10–20 μM tubulin solutions in the cell. The resulting heats were integrated and fitted in Origin (OriginLab) using the standard ‘one set of sites’ model provided by the software package.

Structure determination

Structure solution by X-ray crystallography is described in full in the Supplementary Information. In brief, equimolar amounts of D1, PN2-3 and subtilisin-treated tubulin were mixed and the PN2-3- tubulin-D1 complex was concentrated to ~20 mg/ml. PN2-3-tubulin-D1 samples were complemented with 0.2 mM GDP, 1 mM Colchicine and 5 mM DTT before setting up sitting drop vapor diffusion crystallization trials. Crystals were obtained in a condition containing 20% PEG 550 mono methyl ether (MME) and 0.1 M MES, pH 6.5. X-ray diffraction data were collected at 100K at beamline X06DA at the Swiss Light Source (Paul Scherrer Institut, Villigen, Switzerland). The PN2-3-tubulin-D1 structure was solved by molecular replacement using the αβ-tubulin-D1 complex structure as a search model (PDB ID 4DRX). Data collection and refinement statistics are given in Table S2.

In vitro reconstitution assays

Protein purification for in vitro reconstitution assays is described in full in the Supplementary Information. Reconstitution of microtubule growth dynamics in vitro was performed as described previously (Montenegro Gouveia et al., 2010). In brief, flow chambers were functionalized by sequential incubation with 0.2 mg/ml PLL-PEG-biotin (Susos AG, Switzerland) and 1 mg/ml NeutrAvidin (Invitrogen) in MRB80 buffer (80 mM piperazine-N,N[prime]-bis(2-ethanesulfonic acid), pH 6.8, supplemented with 4 mM MgCl₂, and 1 mM EGTA). GMPCPP-microtubule seeds were attached to coverslips through biotin-NeutrAvidin interactions. The reaction mix with or without CPAP_{mini} proteins (MRB80 buffer supplemented with 15 μM tubulin, 0.5 μM rhodamine-tubulin, 50 mM KCl, 1 mM guanosine triphosphate, 0.2 mg/ml κ-casein, 0.1% methylcellulose, and oxygen scavenger mix [50 mM glucose, 400 μg/ml glucose oxidase, 200 μg/ml catalase, and 4 mM DTT]) was added to the flow chamber. Flow chambers were sealed and dynamic microtubules were imaged immediately at 30 °C using Total Internal Reflection Fluorescence (TIRF) microscopy. Intensity analysis for CPAP_{mini} along microtubules, single-molecule fluorescence intensity analysis of CPAP_{mini}, CPAP_{mini} molecule counting at microtubule tips, analysis of microtubule plus end dynamics and statistical analysis

procedures are all described in full in the Supplementary Information.

Immunofluorescence, antibodies and microscopy

Cells were grown on glass coverslips and fixed in -20°C Methanol for 7 minutes. Cold treatment was carried out by incubating cells in ice-cold PBS, on ice, for 1 hour before fixation. Cells were permeabilized using 0.2% Triton X-100, washed in PBS 0.01% Triton X-100, and blocked for 1 hour in PBS, 1% BSA, 2% FCS. All antibodies were diluted in the blocking solution and incubated for either 1 hour at room temperature or ~ 12 hours at 4°C . Primary antibodies were mouse anti- α -tubulin (DM1a, Sigma), mouse '20H5' anti-centrin-2 (a gift from Jeff Salisbury), rabbit anti-hPOC5 ((Azimzadeh et al., 2009), a gift from Michel Bornens), rabbit anti-CEP63 (Millipore 06-1292), goat anti-GFP (abcam ab6673), and rabbit anti-GFP (a gift from Viesturs Simanis). Secondary antibodies were goat anti-rabbit Alexa Fluor 488, goat anti-mouse Alexa Fluor 568, donkey anti-goat Alexa Fluor 488, donkey anti-mouse Alexa Fluor 568, and donkey anti-rabbit Alexa Fluor 647 (Invitrogen). All primary antibodies were diluted 1000-fold, except Centrin 2 (2000x) and anti- α -tubulin (5000x). All secondary antibodies were diluted 1000-fold. Samples were washed 3 times between, and after, antibody incubations and incubated with $1\ \mu\text{g/ml}$ Hoechst in PBS prior to mounting in PBS, 90% glycerol, 4% N-Propyl gallate.

Confocal imaging was carried out using a Zeiss LSM 700 microscope with a Plan-Apochromat 63 x oil-immersion objective, NA 1.40. Z-sections were imaged at an interval of $\sim 0.2\ \mu\text{m}$. All images shown are maximum intensity projections and were processed using Fiji (Schindelin et al., 2012), maintaining relative intensities within a series.

Correlative light and electron microscopy (CLEM)

CLEM is described in full in the Supplementary Information. In brief, endogenous CPAP was depleted by RNAi for 72 hours, simultaneous with induction of the transgene. For dual marker experiments, cells were transfected with a tagRFP-Centrin 1 expression vector 16 hours prior to fixation. Cells were fixed, then washed thoroughly with cacodylate buffer (0.1 M, pH 7.4), and imaged by light microscopy. Immediately afterwards, samples were post-fixed for 40 minutes in 1.0% osmium tetroxide, then 30 minutes in 1.0% uranyl acetate in water, before being dehydrated through increasing concentrations of alcohol and then embedded in Durcupan ACM resin (Fluka, Switzerland). The coverslips were then placed face down on a glass slide coated with mold releasing agent (Glorex, Switzerland), with approximately 1 mm of resin separating the two. These regions were mounted on blank resin blocks with acrylic glue and trimmed with glass knives to form a block ready for serial sectioning. Series of between 150 and 300 thin sections (50 nm thickness) were cut with a diamond knife mounted on an ultramicrotome (Leica UC7). These sections were contrasted with lead citrate and uranyl acetate and images taken using an FEI Spirit transmission EM equipped with an Eagle CCD camera.

AUTHOR CONTRIBUTIONS

A.S., A.A., N.J.D., E.A.K., M.C., R.A.K., A.Akhmanova, P.G., and M.O.S. designed the experiments. A.S., A.A., N.J.D., D.F., E.A.K., R.J., I.G., and M.C. conducted the experiments. A.S., A.A., N.J.D., A.Akhmanova, P.G., and M.O.S. wrote the manuscript with the input from all authors.

ACKNOWLEDGEMENTS

X-ray data were collected at beamline X06DA of the Swiss Light Source (Paul Scherrer Institut, Villigen, Switzerland). Eribulin was a kind gift from Eisai Co., Ltd. We are grateful to Graham Knott, head of the Bio-EM Facility in the School of Life Sciences at EPFL, for help in setting up CLEM, and to Christian Arquint and Erich Nigg (Basel, Switzerland) for their gift of the U2OS FlpIn TREX cell line. We thank Marileen Dogterom, Virginie Hachet and John Vakonakis for useful comments on the manuscript. This work was supported by an EMBO Long Term Fellowship (to A.S.), as well as by grants from the Swiss National Science Foundation (310030B_138659 and 31003A_166608; to M.O.S.) and from the European Research Council (AdG 340227; to P.G. and Synergy grant 609822; to A.A.).

ACCESSION NUMBERS

Coordinates have been deposited at the Protein Data Bank (PDB) under accession numbers 5ITZ (D1-tubulin-PN2-3)

5

References

- Alday, P.H. and Correia, J.J. (2009). Macromolecular interaction of halichondrin B analogues eribulin (E7389) and ER-076349 with tubulin by analytical ultracentrifugation. *Biochemistry* 48, 7927-7938.
- Azimzadeh, J., Hergert, P., Delouvee, A., Euteneuer, U., Formstecher, E., Khodjakov, A., and Bornens, M. (2009). hPOC5 is a centrin-binding protein required for assembly of full-length centrioles. *J. Cell Biol.* 185, 101-114.
- Azimzadeh, J. and Marshall, W.F. (2010). Building the centriole. *Curr. Biol.* 20, R816-R825.
- Bieling, P., Kandels-Lewis, S., Telley, I.A., van, D.J., Janke, C., and Surrey, T. (2008). CLIP-170 tracks growing microtubule ends by dynamically recognizing composite EB1/tubulin-binding sites. *J Cell Biol.* 183, 1223-1233.
- Bieling, P., Laan, L., Schek, H., Munteanu, E.L., Sandblad, L., Dogterom, M., Brunner, D., and Surrey, T. (2007). Reconstitution of a microtubule plus-end tracking system in vitro. *Nature* 450, 1100-1105.
- Bieling, P., Telley, I.A., and Surrey, T. (2010). A minimal midzone protein module controls formation and length of antiparallel microtubule overlaps. *Cell* 142, 420-432.
- Bond, J. et al. (2005). A centrosomal mechanism involving CDK5RAP2 and CENPJ controls brain size. *Nat. Genet.* 37, 353-355.
- Bornens, M. (2012). The centrosome in cells and organisms. *Science* 335, 422-426.
- Bringmann, H., Skiniotis, G., Spilker, A., Kandels-Lewis, S., Vernos, I., and Surrey, T. (2004). A kinesin-like motor inhibits microtubule dynamic instability. *Science* 303, 1519-1522.
- Brouhard, G.J., Stear, J.H., Noetzel, T.L., Al-Bassam, J., Kinoshita, K., Harrison, S.C., Howard, J., and Hyman, A.A. (2008). XMAP215 Is a Processive Microtubule Polymerase. *Cell* 132, 79-88.
- Chretien, D., Buendia, B., Fuller, S.D., and Karsenti, E. (1997). Reconstruction of the centrosome cycle from cryoelectron micrographs. *J. Struct. Biol.* 120, 117-133.
- Cormier, A., Clement, M.J., Knossow, M., Lachkar, S., Savarin, P., Toma, F., Sobel, A., Gigant, B., and Curmi, P.A. (2009). The PN2-3 domain of centrosomal P4.1-associated protein implements

- a novel mechanism for tubulin sequestration. *J Biol. Chem.* 284, 6909-6917.
- Cottee, M.A., Muschalik, N., Wong, Y.L., Johnson, C.M., Johnson, S., Andreeva, A., Oegema, K., Lea, S.M., Raff, J.W., and van, B.M. (2013). Crystal structures of the CPAP/STIL complex reveal its role in centriole assembly and human microcephaly. *Elife.* 2, e01071.
- Gigant, B., Curmi, P.A., Martin-Barbey, C., Charbaut, E., Lachkar, S., Lebeau, L., Siavoshian, S., Sobel, A., and Knossow, M. (2000). The 4 Å X-ray structure of a tubulin:stathmin-like domain complex. *Cell* 102, 809-816.
- Gigant, B., Wang, C., Ravelli, R.B., Roussi, F., Steinmetz, M.O., Curmi, P.A., Sobel, A., and Knossow, M. (2005). Structural basis for the regulation of tubulin by vinblastine. *Nature* 435, 519-522.
- Gönczy, P. (2012). Towards a molecular architecture of centriole assembly. *Nat. Rev. Mol. Cell Biol.* 13, 425-435.
- Gönczy, P. (2015). Centrosomes and cancer: revisiting a long-standing relationship. *Nat. Rev. Cancer* 15, 639-652.
- Gopalakrishnan, J., Chim, Y.C., Ha, A., Basiri, M.L., Lerit, D.A., Rusan, N.M., and Avidor-Reiss, T. (2012). Tubulin nucleotide status controls Sas-4-dependent pericentriolar material recruitment. *Nat. Cell Biol.* 14, 865-873.
- Gudi, R., Zou, C., Li, J., and Gao, Q. (2011). Centrobilin-tubulin interaction is required for centriole elongation and stability. *J. Cell Biol.* 193, 711-725.
- Hatzopoulos, G.N., Erat, M.C., Cutts, E., Rogala, K.B., Slater, L.M., Stansfeld, P.J., and Vakonakis, I. (2013). Structural analysis of the G-box domain of the microcephaly protein CPAP suggests a role in centriole architecture. *Structure.* 21, 2069-2077.
- Helenius, J., Brouhard, G., Kalaidzidis, Y., Diez, S., and Howard, J. (2006). The depolymerizing kinesin MCAK uses lattice diffusion to rapidly target microtubule ends. *Nature* 441, 115-119.
- Hsu, W.B., Hung, L.Y., Tang, C.J., Su, C.L., Chang, Y., and Tang, T.K. (2008). Functional characterization of the microtubule-binding and -destabilizing domains of CPAP and d-SAS-4. *Exp. Cell Res.* 314, 2591-2602.
- Hung, L.Y., Chen, H.L., Chang, C.W., Li, B.R., and Tang, T.K. (2004). Identification of a novel microtubule-destabilizing motif in CPAP that binds to tubulin heterodimers and inhibits microtubule assembly. *Mol. Biol. Cell* 15, 2697-2706.
- Jana, S.C., Marteil, G., and Bettencourt-Dias, M. (2014). Mapping molecules to structure: unveiling secrets of centriole and cilia assembly with near-atomic resolution. *Curr. Opin. Cell Biol.* 26, 96-106.
- Janson, M.E., de Dood, M.E., and Dogterom, M. (2003). Dynamic instability of microtubules is regulated by force. *J. Cell Biol.* 161, 1029-1034.
- Jiang, K. et al. (2014). Microtubule minus-end stabilization by polymerization-driven CAMSAP deposition. *Dev. Cell* 28, 295-309.
- Kinoshita, K., Arnal, I., Desai, A., Drechsel, D.N., and Hyman, A.A. (2001). Reconstitution of physiological microtubule dynamics using purified components. *Science* 294, 1340-1343.
- Kirkham, M., Muller-Reichert, T., Oegema, K., Grill, S., and Hyman, A.A. (2003). SAS-4 is a *C. elegans* centriolar protein that controls centrosome size. *Cell* 112, 575-587.
- Kitagawa, D., Kohlmaier, G., Keller, D., Strnad, P., Balestra, F.R., Fluckiger, I., and Gönczy, P. (2011). Spindle positioning in human cells relies on proper centriole formation and on the microcephaly proteins CPAP and STIL. *J. Cell Sci.* 124, 3884-3893.
- Kohlmaier, G., Loncarek, J., Meng, X., McEwen, B.F., Mogensen, M.M., Spektor, A., Dynlacht, B.D., Khodjakov, A., and Gönczy, P. (2009). Overly long centrioles and defective cell division upon excess of the SAS-4-related protein CPAP. *Curr. Biol.* 19, 1012-1018.
- Kuriyama, R. and Borisy, G.G. (1981). Centriole cycle in Chinese hamster ovary cells as determined by whole-mount electron microscopy. *J. Cell Biol.* 91, 814-821.
- Leidel, S. and Gönczy, P. (2003). SAS-4 is essential for centrosome duplication in *C. elegans* and is recruited to daughter centrioles once per cell cycle. *Dev. Cell* 4, 431-439.
- Lin, Y.C., Chang, C.W., Hsu, W.B., Tang, C.J., Lin, Y.N., Chou, E.J., Wu, C.T., and Tang, T.K. (2013a). Human microcephaly protein CEP135 binds to hSAS-6 and CPAP, and is required for centriole assembly. *EMBO J.* 32, 1141-1154.
- Lin, Y.N., Wu, C.T., Lin, Y.C., Hsu, W.B., Tang, C.J., Chang, C.W., and Tang, T.K. (2013b). CEP120

- interacts with CPAP and positively regulates centriole elongation. *J. Cell Biol.* 202, 211-219.
- Montenegro Gouveia, S. et al. (2010). In vitro reconstitution of the functional interplay between MCAK and EB3 at microtubule plus ends. *Curr. Biol.* 20, 1717-1722.
- Nigg, E.A. and Raff, J.W. (2009). Centrioles, centrosomes, and cilia in health and disease. *Cell* 139, 663-678.
- O'Shea, E.K., Klemm, J.D., Kim, P.S., and Alber, T. (1991). X-ray structure of the GCN4 leucine zipper, a two-stranded, parallel coiled coil. *Science* 254, 539-544.
- Pecqueur, L., Duellberg, C., Dreier, B., Jiang, Q., Wang, C., Pluckthun, A., Surrey, T., Gigant, B., and Knossow, M. (2012). A designed ankyrin repeat protein selected to bind to tubulin caps the microtubule plus end. *Proc. Natl. Acad. Sci. U. S. A* 109, 12011-12016.
- Prota, A.E., Bargsten, K., Diaz, J.F., Marsh, M., Cuevas, C., Liniger, M., Neuhaus, C., Andreu, J.M., Altmann, K.H., and Steinmetz, M.O. (2014). A new tubulin-binding site and pharmacophore for microtubule-destabilizing anticancer drugs. *Proc. Natl. Acad. Sci. U. S. A.*
- Qian, H., Sheetz, M.P., and Elson, E.L. (1991). Single particle tracking. Analysis of diffusion and flow in two-dimensional systems. *Biophys. J.* 60, 910-921.
- Schindelin, J. et al. (2012). Fiji: an open-source platform for biological-image analysis. *Nat. Methods* 9, 676-682.
- Schmidt, T.I., Kleylein-Sohn, J., Westendorf, J., Le, C.M., Lavoie, S.B., Stierhof, Y.D., and Nigg, E.A. (2009). Control of centriole length by CPAP and CP110. *Curr. Biol.* 19, 1005-1011.
- Smith, J.A., Wilson, L., Azarenko, O., Zhu, X., Lewis, B.M., Littlefield, B.A., and Jordan, M.A. (2010). Eribulin binds at microtubule ends to a single site on tubulin to suppress dynamic instability. *Biochemistry* 49, 1331-1337.
- Sonnen, K.F., Schermelleh, L., Leonhardt, H., and Nigg, E.A. (2012). 3D-structured illumination microscopy provides novel insight into architecture of human centrosomes. *Biol. Open.* 1, 965-976.
- Tang, C.J., Fu, R.H., Wu, K.S., Hsu, W.B., and Tang, T.K. (2009). CPAP is a cell-cycle regulated protein that controls centriole length. *Nat. Cell Biol.* 11, 825-831.
- Tang, C.J., Lin, S.Y., Hsu, W.B., Lin, Y.N., Wu, C.T., Lin, Y.C., Chang, C.W., Wu, K.S., and Tang, T.K. (2011). The human microcephaly protein STIL interacts with CPAP and is required for procentriole formation. *EMBO J.* 30, 4790-4804.
- Van der Vaart, B. et al. (2013). CFEOM1-associated kinesin KIF21A is a cortical microtubule growth inhibitor. *Dev. Cell* 27, 145-160.
- Walker, R.A., O'Brien, E.T., Pryer, N.K., Soboeiro, M.F., Voter, W.A., Erickson, H.P., and Salmon, E.D. (1988). Dynamic instability of individual microtubules analyzed by video light microscopy: rate constants and transition frequencies. *J. Cell Biol.* 107, 1437-1448.
- Widlund, P.O., Stear, J.H., Pozniakovsky, A., Zanic, M., Reber, S., Brouhard, G.J., Hyman, A.A., and Howard, J. (2011). XMAP215 polymerase activity is built by combining multiple tubulin-binding TOG domains and a basic lattice-binding region. *Proc. Natl. Acad. Sci. U. S. A* 108, 2741-2746.
- Zhang, R., Alushin, G.M., Brown, A., and Nogales, E. (2015). Mechanistic Origin of Microtubule Dynamic Instability and Its Modulation by EB Proteins. *Cell.*
- Zhao, L. et al. (2010). Dimerization of CPAP orchestrates centrosome cohesion plasticity. *J Biol. Chem.* 285, 2488-2497.
- Zheng, X. et al. (2014). Conserved TCP domain of Sas-4/CPAP is essential for pericentriolar material tethering during centrosome biogenesis. *Proc. Natl. Acad. Sci. U. S. A* 111, E354-E363.

Supplementary Figures

Suppl. Figure 1

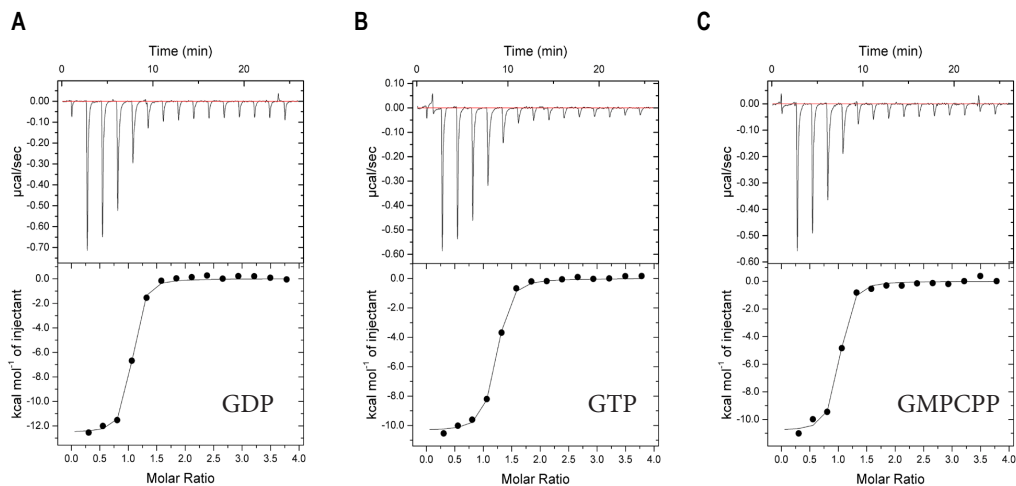


Figure S1, related to Figure 2. Effect of nucleotide state of tubulin on the interaction with PN2-3s. (A-C) ITC analysis of the interaction between PN2-3s and tubulin. Experiments were performed by step wise titration of $200 \mu\text{M}$ PN2-3s in the syringe into $10 \mu\text{M}$ tubulin in the cell. Upper panels display raw data; lower panels show the integrated heat changes and associated curve fits. The derived K_d values are as follows: 75 ± 12 nM for GDP-tubulin (A), 99 ± 13 nM for GTP-tubulin (B), and 97 ± 20 nM for GMPCPP-tubulin (C).

Suppl. Figure 2

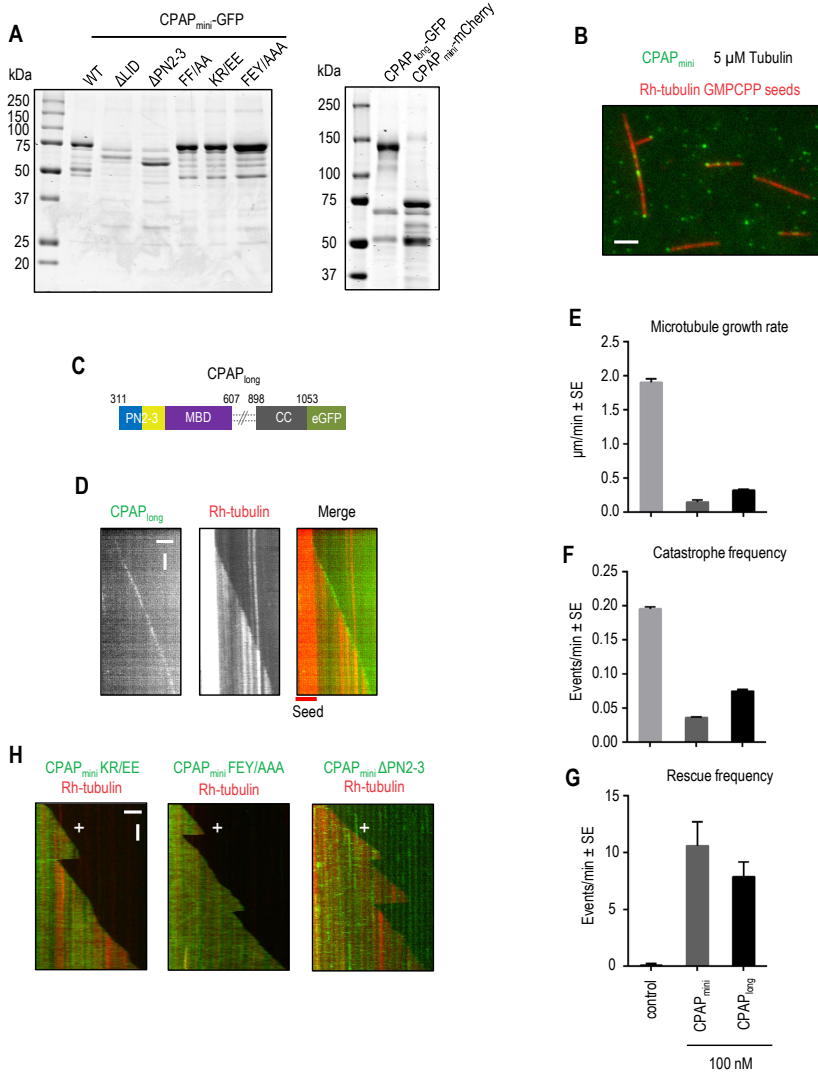


Figure S2, related to Figure 3. Characterization of the effect of CPAP_{mini} on microtubule dynamics in vitro.

(A) Coomassie blue stained gel with CPAP_{long}, CPAP_{mini} and its mutants purified from HEK293T cells.

(B) Localization of CPAP_{mini} (green) on rhodamine-labelled GMPCPP stabilized microtubules (red) in the presence of 5 μM tubulin. Although no microtubule growth is observed in these conditions, CPAP_{mini} preferentially binds to one microtubule end, indicating that its plus-end localization does not depend on microtubule polymerization.

(C) Schematic of the CPAP_{long} construct.

(D) Kymograph of microtubule growth at the plus (+) end from a rhodamine-GMPCPP seed with 100 nM CPAP_{long}. Scale bars, 2 μm (horizontal) and 60 s (vertical).

(E-G) Microtubule plus-end growth rates, catastrophe and rescue frequencies in the presence of rhodamine-tubulin alone or together with CPAP_{mini}-GFP or CPAP_{long}-GFP.

(H) Representative dual-color kymographs showing microtubule plus end dynamics for microtubules grown in the presence of rhodamine-tubulin together with the indicated CPAP_{mini} variants.

Suppl. Figure 3

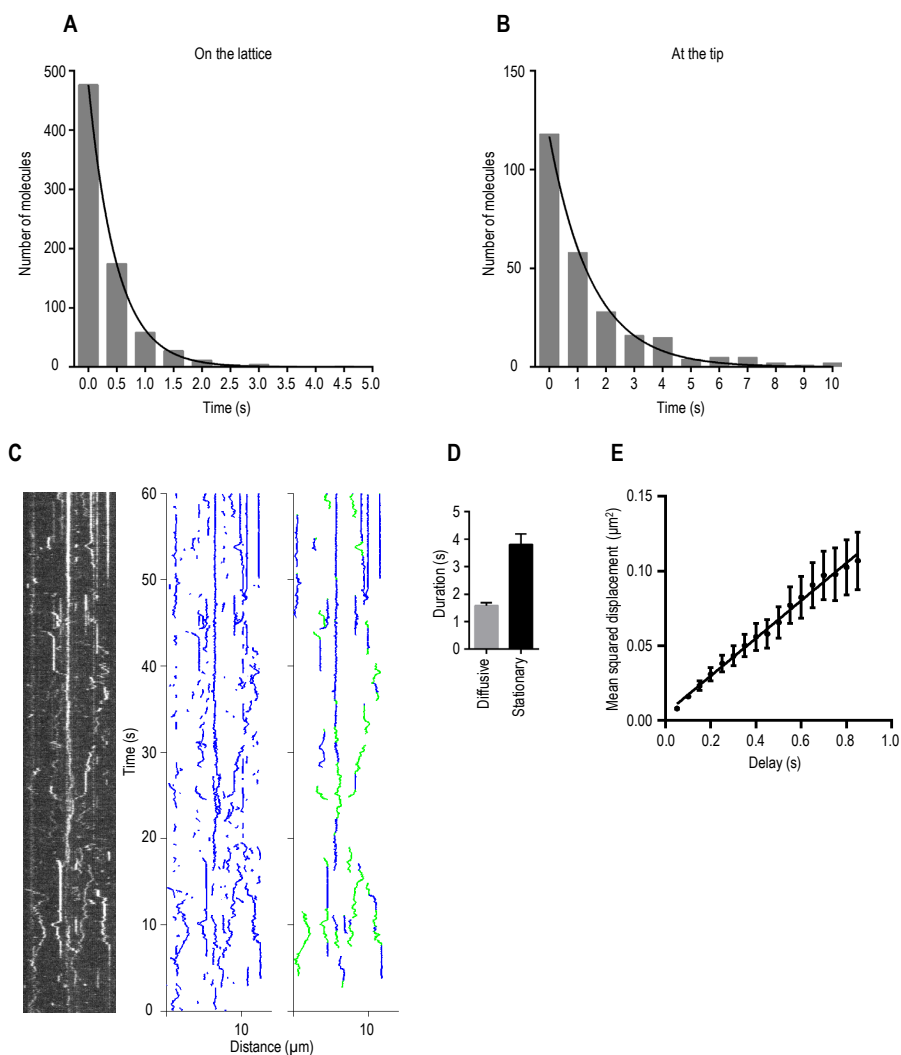


Figure S3, related to Figure 4. Characterization of CPAPmini single molecule behavior at the tip and on the lattice of dynamic microtubules.

(A-B) Exponential fits of the distributions of dwell times on the microtubule lattice (A) and at the tip (B) for single molecules of CPAPmini-GFP.

(C) Representative kymograph illustrating CPAPmini-GFP movement on a microtubule (left), corresponding reconstructed tracking results of individual molecules ($n=192$) (middle), the same tracks filtered for duration (>1.5 s) and color coded depending on the motion behavior: stationary (blue) and diffusive (green) segments ($n=29$) (right).

(D) Average duration of stationary and diffusive stages of CPAPmini-GFP motion ($n=134$, $n=139$).

(E) Average mean squared displacement of the diffusive fragments of tracks shown in (C); the line represents linear fit. Error bars represent SEM.

Suppl. Figure 4

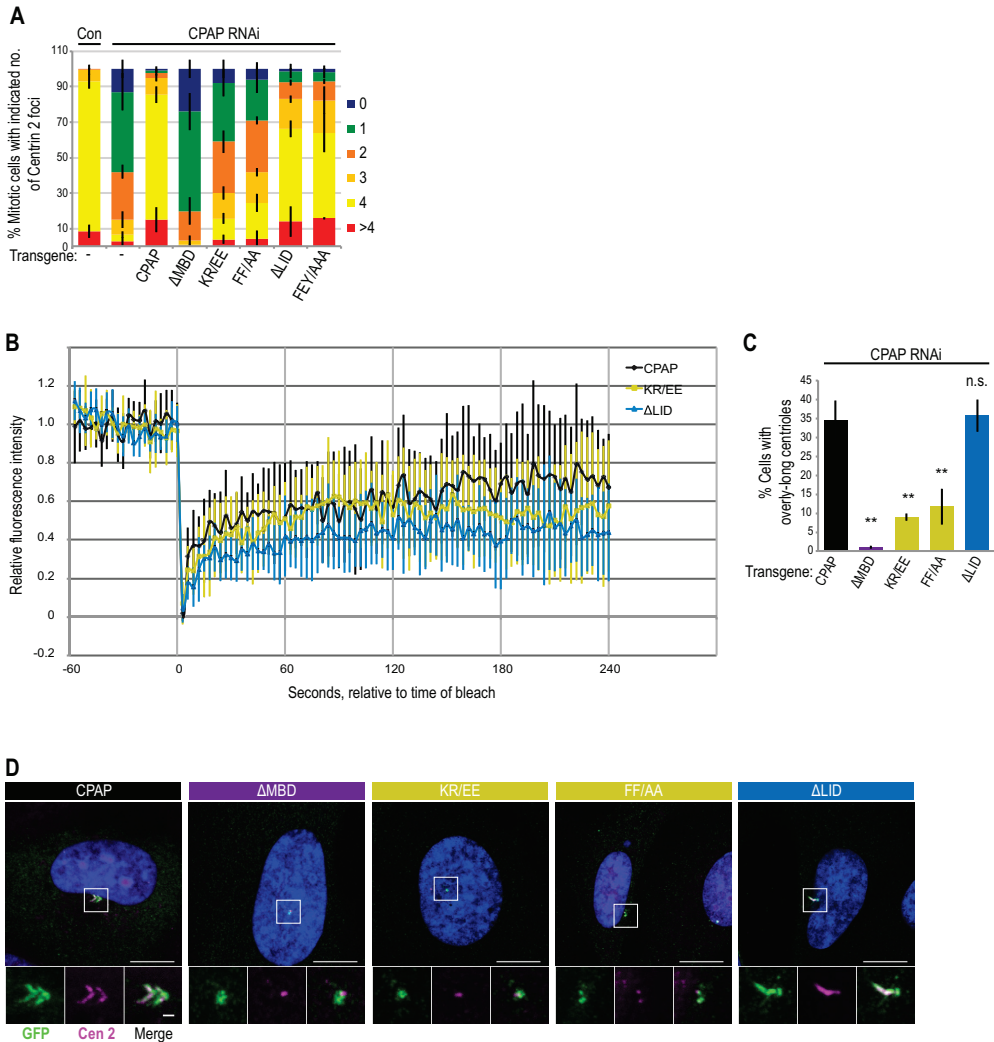


Figure S4, related to Figure 5. CPAP SAC domain and MBD, but not the LID domain, are required for centriole over-elongation

(A) Centrin 2 foci scored in mitotic cells expressing the indicated YFP-CPAP variants and depleted of endogenous CPAP by RNAi. Same experiment as shown in Figure 5I, but with all categories displayed. Error bars show the standard deviation of at least 3 experimental replicates, $n > 100$ cells for each sample.

(B) U2OS *FlyIn* TREX cell lines conditionally expressing indicated YFP-CPAP variants subjected to CPAP RNAi and transgene induction for 72 hours before FRAP analysis. Graph shows mean values, normalized to the mean of the averaged pre-bleach frames for each sample. $N = 11$ (wild type CPAP and KR/EE), and $n = 13$ (Δ LID). Time relative to bleach indicated in seconds. Error bars indicate the standard deviation for each time point.

(C, D) U2OS episomal cell lines conditionally expressing indicated GFP-CPAP variants and depleted of endogenous CPAP using RNAi were fixed and stained with anti-GFP and anti-Centrin 2 antibodies 72 hours after RNAi and transgene induction. Scale bar, 10 μ m, and 1 μ m in insets. Boxes indicate enlarged regions.

(C) Proportion of cells with overly long centrioles amongst cells that contain at least one centriole. Note that in all conditions where cells harbored fewer centrioles (see Figure 6A), overly long centrioles were observed less frequently. Average of 3 experimental replicates shown, $n > 100$ cells per experiment. Error bars show standard deviation. Students' paired two-tailed *t*-test comparing each cell line to the CPAP wild type control: ** indicates $p < 0.01$.

Suppl. Figure 5

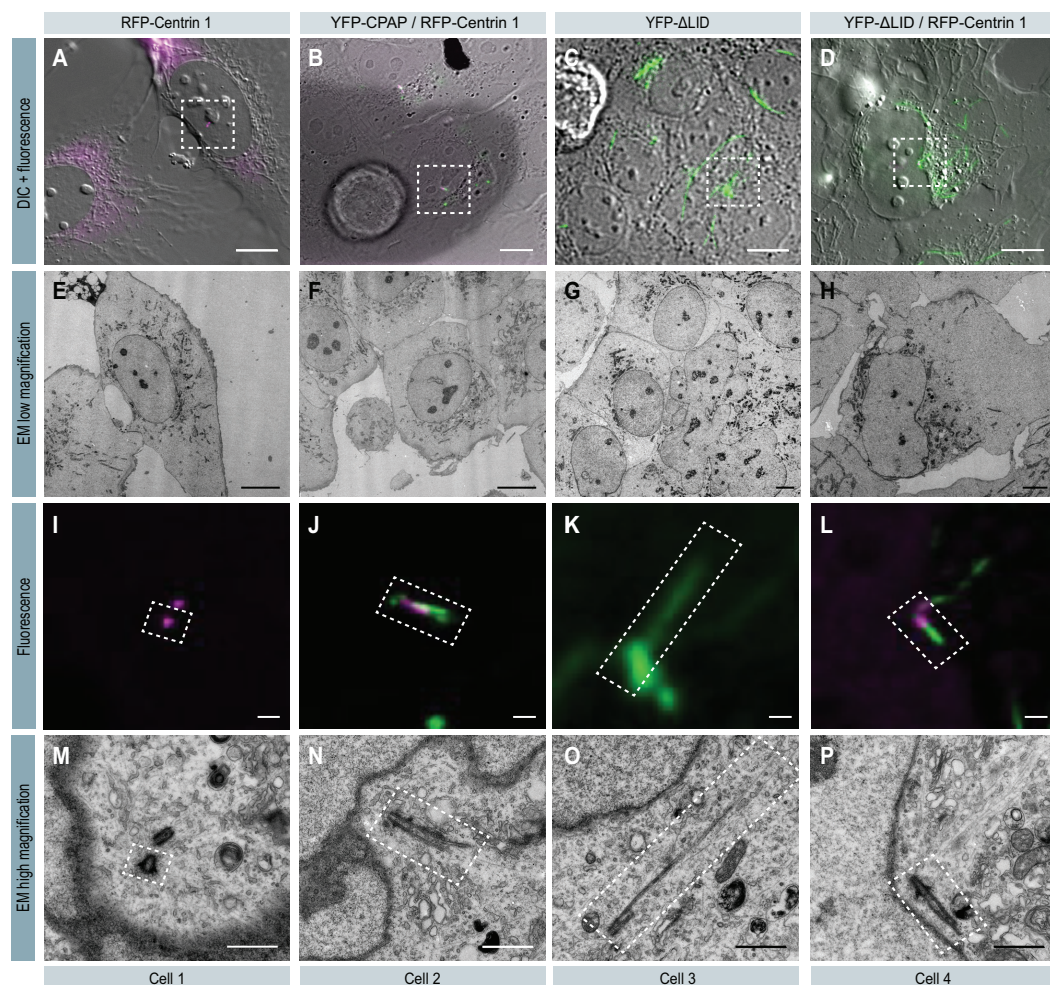


Figure S5, related to Figure 7. Correlative light and electron microscopy of cells expressing YFP-CPAP and YFP-ΔLID

(A-D) Differential interference microscopy (DIC) and fluorescence (YFP, RFP, or both) images of the cells shown in Figure 7. Scale bar, 10 μm . Boxes indicate regions shown in I-P.

(E-H) Corresponding low magnification electron microscopy (EM) images of the above cells of interest. Scale bars, 10 μm .

(I-L) High magnification fluorescence images of the regions of interest indicated in (A, E, I, M). Scale bar, 1 μm . Boxes indicate regions shown in Figure 7.

(M-P) High magnification EM images of the regions shown in (C, G, K, O). Scale bars, 1 μm . Boxes indicate regions shown in Figure 7.

Suppl. Figure 6

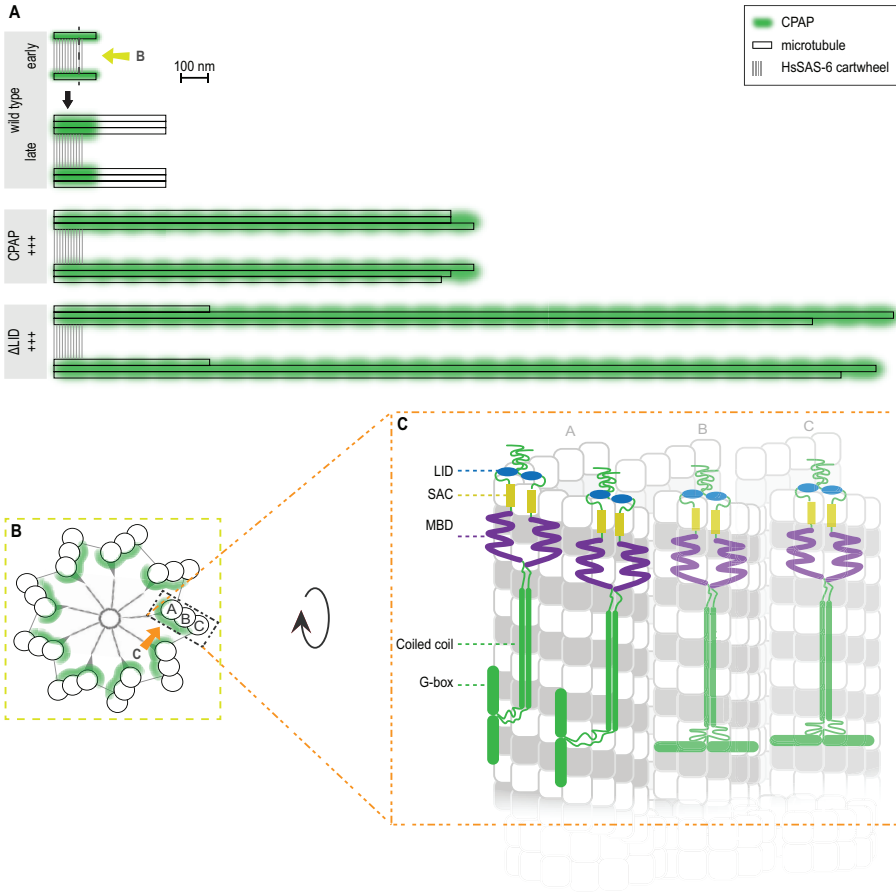


Figure S6, related to Figure 7. Working model of CPAP's mechanism of action in the context of centrioles.

(A) CPAP (green) is recruited after the assembly of the HsSAS-6-containing cartwheel (gray lines) and the first microtubule (black rectangle). At these early stages of procentriole formation, CPAP is located in the region of the cartwheel and extends slightly more distally. It is during these early stages that CPAP is expected to normally exert its regulation of centriolar microtubule growth. At later stages, CPAP remains in the proximal region of the wild type centriole. Upon overexpression of CPAP (CPAP +++), excess protein localizes along the full length of the centriole, causing over-elongation of centriolar microtubules and the entire distal centriole structure that contains Centrin 1 and 2, and POC5. Overexpression of CPAP- Δ LID (Δ LID +++) results in abnormally elongated centriolar microtubules, which are longer, on average, than the overly-long centrioles observed upon CPAP overexpression, more variable in length, and also lack distal centriole markers such as Centrin and POC5. We refer to these structures as centriole fibers. Light green arrow indicates the direction of view for panel B.

(B) Schematic of a cross section of the centriole looking at the cartwheel-containing region from the distal end. A, B, and C indicate one triplet microtubules. Green indicates the expected position of CPAP, and the orange arrow the direction of view for panel C.

(C) View of the inside surface of a centriolar microtubule triplets with a schematic representation of the

the position of CPAP dimers (green). CPAP domains are labeled. CPAP dimers located at the tip of the microtubules have their LID domains bound at the end of the β -tubulin subunit, therefore restricting binding of new tubulin dimers to the growing microtubule plus end. CPAP dimers located further down the lattice no longer have their LID domains engaged with tubulin dimers, as the binding interface is occluded, but the SAC and MBD regions still interact with microtubules (not shown). Note that the G-box of the CPAP dimers located on the left are facing inwards the centriole to denote its known interaction with STIL. Note also that whether CPAP is present on all three microtubules in the triplet, and, if so, in how many copies, is not known at present.

Supplementary Tables

Table S1, related to Figures 1, 2, 3 and 5. Constructs used in this study.

Constructs used for structural and biophysical studies	
PN2-3	HsCPAP 311-422
PN2-3s	HsCPAP 319-394
FF/AA	PN2-3 F375A F385A
KR/EE	PN2-3 K377E R378E
FEY/AAA	PN2-3 F338A E399A Y341A
LIDp	PN2-3 311-372
SACp	PN2-3 370-386
Constructs used for in vitro reconstitution studies	
CPAP _{mini}	HsCPAP 311-607 GCN4-TEV-eGFP
CPAP _{mini} ΔPN2-3	CPAP _{mini} D311-421
CPAP _{mini} ΔLID	CPAP _{mini} D311-369
CPAP _{mini} FF/AA	CPAP _{mini} F375A F385A CPAP _{mini}
KR/EE	CPAP _{mini} K377E R378E CPAP _{mini}
FEY/AAA	CPAP _{mini} F338A E399A Y341A
CPAP _{mini} ΔMBD	CPAP _{mini} D423-607
CPAP _{long}	HsCPAP 312-1053 eGFP
Constructs used for in cellulo studies	
CPAP	HsCPAP
CPAPΔLID	CPAP D337-350
CPAPFF/AA	CPAP F375A F385A CPAP
KR/EE	CPAP K377E R378E CPAP
ΔMBD	CPAP D423-607

Table S2, related to Figure 1. X-Ray Data Collection and Refinement Statistics.

Data Collection^a	
Wavelength, Å	1
Space group	P 1 21 1
Resolution range, Å ^b	51.2 - 2.2 (2.28 - 2.2)
Unit cell a, b, c (Å) a, b, g (°)	61.08 85.34 98.69 90 91.77 90
No. of observed reflections	343192 (34254)
No. of unique reflections	51516 (5113)
Mean I/sigma(I)	18.11 (3.19)
R-merge	0.07782 (0.7067)
R-meas	0.09149
CC _{1/2} ^c	0.999 (0.87)
CC*	1 (0.964)
Refinement	
R-work	0.1744 (0.2656)
R-free	0.2197 (0.3144)
Number of Macromolecules	7716
Number of Ligands	90
Number of Waters	476
Number of Protein residues	990
RMS(bonds) (Å)	0.021
RMS(angles) (°)	1.03
Ramachandran favored (%) ^d	98
Ramachandran outliers (%) ^d	0.1
B-factors	
Average B-factor	46.57
Macromolecules	46.94
Ligands	35.26
Solvent	42.77

^a Highest resolution shell statistics are in parentheses.
^b Resolution cutoffs were chosen based on CC_{1/2} and Mean I/sigma(I) (Karplus and Diederichs, 2012)
^c As defined by Karplus and Diederichs (Karplus and Diederichs, 2012)
^d As defined by MolProbity (Davis et al., 2004)

Table S3, related to Figure 4. Characteristics of CPAP_{mini}-GFP motion.

Parameter	Mean ± SEM
Average duration of stationary fragment (s)	1.58 ± 0.01
Average duration of diffusive motion (s)	3.81 ± 0.38
Fraction of time spent in diffusive motion (%)	19.7
Diffusion coefficient (μm ² /s)	0.0257 ± 0.0004
Total number of tracks before filtering	5130
Total number of tracks after filtering	550
Total number of kymographs analyzed	37

Supplementary Experimental Procedures

Protein and peptide preparation

The PN2-3 domain of human CPAP (residues 311-422) and its shorter variant PN2-3s (residues 319-394) were PCR amplified from a HsCPAP clone (Kitagawa et al., 2011) and inserted into the PSTCm1 vector (Olieric et al., 2010) with a N-terminal 6xHis-tag. The DARPin D1 (Pecqueur et al., 2012) was synthesized (GENEWIZ Inc.) and cloned in a T7 pET-based expression vector (Kammerer et al., 1998) with a N-terminal 6xHis-tag. The various CPAP constructs and mutants used in the study are described in Table S1. All PN2-3 mutants were obtained by PCR based mutagenesis. All clones were sequence verified.

Standard protein expression was carried out in the *E. coli* strain BL21(DE3) by induction with 1 mM IPTG at 20°C. Cells were lysed in a lysis buffer containing 50 mM Tris-HCl, pH 7.5, supplemented with 500 mM NaCl, 10% Glycerol, 10 mM imidazole, 1 mM beta-mercaptoethanol and protease inhibitor cocktail (Roche). Proteins were purified by IMAC using HiTrap Ni-NTA columns (GE Healthcare) followed by size exclusion chromatography on a Superdex 16/60 S75 column. SACp was prepared synthetically using standard peptide synthesis methodology.

Crystallization and structure determination

Bovine brain tubulin was purchased from the Centro de Investigaciones Biológicas (Microtubule Stabilizing Agents Group), CSIC, Madrid, Spain. The flexible C-terminal tails of tubulin were cleaved using subtilisin as described previously (Knipling et al., 1999). Briefly, tubulin was buffer exchanged using a PD-10 desalting column (GE Healthcare) to a buffer containing 10 mM MES pH 6.9, 0.1 mM MgCl₂, 0.1 mM EGTA and 1mM of GTP. Subtilisin (Sigma Cat. no. P8038) was added in a weight ratio of 1:100 to a tubulin solution (3 mg/ml) and incubated for 45 minutes at 25 °C. Cleavage was stopped by adding 1 mM PMSF. The reaction mixture was further incubated on ice for 30 minutes followed by centrifugation for 30 minutes at 300,000 x g using an MLA-130 rotor (Beckman Coulter). The supernatant was collected and cleavage efficiency was accessed by a Coomassie stained 7.5% SDS PAGE (Banerjee et al., 2010). The cleaved tubulin was buffer-exchanged to BRB80 (PIPES-KOH, pH 6.8, supplemented with 80 mM, 1 mM MgCl₂, 1 mM EGTA) using a PD-10 desalting column (GE Healthcare).

Equimolar amounts of D1, PN2-3 and subtilisin-treated tubulin were mixed and the PN2-3-tubulin-D1 complex was concentrated to ~20 mg/ml using a Centriprep device (Mw cutoff 5 kDa; Amicon). PN2-3-tubulin-D1 samples were complemented with 0.2 mM GDP, 1 mM Colchicine and 5 mM DTT before setting up sitting drop vapor diffusion crystallization trials. Crystals were obtained in a condition containing 20% PEG 550 mono methyl ether (MME) and 0.1 M MES, pH 6.5. Precipitant solution supplemented with 10% glycerol was used as a cryo-protectant for freezing crystals. X-ray diffraction data were collected at 100K at beamline X06DA at the Swiss Light Source (Paul Scherrer Institut, Villigen, Switzerland), and were then processed and merged with XDS (Kabsch, 2010).

The PN2-3-tubulin-D1 structure was solved by molecular replacement using the αβ-tubulin-D1 complex structure as a search model (PDB ID 4DRX) and the program Phaser provided in the Phenix

software suite (McCoy et al., 2007). The models were first refined with rigid body refinement and simulated annealing refinement in Phenix (Adams et al., 2010). In the refined structure, the difference electron density for PN2-3 allowed us to model the specific residues of the SAC box using Coot (Emsley and Cowtan, 2004). The resulting model was refined by iterative cycles of model building in Coot and refinement in Phenix. The quality of the structures was assessed with MolProbity (Chen et al., 2010) and figures were prepared using PyMOL (The PyMOL Molecular Graphics System, version 1.4.1; Schrödinger, LLC). Data collection and refinement statistics are given in Table S2. and refinement in Phenix. The quality of the structures was assessed with MolProbity (Chen et al., 2010) and figures were prepared using PyMOL (The PyMOL Molecular Graphics System, version 1.4.1; Schrödinger, LLC). Data collection and refinement statistics are given in Table S2.

ITC experiments

For exchanging the nucleotide of tubulin, bovine brain tubulin was buffer exchanged to a buffer containing 80 mM PIPES-KOH, pH 6.8, supplemented with 1mM EDTA using a PD-10 desalting column (GE Healthcare). 2 mM of GDP, GTP or GMPCPP was added to the samples that were incubated on ice for 10 minutes. Excess nucleotide was removed by another step of buffer exchange using a PD-10 desalting column pre-equilibrated with BRB80 buffer supplemented with 0.5 mM TCEP. PN2-3 variants were buffer exchanged to BRB80 buffer supplemented with 0.5 mM TCEP by overnight dialysis at 4°C.

Standard ITC experiments were performed at 25 °C using an ITC200 system (Microcal). 0.1–0.4 mM PN2-3 variants in the syringe were injected step-wise into a 10–20 μM tubulin solution in the cell. Experiments with tubulin-D1 in the presence of Eribulin (Eisai Co., Ltd) and Maytansine (National Institutes of Health, Open Chemical Repository Collection) were obtained by incubating equimolar amounts of tubulin and ligand at 4°C for 15 minutes before setting up the ITC experiment. The resulting heats were integrated and fitted in Origin (OriginLab) using the standard ‘one set of sites’ model provided by the software package.

5 Protein purification for in vitro reconstitution assays

CPAP_{long}-GFP and CPAP_{mini}-GFP variants used in the in vitro reconstitutions assays (Table S1) were purified from HEK293T cells using the Strep(II)-streptactin affinity purification. Cells were harvested 2 days post transfection. Cells from a 25 cm dish were lysed in 500 μl of lysis buffer (50 mM HEPES, 300 mM NaCl and 0.5% Triton X-100, pH 7.4) supplemented with protease inhibitors (Roche) on ice for 10 minutes. The supernatant obtained from the cell lysate after centrifugation at 16,000 x g for 20 minutes was incubated with 40 μl of StrepTactin Sepharose beads (GE) for 1 hour. The beads were washed 3 times in the lysis buffer without the protease inhibitors. The protein was eluted with 40 μl of elution buffer (50 mM HEPES, 150 mM NaCl, 1 mM MgCl₂, 1 mM EGTA, 1 mM dithiothreitol (DTT), 2.5 mM d-Desthiobiotin and 0.05% Triton X-100, pH 7.4). Purified proteins were snap-frozen and stored at -80 °C. Bacterially expressed mCherry-EB3 was produced as described previously (Montenegro Gouveia et al., 2010) and mCherry-CAMSAP3 was produced in HEK293T cells as described previously (Jiang et al., 2014).

In vitro reconstitution assay

Reconstitution of microtubule growth dynamics in vitro was performed as described previously (Montenegro Gouveia et al., 2010). GMPCPP microtubule seeds (70% unlabeled tubulin, 18% biotin tubulin and 12% rhodamine tubulin) were prepared as described before (Gell et al., 2010). Flow chambers, assembled from plasma-cleaned glass coverslips and microscopic slides were functionalized by sequential incubation with 0.2 mg/ml PLL-PEG-biotin (Susos AG, Switzerland) and 1 mg/ml NeutrAvidin (Invitrogen) in MRB80 buffer (80 mM piperazine-N,N[prime]-bis(2-ethanesulfonic acid), pH 6.8, supplemented with 4 mM MgCl₂, and 1 mM EGTA. The microtubule seeds were attached to coverslips through biotin-NeutrAvidin interactions. Flow chambers were further blocked with 1 mg/ml κ-casein. The reaction mix with or without CPAP_{mini} proteins (MRB80 buffer supplemented with 15

μM porcine brain tubulin, 0.5 μM rhodamine-tubulin, 50 mM KCl, 1 mM guanosine triphosphate, 0.2 mg/ml κ -casein, 0.1% methylcellulose, and oxygen scavenger mix [50 mM glucose, 400 $\mu\text{g}/\text{ml}$ glucose oxidase, 200 $\mu\text{g}/\text{ml}$ catalase, and 4 mM DTT]) was added to the flow chamber after centrifugation in an Airfuge for 5 minutes at $119,000 \times g$. For experiments in the presence of EB3, concentration of mCherry-EB3 was 20 nM and rhodamine-tubulin was excluded from the assay. Rhodamine-tubulin was also excluded from the assay with CPAPmini-GFP and mCherry-CAMSAP3. The flow chamber was sealed with vacuum grease, and dynamic microtubules were imaged immediately at 30 °C using Total Internal Reflection Fluorescence (TIRF) microscopy. All tubulin products were from Cytoskeleton Inc.

TIRF microscopy

The in vitro reconstitutions assays were imaged on a TIRF microscope setup as described in (Mohan et al., 2013) or on an iLas2 TIRF setup. In brief, we used an inverted research microscope Nikon Eclipse Ti-E with the perfect focus system, equipped with Nikon CFI Apo TIRF 100x 1.49 N.A. oil objective and controlled with MetaMorph 7.7.5 software (Molecular Devices). The microscope was equipped with TIRF-E motorized TIRF illuminator modified by Roper Scientific France/PICT-IBiSA, Institut Curie. To keep the in vitro samples at 30 °C, a stage top incubator model INUBG2E-ZILCS (Tokai Hit) was used. For excitation, 491 nm 100 mW Calypso (Cobolt) and 561 nm 100 mW Jive (Cobolt) lasers were used. We used ET-GFP 49002 filter set (Chroma) for imaging of proteins tagged with GFP or ET-mCherry 49008 filter set (Chroma) for imaging of proteins tagged with mCherry. Fluorescence was detected using an EMCCD Evolve 512 camera (Roper Scientific) with the intermediate lens 2.5X (Nikon C mount adapter 2.5X) or using the CoolSNAP HQ2 CCD camera (Roper Scientific) without an additional lens. In both cases the final magnification was 0.063 $\mu\text{m}/\text{pixel}$. iLas2 system (Roper Scientific, Evry, France) is a dual laser illuminator for azimuthal spinning TIRF illumination and with a custom modification for targeted photomanipulation. This system was installed on the Nikon Ti-E microscope with the perfect focus system, equipped with 150 mW 488 nm laser and 100 mW 561 nm laser, 49002 and 49008 Chroma filter sets, EMCCD Evolve mono FW DELTA 512x512 camera (Roper Scientific) with the intermediate lens 2.5X (Nikon C mount adapter 2.5X), CCD camera CoolSNAP MYO M- USB-14-AC (Roper Scientific) and controlled with MetaMorph 7.8.8 software (Molecular Device). To keep the in vitro samples at 30°C, a stage top incubator model INUBG2E-ZILCS (Tokai Hit) was used. The final resolution using Evolve EMCCD camera was 0.065 $\mu\text{m}/\text{pixel}$, using CoolSNAP Myo CCD camera it was 0.045 $\mu\text{m}/\text{pixel}$.

5

Analysis of microtubule plus end dynamics in vitro

Kymographs were generated using the ImageJ plugin KymoResliceWide (<http://fiji.sc/KymoResliceWide>). Microtubule dynamics parameters were determined from kymographs using an optimized version of the custom made JAVA plug in for ImageJ as described previously (Jiang et al., 2014; Montenegro Gouveia et al., 2010; Taylor, 1997). ~100-200 microtubule growth events were analyzed per condition.

Intensity analysis for CPAPmini along microtubules

Intensity profiles extraction and alignment of rhodamine-tubulin and CPAP_{mini} were performed using a custom written Matlab routine. First, we obtained the average intensity of microtubule profile along a 4-pixel wide line using the rhodamine-tubulin channel. The same line was used to obtain an intensity profile in the CPAP_{mini} (GFP) channel. After background subtraction, each intensity profile $I(x)$ was normalized:

$$I_{norm}(x) = \frac{I(x) - I_{min}}{I_{max} - I_{min}} \cdot 100\% \quad I_{normalized} = \left(\frac{I - I_{min}}{I_{max} - I_{min}} \right) \times d$$

with respect to the maximum and minimum intensity values along the whole profile. The normalized intensity profiles of different microtubules were aligned so that the plus end tip position was at the origin of the coordinates (Figure 3C). The plus end position was determined by fitting the rhodamine-

tubulin profile to a Gaussian survival function using equation:

$$I_{norm}(x) = \frac{1}{2} I_{MT} \operatorname{erfc}\left(\frac{x - x_{PF}}{\sqrt{2}\sigma_{PF+PSF}}\right) + I_{BG}$$

where erfc is the complimentary error function, I_{MT} and I_{BG} are average intensities of the microtubule and the background, x_{PF} is the position of plus end tip and σ_{PF+PSF} is the standard deviation of the microtubule tip taper combined with the one for the microscope point spread function.

Single-molecule fluorescence intensity analysis of CPAP_{mini}

Sample preparation for the fluorescence intensity analysis was performed by immobilizing diluted GFP or CPAP_{mini}-GFP proteins non-specifically to the plasma cleaned glass coverslips in flow chambers. After protein addition the flow chambers were washed with MRB80 buffer, sealed with vacuum grease and immediately imaged with a TIRF microscope. 10-20 images of previously unexposed coverslip areas were acquired with 100 ms exposure time and low laser power. GFP and CPAP_{mini}-GFP were located in different chambers of the same coverslip, so the same imaging conditions could be preserved. Single molecule fluorescence spots were detected and fitted with 2D Gaussian function using custom written ImageJ plugin DoM_Utrecht (https://github.com/ekatruxha/DoM_Utrecht). The fitted peak intensity values were used to build fluorescence intensity histograms.

Single molecule diffusion and kinetics analysis

The study of single molecule kinetics of CPAP_{mini} at the tip and lattice of dynamic microtubules was performed in the presence of 100 nM CPAP_{mini}-mCherry, 5 nM CPAP_{mini}-GFP and rhodamine tubulin. Kymographs were generated for each microtubule over 60 seconds with 50 millisecond intervals. The residence times at the microtubule tip and lattice were manually obtained from kymographs. Histograms of times for both conditions were fitted to a single exponential decay function in GraphPad Prism 6. The reported mean residence time at the lattice and tip were obtained from these fits. The mean residence time was corrected for photo bleaching as described (Helenius et al., 2006). The characteristic time constant of photobleaching was estimated by fitting the total field of view intensity of CPAP_{mini} movies over time to a single exponential decay function. The value of averaged photobleaching time constant over 15 movies was used for correction.

Coordinates of individual fluorescent spots of CPAP_{mini}-GFP diffusing along microtubule were derived from the detection performed using the ImageJ plugin DOM_Utrecht as described above. Detections were linked to 2D tracks using nearest neighbor linking algorithm of the same plugin with a search radius of 0.5-1 μm . Coordinates of all time points of all the tracks along the same microtubule were fitted to a straight line and subsequently projected on it resulting in 1D tracks. Only tracks longer than 1.5 seconds were considered. Mean squared displacement (MSD) analysis was performed using msdalyzer Matlab routine (Tarantino et al., 2014). To separate the periods of stationary and diffusive motion for each track MSD (τ) was calculated by internal averaging for a sliding window of 30 frames. The first 7 point (excluding zero) were used to fit $\text{MSD}(\tau) = 0.5D\tau + b$, with D termed the 1D diffusion coefficient and b as a localization precision error. For each fit we calculated the coefficient of determination R^2 characterizing the quality of fit. Track fragments where R^2 was above the threshold of 0.7 were considered as “diffusing state”, since the sliding window MSD fitted well with linear dependence (green tracks in Figure S3C, right panel). The rest of the track was considered being in the “stationary state” (blue fragments in Figure S3C, right panel). The diffusion coefficient reported in Supplementary Table S3 was calculated by averaging all D values from all fits where $R^2 > 0.7$ ($n = 8959$).

CPAP_{mini} molecule counting at microtubule tips

To determine the number of molecules of CPAP_{mini} at a microtubule tip, we immobilized single molecules of CPAP_{mini} onto the coverslip of one of the flow chambers and performed the in vitro reconstitution assay

in the adjacent chamber of the same coverslip. Images of unbleached CPAP_{mini} single molecules were acquired first and using the same imaging/illumination conditions, time lapse imaging was performed on the in vitro assay with CPAP_{mini} using 100 ms exposure and 2 second intervals for 5 minutes. The plus end localized CPAP_{mini} molecules were manually located in each frame and fitted with 2D Gaussian, the amplitude of which was used for the intensity analysis. To build the distributions of CPAP_{mini} molecule numbers at the microtubule tip, each CPAP_{mini} intensity value at the microtubule plus end was normalized by the average CPAP_{mini} single molecule intensity from the adjacent chamber.

Statistical Analysis

The relative standard error for catastrophe frequency was calculated as described (Taylor, 1997). The relative standard error of mean rescue frequency in the experiments with CPAPmini constructs was calculated in the same way as the standard error of the mean catastrophe frequency, i.e.

$$SE_r = \bar{f}_r \frac{SE_{t_{sh}}}{\bar{t}_{sh}}$$

,where \bar{f}_r, \bar{t}_{sh} are average values and $SE_{f_r}, SE_{t_{sh}}$ are standard errors of rescue frequency and shortening time respectively. The number of observed rescue events for control was relatively small as compared to the catastrophes, so we assumed that they follow a Poisson distribution. The standard deviation of the rescue frequency was calculated as the square root of fits mean value and the standard error was calculated according to

$$SE_{f_r} = \frac{\sqrt{\bar{f}_r}}{\sqrt{N_r}}$$

where \bar{f}_r and SE_{f_r} are the average and the standard error of the rescue frequency and N_r is the number of rescues (Smal et al., 2009).

Generation of expression vectors for cell biology

A cDNA encoding siRNA resistant CPAP was cloned into pENTR 1A, as previously described (Kitagawa et al., 2011). This vector was used for site directed mutagenesis reactions to produce KR/EE and FF/AA mutations using Quikchange Site Directed Mutagenesis kit (Agilent). Deletions Δ LID and Δ MDB were generated using Phusion polymerase (NEB). For deletion mutants, linear PCR products were generated with 10 bp overlapping regions and ligated using CloneEZ (GenScript). Entry vectors were then used in LR Clonase reactions (Invitrogen) with pEBTet-EGFP-GW (Kitagawa et al., 2011) or pcDNA5FRT/TO-YFP-GW (gift from Zuzana Hořejší) to produce expression vectors. All Entry clones were sequence-verified.

Cell culture, transfections, cell line generation, and siRNAs

U2OS cells were cultured in high-glucose DMEM with GlutaMAX (Invitrogen) supplemented with 10% fetal calf serum (FCS) in a humidified 5% CO₂ incubator at 37 °C. To generate inducible cell lines with the pEBTet-EGFP vector, cells were transfected with the appropriate vectors using Lipofectamine 2000 (Invitrogen) and selected using 1 μ g/ml puromycin 24 hours after transfection, as previously described (Kitagawa et al., 2011). For generating stable integrated cell lines, we used a U2OS FlpIn TREX cell line, a gift from Erich Nigg (Arquint and Nigg, 2014). U2OS FlpIn TREX cells were transfected using Lipofectamine 2000 with a 3:1 ratio of pcDNA5-FRT/TO-YFP-CPAP vectors:pOG44 (Invitrogen Flp-In System). Cells were selected using 100 μ g/ml Hygromycin B and 10 μ g/ml Blastidicin (both from InvivoGen) for 1-2 weeks, until all untransfected cells were dead. For both types of cell line, 1 μ g/ml doxycycline was used to induce transgene expression (Sigma- Aldrich). CPAP RNAi was carried out at 60 nM as previously described (Kitagawa et al., 2011) and Stealth siRNA Negative Control Lo GC was used as a negative control, also at 60 nM. Unless otherwise indicated, RNAi was carried out for 72 hour before fixation of the cells, with simultaneous induction of transgene expression with 1 μ g/ml Doxycycline.

Note that cells expressing KR/EE often exhibited large globular YFP aggregates, but never microtubule decoration, perhaps explaining the absence of centrosomal fibers in this mutant compared to FF/AA (see Figure 6A).

Correlative light and electron microscopy (CLEM)

Cells were cultured on glass coverslips coated on one side with a 3 nm thick layer of carbon, with an additional layer of 10 nm thickness to reveal a gridded pattern with a coordinate system of letters for locating the cell of interest by light microscopy, and also once the cells were resin embedded. Endogenous CPAP was depleted by RNAi for 72 hours, simultaneous with induction of the transgene. For dual marker experiments, cells were transfected with a tagRFP-Centrin 1 expression vector 16 hours prior to fixation (Keller et al., 2014). Cells were fixed in a solution of 0.1 % glutaraldehyde and 2.0 % paraformaldehyde in 0.1 M phosphate buffer, pH 7.4, for 2 hours, then washed thoroughly with cacodylate buffer (0.1 M, pH 7.4), and imaged by wide field light microscopy using a Zeiss Plan-Apochromat 63 x oil-immersion objective, NA 1.40. Z-sections were imaged at an interval of $\sim 0.3 \mu\text{m}$. Fluorescence images shown in Figure 7 are single plane images deconvolved using Huygens Core 15.10 software (Scientific Volume Imaging, SVI) through the web interface Huygens Remote Manager. A theoretical Point Spread Function (PSF) was used in combination with the “Classic Maximum Likelihood Estimation” algorithm, an automatic background estimation and stopping criteria of 40 iterations and 0.1 quality change. The deconvolution settings and signal to noise ratios were set according to SVI’s recommendations. Immediately after imaging, samples were post-fixed for 40 minutes in 1.0 % osmium tetroxide, then 30 minutes in 1.0% uranyl acetate in water, before being dehydrated through increasing concentrations of alcohol and then embedded in Durcupan ACM resin (Fluka, Switzerland). The coverslips were then placed face down on a glass slide coated with mold releasing agent (Glorex, Switzerland), with approximately 1 mm of resin separating the two. The resin was initially hardened for 12 hours in a 65 °C oven and then the coverslips detached from the resin by immersing them alternately into hot (60 °C) water followed by liquid nitrogen. The smooth resin surface, with the cells embedded, also showed the grid pattern, which was used to locate the region of interest imaged by light microscopy. These regions were mounted on blank resin blocks with acrylic glue and trimmed with glass knives to form a block ready for serial sectioning. Series of between 150 and 300 thin sections (50 nm thickness) were cut with a diamond knife mounted on an ultramicrotome (Leica UC7), and collected onto single-slot, copper grids with a pioloform support film. These sections were contrasted with lead citrate and uranyl acetate, and images taken using an FEI Spirit TEM with Eagle CCD camera. Images of each cell of interest were taken on every section in which it appeared and these images aligned using Photoshop (Adobe). The aligned series was then matched with the light microscopy images to correlate the position of the fluorescent signal with the underlying ultrastructure.

Fluorescence Recovery After Photo-bleaching (FRAP)

Cells were grown in glass bottomed cell culture dishes (Matek) and imaged in a humidified 5% CO₂ incubator at 37 °C in DMEM high glucose medium without phenol red (GE Healthcare), supplemented with 15% FCS, 20 mM HEPES buffer (Gibco), 1 mM sodium pyruvate (Sigma), and Penicillin/Streptomycin (Gibco). We used a Zeiss LSM 710 with an N-Achromat 63x water immersion objective NA 0.90, controlled with Zeiss Zen software to bleach a circular region of 25 pixel diameter (pixel size 0.14 μm) around the centrosome using 10 iterations with the 514 nm laser at 100%, and acquisition of a 60 x 60 pixel region with a pixel dwell time of 2.77 μsec and 2 x averaging. Cells were imaged every 3 seconds, for one minute pre- and 4 minutes post-bleach. Analysis was carried out using Image J, with a plugin to automatically detect a circular region of interest of 15 pixel diameter using a Gaussian blurring factor of 5 and the brightest pixel to center the region of interest. Before measuring fluorescence intensity, the regions of interest were manually curated to ensure that the centrosome was contained within it. All FRAP curves were normalized to the average of the first 20 pre-bleach intensities.

Supplemental References

- Adams, P.D. et al. (2010). PHENIX: a comprehensive Python-based system for macromolecular structure solution. *Acta Crystallogr. D. Biol. Crystallogr.* 66, 213-221.
- Arquint, C. and Nigg, E.A. (2014). STIL microcephaly mutations interfere with APC/C-mediated degradation and cause centriole amplification. *Curr. Biol.* 24, 351-360.
- Azimzadeh, J., Hergert, P., Delouvee, A., Euteneuer, U., Formstecher, E., Khodjakov, A., and Bornens, M. (2009). hPOC5 is a centrin-binding protein required for assembly of full-length centrioles. *J. Cell Biol.* 185, 101-114.
- Banerjee, A., Bovenzi, F.A., and Bane, S.L. (2010). High-resolution separation of tubulin monomers on polyacrylamide minigels. *Anal. Biochem.* 402, 194-196.
- Chen, V.B., Arendall, W.B., III, Headd, J.J., Keedy, D.A., Immormino, R.M., Kapral, G.J., Murray, L.W., Richardson, J.S., and Richardson, D.C. (2010). MolProbity: all-atom structure validation for macromolecular crystallography. *Acta Crystallogr. D. Biol. Crystallogr.* 66, 12-21.
- Davis, I.W., Murray, L.W., Richardson, J.S., and Richardson, D.C. (2004). MOLPROBITY: structure validation and all-atom contact analysis for nucleic acids and their complexes. *Nucleic Acids Res.* 32, W615-W619.
- Emsley, P. and Cowtan, K. (2004). Coot: model-building tools for molecular graphics. *Acta Crystallogr. D. Biol. Crystallogr.* 60, 2126-2132.
- Gell, C. et al. (2010). Microtubule dynamics reconstituted in vitro and imaged by single-molecule fluorescence microscopy. *Methods Cell Biol.* 95, 221-245.
- Helenius, J., Brouhard, G., Kalaidzidis, Y., Diez, S., and Howard, J. (2006). The depolymerizing kinesin MCAK uses lattice diffusion to rapidly target microtubule ends. *Nature* 441, 115-119.
- Jiang, K. et al. (2014). Microtubule minus-end stabilization by polymerization-driven CAMSAP deposition. *Dev. Cell* 28, 295-309.
- Kabsch, W. (2010). XDS. *Acta Crystallogr. D. Biol. Crystallogr.* 66, 125-132.
- Kammerer, R.A., Schulthess, T., Landwehr, R., Lustig, A., Fischer, D., and Engel, J. (1998). Tenascin-C hexameric assembly is a sequential two-step process initiated by coiled-coil alpha-helices. *J. Biol. Chem.* 273, 10602-10608.
- Karplus, P.A. and Diederichs, K. (2012). Linking crystallographic model and data quality. *Science* 336, 1030-1033.
- Kitagawa, D., Kohlmaier, G., Keller, D., Strnad, P., Balestra, F.R., Fluckiger, I., and Gönczy, P. (2011). Spindle positioning in human cells relies on proper centriole formation and on the microcephaly proteins CPAP and STIL. *J. Cell Sci.* 124, 3884-3893.
- Knipling, L., Hwang, J., and Wolff, J. (1999). Preparation and properties of pure tubulin. *Cell Motil. Cytoskeleton* 43, 63-71.
- McCoy, A.J., Grosse-Kunstleve, R.W., Adams, P.D., Winn, M.D., Storoni, L.C., and Read, R.J. (2007). Phaser crystallographic software. *J Appl Crystallogr.* 40, 658-674.
- Mohan, R., Katrukha, E.A., Doodhi, H., Smal, I., Meijering, E., Kapitein, L.C., Steinmetz, M.O., and Akhmanova, A. (2013). End-binding proteins sensitize microtubules to the action of microtubule-targeting agents. *Proc. Natl. Acad. Sci. U. S. A* 110, 8900-8905.
- Montenegro Gouveia, S. et al. (2010). In vitro reconstitution of the functional interplay between MCAK and EB3 at microtubule plus ends. *Curr. Biol.* 20, 1717-1722.
- Olieric, N., Kuchen, M., Wagen, S., Sauter, M., Crone, S., Edmondson, S., Frey, D., Ostermeier, C., Steinmetz, M.O., and Jaussi, R. (2010). Automated seamless DNA co-transformation cloning with direct expression vectors applying positive or negative insert selection. *BMC. Biotechnol.* 10, 56.
- Pecqueur, L., Duellberg, C., Dreier, B., Jiang, Q., Wang, C., Pluckthun, A., Surrey, T., Gigant, B., and Knossow, M. (2012). A designed ankyrin repeat protein selected to bind to tubulin caps the microtubule plus end. *Proc. Natl. Acad. Sci. U. S. A* 109, 12011-12016.
- Schindelin, J. et al. (2012). Fiji: an open-source platform for biological-image analysis. *Nat. Methods* 9, 676-682.
- Smal, I., Grigoriev, I., Akhmanova, A., Niessen, W.J., and Meijering, E. (2009). Accurate estimation of microtubule dynamics using kymographs and variable-rate particle filters. *Conf. Proc. IEEE Eng. Med. Biol. Soc.* 2009, 1012-1015.
- Tarantino, N., Tinevez, J.Y., Crowell, E.F., Boisson, B., Henriques, R., Mhlanga, M., Agou, F., Israel, A., and Laplantine, E. (2014). TNF and IL-1

exhibit distinct ubiquitin requirements for inducing NEMO-IKK supramolecular structures. *J. Cell Biol.* 204, 231-245.

Taylor, J.R. (1997). *An Introduction to Error Analysis*. University Science Books, Sausalito).

6

General Discussion

Amol Aher

Microtubule stability and lifetime are governed by the collective activities of multiple factors like the sequence and structural modifications of tubulin, the cellular microenvironment with other cytoskeletal elements, organelles and the plasma membrane providing a confinement, and the effects of microtubule associated proteins (Akhmanova and Steinmetz, 2015; Dogterom and Yurke, 1997; Janson et al., 2003). In vitro reconstitution approaches to study cellular processes in a test tube provide an opportunity to address the functions of individual proteins and thus to unravel the basic principles of organization that are employed in the complex cellular environment. Apart from its role in supporting the shape and the strength of a cell, microtubule cytoskeleton is critical for different dynamic cellular processes, such as chromosome separation during cell division. Such processes are driven by the ability of microtubules to switch between phases of polymerization and depolymerization (Desai and Mitchison, 1997). In this thesis, we shed light on the activities of multiple mammalian microtubule plus end binding proteins in the regulation of this switching behaviour using in vitro reconstitutions with purified components. We find that the mammalian microtubule plus end complexes include two modules - a growth-stabilizing module with EB, CLASP and CLIP-170, and a polymerization-promoting module consisting of chTOG, SLAIN2 and EB that stimulates fast growth but reduces microtubule stability (Chapters 2-4). In the future, it will be interesting to combine these modules in the same reconstitution to have all of the major microtubule regulators in a single assay and to see if they lead to antagonistic or additive effects.

6 In addition to investigating the dynamics of cytoplasmic microtubules, which rapidly alternate between phases of growth and shrinkage, we also addressed the mechanism governing the elongation of centriolar microtubules. Centrioles are organelles with ultra-stable microtubules that do not exhibit the typical switching behaviour at their ends and attain a final length characteristic for each species (Gonczy, 2012). Building and maintenance of a centriole involves multiple cellular factors, which are required for different steps of assembly. Multiple microtubule and tubulin binding proteins that affect centriole architecture have been characterised in cells. We investigated the molecular mechanism underlying microtubule regulation by one such factor, CPAP/SAS-4 (Chapter 5).

Microtubule growth-stabilizing module

Microtubules grow at their ends by the addition of $\alpha\beta$ -tubulin dimers, with the transient GTP-cap formed by the presence of β -tubulin-bound GTP that is hydrolysed with a delay (Mitchison and Kirschner, 1984). End binding (EB) proteins are autonomous microtubule plus end tracking proteins (+TIPs), which sense the nucleotide state of β -tubulin (Maurer et al., 2012; Zhang et al., 2015) and which have been proposed to be master regulators of microtubule growth, effecting the recruitment of other microtubule associated proteins (Akhmanova and Steinmetz, 2015; Honnappa et al., 2009; Jiang et al., 2012). It has been shown that on their own, EBs destabilize microtubule growth by accelerating the

maturation of their own binding sites and by inducing strain in the lattice, which leads to direct structural destabilization of the cap (Duellberg et al., 2016; Maurer et al., 2014; Zhang et al., 2015). To further the understanding of EB-mediated plus end regulation through other plus end binding proteins, we investigated the effects of CLASP on microtubule plus end dynamics (Chapter 2) and then extended this work to study the effect of CLIP-170-CLASP complex using purified proteins in an *in vitro* reconstitution assay (Chapter 3).

CLASPs (CLIP-associated proteins) are TOG domain-containing proteins that are essential for proper spindle microtubule dynamics and important for the microtubule poleward flux during metaphase (Logarinho et al., 2012; Maiato et al., 2003; Maiato et al., 2005). CLASPs stimulate rescues at the leading edge of migrating cells and play a role in mesenchymal cell migration in a three-dimensional environment, where they seem to enable the load-bearing function of microtubules by suppressing catastrophes at the tips of cell protrusions (Bouchet et al., 2016; Mimori-Kiyosue et al., 2005). In terms of the impact on microtubule dynamics, it was shown that CLASPs can autonomously induce rescues and also promote microtubule pausing when combined with other microtubule associated proteins (Al-Bassam et al., 2010; Moriwaki and Goshima, 2016). Since the majority of CLASP-mediated activities in mammalian cells involve the localization to the plus ends of microtubules, we investigated the importance of CLASP at the plus end together with the end binding protein-3 (EB3). We found that at the plus ends, CLASPs suppressed catastrophes, and this activity was dependent on EB-mediated concentration of CLASPs at the plus end (Chapter 2). Furthermore, we found that CLASP-mediated stabilization of the plus end is also critical for templated microtubule nucleation, where it lowers the kinetic threshold to promote microtubule outgrowth from GMPCPP seeds at sub-optimal tubulin concentrations.

We determined the minimal polypeptide sequence of CLASP sufficient for catastrophe suppression: we showed that the TOG2 domain could recapitulate the activity of the full length CLASP in inhibiting catastrophes when fused to the CH domain (the minimal microtubule plus end-binding moiety) of EB3. A previous structural study proposed that TOG2 was a tubulin binding domain, but since the curvatures of TOG2 and tubulin do not fit, significant conformational changes in either one or both of them would be needed to allow complex formation (Leano et al., 2013). In fact, we found that none of the TOG domains of CLASP bound to tubulin, but TOG2 and TOG3 weakly bound to taxol stabilized microtubules. We showed that the TOG3 domain of CLASP promotes rescue but does not suppress catastrophes. Interestingly, previous work showed that TOG2 and TOG3 bind preferentially to unique tubulin ring like oligomers induced by drugs (Maki et al., 2015). This suggests that TOG2 of CLASP possibly recognizes tubulin in a specific bent conformation present at the plus end and can also induce the transition of the peeling protofilaments in a depolymerising microtubule to the straight ones, thus promoting a switch to microtubule growth.

Cryo-electron microscopy (EM) analysis of microtubules assembled *in vitro* has

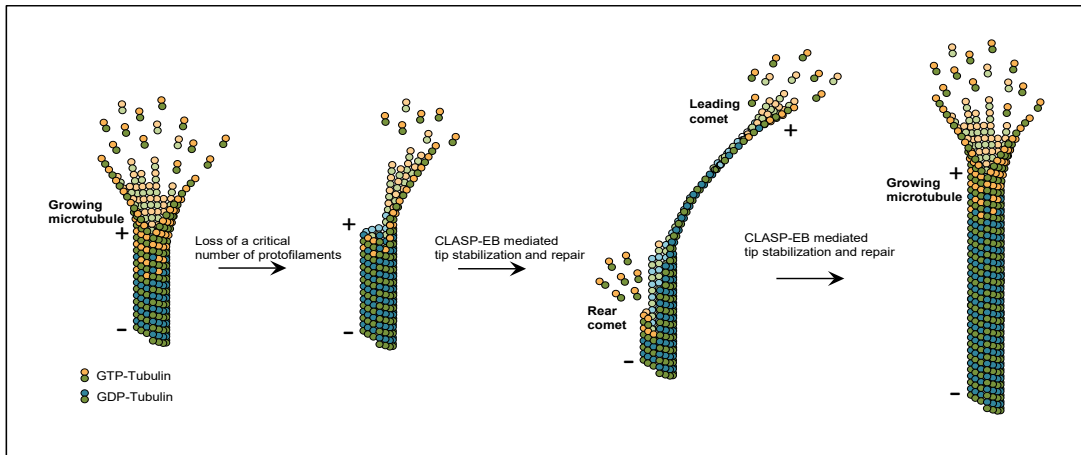


Figure 1. Microtubule tip repair mediated by CLASP and EB.

6 shown that 30-40 % of the growing microtubule ends are tapered and display curved sheet-like extensions that range from 50 to 2000 nanometers in length (Chretien et al., 1995; Mandelkow et al., 1991). Furthermore, it has been proposed that catastrophe induction involves the accumulation of a threshold number of defects in an ageing microtubule (Gardner et al., 2011). The defects lead to destabilization of the growing microtubule resulting in the tapered tip structure that predisposes it to catastrophe (Coombes et al., 2013; Gardner et al., 2011). This goes in line with findings showing that microtubule depolymerisation starts when the number of EB binding sites at the plus end is reduced below a certain threshold (Duellberg et al., 2014; Maurer et al., 2014). Extending these ideas to the EM studies leads to the possibility that the sheet-like extensions observed might correspond to these ageing, catastrophe-prone tip structures. Our experiments demonstrated that CLASP leads to stabilization of the protruding protofilaments and the ones lagging behind, thus providing a better template for the incoming dimers resulting in a faster growing ‘rear comet’ (Figure 1). This suggests that CLASP prevents catastrophes by stabilizing the tapered metastable microtubule end intermediate. Our study demonstrates that the tapering at the growing plus ends bearing a subset of protruding protofilaments is a dynamic and reversible process, with CLASP inducing the “repair” of the partial structure into a complete one.

In cells, microtubule lattices are subjected to mechanical stress due to contacts with other cytoskeletal elements, organelles or microtubules themselves. It has been shown that when microtubules were subjected to repeated bending cycles, they softened, indicating lattice damage; microtubules could recover their mechanical properties when incubated with tubulin, which was incorporated into the damaged lattice (Schaedel et al., 2015). These sites of lattice damage and repair have been shown to coincide with the presence of GTP-bound tubulin and to act as sites of microtubule rescue. This led to the hypothesis that self-repair properties of a microtubule result in the formation of GTP-islands at the lattice-damage sites that can serve as rescue hotspots (Aumeier et al., 2016; de Forges et

al., 2016). Using local laser-induced damage along the microtubule lattice, we investigated the role of CLASP in microtubule repair. Interestingly, we found that CLASP recognized the sites of lattice damage and stabilized the damaged structure leading to recovery of a complete microtubule (Figure 2). The observation that the lattice bent at the damage site undergoes straightening upon repair might reflect conformational differences between GDP and GTP tubulin, but is more likely due to the loss and restoration of some protofilaments.

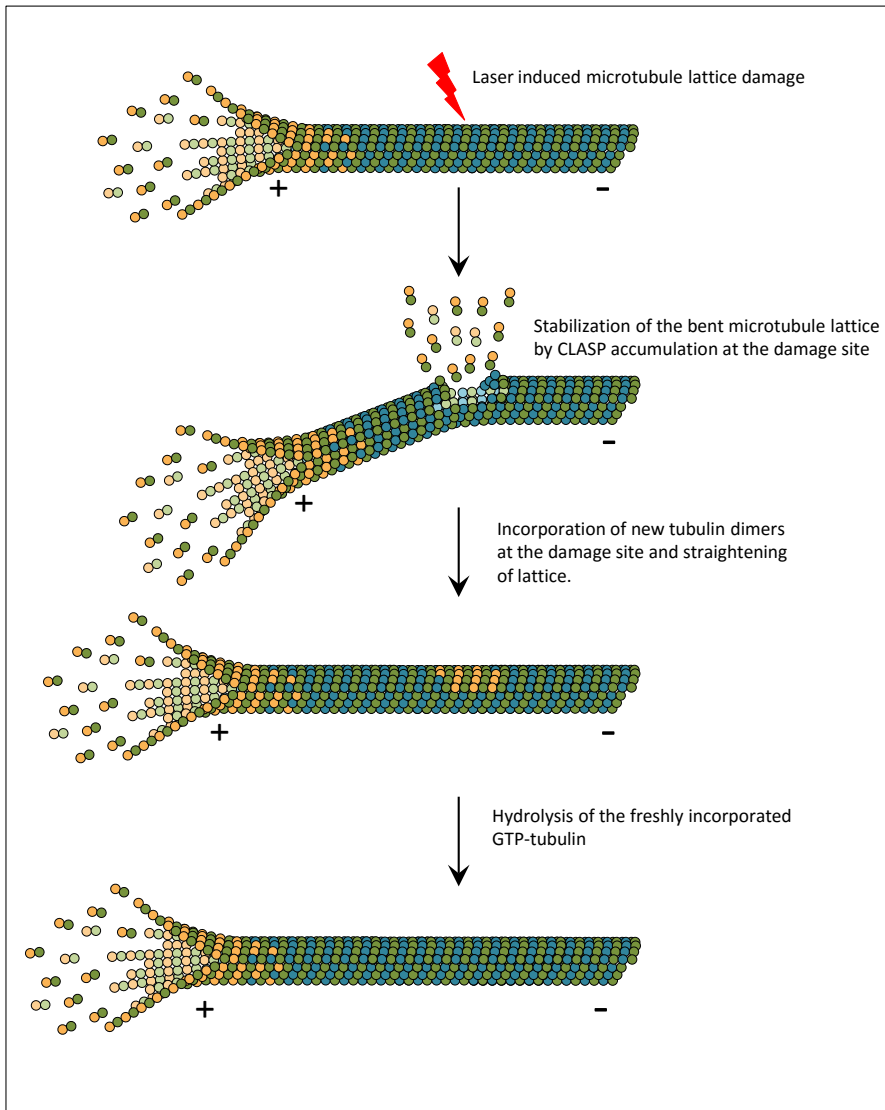


Figure 2. Schematic illustrating CLASP mediated repair of a laser-damaged microtubule lattice.

We extended our in vitro assays in the presence of CLASP to its interacting partner, CLIP-170 (Chapter 3). Reconstitution with CLIP alone suggested that it does not alter microtubule dynamics on its own but enhances CLASP-induced rescues. We found that

CLIP increased the microtubule lattice localization of CLASP possibly due to the formation of CLIP-CLASP complex with increased number of microtubule binding sites. Our experiments showed that rescues were predominantly due to the lattice-bound CLASP. Although preliminary in nature, these findings open the way to understanding rescues in cells, which until now have been proposed to be induced by the recognition of the GTP-islands by CLIP-170 (Aumeier et al., 2016; de Forges et al., 2016; Dimitrov et al., 2008). Our experiments certainly do not exclude, and in fact support the idea that the CLIP-CLASP complex might act at lattice damage sites; however, they do show that rescue can also occur spontaneously along microtubule lattices where no damage is expected.

Early electron microscopy studies of microtubules have shown that a growing microtubule has straight protofilaments which convert to inside-out coiled peeling protofilaments as a microtubule depolymerizes (Chretien et al., 1995; Mandelkow et al., 1991). A rescue involves the same structural transition in reverse, from the peeling protofilaments to the straight ones. This change could be possibly mediated by tubulin alone or by protein domains that bind to the curved peeling protofilaments and convert them into a growth-competent microtubule structure. Although it has been proposed that tubulin exchange by CLASP along the lattice induces rescues (Al-Bassam et al., 2010), structural studies have shown that the curvature of the putative tubulin binding TOG domains of CLASP is incompatible with the reported tubulin dimer curvatures (Leano et al., 2013). Furthermore, our own experiments showed that the TOG domains of CLASP and tubulin do not bind to each other. These data suggest that CLASP possibly mediates rescue by binding to the curled protofilaments of a depolymerizing microtubule, where the curvature of tubulin dimers differs from that of tubulin in solution.

6 Microtubule polymerization promoting module

Acceleration of microtubule growth by the XMAP215/chTOG/Stu2 family of polymerases has been reported to be effected through their autonomous tip tracking. EBs could contribute to this process through an allosteric effect on the microtubule tip structure, or through direct recruitment mediated by proteins bridging the EB and the polymerase (Brouhard et al., 2008; Kinoshita et al., 2001; Li et al., 2012; van der Vaart et al., 2011; Zanic et al., 2013). Although microtubule growth rates observed in cells can be reproduced in the presence of EB and XMAP215 alone (Zanic et al., 2013), alternative pathways to ensure robust fast polymerization may exist in the crowded environment of the microtubule plus end. In Chapter 4, we investigated this possibility by reconstitution of the SLAIN2-chTOG complex-mediated microtubule growth.

In accordance with previous findings (Zanic et al., 2013), we found that EB3 and chTOG were sufficient to promote *in vitro* microtubule growth rates close to the ones observed in cells. This effect depended on the concentration of chTOG and EB3, and SLAIN2, which acts as an adaptor between them, accelerated microtubule plus end growth when the concentrations of chTOG and EB3 were relatively low. Furthermore, we

observed that catastrophes were not suppressed by SLAIN2 alone or together with chTOG, which contradicts previous work suggesting that the SLAIN2-chTOG complex acts as a catastrophe inhibitor in cells (Bouchet et al., 2016; van der Vaart et al., 2011). SLAIN2 tracks growing plus ends by binding to EB3 and it has also been shown to bind to plus end stabilizing factors like CLIP-170 and CLASP (van der Vaart et al., 2011). It is possible that perturbation of SLAIN2 results in a less robust activity of CLASP, which by itself can promote processive microtubule plus end growth (Chapter 2). Alternatively, in the absence of chTOG, slowly growing microtubule ends can be more susceptible to catastrophes induced by physical barriers or other cellular factors. Finally, the shortening of the GTP cap caused by the loss of SLAIN2 and chTOG would result in reduced recruitment of EB-binding stabilizing proteins and thus increased catastrophe frequency.

chTOG is an autonomous plus end tracking protein that recognizes the curved conformation of tubulin at the growing plus end through its TOG domains and increases microtubule polymerization rates by concentrating tubulin in the vicinity of the plus end (Ayaz et al., 2014; Ayaz et al., 2012). Although SLAIN2 is not essential for targeting chTOG to the plus ends, it is tempting to speculate that it has a role in robust recruitment of chTOG in the crowded plus end environment. In the future, it will be interesting to test if there is competition between the TOG domains of CLASP, which possibly recognize certain tubulin curvatures at the plus end (Chapter 2), and the TOG domains of chTOG. Fast microtubule polymerization promoted by chTOG results in a longer GTP-cap due to rapid GTP-tubulin subunit addition coupled to the delay in GTP hydrolysis. The maximum GTP cap sizes reported in vitro (approximately 100-200 tubulin subunits) are several times smaller than the ones observed in cells (approximately 750 subunits) (Seetapun et al., 2012; Walker et al., 1991). However, the cap size estimation in vitro was done in the presence of tubulin alone. It would be interesting to investigate the GTP cap sizes in the in vitro growing microtubules exhibiting physiological growth rates and to test whether fast polymerization alone is sufficient to produce the long GTP caps seen in cells.

The localization, and thereby the activity of a +TIP on microtubule dynamics is determined by a multitude of factors like its intracellular concentration, the affinity to its binding site, post translational or structural modifications of the binding site and the competition with other proteins (Akhmanova and Steinmetz, 2008; Bieling et al., 2008; Duellberg et al., 2014; Kumar et al., 2009). For example, CLIP-170, which binds to a composite site made by the tyrosinated tails of α -tubulin and EB, is no longer recruited to the plus ends in the presence of an excess of an SxIP peptide (Bieling et al., 2008; Duellberg et al., 2014). This has been proposed to be due to the structuring of the disordered tail region of EB3 upon SxIP peptide binding to the EBH domain. SLAIN2 has been proposed to act as an adhesive +TIP due to its ability to bind multiple +TIPs; it has multiple SxIP-like motifs to ensure its recruitment by EBs (van der Vaart et al., 2011). It would be interesting to test if SLAIN2 can promote plus end tracking of CLASP in the presence of an excess of SxIP peptide, in a situation when the SxIP motifs of CLASP would not be able to recruit

it to the plus end.

Centriolar microtubule growth regulation by CPAP

Centrioles are non-compartmentalized microtubule based organelles that template the formation of cilia, flagella and centrosomes, which are critical for fundamental cellular processes like motility and division (Azimzadeh and Marshall, 2010; Gonczy, 2012; Jana et al., 2014). They are characterised by radial 9-fold symmetrically arranged microtubule triplets with a central hub. Each microtubule triplet has a complete A-microtubule and partial B and C microtubules with 10 protofilaments each (Guichard et al., 2012; Paintrand et al., 1992). In the past decade, several molecular players that are required for the centriole formation have been characterised for their activity. In particular, several tubulin interacting proteins like CEP-120, CEP-135 and CPAP have been characterised for their influence on centriole length regulation (Gudi et al., 2011; Hsu et al., 2008; Lin et al., 2013a; Lin et al., 2013b). The molecular mechanisms underlying the activities of these proteins and their possible synergistic effects on centriole length still remain elusive. Understanding these mechanisms is of great interest not only from a fundamental point of view, but also because mutations in some centriolar proteins lead to a brain development disorder, microcephaly (Woods et al., 2005).

One of the important questions in centriole assembly has been the extremely slow polymerization of centriolar microtubules, which is puzzling because they are exposed to the cytoplasmic pool of tubulin. The general view is that a network of multiple tubulin binding proteins tightly regulates tubulin incorporation in centriolar microtubules. We studied the molecular mechanism of action of one of the evolutionarily conserved regulators of centriolar microtubule growth - CPAP/SAS-4 (Chapter 5). Using X-ray crystallography and biochemical assays, we determined the atomic model of binding of the PN2-3 domain of CPAP to a tubulin dimer. Extrapolation of this information to the context of a microtubule led to a model proposing that the PN2-3 domain binds to the outermost tubulin dimer exposed at the plus end: with its LID domain, PN2-3 engages the top surface of β -tubulin, which is involved in longitudinal tubulin-tubulin interactions, while the SAC domain of PN2-3 binds to the lateral surface of the tubulin dimer.

Our reconstitution experiments using dynamic microtubules and a purified short version of CPAP (CPAP_{mini}), which contained the PN2-3 domain, the microtubule binding domain (MBD) and a dimerization motif demonstrated that it acts as an autonomous +TIP and dampens microtubule dynamics by slowing down microtubule growth and suppressing catastrophes. The tandem arrangement of the LID, SAC and MBD domains enables the specific microtubule plus end recognition. We propose that CPAP_{mini} slows down microtubule growth by the capping activity of the LID domain, whereas the dimerization of the MBDs provides stabilization of the lateral contacts between neighbouring protofilaments and thus leads to catastrophe suppression (Figure 3). These experiments demonstrate the impact of one of the centriolar regulators on microtubule

assembly.

CPAP_{mini} slowed down microtubule growth by 5-8 fold. However, centriolar microtubules exhibit growth rates in the order of a few tens of nanometers per hour (Chretien et al., 1997; Kuriyama and Borisy, 1981), which is still three orders of magnitude lower than the growth rate observed in our assays. Specific tubulin isotypes may confer slow assembly to centriolar microtubules since tubulin isotypes alone can alter microtubule dynamics (Pamula et al., 2016; Vemu et al., 2016). Furthermore, antagonistic effects on centriole length have been reported for CPAP and CP110, the capping protein located at the distal end of the centriole and known to restrict its length (Kleylein-Sohn et al., 2007; Schmidt et al., 2009). CPAP might also cooperate with other centriolar proteins such as SPICE1 or CEP-120, which interact with it to ensure proper centriole assembly (Comartin et al., 2013). How the assembly of centriolar microtubules is coupled to the mechanisms restricting their length is still an open question. Further characterization of the interactions between centriolar proteins and the investigation the molecular mechanisms underlying their individual and collective activities are needed to elucidate the process of centriole assembly.

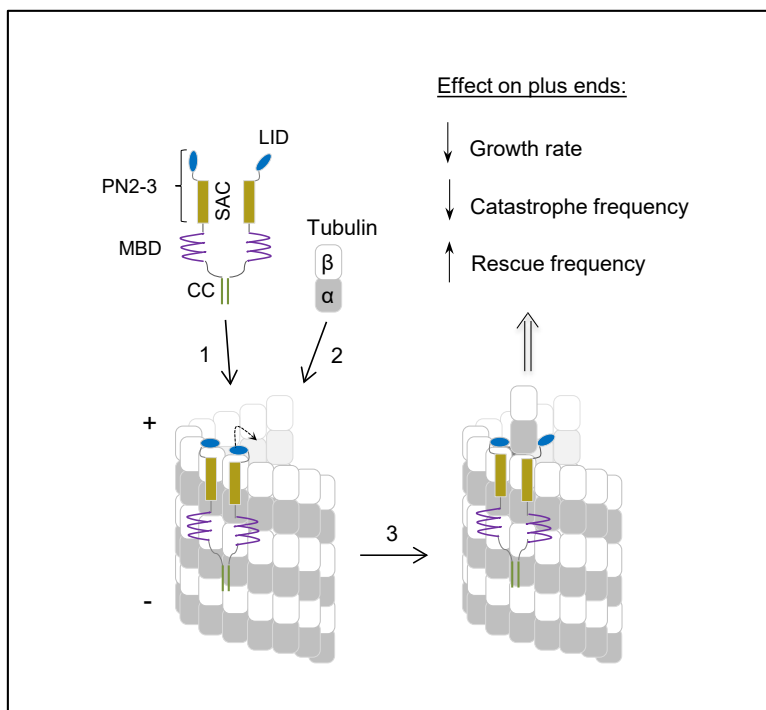


Figure 3. Working model of how CPAP_{mini} ensures slow processive microtubule growth. CPAP recognizes the microtubule plus end via tandemly arranged LID, SAC, and MBD domains (1). This stabilizes the interaction of the terminal tubulin dimers, “caps” the corresponding protofilaments, and stabilizes the microtubule lattice. “Opening” of LID (dashed curved arrow), spontaneously and/or induced by an incoming tubulin dimer (2), enables processive microtubule tip elongation (3).

Concluding remarks

The regulation of transitions between phases of microtubule growth and shrinkage by multiple cellular factors has been studied extensively over the past decade. In this thesis, we extended these studies to mammalian +TIPs and addressed their individual and combined activities through increasingly complex reconstitution assays. In the final chapter, we demonstrated that the centriolar protein CPAP is an unusual +TIP with a novel mechanism of action. Taken together, our results pave the way to achieving a profound understanding the self-organizing principles that underlie the ability of cells to generate different microtubule networks with a particular size, density and dynamic properties.

References

- Akhmanova, A., and M.O. Steinmetz. 2008. Tracking the ends: a dynamic protein network controls the fate of microtubule tips. *Nat Rev Mol Cell Biol.* 9:309-322.
- Akhmanova, A., and M.O. Steinmetz. 2015. Control of microtubule organization and dynamics: two ends in the limelight. *Nat Rev Mol Cell Biol.* 16:711-726.
- Al-Bassam, J., H. Kim, G. Brouhard, A. van Oijen, S.C. Harrison, and F. Chang. 2010. CLASP promotes microtubule rescue by recruiting tubulin dimers to the microtubule. *Dev Cell.* 19:245-258.
- Aumeier, C., L. Schaedel, J. Gaillard, K. John, L. Blanchoin, and M. Thery. 2016. Self-repair promotes microtubule rescue. *Nat Cell Biol.* 18:1054-1064.
- Ayaz, P., S. Munyoki, E.A. Geyer, F.A. Piedra, E.S. Vu, R. Bromberg, Z. Otwinowski, N.V. Grishin, C.A. Brautigam, and L.M. Rice. 2014. A tethered delivery mechanism explains the catalytic action of a microtubule polymerase. *Elife.* 3:e03069.
- Ayaz, P., X. Ye, P. Huddleston, C.A. Brautigam, and L.M. Rice. 2012. A TOG:alpha-tubulin complex structure reveals conformation-based mechanisms for a microtubule polymerase. *Science.* 337:857-860.
- Azimzadeh, J., and W.F. Marshall. 2010. Building the centriole. *Curr Biol.* 20:R816-825.
- Bieling, P., S. Kandels-Lewis, I.A. Telley, J. van Dijk, C. Janke, and T. Surrey. 2008. CLIP-170 tracks growing microtubule ends by dynamically recognizing composite EB1/tubulin-binding sites. *J Cell Biol.* 183:1223-1233.
- Bouchet, B.P., I. Noordstra, M. van Amersfoort, E.A. Katrukha, Y.C. Ammon, N.D. Ter Hoeve, L. Hodgson, M. Dogterom, P.W. Derksen, and A. Akhmanova. 2016. Mesenchymal Cell Invasion Requires Cooperative Regulation of Persistent Microtubule Growth by SLAIN2 and CLASP1. *Dev Cell.* 39:708-723.
- Brouhard, G.J., J.H. Stear, T.L. Noetzel, J. Al-Bassam, K. Kinoshita, S.C. Harrison, J. Howard, and A.A. Hyman. 2008. XMAP215 is a processive microtubule polymerase. *Cell.* 132:79-88.
- Chretien, D., B. Buendia, S.D. Fuller, and E. Karsenti. 1997. Reconstruction of the centrosome cycle from cryoelectron micrographs. *J Struct Biol.* 120:117-133.
- Chretien, D., S.D. Fuller, and E. Karsenti. 1995. Structure of growing microtubule ends: two-dimensional sheets close into tubes at variable rates. *J Cell Biol.* 129:1311-1328.
- Comartin, D., G.D. Gupta, E. Fussner, E. Coyaud, M. Hasegan, M. Archinti, S.W. Cheung, D. Pinchev, S. Lawo, B. Raught, D.P. Bazett-Jones, J. Luders, and L. Pelletier. 2013. CEP120 and SPICE1 cooperate with CPAP in centriole elongation. *Curr Biol.* 23:1360-1366.
- Coombes, C.E., A. Yamamoto, M.R. Kenzie, D.J. Odde, and M.K. Gardner. 2013. Evolving tip structures can explain age-dependent microtubule catastrophe. *Curr Biol.* 23:1342-1348.
- de Forges, H., A. Pilon, I. Cantaloube, A. Pallandre, A.M. Haghiri-Gosnet, F. Perez, and C. Pous. 2016. Localized Mechanical Stress Promotes Microtubule Rescue. *Curr Biol.* 26:3399-3406.
- Desai, A., and T.J. Mitchison. 1997. Microtubule polymerization dynamics. *Annu Rev Cell Dev Biol.* 13:83-117.
- Dimitrov, A., M. Quesnoit, S. Moutel, I. Cantaloube, C. Pous, and F. Perez. 2008. Detection of GTP-tubulin conformation in vivo reveals a role for GTP remnants in microtubule rescues. *Science.* 322:1353-1356.
- Dogterom, M., and B. Yurke. 1997. Measurement

- of the force-velocity relation for growing microtubules. *Science*. 278:856-860.
- Duellberg, C., N.I. Cade, D. Holmes, and T. Surrey. 2016. The size of the EB cap determines instantaneous microtubule stability. *Elife*. 5.
- Duellberg, C., M. Trokter, R. Jha, I. Sen, M.O. Steinmetz, and T. Surrey. 2014. Reconstitution of a hierarchical +TIP interaction network controlling microtubule end tracking of dynein. *Nat Cell Biol*. 16:804-811.
- Gardner, M.K., M. Zanic, C. Gell, V. Bormuth, and J. Howard. 2011. Depolymerizing kinesins Kip3 and MCAK shape cellular microtubule architecture by differential control of catastrophe. *Cell*. 147:1092-1103.
- Gonczy, P. 2012. Towards a molecular architecture of centriole assembly. *Nat Rev Mol Cell Biol*. 13:425-435.
- Gudi, R., C. Zou, J. Li, and Q. Gao. 2011. Centrobintubulin interaction is required for centriole elongation and stability. *J Cell Biol*. 193:711-725.
- Guichard, P., A. Desfosses, A. Maheshwari, V. Hachet, C. Dietrich, A. Brune, T. Ishikawa, C. Sachse, and P. Gonczy. 2012. Cartwheel architecture of *Trichonympha* basal body. *Science*. 337:553.
- Honnappa, S., S.M. Gouveia, A. Weisbrich, F.F. Damberger, N.S. Bhavesh, H. Jawhari, I. Grigoriev, F.J. van Rijssel, R.M. Buey, A. Lawera, I. Jelesarov, F.K. Winkler, K. Wuthrich, A. Akhmanova, and M.O. Steinmetz. 2009. An EB1-binding motif acts as a microtubule tip localization signal. *Cell*. 138:366-376.
- Hsu, W.B., L.Y. Hung, C.J. Tang, C.L. Su, Y. Chang, and T.K. Tang. 2008. Functional characterization of the microtubule-binding and -destabilizing domains of CPAP and d-SAS-4. *Exp Cell Res*. 314:2591-2602.
- Jana, S.C., G. Marteil, and M. Bettencourt-Dias. 2014. Mapping molecules to structure: unveiling secrets of centriole and cilia assembly with near-atomic resolution. *Curr Opin Cell Biol*. 26:96-106.
- Janson, M.E., M.E. de Dood, and M. Dogterom. 2003. Dynamic instability of microtubules is regulated by force. *J Cell Biol*. 161:1029-1034.
- Jiang, K., G. Toedt, S. Montenegro Gouveia, N.E. Davey, S. Hua, B. van der Vaart, I. Grigoriev, J. Larsen, L.B. Pedersen, K. Bezstarosti, M. Lince-Faria, J. Demmers, M.O. Steinmetz, T.J. Gibson, and A. Akhmanova. 2012. A Proteome-wide screen for mammalian SxIP motif-containing microtubule plus-end tracking proteins. *Curr Biol*. 22:1800-1807.
- Kinoshita, K., I. Arnal, A. Desai, D.N. Drechsel, and A.A. Hyman. 2001. Reconstitution of physiological microtubule dynamics using purified components. *Science*. 294:1340-1343.
- Kleylein-Sohn, J., J. Westendorf, M. Le Clech, R. Habedanck, Y.D. Stierhof, and E.A. Nigg. 2007. Plk4-induced centriole biogenesis in human cells. *Dev Cell*. 13:190-202.
- Kumar, P., K.S. Lyle, S. Gierke, A. Matov, G. Danuser, and T. Wittmann. 2009. GSK3beta phosphorylation modulates CLASP-microtubule association and lamella microtubule attachment. *J Cell Biol*. 184:895-908.
- Kuriyama, R., and G.G. Borisy. 1981. Microtubule-nucleating activity of centrosomes in Chinese hamster ovary cells is independent of the centriole cycle but coupled to the mitotic cycle. *J Cell Biol*. 91:822-826.
- Leano, J.B., S.L. Rogers, and K.C. Slep. 2013. A cryptic TOG domain with a distinct architecture underlies CLASP-dependent bipolar spindle formation. *Structure*. 21:939-950.
- Li, W., T. Moriwaki, T. Tani, T. Watanabe, K. Kaibuchi, and G. Goshima. 2012. Reconstitution of dynamic microtubules with *Drosophila* XMAP215, EB1, and Sentin. *J Cell Biol*. 199:849-862.
- Lin, Y.C., C.W. Chang, W.B. Hsu, C.J. Tang, Y.N. Lin, E.J. Chou, C.T. Wu, and T.K. Tang. 2013a. Human microcephaly protein CEP135 binds to hSAS-6 and CPAP, and is required for centriole assembly. *EMBO J*. 32:1141-1154.
- Lin, Y.N., C.T. Wu, Y.C. Lin, W.B. Hsu, C.J. Tang, C.W. Chang, and T.K. Tang. 2013b. CEP120 interacts with CPAP and positively regulates centriole elongation. *J Cell Biol*. 202:211-219.
- Logarinho, E., S. Maffini, M. Barisic, A. Marques, A. Toso, P. Meraldi, and H. Maiato. 2012. CLASPs prevent irreversible multipolarity by ensuring spindle-pole resistance to traction forces during chromosome alignment. *Nat Cell Biol*. 14:295-303.
- Maiato, H., E.A. Fairley, C.L. Rieder, J.R. Swedlow, C.E. Sunkel, and W.C. Earnshaw. 2003. Human CLASP1 is an outer kinetochore component that regulates spindle microtubule dynamics. *Cell*.

- 113:891-904.
- Maiato, H., A. Khodjakov, and C.L. Rieder. 2005. *Drosophila* CLASP is required for the incorporation of microtubule subunits into fluxing kinetochore fibres. *Nat Cell Biol.* 7:42-47.
- Maki, T., A.D. Grimaldi, S. Fuchigami, I. Kaverina, and I. Hayashi. 2015. CLASP2 Has Two Distinct TOG Domains That Contribute Differently to Microtubule Dynamics. *J Mol Biol.* 427:2379-2395.
- Mandelkow, E.M., E. Mandelkow, and R.A. Milligan. 1991. Microtubule dynamics and microtubule caps: a time-resolved cryo-electron microscopy study. *J Cell Biol.* 114:977-991.
- Maurer, S.P., N.I. Cade, G. Bohner, N. Gustafsson, E. Boutant, and T. Surrey. 2014. EB1 accelerates two conformational transitions important for microtubule maturation and dynamics. *Curr Biol.* 24:372-384.
- Maurer, S.P., F.J. Fourniol, G. Bohner, C.A. Moores, and T. Surrey. 2012. EBs recognize a nucleotide-dependent structural cap at growing microtubule ends. *Cell.* 149:371-382.
- Mimori-Kiyosue, Y., I. Grigoriev, G. Lansbergen, H. Sasaki, C. Matsui, F. Severin, N. Galjart, F. Grosveld, I. Vorobjev, S. Tsukita, and A. Akhmanova. 2005. CLASP1 and CLASP2 bind to EB1 and regulate microtubule plus-end dynamics at the cell cortex. *J Cell Biol.* 168:141-153.
- Mitchison, T., and M. Kirschner. 1984. Dynamic instability of microtubule growth. *Nature.* 312:237-242.
- Moriwaki, T., and G. Goshima. 2016. Five factors can reconstitute all three phases of microtubule polymerization dynamics. *J Cell Biol.* 215:357-368.
- Paintrand, M., M. Moudjou, H. Delacroix, and M. Bornens. 1992. Centrosome organization and centriole architecture: their sensitivity to divalent cations. *J Struct Biol.* 108:107-128.
- Pamula, M.C., S.C. Ti, and T.M. Kapoor. 2016. The structured core of human beta tubulin confers isotype-specific polymerization properties. *J Cell Biol.* 213:425-433.
- Schaedel, L., K. John, J. Gaillard, M.V. Nachury, L. Blanchoin, and M. Thery. 2015. Microtubules self-repair in response to mechanical stress. *Nat Mater.* 14:1156-1163.
- Schmidt, T.I., J. Kleylein-Sohn, J. Westendorf, M. Le Clech, S.B. Lavoie, Y.D. Stierhof, and E.A. Nigg. 2009. Control of centriole length by CPAP and CP110. *Curr Biol.* 19:1005-1011.
- Seetapun, D., B.T. Castle, A.J. McIntyre, P.T. Tran, and D.J. Odde. 2012. Estimating the microtubule GTP cap size in vivo. *Curr Biol.* 22:1681-1687.
- van der Vaart, B., C. Manatschal, I. Grigoriev, V. Olieric, S.M. Gouveia, S. Bjelic, J. Demmers, I. Vorobjev, C.C. Hoogenraad, M.O. Steinmetz, and A. Akhmanova. 2011. SLAIN2 links microtubule plus end-tracking growth proteins and controls microtubule growth in interphase. *J Cell Biol.* 193:1083-1099.
- Vemu, A., J. Atherton, J.O. Spector, A. Szyk, C.A. Moores, and A. Roll-Mecak. 2016. Structure and Dynamics of Single-isoform Recombinant Neuronal Human Tubulin. *J Biol Chem.* 291:12907-12915.
- Walker, R.A., N.K. Pryer, and E.D. Salmon. 1991. Dilution of individual microtubules observed in real time in vitro: evidence that cap size is small and independent of elongation rate. *J Cell Biol.* 114:73-81. nucleating activity of centrosomes in Chinese hamster ovary cells is independent of the centriole cycle but coupled to the mitotic cycle. *J Cell Biol.* 91:822-826.
- Woods, C.G., J. Bond, and W. Enard. 2005. Autosomal recessive primary microcephaly (MCPH): a review of clinical, molecular, and evolutionary findings. *Am J Hum Genet.* 76:717-728.
- Zanic, M., P.O. Widlund, A.A. Hyman, and J. Howard. 2013. Synergy between XMAP215 and EB1 increases microtubule growth rates to physiological levels. *Nat Cell Biol.* 15:688-693.
- Zhang, R., G.M. Alushin, A. Brown, and E. Nogales. 2015. Mechanistic Origin of Microtubule Dynamic Instability and Its Modulation by EB Proteins. *Cell.* 162:849-859.

Addendum

Summary
Samenvatting
Curriculum Vitae
List of publications
Acknowledgements

Summary

Tipping microtubule polymerization: Insights from in vitro reconstitution

Microtubules are biopolymers composed of $\alpha\beta$ -tubulin dimers that associate in a head-to-tail fashion into protofilaments, which interact laterally to form a tube. Tubulin dimers are incorporated at the growing microtubule ends in a GTP-bound form. Within a polymerized microtubule lattice, GTP is hydrolysed to GDP, but this process occurs with a time delay. This leads to the formation of a transient GTP cap that stabilizes the growing microtubule, whereas its loss results in a switch to shrinkage, termed catastrophe. Control of the transitions from microtubule growth to shrinkage is critical for fundamental processes like cell division, morphogenesis and migration. Multiple intrinsic and extrinsic factors shape microtubule networks by regulating these transitions, as discussed in Chapter 1.

CLASP is one of the conserved regulators of microtubule dynamics important to maintain the microtubule polymer mass in interphase and proper spindle microtubule dynamics during mitosis. The major biochemical activity previously reported for CLASP was microtubule rescue, the transition from shrinkage to growth. We revisited the role of CLASP in the context of its localization at the microtubule plus end and found that it acts as a microtubule stabilizing factor, which suppresses both spontaneous and induced catastrophes (Chapter 2). We dissected the minimal biochemical modules of CLASP that lead to catastrophe suppression and rescue activity. We further found that CLASP stabilizes partial structures at the microtubule plus end and in damaged microtubule lattices, leading to their restoration.

In Chapter 3, we extended our reconstitution to the complex of CLASP with CLIP-170, a reported microtubule rescue factor. Characterization of the effects of CLIP-170 on dynamic microtubules revealed that it does not alter microtubule dynamics autonomously at the concentrations we used. However, we found that CLIP-170 increased CLASP-mediated rescues by promoting CLASP association with the microtubule lattice.

In Chapter 4, we investigated the regulation of microtubule growth by the complex of the mammalian microtubule polymerase chTOG with EB3 and the adaptor protein SLAIN2. We found that microtubule growth rates observed in cells could be recapitulated in vitro with certain concentrations of purified EB3 and chTOG. We next tested the effects of SLAIN2 and found that, when combined with chTOG, it enhanced the effect of this microtubule polymerase by further increasing microtubule growth rate and catastrophe frequency. Fast microtubule polymerization by chTOG alone or the SLAIN-chTOG complex could antagonize the ability of the microtubule-depolymerizing kinesin-13 MCAK to block microtubule growth. However, SLAIN and chTOG did not suppress the catastrophes induced by MCAK.

In addition to investigating the regulation of cytoplasmic microtubules, we also studied the regulation of centriolar microtubules, focussing on a conserved centriolar protein CPAP/SAS-4 (Chapter 5). We found that the PN2-3 domain of CPAP could potentially

interfere with the addition of new tubulins at the microtubule tip by binding to the outer surface of the terminal tubulin dimers. We engineered a truncated version of CPAP containing the tubulin and microtubule binding domains and showed that it autonomously tracked the plus ends, reduced microtubule growth rate and suppressed catastrophes. We further extended this work to look at the importance of CPAP for centriole assembly in cells and showed that the CPAP mutants impaired in blocking microtubule plus end growth induced over-elongation of the centriole.

To summarise, we showed that different protein assemblies regulate distinct aspects of microtubule dynamics by virtue of their specialized domains and interactions. As discussed in Chapter 6, our study highlights the complexity of the molecular mechanisms utilised by microtubule associated proteins, which determine the architecture of microtubule arrays by regulating microtubule dynamics at the plus end.



Samenvatting

Het controleren van microtubuli polymerisatie: inzichten van in vitro reconstituties

Microtubuli zijn biopolymeren bestaande uit $\alpha\beta$ -tubuline dimeren die, door toedoen van kop-staart interacties, associëren in protofilamenten. Deze protofilamenten ondergaan laterale interacties waarbij buisjes wordt gevormd. Tubuline dimeren worden in een GTP gebonden vorm geïncorporeerd in de uiteinden van groeiende microtubuli. Eenmaal in de microtubuli wordt GTP gehydrolyseerd naar GDP. Dit proces vindt plaats met een vertraging wat leidt tot de vorming van een dynamische GTP-kap die groeiende microtubuli stabiliseert. Verlies van de GTP-kap resulteert in de afbraak van microtubuli, ook wel bekend als een catastrofe. Controle over de transitie van microtubuli groei naar afbraak is essentieel voor fundamentele processen als celdeling, morfogenese en migratie. Meerdere intrinsieke en extrinsieke factoren beïnvloeden microtubuli netwerken door deze transities te reguleren zoals beschreven in Hoofdstuk 1.

CLASP is één van de geconserveerde regulatoren van microtubuli dynamica welke belangrijk zijn voor het behoud van de microtubuli polymeer massa in interfase en voor microtubuli dynamica in de mitotische spindel tijdens celdeling. De belangrijkste biochemische activiteit voorheen beschreven voor CLASP was microtubuli 'rescue', de transitie van afbraak naar groei. We hebben de rol van CLASP opnieuw onderzocht in de context van de localisatie op de plus-einden van microtubuli. Daarbij hebben we ontdekt dat CLASP fungeert als een microtubuli stabiliserende factor, welke zowel spontane als geïnduceerde catastrofes onderdrukt (Hoofdstuk 2). Wij hebben de minimale biochemische modules van CLASP ontleed welke leiden tot de catastrofe suppressie en 'rescue' activiteit. Daarnaast hebben we ontdekt dat CLASP de structuren aan de microtubuli plus-einden en beschadigde microtubuli oppervlakken stabiliseert wat resulteert in herstel van de microtubuli.

In Hoofdstuk 3 hebben we onze reconstitutie van het CLASP complex uitgebreid met CLIP-170, een eiwit voorheen beschreven als microtubuli 'rescue' factor. Het in kaart brengen van de effecten van CLIP-170 op microtubuli dynamica onthulde dat CLIP-170, bij de door ons gebruikte concentraties, geen effect had op microtubuli dynamica. CLIP-170 verhoogde daarentegen de CLASP-afhankelijke 'rescues' door de interactie tussen CLASP en microtubuli te verhogen.

In Hoofdstuk 4 hebben we de rol van het eiwitcomplex bestaande uit de microtubuli polymerase chTOG, EB3 en het adapter eiwit SLAIN2 in regulatie van microtubuli groei bestudeerd. We hebben ontdekt dat de groeisnelheden van microtubuli in cellen kunnen worden benaderd met bepaalde concentraties van opgezuiverd EB3 en chTOG in vitro. Vervolgens hebben we de effecten van SLAIN2 bestudeerd, wat resulteerde in de bevinding dat, in combinatie met chTOG, SLAIN2 het effect van deze microtubuli polymerase vergroot door zowel de groeisnelheden als catastrofe frequenties van microtubuli te

verhogen. Snelle microtubuli polymerisatie veroorzaakt door chTOG of het SLAIN-chTOG complex was voldoende om de inhibitie van de groei van microtubuli door de microtubuli-depolymeriserende kinesine-13 MCAK te neutraliseren. Echter, SLAIN en chTOG waren niet in staat om de door MCAK geïnduceerde catastrofes te onderdrukken.

Naast het onderzoeken van de regulatie van cytoplasmatische microtubuli, hebben we ook de regulatie van centriool gebonden microtubuli onderzocht. Hierbij hebben we ons gefocust op het geconserveerde centriool eiwit CPAP/SAS-4 (Hoofdstuk 5). We hebben ontdekt dat het PN2-3 domein van CPAP kan interfereren met de toevoeging van nieuwe tubulines aan de uiteinden van microtubuli door aan de buitenkant van tubuline dimeren te binden. We hebben een verkorte versie van CPAP ontwikkeld die zowel de tubuline als de microtubuli bindende domeinen bevat. Dit construct lokaliseert specifiek naar de plus-einden van de microtubuli waar het zowel de microtubuli groei als catastrofes onderdrukte. Dit werk hebben we uitgebreid door de rol van CPAP in centriool ontwikkeling van cellen te bestuderen. Hier hebben we aangetoond dat CPAP mutanten die niet in staat waren de plus-einden van microtubuli te blokkeren, overgroei van centriolen induceren.

Samengevat hebben we laten zien dat verschillende eiwitcomplexen, op grond van gespecialiseerde domeinen en interacties, verschillende aspecten van microtubuli dynamica reguleren. Zoals bediscussieerd in Hoofdstuk 6 beschrijft onze studie de complexiteit van de moleculaire mechanismes die de architectuur van microtubuli netwerken bepalen door de dynamica van de microtubuli plus-einden te reguleren.



Curriculum Vitae

Amol Aher was born on April 19th, 1989 in Aurangabad, India. He started his university studies in 2006 at the Institute of Bioinformatics and Biotechnology, Pune, India. As a part of the Integrated Master's program, he performed a research internship under the supervision of Prof. Krishanu Ray at the Department of Biological Sciences, Tata Institute of Fundamental Research, Mumbai, India. During this internship, he focused on mapping kinesin 2-microtubule interactions. After graduating in 2011, he started working as a project assistant with Dr. Ravi Manjithaya at the Molecular Biology and Genetics Unit, Jawaharlal Nehru Centre for Advanced Scientific Research in Bangalore, India. As a project assistant, he investigated the role of different cytoskeletal elements in selective autophagy in yeast until 2013. In 2013, he started his PhD studies under the supervision of Prof. dr. Anna Akhmanova in the Cell Biology division of Utrecht University. The results of the research are described in this thesis.



List of publications

CLASP suppresses catastrophes by stabilizing incomplete microtubule plus ends through a single TOG domain.

Amol Aher, Maurits Kok, Ashwani Sharma, Ankit Rai, Natacha Olieric, Ruddi Rodriguez-Garcia, Eugene A. Katrukha, Tobias Weinert, Vincent Olieric, Lukas C. Kapitein, Michel O. Steinmetz, Marileen Dogterom and Anna Akhmanova.

(Submitted)

Deconvolution of Buparlisib's mechanism of action defines specific PI3K and tubulin inhibitors for therapeutic intervention.

Thomas Bohnacker, Andrea E. Prota, Florent Beauflis, John E. Burke, Anna Melone, Alison J. Inglis, Denise Rageot, Alexander M. Sele, Vladimir Cmiljanovic, Natasa Cmiljanovic, Katja Bargsten, Amol Aher, Anna Akhmanova, J. Fernando Díaz, Dorian Fabbro, Marketa Zvelebil, Roger L. Williams, Michel O. Steinmetz and Matthias P. Wymann.

Nature Communications, 2017. 8:14683.

Centriolar CPAP/SAS-4 imparts slow processive microtubule growth.

Ashwani Sharma,* Amol Aher,* Nicola J. Dynes,* Daniel Frey, Eugene A. Katrukha, Rolf Jaussi, Ilya Grigoriev, Marie Croisier, Richard A. Kammerer, Anna Akhmanova, Pierre Gonczy, and Michel O. Steinmetz.

Developmental Cell 37, 362–376.

*These authors contributed equally to the work.

The C-terminal tails of heterotrimeric kinesin-2 motor subunits directly bind to α -tubulin1: Possible implications for cilia- specific tubulin entry.

Mukul Girotra, Shalini Singh, Anuttama Kulkarni, Debnath Ghosal, Pavithra Devan, Kratika Bobra, Amol Aher, Akanksha Jain, Dulal Panda and Krishanu Ray.

Traffic, 2016. 1-11.



Acknowledgements

I still vividly remember the day I arrived in the Netherlands. After realising that I was really away from everyone and everything I knew before, I kept staring at the Schiphol airport arrivals for a while and wondering if the same plane I arrived in could take me back home. Now I am faced with a similar feeling when it is almost time to say goodbye. It has been an incredible journey for me as a scientist and as a person for the past 4 and half years which would not have been possible if not for the amazing people around me. This thesis is the result of the collaborations and inputs from multiple people across different groups. I would like to express my gratitude towards them.

First of all, I would like to thank my supervisor- Anna. I have learnt so many things about science and life in general from you and still feel there is such a long way to go. I am grateful to you for the guidance and encouraging me through the years. Your infectious passion for science has been a constant source of inspiration for me. Your prompt attitude towards problem solving and research in general has changed the way I approach things. I have thoroughly enjoyed discussing projects and ideas with you in the weekly meetings and emails over the years. Like everyone else, I am always amazed by your vast knowledge and critical inputs during meetings. Your constant emphasis on combining both cellular and reconstitution approaches has hopefully rubbed off a bit on me. I am thankful to you for letting me pursue projects that I found interesting and also for the opportunity for supervising students which I enjoyed a lot. I wish you the best for the future. I am sure our paths will cross in future in my scientific endeavour and I hope we stay in touch.

I have had the opportunity to interact and collaborate with multiple PI's and groups which has shaped this thesis. During the course of my PhD, I collaborated extensively with the lab of Michel. Michel, it has always been a pleasure to discuss the ongoing projects and ideas with you at the conferences and retreats over the years. Your systematic and thorough way of addressing questions has been always helpful. I enjoyed a lot my brief stay at your lab and wish you all the best for the future. I am thankful to all the members of the synergy consortium and in particular Marileen. Your feedback and unique inputs during the synergy meetings and otherwise have helped a lot. Your philosophy towards reconstitution and bottom-up biology approaches to understand workings of a system has definitely shaped my way of thinking and addressing questions. I wish you all the best for all the cool reconstitutions and experiments in the future. I am also thankful to other members of the synergy consortium- Prof. Gijse Koenderink, Prof. Bela Mulder and members of their laboratories for the inputs during the meetings. I would like to express my gratitude towards Pierre for the fantastic collaboration on the CPAP project and it was always a joy discussing the project with you at the centriole retreat and the skype meetings. I would like to extend my gratitude towards Casper and Susanne for the opportunity to

&

collaborate and the discussions on the projects.

I am grateful to Lukas for all the discussions on my experiments and most of all for the shared passion for microtubules and in vitro reconstitutions. I have always felt more enthusiastic about my data after discussing it with you and your amazing super-resolution eye and the ability to stare at movies has taught me you can observe a lot by watching. I wish you all the best for the future scientific pursuits. I would like to thank all of the faculty and their lab members from the departments of Cell biology and Developmental biology for their inputs over the years at the work discussions and lunch meetings.

I would also like to thank all the thesis committee members- Marileen Dogterom, Geert Kops, Susanne Lens, Friedrich Förster and Marc Baldus for taking out time to evaluate my thesis.

I would like to thank all my collaborators who contributed to the book with their expertise. Ashwani, I am thankful to you for the efforts in both CPAP and CLASP projects and your 3-week visit to Utrecht was the most productive time I had in my PhD. I believe this is just a beginning and hope we stay in touch in future as well. Natacha, it was fun to work with you on EM during my visit to Switzerland. Many thanks for all the experiments and the proteins you purified over the years for us. I wish you the best for future. I would like to thank Nicola and members of the Gönzy lab for their feedback and contributions to the CPAP project. Maurits, we started working together as part of the synergy consortium. I am always amazed by your persistence towards troubleshooting experiments and I have enjoyed working together with you at Delft and Utrecht. I wish you all the best for finishing up and best of luck for the future. I am also grateful to Ingrid and Amélie who I started collaborating towards the end of my PhD which has led to exciting results. It was always refreshing to brainstorm about the central spindle and how the axon initial segment is built. I wish you both good luck with the projects and your future scientific endeavours.

Over the years, I have had a great company of lab-mates in the Akhmanova lab. First and foremost, I would like to thank Ivar, my first friend at cell biology and a bestie now. I think you are one of the kindest people I know. It was always fun with you at all the parties, retreats, masterclass and outings and your wedding (It was such an amazing party!). I will miss all those practice runs and competing at the singelloop. I will especially remember our adventurous drives through the storm in Germany and USA :) I am looking forward to graduating on the same day! I wish you and Lilian the best in Australia and I am sure we will meet again some place some time in future. Kai or super-kai (as most people would agree), I believe you have been more of a co-supervisor to me. To be honest, I have never seen any other person who is so dedicated and immersed in his work. I am grateful to you for all the scientific discussions at the meetings or at the lab. I have always looked up to



you whenever I felt things were not going smoothly. I am thankful to you and Shasha for all the help in the lab and all the possibilities with reconstitution. I wish you both the best for your lab and future. I would like to thank our microscopy guru- Ilya for all the help from introducing me to the TIRF microscopes and teaching me how cool it is to shoot microtubules with lasers. You are a very funny person and it was nice collaborating with you on multiple occasions and thank you for the help with the cover. Wish you all the best for the future. I am also grateful to Hari for helping me during the early period of my PhD and teaching me protein purifications and trouble shooting in vitro assays. Jingchao, the local knock-out expert, it has always been fun having you around. I enjoyed a lot all the outings together with Ivar especially the Germany trip. You have a unique sense of humour. I wish you all the best with the postdoc and hope to see you in the future as well. Ben, I am grateful to you for teaching me cell culture, all the extensive discussions about CLASP and of course the never-ending discussions on movies.

Ankit, I am grateful to you for all the help with the experiments and analysis for the CLASP paper. I am always amazed by your patience and thanks for all the amazing indian food at your place. Best of luck for your future. Ruddi, it has always given me a lot of pleasure discussing about microtubules with you in the hallway or lab. I am also thankful to you for all the contributions to the CLASP paper and wish you the very best for your future. Maud, it is amazing the way you manage your work and family time. I wish you all the best for your papers and with starting your group in Belgium. I would like to thank Fangrui for all the nice conversations in the lab and best of luck with the projects. Chao, the EB expert of the lab, good luck with finishing up. Eugene, like many people in the department, I cannot imagine how hard it would have been without your help to perform all the single molecule analysis. You are one of the most approachable and friendliest people in the department. I have always enjoyed our conversations about the big questions in science at the borrels. I wish you the best for your career and life in general. We still need to plan the India trip!

&

I would like to thank all the previous members of my office- Renu, thank you for introducing me to the world of in vitro reconstitution, Carol, you had been a great support system during the beginning of my PhD, I wish you all the best for your future. Helma, over the years we became good friends. It was always comforting to talk to you about things going wrong in the lab and the occasional cool experiments. It was quite an amazing experience being your paranimf. Thank you for hosting the photography workshop together with Roel and I wish you and your family the best for future. I would like to thank Andrea and Qingyang for the nice and friendly environment at the office. A special thanks to Qingyang for running all the mass-spectrometry samples for me. Peter Jan, the MAP- and the ICT-guy, you have been around first as a master's student and now as a PhD. It was always a blast organizing all the defence parties with you and York. I am glad our research paths finally crossed at the magical component-MAP7 ;) I wish you all the best and I am

sure you will keep doing great in the coming time as well. York, I believe you are the most organized person in our lab and thanks for all the nice chats at lunch and getting things in the lab in order. Chiung-Yi, the sole physicist of our office, it has been fun having you around and I wish you all the best for your PhD. I wish all the best to the newbies of the Akhmanova lab- Dipti and Cynthia.

During my PhD, I have had the opportunity of supervising students during various courses and for internships. I have always enjoyed a lot participating in the Molecular and Cellular Biology course for the Bachelor students. I would like to thank Fons and Laurens for giving me a chance to participate in the course. Martyna, you were my first student and I was always amazed by your systematic and independent ways of doing things in the lab. Thank you for the initial work on CLASP in mitosis and I wish you the very best for your future. Wouter, I think you have worked with me the most, starting with the Fons course, a short internship and for the major master's internship. Right from the very beginning, there was something peculiar about you that made working with you a lot of fun. You are a very honest and hard-working person and the CLIP chapter would not have materialised without you. I am sure a great future lies ahead of you and all the best for your next journey! Tonja, initially I was sceptical about having 2 students at the same time but my opinion changed after you started working in the lab. Your patience with testing new things and maintaining hundreds of cell lines always amazes me. I wish you all the best for the future!

I would like to thank people from cell biology and developmental biology who I have had the chance to interact with and made it a nice environment to be in. I would like to thank members of Lukas lab- for all the fun at the lab outings and parties. Roderick, you are one of the most passionate about microtubules people I know, keep it up and good luck with your projects. Wilco, thank you for all the wise suggestions on imaging mitotic cells and all the inputs during meetings. Anael, you will be badly missed at all the parties; all the philosophical and scientific chats with you were always very intriguing. Anne, thanks for all the nice chats at the borrels. Mithila, thank you for being there to have a look at all the cool in vitro assays and all the discussions with you about different projects have always added a new perspective to my thinking. I would like to thank Desiree and Eliana for all the fun at parties. I would also like to thank members of Casper lab- Phebe and Bart for their prompt help with ordering and fixing things around in the lab. Martin, your inputs at the work discussions have always been helpful and all the hallway chats have been very interesting. I would like to thank Riccardo and Robin for all the short breaks and conversations over lunch or coffee breaks and best of luck with your projects. Hai-yin, your patience with the experiments on two-photon still fascinates me. I wish you the best finishing up and good luck with the future. I would like to thank Esther, Harold, Sabrina, Paul and Corette and members of their groups for all the inputs over the years and best of



luck for their scientific journey. Josta, Cátia, Nora and Hanna, thank you for all the fun and crazy times as part of the amazing lab outing committee 2014. Vincent and Bram, of course for saving my life ;) Lars, the worm guy, you are always enthusiastic and curious about experiments and possibilities. Conversations with you in the hallway are always very cheerful. Best of luck with finishing up and best wishes for the future. Suzanne, Ruben, all the best for future!

I am grateful to an amazing group of people who kept me sane over the years and were part of the group addiction to stay airborne. I would like to thank Petra and Max for organizing the awesome trip in French Alps and introducing me to the amazing world few hundred metres above. I wish you both the best of luck in USA and hope to see you again and hopefully fly together sometime in the future. Bas or Bassie, the party animal of cell biology, you have a great sense of humour and it has always been fun on all our flying trips together with Marina. I hope there are more to come in the future. Marina, one of the most cheerful and ever smiling person on the floor, it has always been very relaxing and comforting to talk to you. I have always looked up to you for being a positive, hard-working and a kind person. Thank you for hosting me at your department for a talk and for the endless stories and fun during all the para-holidays. I wish you the best for your lab and towards becoming an independent pilot!

Last but not the least I would like to thank all my friends and family back in India for their support through the years. I am indebted forever to my parents and my brother for their unconditional love and support.

